

FOLLOWING CARBON'S EVOLUTIONARY PATH: FROM NUCLEOSYNTHESIS
TO THE SOLAR SYSTEM

by

Stefanie Nicole Milam

Copyright © Stefanie Nicole Milam 2007

A Dissertation Submitted to the Faculty of the

DEPARTMENT OF CHEMISTRY

In Partial Fulfillment of the Requirements

For the Degree of
DOCTOR OF PHILOSOPHY

In the Graduate College

THE UNIVERSITY OF ARIZONA

2007

THE UNIVERSITY OF ARIZONA
GRADUATE COLLEGE

As members of the Dissertation Committee, we certify that we have read the dissertation prepared by **Stefanie Nicole Milam**

entitled **Following Carbon's Evolutionary Path: From Nucleosynthesis to the Solar System**

and recommend that it be accepted as fulfilling the dissertation requirement for the Degree of **Doctor of Philosophy**

_____ Date: October 24, 2007
Dr. Lucy M. Ziurys

_____ Date: October 24, 2007
Dr. Stephen Kukolich

_____ Date: October 24, 2007
Dr. Andrei Sanov

_____ Date: October 24, 2007
Dr. Christopher K. Walker

_____ Date: October 24, 2007
Dr. Susan Wyckoff

Final approval and acceptance of this dissertation is contingent upon the candidate's submission of the final copies of the dissertation to the Graduate College.

I hereby certify that I have read this dissertation prepared under my direction and recommend that it be accepted as fulfilling the dissertation requirement.

_____ Date: October 24, 2007
Dissertation Director: **Dr. Lucy M. Ziurys**

STATEMENT BY AUTHOR

This dissertation has been submitted in partial fulfillment of requirements for an advanced degree at the University of Arizona and is deposited in the University Library to be made available to borrowers under rules of the Library.

Brief quotations from this dissertation are allowable without special permission, provided that accurate acknowledgment of source is made. Requests for permission for extended quotation from or reproduction of this manuscript in whole or in part may be granted by the copyright holder.

SIGNED: Stefanie Nicole Milam

ACKNOWLEDGEMENTS

I would like to first acknowledge my advisor, Dr. L. M. Ziurys, for her support and guidance throughout my graduate career. She has helped me achieve numerous tasks that surpassed even my expectations.

Many thanks to Drs. S. Wyckoff, N. Woolf, A. Remijan, and A. Apponi for guidance, patience, mentorship, and support over the last few years. These individuals never gave up on me and helped me through even the roughest of times.

I would also like to recognize key individuals in my education including my committee members, A. Sanov, S. Kukolich, and C. Walker, as well as my undergraduate mentors D. Hanna and Y. Chiang. These people have given me the education and guidance I need for a career in the physical sciences.

Recognition is given to my fellow graduate students C. Savage, P. Sheridan, and M. Flory for their continued patience, support, and friendship. Also, a special thanks goes to the Arizona Radio Observatory engineers and staff for all their hard work to keep the telescopes in excellent condition.

Finally, a special acknowledgement goes to my family; my mother and father for their support in my decision to pursue this degree and my husband, Lawrence, for absolutely everything.

TABLE OF CONTENTS

LIST OF FIGURES	7
LIST OF TABLES	8
ABSTRACT	9
CHAPTER 1. INTRODUCTION	11
CHAPTER 2. TELESCOPES	13
a. Arizona Radio Observatory 12 m	15
b. Arizona Radio Observatory Submillimeter Telescope	16
CHAPTER 3. FORMATION OF CARBON: $^{12}\text{C}/^{13}\text{C}$ IN CIRCUMSTELLAR ENVELOPES	18
a. CN ($X^2\Sigma^+$)	20
b. $^{12}\text{C}/^{13}\text{C}$	21
c. Implications and Nucleosynthesis	26
d. VY Canis Majoris	30
e. Planetary Nebulae	32
CHAPTER 4. CARBON IN THE INTERSTELLAR MEDIUM: $^{12}\text{C}/^{13}\text{C}$ RATIOS	36
a. $^{12}\text{CN}/^{13}\text{CN}$ $N=1\rightarrow 0$	37
b. $^{12}\text{CN}/^{13}\text{CN}$ From Multiple Transitions	40
CHAPTER 5. CARBON IN THE SOLAR SYSTEM: COMETS	45
a. H_2CO and CO Extended Source	47
b. Other Organics and Planetary Distribution	49
CONCLUSIONS	51
APPENDIX A. HCO^+ OBSERVATIONS TOWARDS COMET HALE-BOPP (C/1995 O1): ION-MOLECULE CHEMISTRY AND EVIDENCE FOR A VOLATILE SECONDARY SOURCE	52
APPENDIX B. THE $^{12}\text{C}/^{13}\text{C}$ ISOTOPE GRADIENT DERIVED FROM MILLIMETER TRANSITIONS OF CN: THE CASE FOR GALACTIC CHEMICAL EVOLUTION	62
APPENDIX C. FORMALDEHYDE IN COMETS C/1995 O1 (HALE-BOPP), C/2002 T7 (LINEAR) AND C/2001 Q4 (NEAT): INVESTIGATING THE COMETARY ORIGIN OF H_2CO	70

TABLE OF CONTENTS – *Continued*

APPENDIX D. CHEMICAL COMPLEXITY IN THE WINDS OF THE OXYGEN-RICH SUPERGIANT STAR VY CANIS MAJORIS	80
APPENDIX E. DETECTION OF NaCl TOWARDS IK Tau AND VY CMa: OXYGEN-RICH MASS LOSS WITH A PINCH OF SALT	87
APPENDIX F. CONSTRAINING PHOSPHORUS CHEMISTRY IN CARBON- AND OXYGEN-RICH CIRCUMSTELLAR ENVELOPES: OBSERVATIONS OF PN, HCP, AND CP	92
APPENDIX G. THE DISTRIBUTION, EXCITATION AND FORMATION OF COMETARY MOLECULES: METHANOL, METHYL CYANIDE AND ETHYLENE GLYCOL	120
APPENDIX H. A SURVEY OF CIRCUMSTELLAR $^{12}\text{C}/^{13}\text{C}$ ISOTOPE RATIOS DERIVED FROM CN AND CO: NUCLEOSYNTHESIS IN VARIOUS TYPES OF STARS	155
APPENDIX I. THE CN N=2→1 ISOTOPE GRADIENT: FURTHER STUDIES OF GALACTIC CHEMICAL EVOLUTION	241
REFERENCES	278

LIST OF FIGURES

Figure 2.1. Atmospheric Transmission Plot	13
Figure 2.2. LO Source and Phase Lock Loop for Arizona Radio Observatory	15
Figure 3.1. Energy Level Diagram for CN ($X^2\Sigma^+$)	19
Figure 3.2. ^{12}C N and ^{13}C N Observations Towards CRL 2688	20
Figure 3.3. Sample Spectra of CN N=2→1 Towards Y CVn	21
Figure 3.4. Modeled Line Profiles of CN	25
Figure 3.5. $^{12}\text{C}/^{13}\text{C}$ Circumstellar Ratios vs. C/O	27
Figure 3.6. Detection of HCO^+ Towards VY CMa	30
Figure 3.7. CCH Observed Towards Three Evolved Planetary Nebulae	34
Figure 4.1. Galactic Gradient of $^{12}\text{C}/^{13}\text{C}$ as a Function of Distance to the Galactic Center	38
Figure 4.2. H_2CO , CN, and CO Chemical Network in Molecular Clouds	39
Figure 4.3. Sample Spectra of CN N=2→1 in Molecular Clouds	40
Figure 4.4. Observed Self-Absorption Profile Towards W31	41
Figure 4.5. Rotational Diagram of ^{12}C N in Orion Bar	42
Figure 5.1. Spectra of H_2CO with Second Velocity Component in T7 LINEAR	48
Figure 5.2. CH_3CN Measured Towards Hale-Bopp	49

LIST OF TABLES

Table 1. Frequencies and Relative Intensities of CN	24
Table 2. $^{12}\text{C}/^{13}\text{C}$ Ratios Measured Towards Circumstellar Envelopes	29
Table 3. List of Confirmed Molecules in VY CMa	31
Table 4. $^{12}\text{C}/^{13}\text{C}$ Ratios From CN, CO, and H_2CO Towards Molecular Clouds	44
Table 5. Molecules and Abundances in Comets	45

ABSTRACT

Studies of carbon's evolutionary path have been conducted via millimeter and submillimeter observations of circumstellar envelopes (CSEs), planetary nebulae (PNe), molecular clouds and comets. The $^{12}\text{C}/^{13}\text{C}$ isotope ratio was measured in Galactic molecular clouds using the CN isotopologs. A gradient of $^{12}\text{CN}/^{13}\text{CN}$ was determined to be $^{12}\text{C}/^{13}\text{C} = 6.01 D_{\text{GC}} + 12.28$, where D_{GC} is distance from the Galactic center. The results of CN are in agreement with those of CO and H₂CO indicating a true ratio not influenced by fractionation effects or isotope-selective photodissociation. The $^{12}\text{C}/^{13}\text{C}$ isotope ratios in the envelopes of various types of stars were also measured from both CO and CN isotopologs. Such objects as carbon and oxygen-rich asymptotic giant branch (AGB) stars, supergiants, planetary nebulae, and S-type stars were observed. Results from this study indicate $^{12}\text{C}/^{13}\text{C}$ values for supergiants ~ 10 and AGB stars $^{12}\text{C}/^{13}\text{C} \sim 20$ -76. Theory would suggest a lower ratio for objects undergoing third dredge-up, though this is seemingly not the case. Multiple carbon-bearing species including CO, HCN, HNC, CN, CS, and HCO⁺ have also been observed towards the oxygen-rich supergiant, VY CMa. This object has recently revealed a unique chemistry where carbon is not solely contained in CO, and may play a more important role in the chemical network of oxygen-rich circumstellar envelopes. Additionally, observations of species with carbon-carbon bonds, such as CCH and c-C₃H₂, have been conducted towards evolved planetary nebulae, such as the Helix and Ring nebulae. There is a close agreement in the inventories of species found in PNe and diffuse clouds, suggesting a potential molecular precursor to the interstellar medium. Observations of carbon-bearing species (H₂CO and

CO) in comets C/1995 O1 (Hale-Bopp), C/2001 Q4 (NEAT), and C/2002 T7 (LINEAR) have been conducted. Formaldehyde is known to have an extended distribution in these objects, likely arising from silicate-organic grains. Evidence of cometary fragmentation was also obtained for H₂CO in comet T7 LINEAR as well as for HNC and HCO⁺ in Hale-Bopp. Such events could contribute to planetary distribution of organics.

CHAPTER 1. INTRODUCTION

Where do we come from? Are we alone? Where are we going? These questions have been contemplated by philosophers and scientists for centuries. In fact, NASA has created the Astrobiology Institute in order to address these questions. My research focuses on the evolution of our galaxy and where the initial precursors of carbon-based life are formed throughout the universe. Carbon is the cornerstone of all biological process; hence, the study of this atom is fundamental in understanding the origin of life. Carbon has two major isotopes, ^{12}C and ^{13}C . The abundance ratio of these two isotopes provides important information about the chemical complexity of the material in which they are found and the conditions from which they are formed.

The interstellar medium is enriched in both carbon isotopes when evolved stars begin to eject their outer layers of mass into the surrounding regions of space; this material is known as the circumstellar envelope (CSE). The star's dust then drifts through space until it either forms its own molecular cloud or merges with another cloud. Molecular clouds then form new stars by gravitationally collapsing, thus recycling the dust and molecules of the original star. At this stage, the new stars can evolve to form planetary systems that will be greatly enriched by stellar material from previous generations.

Material flowing from the star, in the CSE, is rapidly expanding, lowering the density to $\sim 10^4$ particles cm^{-3} and effectively cooling the dust and gas to low temperatures (~ 25 K). The gas found in molecular clouds is also cool (~ 10 -50 K) and dense and are therefore excited primarily by collisions limiting the observable

wavelengths to the rotational levels of molecules. Pure rotational spectroscopy is ideal for determining the composition as well as other source properties in this medium because it is conducted at high resolutions. Rotational spectroscopy of various molecules yields a key pattern specific to each species, making the interstellar identification fairly direct.

The results presented in this thesis follow carbon's evolutionary path from its formation in stars, distribution through the stellar lifecycle into the interstellar medium (ISM) and planetary systems. Comets are known for their pristine nature and thus are employed to gain understanding into the medium from which our sun and planets have formed. The oxygen-rich nature of our Solar System makes the presence of a carbon-dominated organic chemistry difficult to explain, though this work will help lead to resolving these fundamental questions.

CHAPTER 2. TELESCOPES

In order to conduct high resolution millimeter/submillimeter molecular observations, a balance between receiver sensitivity and noise enhancements must be maintained. First, one must realize receiver limitations at these wavelengths: atmospheric window, waveguide bands, and the local oscillator (LO) bandwidth.

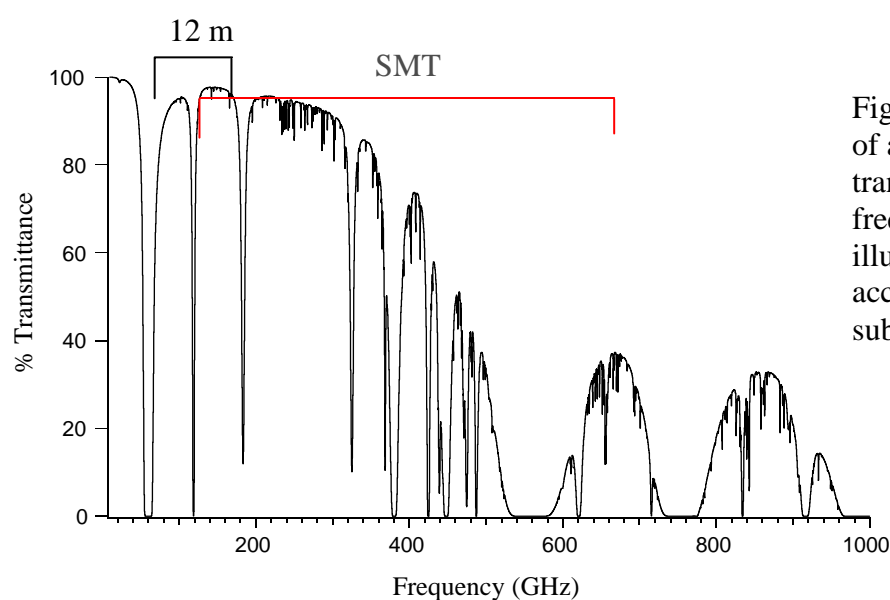


Figure 2.1. A plot of atmospheric transmission vs. frequency, illustrating the accessible mm and sub-mm windows.

Receivers are built and optimized for the various atmospheric windows, which for the Arizona Radio Observatory include the frequency coverage from ~ 68-500 GHz.

Receivers must have radiation guided to them for proper detection. The optical elements of the ARO facilities are both Cassegrain systems. The main reflector, or primary, is either a 10 m or 12 m diameter paraboloid and the secondary or subreflector is a hyperboloid mirror. Ray optics do not describe the behavior of radiation at millimeter wavelengths, thus Gaussian beam optics must be employed to direct the radiation into either one of two receiver systems. The radiation is channeled through the optical system of the telescope into a cross grid, which delivers two orthogonal polarizations into a three

stage dewar. Each polarization has its own receiver, which is a heterodyne system preserving both phase and frequency. Since heterodyne receivers are sensitive to only polarized radiation, half the signal would be lost without the use of the cross-grid.

The signal enters the receiver through a Teflon lens which directs it into a feedhorn. The sky signal is then coupled with the local oscillator (LO) signal from a source outside of the dewar. The two signals are then mixed within the superconductor-insulator-superconductor (SIS) mixer to yield an intermediate frequency (ν_{IF}). A superconductor functions when a photon impinges upon a superconducting material, producing an electron which then combines with another electron creating a ‘‘Cooper pair’’. These pairs can be separated when twice the binding energy is applied to them. This separation is the energy of the bandgap in the superconductor. When a voltage is applied to a SIS structure, the energy states between the two superconductors are shifted, and Cooper pairs can tunnel through the insulator to the opposite superconductor and a current is detected. The two input signals, sky and local oscillator, of the nonlinear device give an output current of:

$$I = a[V_o + V_s \sin(2\pi f_s t) + V_l \sin(2\pi f_l t)]^2, \quad (1)$$

where V_o is the applied voltage, V_s is the sky voltage with frequency f_s , and V_l is the LO voltage with frequency f_l .

The LO source for the receivers at ARO are solid-state Gunn oscillators. These devices give a pure signal with minimal driving power (~ 10 V). The problem with Gunn oscillators is that their output frequency drifts with time (exponential time dependence). In order to correct for this, a phase lock loop (Figure 2.2) is utilized to sample the Gunn

frequency and correct for deviations that occur in time. The loop takes a small portion of the Gunn signal and mixes it with a synthesizer signal to make the IF output from the SIS mixer 1.5 GHz for the 12 m and 4-6 GHz for the SMT. Once the two signals are mixed,

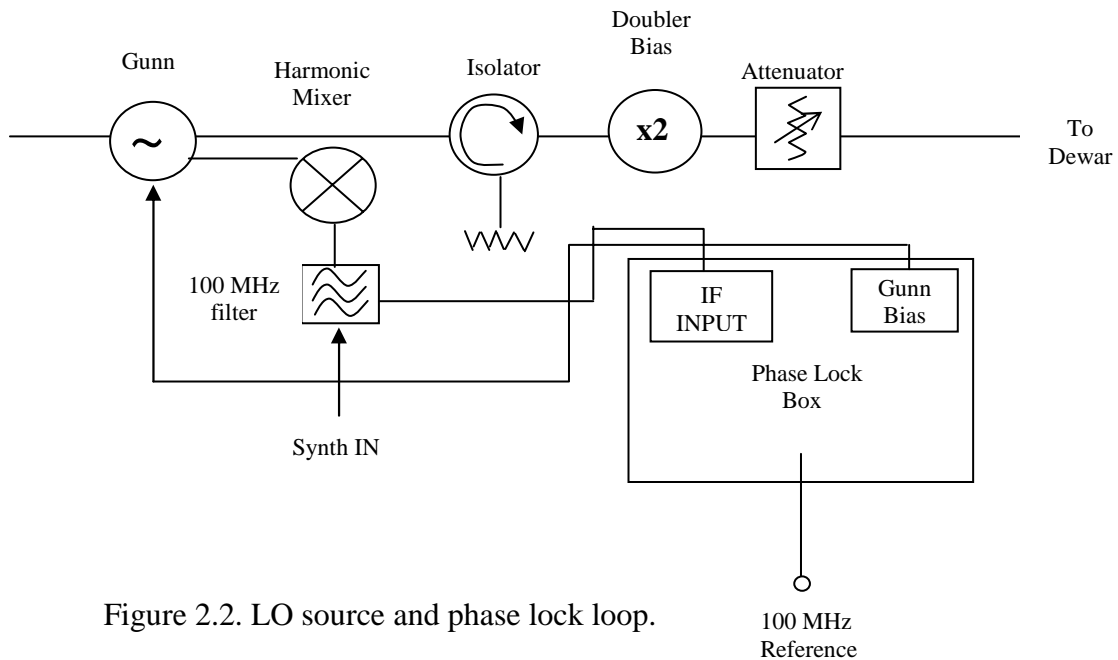


Figure 2.2. LO source and phase lock loop.

the new frequency is on the order of 100 MHz and is compared to a “reference” signal. The reference signal is stabilized by a Rubidium standard set at 100 MHz. A phase comparator distinguishes the phase difference between the Gunn signal and the reference and adjusts the Gunn bias to alter the Gunn output frequency. This is a continuous cycle that keeps the LO stable for long period of time, allowing for longer integrations at a single sky frequency.

a. Arizona Radio Observatory 12 m

Parts of the data collected for this research were measured with the Arizona Radio Observatory (ARO) 12 m telescope located on Kitt Peak, AZ. At 6280 feet, this telescope gets optimal weather for observations at millimeter wavelengths. With a

Cassegrain configuration and a 12 m paraboloid primary dish, the f/D ratio is 13.8 for this particular radio telescope.

Currently there are three sets of dual-channel SIS receivers: 2mm, 3mmlo and 3mmhi. These receivers cover the frequency range from 68-178 GHz and are all part of heterodyne systems. There are two types of backend spectrometers for this telescope, filterbanks and an auto-correlator. There are 8 different filterbanks with six different resolutions; 30 kHz, 100 kHz, 250 kHz, 500 kHz, 1 MHz (2 sets), and 2 MHz (2 sets). All but the 30 kHz filters have 256 channels/bank. The different filterbanks can be configured in either series or parallel observing modes. A parallel configuration is usually used for spectral line observations, while series mode is good for surveys or broadband observations. The Millimeter Auto-Correlator (MAC) is a digital device comprising of comparators and multiple delays. The total bandwidth designations for the MAC are: 100, 200, 400, or 800 MHz, which allows for this particular device to have as high a resolution as 37 kHz.

b. Arizona Radio Observatory Submillimeter Telescope

The main reflector of the ARO Submillimeter telescope (SMT), or primary, is a 10 m diameter ($f=0.35$) paraboloid made of molded carbon fiber reinforced plastic (CFRP) panels with an aluminum coating. CFRP is a very insensitive to temperature fluctuations making the primary dish and the support structure very stable on a day-to-night basis. The accuracy of the primary was measured by holography in 2000 resulting in a RMS of 15 μm over the entire surface. The secondary or subreflector is a 0.69 m

hyperboloid ($f=13.8$). The telescope has a dual Nasmyth (or bent Cassegrain) focus directing radiation into either one of two receiver rooms.

The main receiver system used for the research described here was the new ALMA Band 6 side-band separating mixers (Lauria et al. 2006). This device, coupled with the large bandwidth filterbanks allow for ~ 4 GHz of frequency coverage simultaneously. A dual-channel mode can also be employed for simultaneous parallel and perpendicular radiation detection. This mixer allowed for single-sideband (SSB) system temperatures ~ 100 K at the center of the band. Rejection for this device is typically 20 dB for the lower sideband and ~ 12 for the upper sideband. The IF employed for this system is steerable from 4-6 GHz making for a versatile bandwidth coverage that can be tweaked to optimize observations for both sidebands.

CHAPTER 3. FORMATION OF CARBON: $^{12}\text{C}/^{13}\text{C}$ IN CIRCUMSTELLAR ENVELOPES

Carbon-12 is predicted to be formed in the triple alpha reaction (Timmes, Woosley, and Weaver 1995), where three helium atoms fuse together. The less abundant isotope, carbon-13, is formed during the carbon-nitrogen-oxygen (CNO) cycle occurring in older stars that have evolved from the main sequence. The transition from a main sequence star to a Red Giant occurs after shell hydrogen-burning begins and the stellar radius grows with a decrease in the effective temperature. The star will then begin convection and the first dredge-up, where hydrogen-burning ashes are brought to the surface and reprocessed in the burning shells of the star. This effectively lowers the $^{12}\text{C}/^{13}\text{C}$ ratio by the conversion of the newly exposed core material to form nitrogen via CNO processing (Iben & Renzini 1983). A second dredge-up phase then follows ($M > 4 M_{\odot}$) when the core helium is exhausted and nearly all the ^{12}C and ^{16}O has been transformed into ^{14}N and there are both hydrogen- and helium-burning shells in close proximity to one another. After these processes have occurred and the hydrogen-shell becomes extinct, the star will begin to thermally pulse and this phase is known as the asymptotic giant branch (TP-AGB) phase. Here, pure ^{12}C is mixed into the envelope thereby raising the $^{12}\text{C}/^{13}\text{C}$ ratio and the C/O ratio; potential for carbon-star formation. The dredge-up properties of AGB stars are not well understood (Herwig and Austin 2004), but obviously have significant impact for interstellar isotope abundances.

Isotope studies towards AGB and Red Giant stars have been primarily focused on carbon-rich CSEs (e.g. Kahane et al. 1992; Lambert et al. 1986; Schoier & Olofsson

2000). Molecular $^{12}\text{C}/^{13}\text{C}$ ratios in O-rich envelopes are rare in that these observations were typically constrained to CO for a few objects – assuming that all the carbon in an oxygen shell is locked into CO. HCN was employed for one study, though saturation effects may play a role in the $^{12}\text{C}/^{13}\text{C}$ values obtained (Nercessian et al. 1989). Optical and infrared results suggest low ratios indicative of CNO processing and substantial mixing of the core with the outer layers of these stars (Lambert et al. 1986). Of all the previous studies to gain understanding in the nucleosynthesis and processes that occur in stars that have evolved off the main sequence, only a few had a variety of objects at various evolutionary stages and chemistries. Here, a self-consistent study of the $^{12}\text{C}/^{13}\text{C}$ isotope ratios towards oxygen-rich and carbon-rich AGB envelopes, as well as S-type stars (C ~ O), proto-planetary nebulae, and supergiants have been determined and compared. The ratio was obtained from

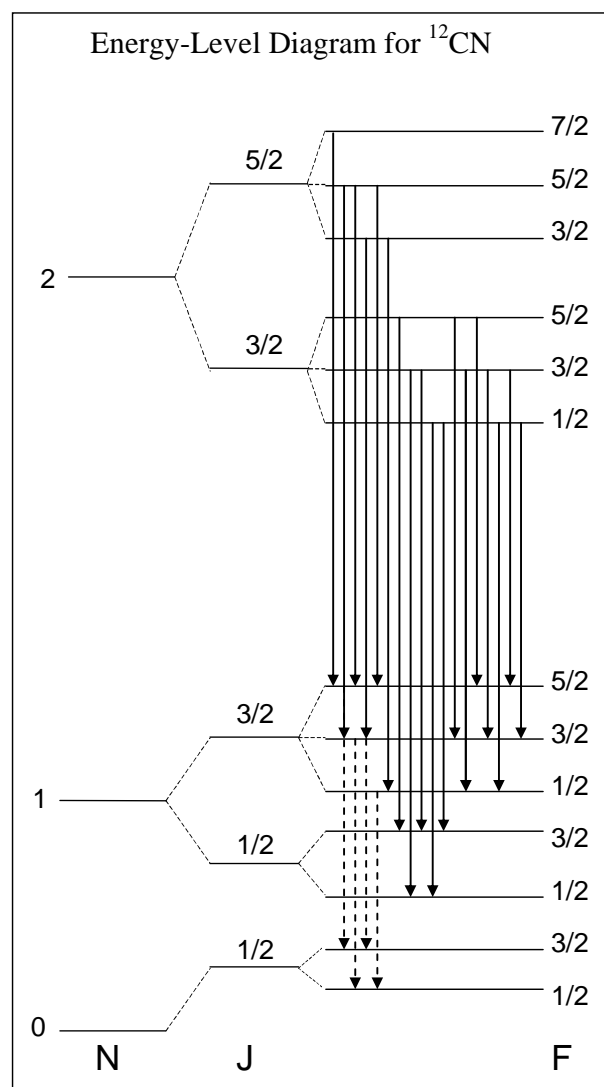


Figure 3.1. Energy level diagram of ^{12}CN and observed transitions.

the pure rotational spectra of CO and CN, with their corresponding isotopologs, at millimeter wavelengths.

a. $\text{CN X } ^2\Sigma^+$

The CN radical has a $X ^2\Sigma$ ground state, thus a complex rotation spectrum, Figure 3.1 (see Savage et al. 2002; Milam et al. 2005). An example of the hyperfine structure in both isotopologs for the $N=1\rightarrow 0$ and $N=2\rightarrow 1$ transitions are shown in Figure 3.2.

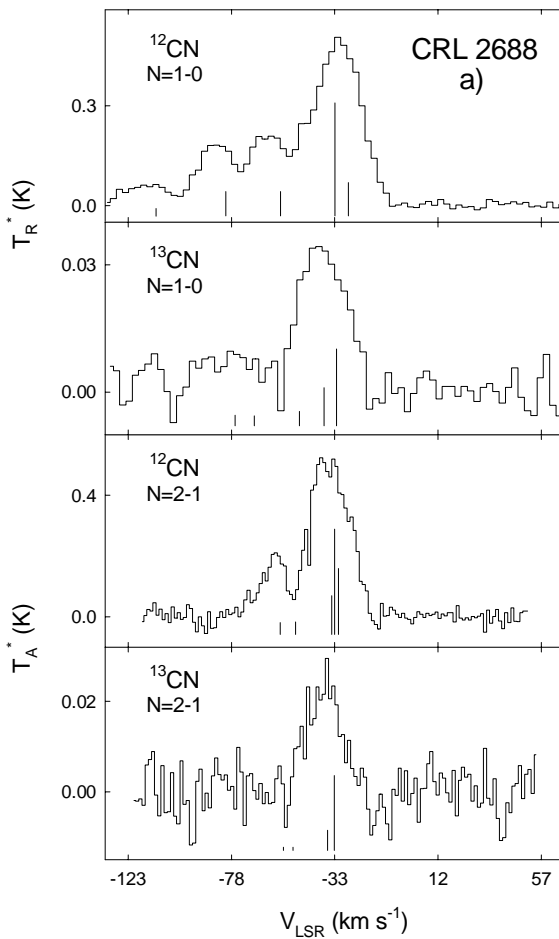


Figure 3.2. ^{12}CN and ^{13}CN observations towards CRL 2688.

The strongest features of the $N=1\rightarrow 0$ rotational transition of both ^{12}CN ($J=3/2\rightarrow 1/2$ spin component) and ^{13}CN ($F_1=1\rightarrow 0, F_2=2\rightarrow 1$ spin component) are displayed in these references. Each transition is split into multiple features resulting from the nuclear spins of nitrogen ($I=1$) and carbon-13 (^{13}CN only; $I=1/2$), whose relative intensities are plotted beneath the observed spectra in Figure 3.2. This $J=3/2\rightarrow 1/2$ spin component of ^{12}CN consists of five individual hyperfine (hf) components, indicated by the quantum number F .

The $N=2\rightarrow 1$ spectra of ^{12}CN is far

more complex with over 15 observable transitions, Figure 3.1, in the large bandwidth of

the SMT. Figure 3.3 shows an example of the full spectrum of the $N=2 \rightarrow 1$ features observed towards Y CVn. The $N=1 \rightarrow 0$ transition in ^{13}CN also consists of five hyperfine components, but these lie closer in frequency, hence most are blended together. The ^{13}CN spectrum is more complicated because the ^{13}C nucleus has a spin of $I=1/2$. Here, the two spins are coupled to the rotational motion to generate quantum numbers F_1 , F_2 , and F . The $N=2 \rightarrow 1$ transition of ^{13}CN is as highly complex as that of ^{12}CN , however, the strongest feature is a blend of the $F=3 \rightarrow 2$, $F=4 \rightarrow 3$ and $F=2 \rightarrow 1$ components of the $F_1=2 \rightarrow 1$, $F_2=3 \rightarrow 2$ lines.

b. $^{12}\text{C}/^{13}\text{C}$ Ratios

In order to obtain a self consistent, directly comparable dataset, the CO observations were modeled by a radiative transfer code to derive the fractional abundance of each isotopolog and therefore an accurate isotope ratio. The model was employed for those objects that had at least two transitions of ^{12}CO . From the main isotope parameters,

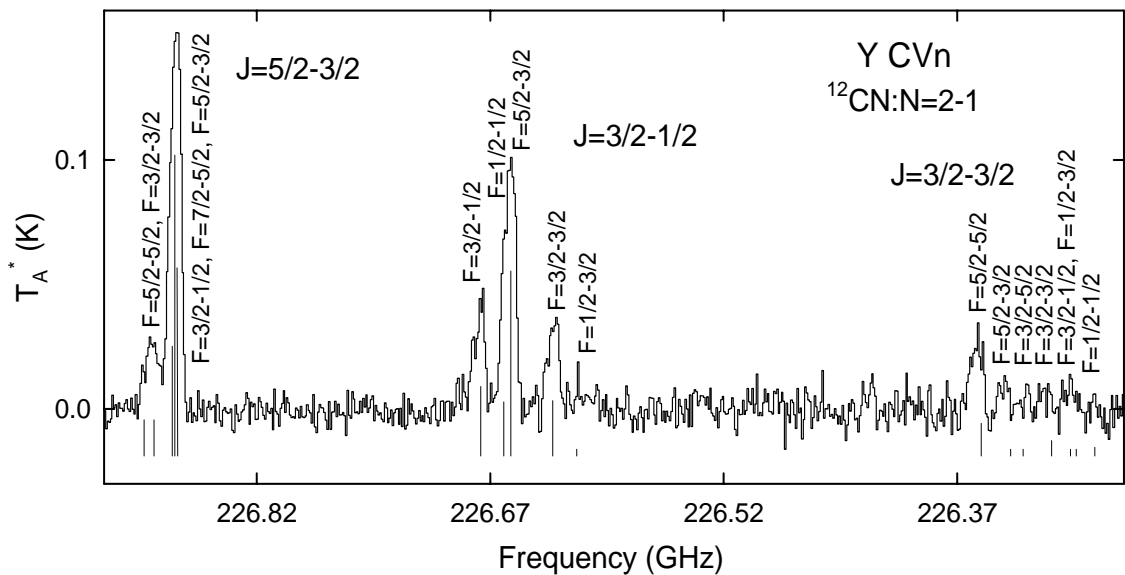


Figure 3.3. The $N=2 \rightarrow 1$ transition of ^{12}CN displaying all fine and hyperfine structure.

the ^{13}CO data was then fit to the observations. For objects with only one measured transition of each isotopolog, a $^{12}\text{C}/^{13}\text{C}$ ratio was derived from the line intensity ratios corrected for beam efficiencies. This methodology is an approximation to the true ratio since opacity effects are not taken into consideration. Thus, a lower limit on the ratio is obtained in these few cases.

Molecular abundances of CO towards the circumstellar envelopes were determined from the radiative transfer code developed by Bieging and Tafalla (1993) for spherical shells. Statistical equilibrium equations are solved in an iterative fashion considering collisional excitation of rotational levels of the ground vibrational state of each molecule considered. Collisional cross-sections were available for ^{12}CO and were employed for ^{13}CO . The envelope, or envelope sections, is divided into a number of shells and the equations are solved at a specified inner radius and successively stepped through each shell, or section. Model output is in terms of level populations for a given species as a function of radius. Excitation temperature and opacities are determined at each radius for a given rotational transition. The radiative transfer equation is then integrated yielding the brightness temperature as a function of radius and observed velocity. This 2-dimensional brightness distribution is then convolved with a circular Gaussian function, representative of the given telescope beam, yielding the predicted spectrum for a given rotational transition.

The line profiles are modeled for a given molecule, telescope beam size and transition. Input parameters necessary for the modeling are distance to the object,

outflow velocity, mass-loss rate, and temperature and density profiles. If a source radius was unknown, this value in cm was determined from:

$$R_*(cm) = 6.96 \times 10^{10} \sqrt{\frac{L_*}{(T_*/5780)^4}} \quad (2),$$

where L_* is in units of L_\odot , and T_* is in K. The gas temperature profile was defined as:

$$T_{Kin} = T_{Kin0} \left(\frac{r}{r_{Kin0}} \right)^{-0.7} \quad (3),$$

The initial temperature, T_{kin0} , was assumed to be the effective temperature of the star and r_{kin0} was defined as the stellar radius. The exponent value of -0.7 was chosen on the basis of other profiles from evolved stars (see Kemper et al. 2003 & Keady et al. 1988). This is an averaged temperature distribution over the entire shell and yields comparable abundances for most objects to those studied in detail (see Appendix H). A density distribution dependence of r^{-2} was assumed for all calculations, and the outflow velocity was established individually from the line profiles for a given species. The density profile is defined by the given mass loss rate of a particular object. Fits to the observed line profiles were obtained by varying two parameters: the molecular abundance and the source radius. The source radius was defined as the position from the star where the abundance decreased by $1/e$, assuming a spherical distribution. For optically thick species, this does not necessarily define the total distribution of the molecule in a particular object, due to the fact that a $1/e$ decrease in abundance is likely still observable.

Table 1. Frequencies, Relative Intensities, and Efficiencies of CN

Line	Transition	Component	Frequency (MHz)	Relative Intensity	η_c (12m)	η_b (10m)				
¹² CN	N=1→0	J=3/2→1/2	F=3/2→1/2	113488.142	0.1235	0.82				
			F=5/2→3/2	113490.985	0.3333					
			F=1/2→1/2	113499.643	0.0988					
			F=3/2→3/2	113508.934	0.0988					
			F=1/2→3/2	113520.414	0.0123					
	N=2→1	J=3/2→3/2	F=1/2→1/2	226287.393	0.0062	0.53	0.78			
			F=1/2→3/2	226298.896	0.0049					
			F=3/2→1/2	226303.049	0.0049					
			F=3/2→3/2	226314.552	0.0120					
			F=3/2→5/2	226332.519	0.0053					
		J=3/2→1/2	F=5/2→3/2	226341.919	0.0053					
			F=5/2→5/2	226359.887	0.0280					
			F=1/2→3/2	226616.520	0.0062					
			F=3/2→3/2	226632.176	0.0494					
			F=5/2→3/2	226659.543	0.1667					
		J=5/2→3/2	F=1/2→1/2	226663.685	0.0494					
			F=3/2→1/2	226679.341	0.0617					
			F=5/2→3/2	226874.183	0.1680					
			F=7/2→5/2	226874.764	0.2667					
			F=3/2→1/2	226875.896	0.1000					
		F=3/2→3/2	226887.399	0.0320						
		F=5/2→5/2	226892.151	0.0320						
		F=3/2→5/2	226905.366	0.0013						
¹³ CN	N=1→0	F ₁ =1→0	F ₂ =2→1	F=3→2	108780.200	0.2000	0.84			
				F=2→1	108782.374			0.1070		
				F=1→0	108786.982			0.0480		
				F=1→1	108793.753			0.0360		
				F=2→2	108796.400			0.0360		
	N=2→1	F ₁ =2→1	F ₂ =3→2	F=4→3	217467.150	0.1550	0.55	0.78		
				F=3→2	217467.150				0.1068	
				F=2→1	217469.155				0.0724	
				F=2→2	217480.559				0.0138	
				F=3→3	217483.606				0.0138	

Two rotational transitions per molecule were simultaneously fit, in most cases, to constrain these variables. When available, data from other telescopes were incorporated into the model for additional constraints. Surveys from Groenewegen et al. (1996), Greaves and Holland (1997), Bujarrabal et al. (1994), and Teyssier et al. (2006) were primarily employed. These assumptions are highly generalized, though minor effects should cancel out in the ratio obtained. However, by standardizing the model, the analysis is directly comparable from one source to the next. Modeled CO abundances should be taken lightly and emphasis will be placed only on the $^{12}\text{CO}/^{13}\text{CO}$ ratios.

The radiative transfer model was not employed for the CN analysis due to the lack of measured collisional cross sections for the various hyperfine (hf) transitions. However, the $^{12}\text{CN}/^{13}\text{CN}$ isotope ratios can be evaluated based on the relative intensities of the ^{12}CN hyperfine components (Table 1) to derive τ , the optical depth, and T_{ex} , the excitation temperature. This analytical technique is

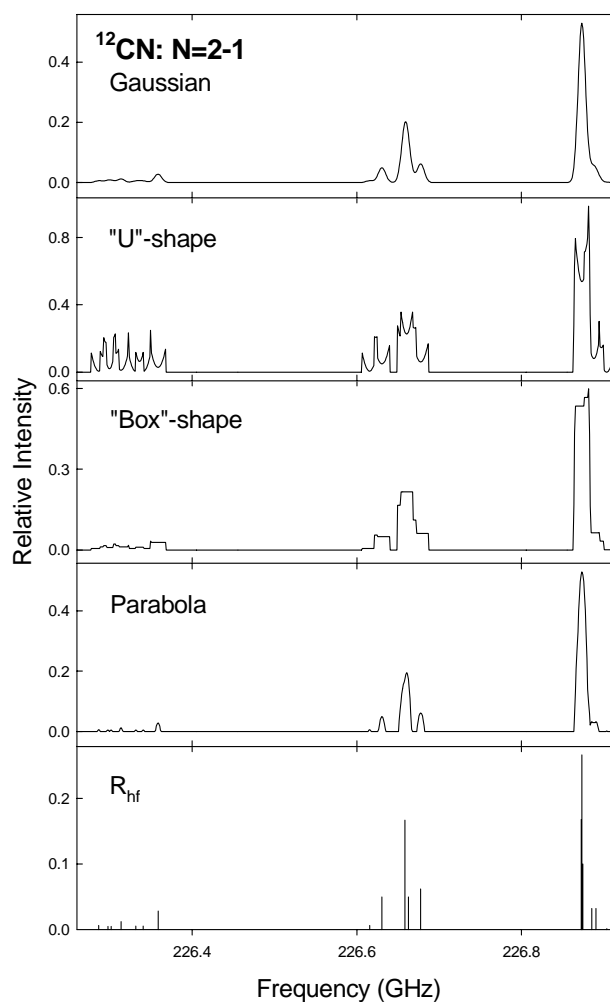


Figure 3.4. Modeled line profiles for various distributions of ^{12}CN $N=2 \rightarrow 1$.

described in detail by Savage et al. (2002) and Milam et al. (2005; Appendix B). For objects with narrow linewidths, this is a fairly direct technique. However, most sources included in this study have a FWHM \gg 2 MHz, therefore blended features need to be accurately accounted for. For such circumstances, the line profiles were modeled, in the optically thin limit, as either gaussian, parabolic, “U”-shaped or “box”-shaped profiles for each hf component, see Figure 3.4 for an example of the modeled profiles. The synthetic spectra yielded a correction factor for blended features. This factor was applied to the actual observed intensities to account for the true intensity of a given hf line. The corrected intensities were utilized the hyperfine analysis to derive the optical depth and excitation temperature. The $^{13}\text{C/N}$ analysis assumed optically thin emission for both the $N=1\rightarrow 0$ and $N=2\rightarrow 1$ transitions and the strongest hf component was used for both transitions as well, Figure 3.4.

The ratios obtained for CO and CN are found in Table 2. Also listed are $^{12}\text{C}/^{13}\text{C}$ values derived from others with their corresponding references and molecules. There is excellent agreement among the various methods employed to derive the ratios as well as values obtained from photospheric measurements to those of the cool circumstellar material. The ratios established are plotted as a function of the C/O ratio (Figure 3.5).

c. Implications and Nucleosynthesis

For many years, observational measurements of CNO isotopes remained non-reproducible by theoretical models of nucleosynthesis. These unexplained values lead to a focused dedication to Red Giant and AGB yields in the theoretical community. The suggestion of an “extra mixing” phenomena was invoked to reconcile the counterintuitive

CNO ratios to theory (Boothroyd & Sackmann 1999). Other mechanisms proposed to account for the low $^{12}\text{C}/^{13}\text{C}$ ratios included rotation (e.g. Charbonnel 1995), magnetic fields (e.g. Hubbard & Dearborn 1980), and most recently molecular weight inversion (Eggleton 2006; Eggleton, Dearborn & Lattanzio 2007). While these newer models are getting closer, they still can't account for all post-main sequence objects.

The results plotted in Figure 3.5 may help elucidate the mechanisms by which the $^{12}\text{C}/^{13}\text{C}$ ratio is manipulated in Red Giant and AGB stars. Assuming a solar composition from the main sequence ($C/O \sim 0.5$ and $^{12}\text{C}/^{13}\text{C} \sim 89$) a star becomes enriched by CNO-cycled material after the first dredge up. This effectively lowers the $^{12}\text{C}/^{13}\text{C}$ ratio and maintains a C/O ratio barely affected at all. Once the star undergoes third dredge-up

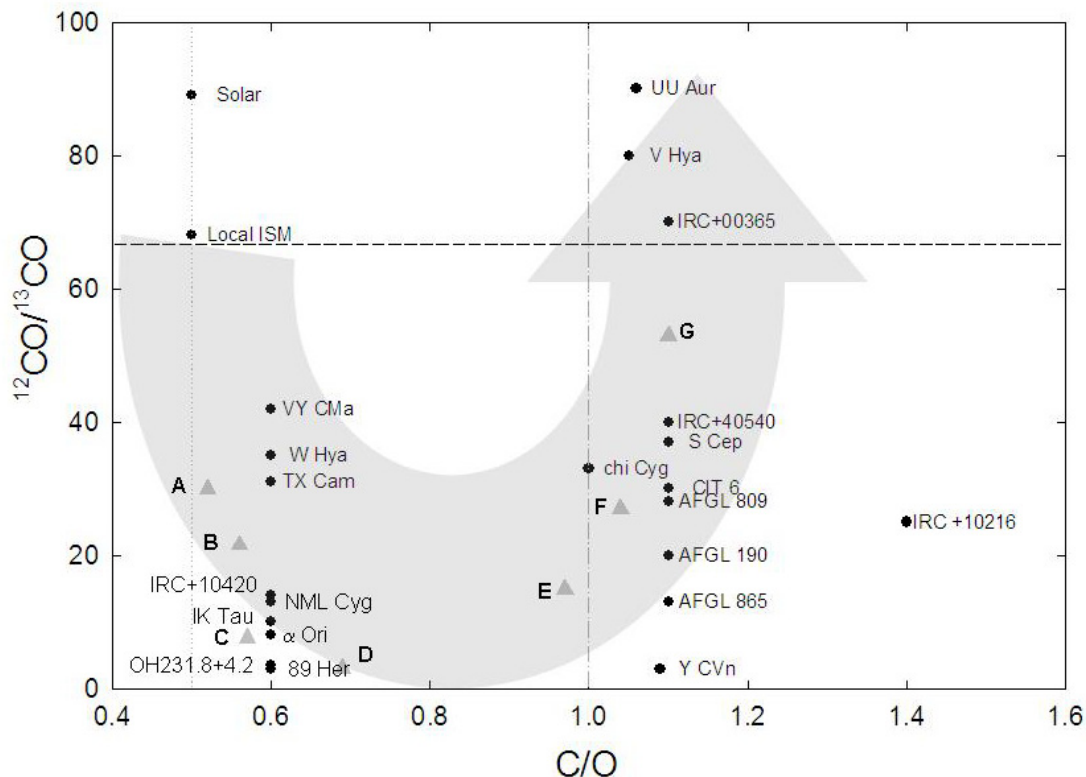


Figure 3.5. $^{12}\text{C}/^{13}\text{C}$ ratio as a function of the C/O ratio in stars.

events, the C/O ratio increases to ≥ 1 and the $^{12}\text{C}/^{13}\text{C}$ ratio begins to rise accordingly with triple alpha product enrichment. Then the object will begin to thermally pulse mixing the hydrogen and helium burning shells and fluctuating the $^{12}\text{C}/^{13}\text{C}$ ratio while somewhat maintaining a C/O ratio > 1 . A distinctive feature presented in Figure 3.5 is the exceptionally high value of $^{12}\text{C}/^{13}\text{C}$ found for the Sun. This may be due to the proto-solar disk being enriched in carbon-12 by either nearby carbon-rich Red Giants or possibly a supernovae.

Table 2. $^{12}\text{C}/^{13}\text{C}$ Ratios Measured in Circumstellar Envelopes

Source	$^{12}\text{CO}/^{13}\text{CO}$	$^{12}\text{CN}/^{13}\text{CN}$	Other
AFGL 190	≥ 20	> 5	$> 22^a$
AFGL 809	≥ 28	> 5	-
AFGL 865	≥ 13	> 14	$> 15^a$
IRC +40540	40	15-20	55^f
CRL 2688	-	57-66	$32^d, 20^h$
CRL 618	-	> 32	$30^d, 12^h$
CIT 6	30	11-37	$12-35^c, 17-31^{a, d}$
IRC +10216	25	> 36	$32^b, 25-45^c, 44^d,$ 50^f
V Hya	23-35	> 16	$33^e, 69^i$
Y CVn	3	2-8	$2.5^f, 3.4^e$
S Cep	37	> 16	$> 15^a$
IRC +10420	14	-	7^l
α Ori	8	-	$7^g, 4^k$
VY CMa	46, 25*	> 3	36^l
IRC +00365	70	> 7	$\sim 57^b$
UU Aur	90	-	$\sim 45^f$
89 Her	3-4	-	-
χ Cyg	33	> 11	$25^g, 35-63^h$
OH231.8+4 .2	~ 3	-	$5-10^j$
TX Cam	31	> 3	-
W Hya	35	-	-
NML Cyg	13	> 1	10^l
IK Tau	10	> 1	10^l

References: Italicized values are measurements derived from the photosphere. (a) Groenewegen, et al. 1996 – CO; (b) Greaves & Holland 1997 – CO; (c) Woods et al. 2003 – CO and CN; (d) Kahane et al. 1992 – CO (e) Jura, Kahane, & Omont 1988 – CO (f) Schoier & Olofsson 2000 – CO; (g) Hinkle, Lambert, & Snell 1976 – photosphere CO and CN; (h) Wannier and Sahai 1987 – CO; (i) Lambert et al. 1986 – photosphere CN; (j) Sanchez Contreras et al. 2000 – HCN; (k) Huggins 1987 – CO; (l) Nercessian et al. 1989 – HCN

* From outflows vs. spherical wind (see text).

d. VY Canis Majoris

Part of this study involved the investigation of the chemistry in an oxygen-rich envelope once believed to be chemically benign. The object chosen was VY Canis Majoris (VY CMa), a supergiant star known as one of the brightest objects in the infrared catalog. Though this object is located 1500 pc away from the sun, the high mass loss rate of $\sim 2 \times 10^{-4} M_{\odot} \text{ yr}^{-1}$ (Humphreys et al. 2007) makes it an ideal candidate for gas-phase circumstellar chemistry. The goal was to obtain an unbiased molecular survey at $\lambda \sim 1\text{-}3$ mm and inventory the chemical composition for comparison to the well studied, proto-typical carbon-rich AGB envelope, IRC +10216. Observations began at 3mm wavelengths with the ARO 12 m telescope and initially yielded few species at weak intensities including SiO, SO₂, and HCN. Upon taking advantage of the 12 m capabilities

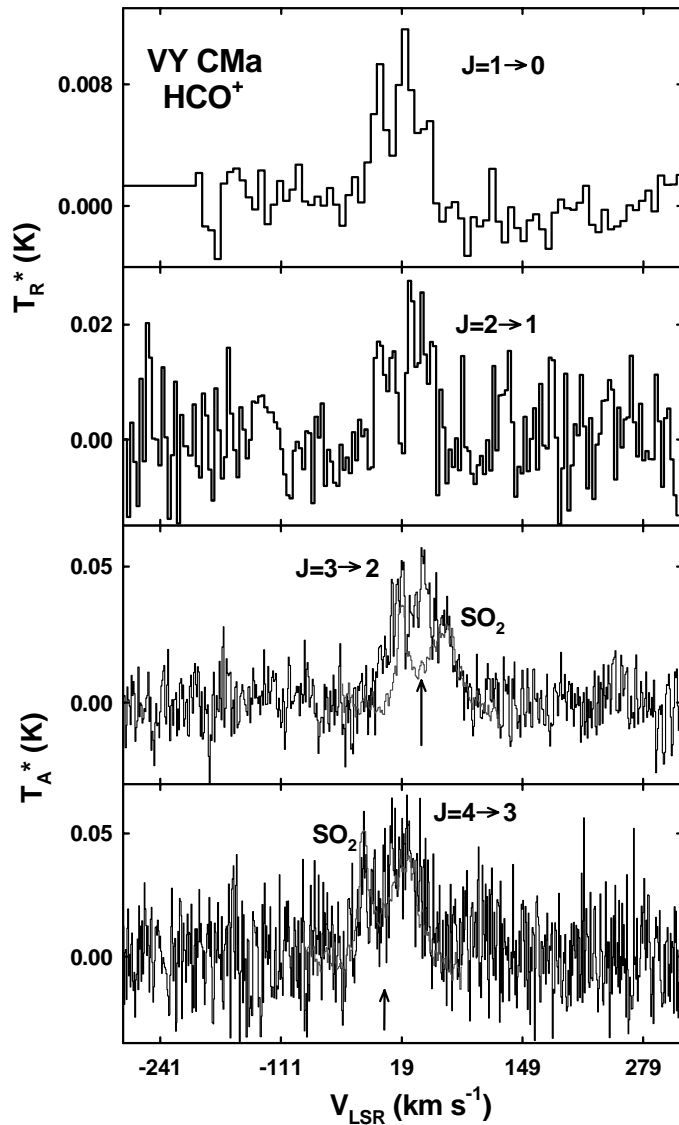


Figure 3.6. Detection of HCO⁺ towards VY CMa, and oxygen-rich supergiant.

to observed the far end of the 2mm window, we discovered at feature at 178.375 GHz, coincident with HCO^+ ($J=2\rightarrow 1$). This detection was later verified at three other frequencies to prove the presence of the first circumstellar cation, HCO^+ , towards an oxygen-rich Red Giant star (see Figure 3.6.).

This object only proved more interesting as the survey moved to the 1 mm spectral window. Not only were eight new molecules detected in this object (see Table 3, bold species), but each species traced a distinct physical region of the source. Three

Table 3: Confirmed Molecular Species Towards VY CMa

CO	SiS
CS	SO
CN	SO ₂
HCN	NaCl
HNC	H ₂ O
HCO⁺	OH
PN	NH ₃
H ₂ S	SiO
NS	PO

* Bold denotes new detection towards this source.

regions were identified based on a comparison to the spectral line shapes to the infrared and optical images labeled as a spherical wind and a red- and blue-shifted outflow (see Appendix D). The new molecules observed included refractories such as NaCl (Appendix E) and PN (Appendix F) as well as a rich carbon chemistry (see Appendix E and Ziurys et al., in preparation). Molecular abundances were derived from the circumstellar radiative transfer model described in §2b. To account for the red- and blue-shifted components the convolution program, which converts the brightness distribution to a spectral line by convolving the source with the gaussian beam of the telescope, was modified to create a source with a specified angle to the line of sight and the outflows opening angle (see Appendix D for details).

The new detections of various refractory species lead to investigations of the local thermodynamic equilibrium (LTE) chemistry found in oxygen-rich envelopes and how it

compares to that of carbon-rich ones. To do this, a LTE model was adapted from Tsuji (1973) to compare the sodium and phosphorus species found for each type of envelope. This model inputs a series of atomic abundances, taken to be solar for the oxygen-rich case, and solar abundances for the carbon-rich case except for C/O \sim 1.5. The model is run for a given pressure or density, assuming an ideal gas in the photosphere of a star, and yields fractional abundances for a given temperature. The density for a given object was determined from an ideal gas with an effective temperature and mass-loss rate where the H₂ density of a spherical envelope is then:

$$\rho(H_2) = \frac{\dot{M}}{4\pi r^2 V_{\text{exp}}}, \quad (4)$$

where, \dot{M} is the mass loss rate of an object in $M_{\odot} \text{ yr}^{-1}$, r is the stellar radius, and V_{exp} is the expansion velocity of the source. See Appendix E and F for results and a discussion of these models.

e. Planetary Nebulae

The matter ejected from evolved stars, however, is subject to a changing environment. The central stars of these objects slowly lose their dust shroud, creating proto-planetary nebula (PPN) and then planetary nebula with an influx of hot UV radiation (Kwok 2004). The material that enters the diffuse interstellar medium (ISM) is subsequently exposed to the UV field of the galaxy before presumably collapsing into dense interstellar clouds. For planetary nebulae, the product of the UV flux times the lifetime ($\sim 10^4$ years) is roughly similar to that for diffuse clouds (Black & van Dishoeck 1988). Both environments could potentially destroy molecules.

Molecular observations have shown that many species found in circumstellar envelopes are no longer present in PNe (e.g. Bachiller et al. 1997a). Studies of PPNe and PNe indicate that radicals and molecular ions are heavily favored to survive. The list of survivor species is nonetheless striking in two ways. First, the compounds routinely found in PNe (CO, HCO⁺, CN, HCN and HNC) are carbon-rich. Secondly, there is a close similarity to the molecules found in diffuse clouds (e.g. Liszt et al. 2006).

Recent observations by Liszt and Lucas (e.g. 1995, 1996, 1998, 2001, 2002), Lucas and Liszt (e.g. 1996, 1998, 2000, 2002) and Liszt et al. (2006) have shown that molecules with as many as five atoms are routinely found in diffuse gas. In the past, such gas has been considered to be the regime of only atoms and diatomic species. The molecules CO, HCO⁺, CN, HCN, HNC, C₂H, C₃H₂, CS, SO, NH₃, and H₂CO have been found in these environments towards many lines of sight. It is therefore possible, but so far unproven, that the bulk destruction of circumstellar molecules has already happened in the planetary nebulae phase. If so, there should be a fairly close correspondence between the molecules observed in older PNe and those found in the diffuse medium (Ziurys 2006).

In an earlier paper, Howe, Hartquist and Williams (1994) predicted that CCH should be detectable in evolved PNe, in particular the Helix Nebula (NGC 7293). More recent calculations by Ali et al. (2001) also suggest detectable concentrations of this radical in such objects. Yet, the study of Bachiller et al. (1997a) suggests that molecules with carbon-carbon bonds do not survive into the planetary nebulae stage. Indeed, their observations show that the proto-typical carbon chain molecule HC₃N is destroyed. On

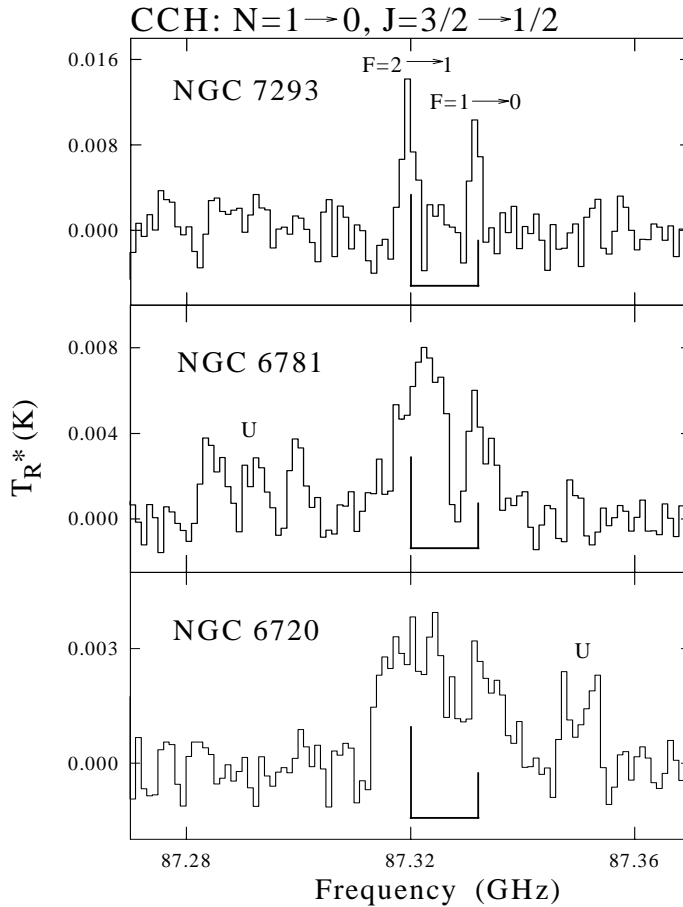


Figure 3.7. CCH observed towards evolved planetary nebulae. U denotes unidentified feature.

transitions are shown, measured towards NGC 7293 (Helix), NGC 6720 (Ring), and NGC 6781.

Abundances were derived for CCH assuming that each source filled the telescope main beam. Total column densities (N_{tot}) were calculated from the following equation, derived in the Rayleigh-Jeans limit, neglecting the cosmic background:

$$N_{\text{tot}} = 3k10^5 \int T_{\text{R}} dV_{\text{rot}} e^{-\Delta E/kT_{\text{rot}}} / (8\pi^3 \nu R_{\text{hf}} S_{\text{ij}} \mu_0^2) \quad (5).$$

the other hand, observations have demonstrated that species with unsaturated carbon-carbon bonds, CCH and C_3H_2 , are present in diffuse clouds with $N_{\text{tot}} \sim 1.5 \times 10^{13} \text{ cm}^{-2}$ and $\sim 7.0 \times 10^{11} \text{ cm}^{-2}$, respectively. Have such species survived the PN phase, or are they reconstructed in the diffuse medium?

CCH was detected in all four older PN, as illustrated in Figure 3.7. Here the spectra of the $J = 3/2 \rightarrow 1/2$ spin component of the $N = 1 \rightarrow 0$

Here ν is the transition frequency (Hz), $\int T_R dV$ is the integrated line intensity (K km s^{-1}), S_{ij} is the line strength ($S_{ij} \propto N+1$), R_{hf} is the relative intensity of the observed hf component, μ_o is the permanent dipole moment (esu-cm) and ζ_{rot} is the rotational partition function. The column densities for the four older PNe fall in the range $N_{\text{tot}} = 0.32\text{-}1.37 \times 10^{13} \text{ cm}^{-2}$ (see Tenenbaum et al., in preparation).

To date, all species now known in evolved PNe have been detected in diffuse clouds (Liszt et al. 2006; Bachiller et al. 1997a; Josselin & Bachiller 2003), including CN, HCN, HNC, HCO^+ , and CO as well as the recently detected CCH, c- C_3H_2 and H_2CO (Tenenbaum et al., in preparation). The molecules in PNe probably survive because they are contained in self-shielding, dusty knots (Howe et al. 1994). The clumps are created by Parker instabilities in the remnant shell. These globules may continue to survive as the shell material is dispersed into the diffuse ISM. The persistence of these globules at some level may be the connection between molecules in evolved PNe and diffuse gas. As suggested by these results, even with some additional molecular destruction, there is sufficient column density left in the evolved PNe to account for observed abundances in diffuse gas.

CHAPTER 4. CARBON IN THE INTERSTELLAR MEDIUM: $^{12}\text{C}/^{13}\text{C}$ RATIOS

Isotope ratios have been studied in the interstellar medium for nearly 30 years (Penzias 1980) and have proven Galactic chemical enrichment of carbon-13 at the center of the Galaxy. This enhancement has been attributed to the large star formation rate near the Galactic center.

Due to the cold, dense nature of interstellar gas, the carbon isotope ratio is hard to obtain in an atomic form. Thus, measurements of molecular isotopologs are assumed to trace those of the true, atomic, abundances. From a first order approximation this seems rational and a fairly direct method. However, molecular species with abundances large enough to detect the carbon-13 isotopolog are often limited to only a few species. Traditionally, CO has been employed due to this reason. It is found in vast areas of the ISM (Dame et al. 1987) in large quantities, such that a $^{12}\text{C}/^{13}\text{C}$ ratio approaching solar (89) can be easily observed. However, this molecule is so abundant that saturation effects, or large opacities, are hard to overcome. These effects are easily disguised by CO since it is a closed shell species with no hyperfine structure. Thus, ratios obtained from the direct intensity ratio of $^{12}\text{CO}/^{13}\text{CO}$ are usually lower limits to the true abundance ratio. This has been overcome by the use of double isotope ratios ($^{18}\text{O}/^{16}\text{O}$) and/or LVG models where the line intensity is modeled for various densities and temperatures. Other species employed to derive the $^{12}\text{C}/^{13}\text{C}$ isotope ratio in molecular clouds have been H_2CO , HCO^+ , and HCN . These species are not as abundant as CO, but can still deceive the true ratio from opacity effects or yield only an upper limit to the ^{13}C isotopolog.

Recently, the CN radical has been employed to measure the $^{12}\text{C}/^{13}\text{C}$ ratio across the Galaxy (Savage et al. 2002; Milam et al. 2005; Appendix B). This technique has proved useful in that opacity effects are directly measured from the relative intensities of the hyperfine structure (see §3b and Appendix B for details). By employing this method, the need for models or double isotope ratios are eliminated, thus, this species is a model in itself.

a. $^{12}\text{CN}/^{13}\text{CN}$ $N=1\rightarrow 0$

The $^{12}\text{C}/^{13}\text{C}$ isotope ratio was established for 18 molecular clouds ranging from 0.1 kpc to 16 kpc from the Galactic center. The ratios were obtained by observations of the $N=1\rightarrow 0$ transition of ^{12}CN and ^{13}CN . Hyperfine analysis was employed to derived opacities and excitation temperatures for each source, thus a $^{12}\text{C}/^{13}\text{C}$ ratio. This is a direct analytical technique where the abundance is directly related to the relative intensities of each hyperfine component (see §3b and Appendix B).

This work was a continuation of the work done by Savage et al. (2002), Langer and Penzias (1990), and Henkel et al. (1980; 1982; 1983; 1985). Ratios obtained from this study were in excellent agreement with those found for CO and H_2CO . The calculated $^{12}\text{C}/^{13}\text{C}$ values were plotted as a function of distance to the Galactic center (Figure 4.1). It is obvious from this figure that a gradient is present for the ratio ranging from ~ 20 at the Galactic center to ~ 130 at 16 kpc. The $^{12}\text{CN}/^{13}\text{CN}$ values from this study are the only ones present beyond ~ 10 kpc and are thus the most significant to the measured gradient (see Appendix B).

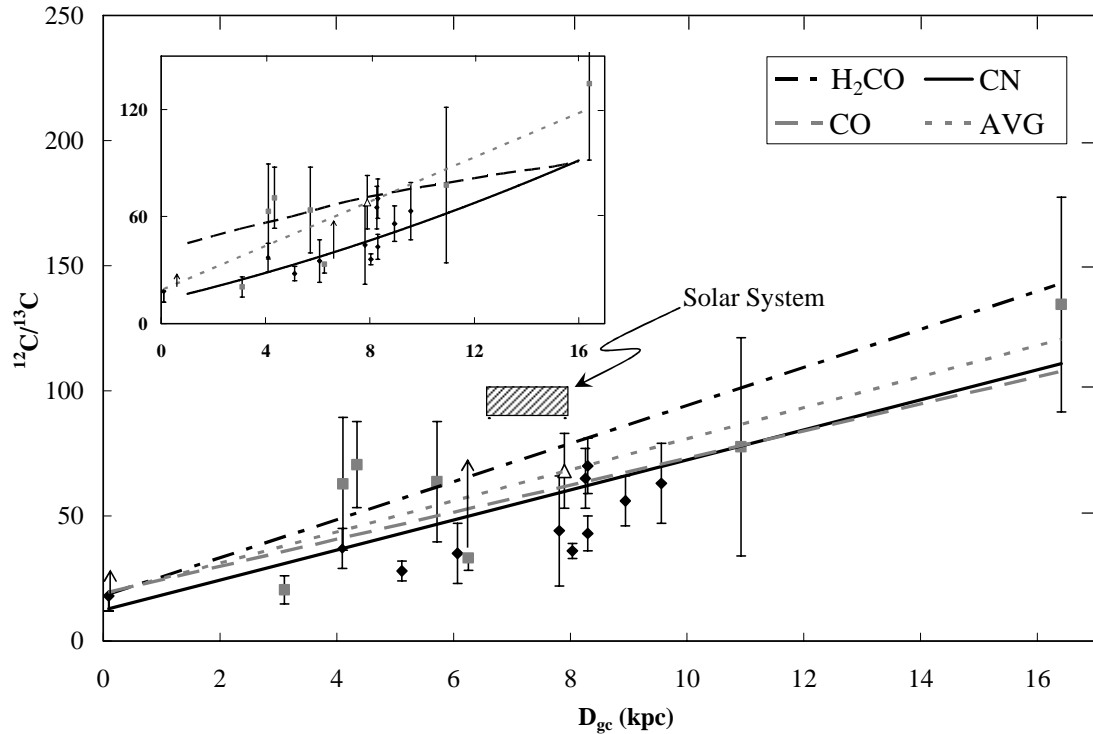
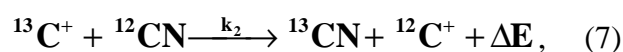
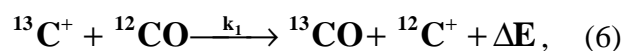


Figure 4.1. Galactic gradient determined from $^{12}\text{C}/^{13}\text{C}$ ratios for CO, CN, and H_2CO as a function of distance to the Galactic center, D_{gc} .

Chemical effects such as isotope-selective photodissociation and fractionation are expected to alter the molecular $^{12}\text{C}/^{13}\text{C}$ ratios from the true value. Isotope-selective photodissociation is expected to enhance the ratio by destroying the less abundant (carbon-13) isotopolog while the main isotopic species is self-shielded. Two objects in this study are expected to be affected by such enhancements, NGC 2024 and Orion Bar. Both objects have $^{12}\text{C}/^{13}\text{C} \sim 70$ which agrees with other values in the near vicinity, thus eliminating the significance of this effect. Additionally, CN should trace denser gas than CO with critical densities approximately 2 orders of magnitude higher. This would restrict the amount of UV flux that penetrates CN gas when compared to CO. However,

the ratios obtained from CO and CN are in good agreement, therefore this effect is expected to be at most minimal.

Chemical fractionation is also considered a significant effect for molecular isotope ratios. Here, isotope exchange reactions are expected to occur via:



where ΔE is the zero-point energy difference between the ^{12}C and ^{13}C isotopologs; for CO $\Delta E \sim 35$ K and CN $\Delta E \sim 34$ K. These mechanisms suggest at low temperatures, the ^{13}C isotopolog will be favored. To investigate these effects, a chemical network was derived for molecular clouds involving the major formation pathways of CO, CN, and H_2CO (see Figure 4.2; Appendix B). All three species are formed from completely

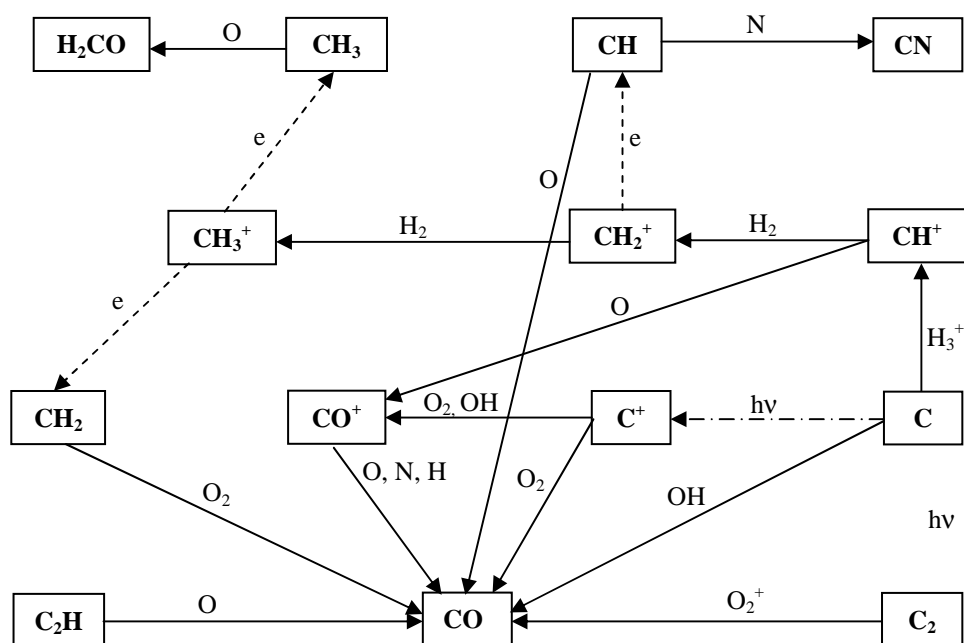


Figure 4.2. Chemical network for the formation of CN, CO, and H_2CO in molecular clouds.

individual pathways. If fractionation effects were significant in these objects, the derived ratios would be reflected by three distinct gradients. However, this is not seemingly the case since all three gradients found in Figure 4.1 are in good agreement.

b. $^{12}\text{CN}/^{13}\text{CN}$ From Multiple Transitions

For a comparison, the $^{12}\text{CN}/^{13}\text{CN}$ ratios were measured via the $N=2\rightarrow 1$ transition in almost all the objects studied in the previous section, as well as the ^{12}CN $N=3\rightarrow 2$

spectrum. By studying multiple transitions, a better ratio can be established as well as accurate column densities and temperatures for the given sources, via rotational diagram analysis or modeled abundances with a LVG approximation. This survey began with the ARO 12 m telescope until the large bandwidth filterbanks were installed with the new 1 mm receiver. The new system allowed for simultaneous observations of all three J-

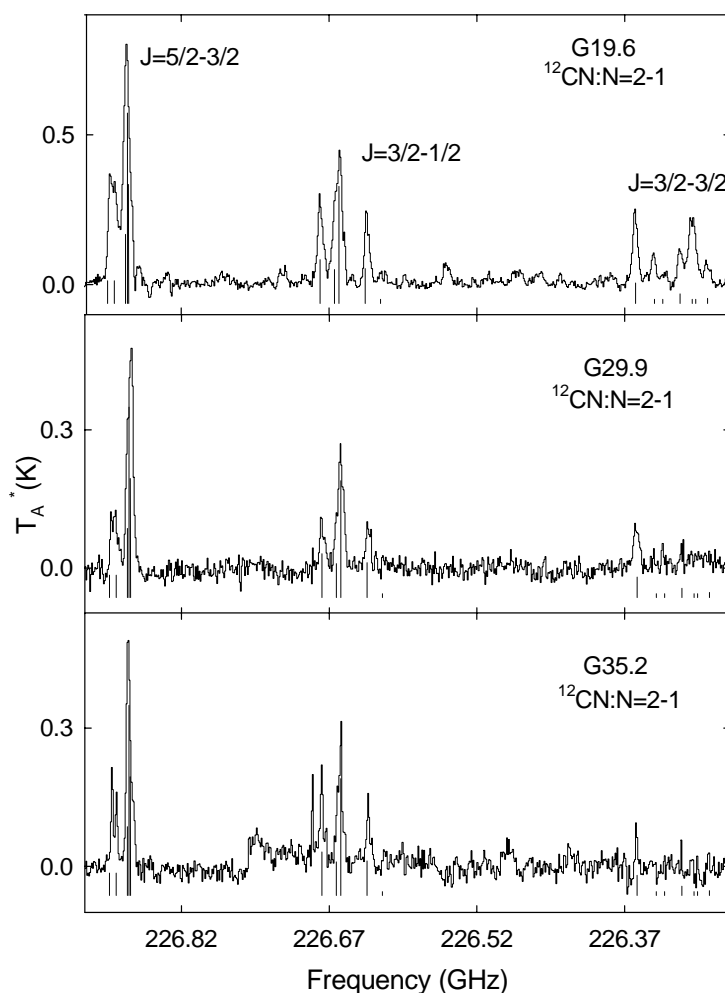


Figure 4.3. Sample spectra of the ^{12}CN $N=2\rightarrow 1$ data obtained towards molecular clouds with the new

components for the $N=2 \rightarrow 1$ transition. The multiple lines observed for the higher transitions along with the $N=1 \rightarrow 0$ data would make this the most complete, self-consistent dataset for $^{12}\text{C}/^{13}\text{C}$ ratios studied towards molecular clouds. See Figure 4.3 (Appendix I) for an example of the $N=2 \rightarrow 1$ data obtained with the ALMA receiver at the SMT.

Analysis of these data proved difficult. Three different methods were employed to derive the opacities and excitation temperatures based on the relative intensities of the hyperfine components. The three methods yielded similar results; all objects were on the

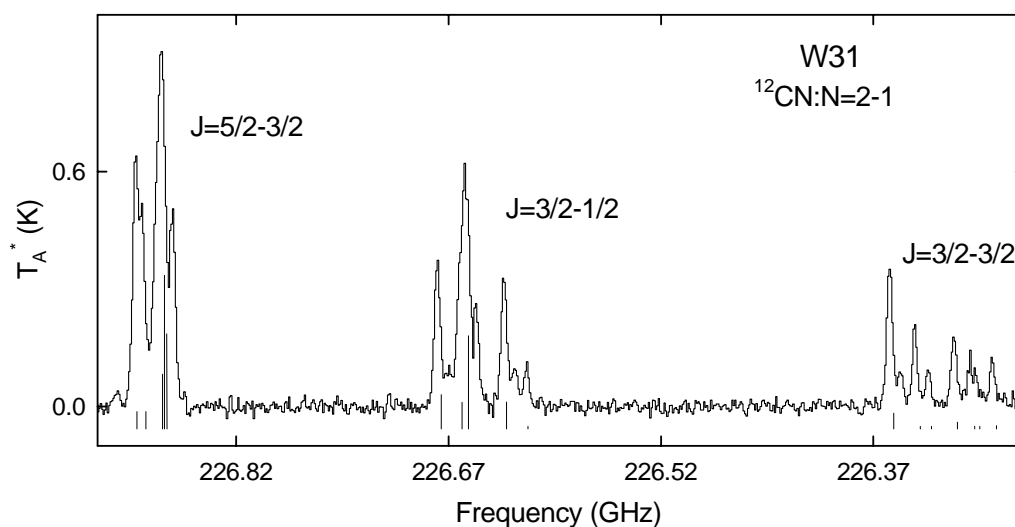


Figure 4.4. The $N=2 \rightarrow 1$ spectrum of W31 which exhibits self absorption in the stronger hf components.

extreme end of high opacity as well as isotope ratios > 100 for most sources. Closer inspection of the data revealed self-absorption in some of the clouds observed, see Figure 4.4. The self-absorption could not be attributed to infinitely high opacities, but likely due to structure being resolved towards each object. This is verified by the smaller beam size of the $N=2 \rightarrow 1$ frequencies as well as the relative intensities for the given hyperfine

components did not approach a ratio of 1. These effects were overcome by employing the weakest component with no absorption and a limit to the ratio was derived. Those objects for which there was no self-absorption may be optically thick in the ^{13}CN isotopolog. However, the hyperfine structure for this isotopolog was not resolved due to the relatively low abundance of this species and lack of signal to noise, therefore the opacity could not be accurately measured. The ratios obtained in these cases may be overestimated should the opacity be > 1 . An approximation for the ratio can be obtained by employing the weakest components of the ^{12}CN and assume that the intensity for that line and the ^{13}CN line is optically thin. These values are listed in Table 4.

The total abundance of ^{12}CN can be determined from a rotational diagram analysis since three transitions have been observed. If the opacity and excitation

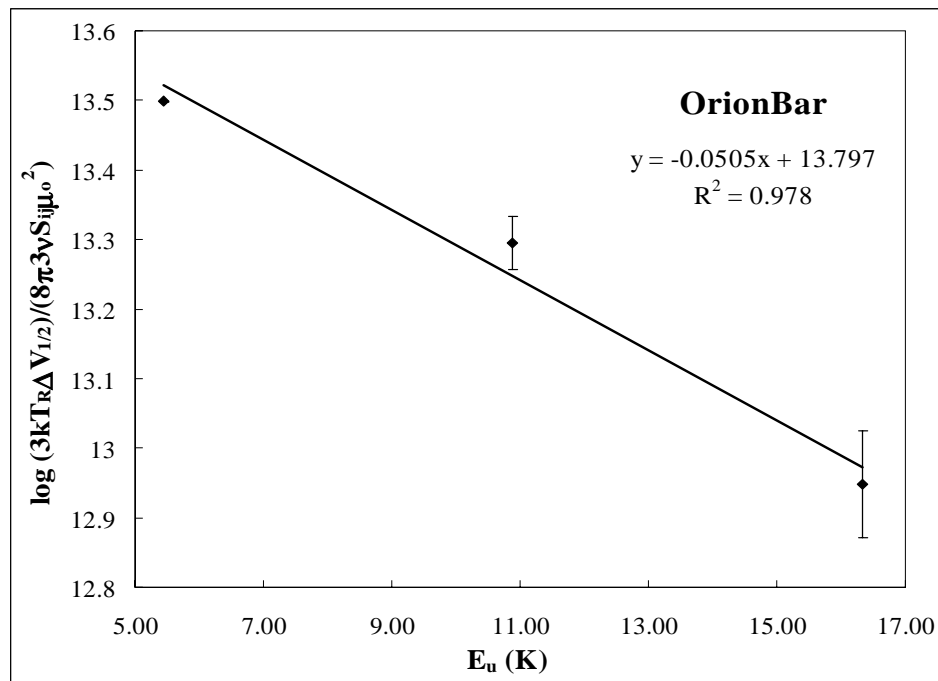


Figure 4.5. Rotational diagram of ^{12}CN for Orion Bar yielding $N_{\text{tot}} \sim 6 \times 10^{14} \text{ cm}^{-2}$ and $T_{\text{rot}} \sim 9 \text{ K}$.

temperature was determined for a given transition, it was employed in the analysis, otherwise the weakest component was used. Figure 4.5 is an example of this method for Orion Bar yielding a total column density of $\sim 6 \times 10^{14} \text{ cm}^{-2}$ and $T_{\text{rot}} \sim 9 \text{ K}$. Results for this analysis are given in Table 4 and data can be found in Appendix I. All sources are in close agreement to these values suggesting similar conditions from object to object as well as chemistry. This implies that the ^{13}CN abundance is what varies in the sources samples and may be a direct effect from Galactic chemical evolution.

Another method to determine this abundance is to utilize a radiative transfer combined with statistical equilibrium analysis in a large velocity gradient (LVG) assumption. Here, under an assumed density and temperature, energy level populations are filled which can then be used to predict observed intensities for a given telescope. These models can be fairly effective at predicting molecular abundances for closed shell species such as CO. However, these types of calculations have only recently been employed for hyperfine structure, where agreement between and LTE, line intensity proportional to relative intensity, vs. LVG approximation is still at least a factor of 2 off (Daniel et al. 2006). Determining the ^{12}CN and ^{13}CN abundances from an LVG model should be employed for verification of the ratios determining in a LTE assumption, hyperfine intensity ratios. Unfortunately, the collisional cross-section for these species have yet to be measured and/or calculated. In the past, the values of CO or CS have been employed, and yield lower opacities and can affect the abundance by up to a factor of 15 (see Pratap et al. 1997; Churchwell 1980). A model is currently being modified to

account for fine and hyperfine structure of ^{12}CN and ^{13}CN , though the ratios derived should be assumed to have an error of at least a factor of 2.

Table 4. $^{12}\text{C}/^{13}\text{C}$ Isotope Ratios Towards Molecular Clouds from CO, CN, and H_2CO

Source	D_{GC} (kpc)	T_{rot} (K)	N_{tot} (cm^{-2})	$^{12}\text{C}/^{13}\text{C}$: CN ($N=1\rightarrow 0$)	$^{12}\text{C}/^{13}\text{C}$: CN ($N=2\rightarrow 1$) ^{a)}	$^{12}\text{C}/^{13}\text{C}$: CO	$^{12}\text{C}/^{13}\text{C}$: H_2CO
SgrB2(OH)	0.1			≥ 18.6	18	24 ± 1	10
G29.9	4.1	2	9×10^{15}	63 ± 27			45 ± 5
G49.2	6.3	5	8×10^{14}	≥ 33.13	40		58 ± 4
W33	4.1	5	2×10^{15}	37 ± 8	30	39 ± 1	100
G19.6	4.3			71 ± 17	30		41 ± 4
W31	3.1	6	2×10^{15}	20 ± 6	65		37 ± 6
G34.3	5.1	10	8×10^{14}	28 ± 4	21		58 ± 5
G35.2	5.7	3	1×10^{15}	64 ± 24			55 ± 5
W51M	6.1	6	2×10^{15}	35 ± 12	49	45 ± 2	
W49	7.8			44 ± 22		49 ± 6	74 ± 20
DR-21(OH)	8.0	4	3×10^{15}	36 ± 3		53 ± 2	66
Orion A	8.3	13	6×10^{14}	43 ± 7	56	79 ± 7	
NGC 2024	8.3			65 ± 12	80		68 ± 11
Orion Bar	8.3	9	6×10^{14}	70 ± 11	69	$75 \pm 9^{\text{h)}$	
NGC 7538	8.9	8	8×10^{14}	56 ± 10	57		
W3(OH)	9.6	15	5×10^{14}	63 ± 16	45	66 ± 4	91 ± 16
S156	10.9			78 ± 44	80		
WB89-391	16.4			134 ± 43			

^{a)} Derived from the weakest hf component in the ^{12}CN isotopolog.

CHAPTER 5. CARBON IN THE SOLAR SYSTEM: COMETS

Comets are appealing to astronomers because they are thought to contain pristine material of the early solar system. It is postulated that comets were formed in a broad region of the proto-solar disk, likely $5 < r < 40$ AU, and therefore document the chemical history and extent of mixing within this region. Recent STARDUST results imply extensive mixing with particulate material from the inner radii of the disk (Zolensky et al.

Table 5. Molecules Observed
Towards Hale-Bopp

Molecule	Q/Q(H ₂ O)	
CH ₃ CHO	0.02	2006). The dust and ice then coagulate to
CH ₂ OHCHO	< 0.04	form cometary bodies confined to the outer
(CH ₂ OH) ₂	0.25	edges of the solar system. The two distinct
HNCO	0.1	regions where comets are primarily found
HC ₃ N	0.02	are the Oort cloud and the Kuiper belt.
SO	0.3	Models have implied that these two areas
OCS	0.4	have different histories which should be
NH ₂ CHO	0.015	reflected in cometary composition.
NaOH	< 0.0003	Observations of long period (Oort cloud) vs.
NaCl	< 0.0008	short period (Kuiper belt) may help
HCOOH	0.09	distinguish these unknown parameters.
HCOOCH ₃	0.08	Comets are typically studied as they
SO ₂	0.2	approach the sun, where a small amount of
CO	12-23	the frozen material sublimates, of which a few
CO ₂	6	percent ionizes, forming a gaseous tail
CH ₄	1.5	whose composition can be analyzed using
C ₂ H ₂	0.1-0.3	
C ₂ H ₆	0.6	
CH ₃ OH	2.4	
H ₂ CO	1.1	
NH ₃	0.7	
HCN	0.25	
HNC	0.04	
CH ₃ CN	0.02	
H ₂ S	1.5	
CS ₂	0.2	
H ₂ CS	0.05	
NS	> 0.02	

molecular-line radio astronomy.

Comet C/1995 O1 (Hale-Bopp) is currently the most well studied due to its close approach in the spring of 1997 and a water production rate on the order of $\sim 10^{31} \text{ s}^{-1}$. This object had detections of more than 20 molecules, see Table 5 (see Bockelee-Morvan et al. 2004) including at least 10 new species from ions (HCO^+) to large organics ($\text{HOCH}_2\text{CH}_2\text{CH}_2\text{OH}$; Crovisier et al. 2004).

Observations from the 12 m by Milam et al. (2004; Appendix A) illustrated the comet's frailty with the detection of a secondary component in multiple transitions of HCO^+ as well as in HNC. The secondary component of this ion was determined to be composed of a localized debris field of submicron grains. Comet fragmentation is a well known area and has been observed in multiple objects (see Appendix A and C). Milam et al. (2004) suggest that the parent material for this secondary component is most likely organic grains composed of carbon, hydrogen, oxygen, and nitrogen (CHON).

Of all the known cometary species, a vast number are organic in nature and play a key role in terrestrial biological systems. Some of these molecules are simple carbon species that are considered to be the reactants for the larger, more complex species such as acetaldehyde, methyl formate and ethylene glycol (Crovisier et al. 2004).

Formaldehyde (H_2CO) was first observed at radio wavelengths by Snyder et al. (1989) towards comet Halley using the Very Large Array (VLA). This molecule is found in large abundance towards comets, exceeded by H_2O , CO , H_2S , and CH_3OH (Crovisier and Bockelee-Morvan 1999). The first cometary observation of methanol (CH_3OH) was towards comet Austin (1990 V) by Bockelee-Morvan et al. (1990). Both CH_3OH and

H₂CO are currently considered as the interstellar precursors to the sugar, glycolaldehyde (i.e. Halfen et al. 2005; Sorrell 2001); which may lead to other prebiotic species such as ribose. Observations of these molecules in comets would provide an opportunity to explain planetary “seeding” through the dissociation of cometary bodies as they approach perihelion, thus ejecting prebiotic material into the inter-planetary system from fragmentation events or sublimation. Likewise, complete cometary bombardment would also be a mechanism by which organics are distributed to these larger bodies.

a. H₂CO and CO Extended Source

Formaldehyde has an interesting history in comets indicating that it arises from a source extended beyond the comet nucleus (Snyder et al. 1989). This was confirmed by the Halley flyby missions where the scale length of H₂CO was determined to be ~ 1.2 times the photodissociation scale length (Meier et al. 1993). The proposed “parent” species of H₂CO was attributed to a formaldehyde polymer known as polyoxymethylene or POM (Wickramasinghe 1975). This hypothesis carried through based on one instrument data analysis, RPA-PICCA (Reme plasma analyzer-positive ion cluster composition analyzer), where repetitive mass peaks were found (see Korth et al. 1986). However, this was not found in other objects and was discredited (Meier et al. 1993). This was investigated further and eventually explained to arise from CHON particles by Mitchell et al. (1992) and Schutte et al. (1993).

Spectral line observations towards Hale-Bopp, C/2002 T7 (LINEAR), and C/2001 Q4 (NEAT) were compared to the BIMA and 12 m (single dish) maps of H₂CO towards Hale-Bopp. The spatial distribution of H₂CO suggested that this molecule, when

compared to CO, was extended implying a different formation mechanism for this molecule (see Appendix C). A modified Monte Carlo model was used to calculate the H₂CO production rates. Here, formaldehyde was considered as a daughter product to organic refractory particles (CHON grains). The derived production rates were

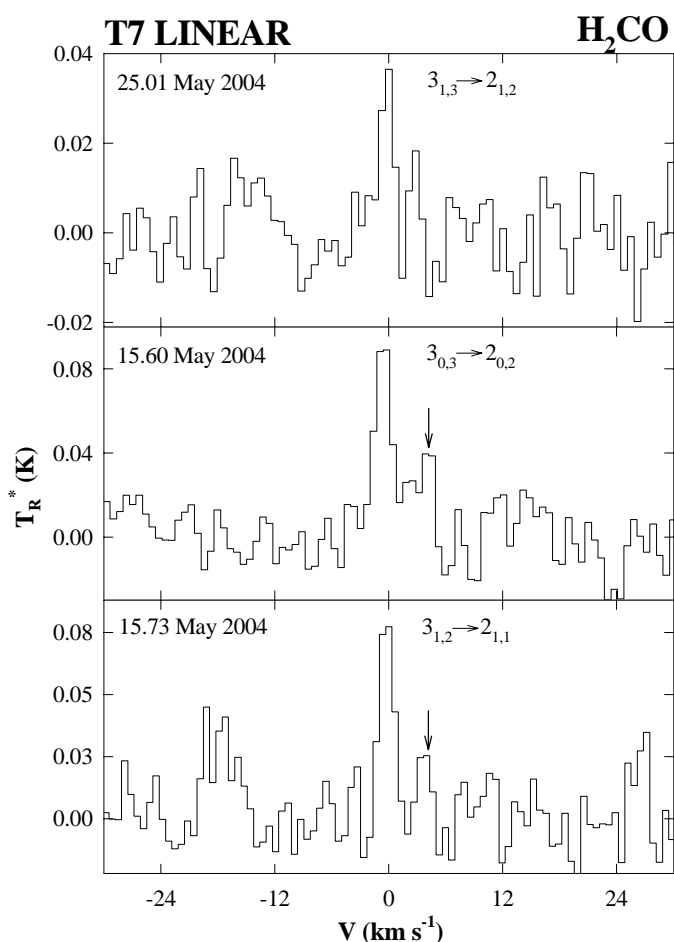


Figure 5.1. Spectra of H₂CO for comet T7 LINEAR with second velocity component denoted by a black arrow.

comet by Kawakita et al. (2004) at larger distances (~ 3.5 AU). These grains could bear organic material, released at the thermal degradation limit. This agrees to the CHON parent species of H₂CO proposed. These cometary fractionation events are frequent and

somewhat higher than the assumed parent production rates and are in agreement with the maps suggesting that H₂CO is formed from a source other than the comet nucleus.

Surprisingly, a second component was detected in the T7 LINEAR H₂CO data (see Figure 5.1), thus providing further evidence of comet fragmentation with a possible organic complex as a precursor.

Water ice and silicate grains were observed towards this

large scale, enough so at least to be observed in various molecules and multiple comets, such that the material released may seed planetary systems with rich organic material.

b. Organics in Comets and Planetary Distribution

The benefits to comparing large scale array data to single dish observations were highly successful and thus employed for another molecular investigation towards Hale-Bopp. Both the ARO 12 m and BIMA interferometer obtained data for CH₃OH and CH₃CN and verified the source as the comet nucleus (Appendix G). The numerous transitions observed for both molecules were simultaneously fit to derive a total column density of $9 \times 10^{14} \text{ cm}^{-2}$ and $T_{\text{rot}} \sim 105 \text{ K}$ for CH₃OH and $N_{\text{tot}} \sim 2.6 \times 10^{12} \text{ cm}^{-2}$ and $T_{\text{rot}} \sim 200 \text{ K}$ for CH₃CN in Hale-Bopp at $\sim 1 \text{ AU}$.

This study also investigated the formation and distribution of other organic species predicted to be in cometary coma. The lack of detection of the previously

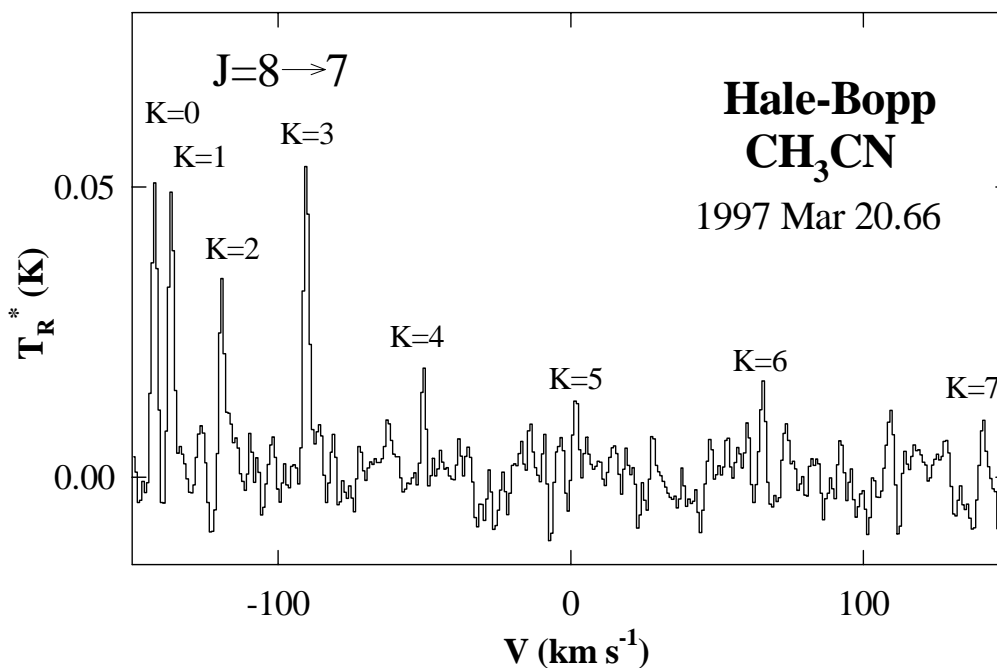


Figure 5.2. The J=8→7 transition of CH₃CN observed towards Hale-Bopp.

observed $(\text{CH}_2\text{OH})_2$ towards Hale-Bopp with the 12 m telescope suggests that this species has a nucleus source $< 9''$. Ethylene glycol is a proposed parent of the known interstellar species, glycolaldehyde, which was not detected in this comet (Crovisier et al. 2004). The distribution of this molecule, should it be the photodissociation product of $(\text{CH}_2\text{OH})_2$, would only be detectable at large, single-dish telescopes operating at lower frequencies or at medium-sized telescopes at higher frequencies (see Appendix G).

CONCLUSIONS

Through observations of various species and their isotopic compositions, the cyclic nature of molecular material in stellar evolution has been monitored. These studies have shown that the isotopic composition of the interstellar medium is highly dependent upon nearby evolved stars. However, this is seemingly independent of the chemical composition of these objects; carbon-rich or oxygen-rich. Observations have shown that oxygen-rich circumstellar envelopes have a richer carbon-chemistry than once considered. The solar $^{12}\text{C}/^{13}\text{C}$ ratio is indicative of further enhancement by either a large presence of carbon-rich AGB envelopes or a supernova. As Red Giants evolve into planetary nebulae, molecular material rich in carbon has been shown to endure this destructive phase. Additionally, matter may survive from planetary nebulae into the diffuse interstellar medium as the inventories of both regions are now converging. As the gas and dust condense into new stars and potentially planetary systems, the material is seemingly recycled in a molecular form. This is traced by the pristine composition of comets, meteors, and interplanetary dust particles. It has also been shown that comets may seed planetary systems with organic species during fragmentation or bombardment events – with possible extra-solar origins. These results suggest that carbon-bearing species found in planetary systems may have originated, at least in part, in circumstellar envelopes and survived the various processing that occurs throughout stellar evolution.

APPENDIX A

HCO⁺ OBSERVATIONS TOWARDS COMET HALE-BOPP (C/1995 O1): ION-
MOLECULE CHEMISTRY AND EVIDENCE FOR A VOLATILE SECONDARY
SOURCE

S.N. Milam, C. Savage, L.M. Ziurys, & S. Wyckoff 2004, *Astrophys. J.*, **615**, 1054-1062.

Reproduced by permission of the AAS.

HCO⁺ OBSERVATIONS TOWARD COMET HALE-BOPP (C/1995 O1): ION-MOLECULE CHEMISTRY AND EVIDENCE FOR A VOLATILE SECONDARY SOURCE

S. N. MILAM, C. SAVAGE, AND L. M. ZIURYS

Department of Chemistry, Department of Astronomy, and Steward Observatory, 933 North Cherry Avenue,
 University of Arizona, Tucson, AZ 85721

AND

S. WYCKOFF

Department of Physics and Astronomy, Arizona State University, Tempe, AZ 85287

Received 2004 February 20; accepted 2004 July 19

ABSTRACT

Several millimeter-wave transitions of HCO⁺ have been detected toward comet Hale-Bopp (C/1995 O1) using the Arizona Radio Observatory 12 m telescope. The $J = 2 \rightarrow 1$ transition at 178 GHz was observed toward the comet nucleus near perihelion on 1997 March 10 and 20, as well as the $J = 3 \rightarrow 2$ transition at 268 GHz on 1997 March 9, with angular resolutions of 36'' and 23'', respectively. These data all show a slight velocity shift (~ 1.2 km s⁻¹) from the nominal comet velocity, and the $J = 3 \rightarrow 2$ profile is asymmetric with a redshifted wing. These differences likely arise from ion acceleration by the solar wind. A rotational diagram analysis of the data yielded a column density of 1.1×10^{12} cm⁻² for HCO⁺ in Hale-Bopp, which corresponds to an average number density of 36 cm⁻³. The data taken on March 9 show a second velocity component redshifted by 7.0 ± 0.6 km s⁻¹, which is considerably weaker than the main feature and appears to have a counterpart in the HNC, $J = 3 \rightarrow 2$ data, observed within an hour of the HCO⁺ measurements. The velocity difference between the main and secondary emission lines deprojected onto the extended solar radius vector is ~ 10 km s⁻¹ for both HCO⁺ and HNC, and the weak-to-strong line intensity ratios ($\sim 5\%$) are identical to within observational errors, suggesting a common high-velocity volatile secondary source. A plausible model that may account for the redshifted velocity components is a comoving, localized debris field of submicron refractory grains accelerated by solar radiation pressure located $\sim 10^5$ – 10^6 km from the nucleus. The parent material of the weaker redshifted HNC and HCO⁺ lines may be predominately complex organic polymers. An examination of the production rates for HCO⁺ suggests that the reaction $\text{H}_2 + \text{CO}^+$ is likely to be an important route to this ion in the outer coma beyond the collisionopause, where it has its peak abundance.

Subject headings: astrochemistry — comets: individual (Hale-Bopp (C/1995 O1)) — line: profiles — molecular data — radio lines: solar system — solar wind

1. INTRODUCTION

Comets are thought to contain pristine material relatively well preserved from the early solar system. These objects were probably created in the outer presolar nebula and therefore document the chemical history of this era and that of the protoplanetary disk. Whipple's (1950) "dirty snowball" model with a small solid nucleus of refractory material mixed with ices and other frozen matter has been well substantiated by observations of many comets (e.g., Crovisier & Encrenaz 2000). As a comet approaches the Sun, a small amount of the frozen material sublimates to form an expanding coma of gas and dust. A small fraction of the coma gas is photoionized, some of which is accelerated in the antisolar direction to form the plasma tail.

Because of its extreme brightness, comet C/1995 O1 (Hale-Bopp) was one of the most extensively observed comets. At 7 AU, this object was already 100 times brighter than comet Halley, with a visual magnitude of 11 (e.g., Crovisier & Encrenaz 2000). The comet was observed at multiple wavelengths, including IR, UV, visible, X-ray, and radio (e.g., Dello Russo et al. 2000; Owens et al. 1999; Lis et al. 1999; Lovell et al. 1998; Ziurys et al. 1999). Because it has a long period and a highly inclined orbit, Hale-Bopp most likely arises from the Oort Cloud.

With the appearance of Hale-Bopp, the inventory of known chemical compounds in comets tripled (Bockelée-Morvan et al. 2000), including the addition of several new molecular ions. Investigating ions is important because they help to establish physical and chemical processes in the coma, as well as comet-solar wind interactions. The latter effect in fact causes a small acceleration (~ 1 – 10 cm s⁻²) of the ions in the antisolar direction that has been observed in many comets, including Hale-Bopp (e.g., Lovell et al. 1998; Crovisier & Bockelée-Morvan 1999). Because the species frozen in the cometary ice are likely to only be neutrals, ions must form from sublimated gas by some combination of photoionization, charge exchange, electron impact, and ion-molecule reactions in the comet coma (Crovisier & Encrenaz 2000).

HCO⁺ is an ion of particular interest for cometary studies. Although this species is fairly ubiquitous in molecular clouds, it has only recently been observed in comets. The first detection of HCO⁺ occurred in Hale-Bopp in 1997 February, where the $J = 1 \rightarrow 0$ transition at 89 GHz was measured using the BIMA antennas in autocorrelator mode (Veal et al. 1997). Other rotational transitions were subsequently observed, including the $J = 3 \rightarrow 2$ and $J = 4 \rightarrow 3$ lines at 268 and 357 GHz, respectively, using the Submillimeter Telescope (SMT) on March 5 and 9 (Narayanan et al. 1997). Lis et al. (1999) also detected the $J = 3 \rightarrow 2$ transition on March 26 using the Caltech

Submillimeter Observatory telescope. All millimeter detections occurred within a 5 month period, when the comet was brightest, from 1997 January to May, with most observations conducted from February to March.

In addition to spectral line detections, the spatial distribution of HCO⁺ was also measured in Hale-Bopp. Lovell et al. (1998, 1999), for example, mapped the $J = 1 \rightarrow 0$ transition of this ion in the comet using the Five College Radio Astronomy Observatory (FCRAO) 14 m antenna during the period of March 21 to April 27. These authors discovered a local emission minimum centered on the nominal position of the comet nucleus on several dates, as well as an asymmetric ring around the nucleus with a strong anti-sunward peak. The HCO⁺ emission region also proved to be time variable and quite extended; the species was detected 50,000–300,000 km from the nucleus. Furthermore, during March, Womack et al. (1999) mapped the $J = 1 \rightarrow 0$ line using the NRAO 12 m telescope using the on-the-fly technique and found a similar “void” at the nucleus in HCO⁺ emission. These authors explained the void as arising in the “diamagnetic cavity” where low electron temperatures in this magnetic field-free region increased the ion dissociative recombination rate and hence the destruction of HCO⁺ and other ions. Wright et al. (1998) also published mosaicked images and spectra on the $J = 1 \rightarrow 0$ transition of HCO⁺, using the BIMA interferometer. This map does not show a void near the nucleus on May 6, providing further evidence of the variability of the HCO⁺ distribution.

The unusual and time-variable distribution of ions such as HCO⁺ in Hale-Bopp, as well as recent studies of other bright comets, clearly requires a coma source more complex than Whipple’s (1950) single-source nucleus model. In situ *Giotto* spacecraft data collected from the coma of comet Halley, for example, indicated that about half of the CO and virtually all of the H₂CO were both slowly released from a distributed source extending $\sim 10^4$ km from the nucleus and likely attributable to long-lived small organic particles composed mostly of the elements carbon, hydrogen, oxygen, and nitrogen (CHON; Eberhardt 1999). Dust coma sources, accounting for about half of the CO and CN and virtually all of the H₂CO, have been reported for several comets (A’Hearn et al. 1986; Wink et al. 1999; Disanti et al. 1999). Additional evidence for extended circumnuclear source regions comes from jets spatially offset from the nucleus, as well as coma knots, condensations, and arclets, all indicative of secondary coma source regions in the form of fragments co-orbiting or released from the comet nuclei (Harris et al. 1997; Desvoivres et al. 1999; Blake et al. 1999; Gunnarsson et al. 2003).

Puzzling parallel bands (striae) observed in dust tails of many bright comets have been attributed to the disintegration of fragments of long-lived friable material located far ($>10^6$ km) from the comet nucleus (Sekanina & Farrell 1980). Striae are possibly related to interplanetary dust particles (e.g., Arpigny et al. 2003) and meteoritic material collected in the Earth’s atmosphere that have been identified as comet debris (e.g., Sekanina & Farrell 1980). The icy material comprising comet solids probably has a very low tensile strength (Whipple 1999), and a few percent of comet nuclei have split or entirely disintegrated (Sekanina 1982; Weaver et al. 2001; Boehnhardt 2002), apparently as a consequence of their low tensile strengths, not tidal interactions with planets or the Sun. Hence a picture is emerging of a friable water ice-dominated comet nucleus surrounded by circumnuclear icy fragments with size scales ranging from submicron to tens of meters that slowly degrade into successively smaller, refractory-rich fragments (<2 AU).

The refractory debris contributes to the expanding coma and further thermally degrades over long timescales ($\sim 10^5$ – 10^6 s; Sekanina & Farrell 1980) into complex organic parent molecules of the observed HNC, CO, and H₂CO (e.g., Sekanina & Farrell 1980; Huebner et al. 1987, 1991; Jewitt & Matthews 1999; Rodgers & Charnley 2001; Charnley et al. 2002; Cottin et al. 2001).

In this paper, we report independent detections of the $J = 2 \rightarrow 1$ and $J = 3 \rightarrow 2$ transitions of HCO⁺ toward the comet, using the Kitt Peak 12 m telescope. The $J = 2 \rightarrow 1$ transition had not been previously observed. From these spectra, a column density and rotational temperature were determined. In addition to a broad, redward Doppler-shifted wing, a weak high-velocity (~ 7 km s⁻¹) component appears in the HCO⁺ spectra on March 9 that has a counterpart in the HNC spectrum observed on the same day. Here we suggest that these weak line components may have arisen from a transient secondary coma source created when a coma fragment abruptly disintegrated into a debris field rich in organic grains, such as CHON particles or complex organic polymers (Huebner et al. 1991; Rogers & Charnley 2001; Cottin et al. 2001). Submicron grains were then selectively accelerated by solar radiation pressure to ~ 10 km s⁻¹ on a timescale of ~ 1 – 2 days. In this scenario the weak, redshifted components of both HCO⁺ and HNC arose from thermal degradation of the accelerated debris field located roughly 10^5 – 10^6 km on the antisolar side of the nucleus.

2. OBSERVATIONS

Measurements of HCO⁺ were carried out during the period 1997 March 9 to March 20. The observations were made using the former NRAO 12 m telescope at Kitt Peak, Arizona.¹ The receivers used were dual-channel SIS mixers, operated in single-sideband mode with image rejection around 20 dB, covering the 2 and 1.2 mm bands. The back ends employed were filter banks with 250 kHz, 500 kHz, or 1 MHz resolution, depending on the given frequency. The temperature scale was determined by the chopper-wheel method and is given in terms of T_R^* , corrected for forward spillover losses (η_{fs}). Radiation temperature is then determined using η_c , the corrected beam efficiency, where $T_R = T_R^*/\eta_c$. The position of the comet was determined through a two-body ephemeris program using the orbital elements provided by D. Yeomans of JPL. The telescope was pointed toward the nominal ephemeris position of the nucleus and tracked at the comet’s predicted ephemeris rates during the observations. To ensure positional accuracy, periodic pointing and focusing on Jupiter and Saturn were conducted. Data were collected by position-switching with the off position 30’ west in azimuth.

Observing frequencies used for HCO⁺ are listed in Table 1. Also given are the beam efficiencies at these frequencies and the respective angular and linear beam sizes projected at the comet, as well as the comet’s heliocentric (R_h) and geocentric (Δ) distances.

3. RESULTS

Table 1 summarizes the observational results for HCO⁺. As the table shows, the $J = 2 \rightarrow 1$ line of HCO⁺ at 175 GHz was

¹ The National Radio Astronomy Observatory is a Facility of the National Science Foundation operated under cooperative agreement by the Associated Universities, Inc. The Kitt Peak 12 m telescope is currently operated by the Arizona Radio Observatory at Steward Observatory (the University of Arizona), with support from the Research Corporation.

TABLE 1
OBSERVATIONS AND ABUNDANCES TOWARD COMET HALE-BOPP

Molecule	Transition ($J+1 \rightarrow J$)	UT Date (1997)	ν (MHz)	θ_b (arcsec)	D (km)	η_c	T_R^* (K)	$\Delta v_{1/2}$ (km s^{-1})	R_b (AU)	Δ (AU)	N_{tot} (cm^{-2})
HCO ⁺	3 → 2	Mar 9.95	267,557.6	23	23,640	0.42	0.52 ± 0.01	3.5 ± 0.3	1.003	1.387	1.08 × 10 ^{12a}
	0.08 ± 0.03 ^b	1.5 ± 1.2 ^b
	2 → 1	Mar 10.59	178,375.1	36	35,950	0.67	0.51 ± 0.09	3.7 ± 0.6	0.996	1.377	1.08 × 10 ^{12a}
	2 → 1	Mar 20.63	178,375.1	36	34,410	0.67	0.45 ± 0.04	3.3 ± 0.3	0.940	1.318	4.31 × 10 ^{11c}
HNC ^d	3 → 2	Mar 9.92	271,981.1	23	23,184	0.38	0.66 ± 0.05	2.3 ± 0.3	1.003	1.387	3.4 × 10 ¹²
	0.08 ± 0.03 ^b	1.1 ± 0.9 ^b

NOTE.—Errors are 3 σ .

^a N_{tot} derived from rotational diagram (see text).

^b The second component redward of the main line in Fig. 1.

^c Assumes $T_{\text{rot}} = 7$ K.

^d From Ziurys et al. (1999).

observed on the UT dates March 10 and March 20. The $J = 3 \rightarrow 2$ transition of HCO⁺ at 267 GHz and the $J = 3 \rightarrow 2$ transition of HNC at 272 GHz were measured on March 9 only. Line parameters are also given in this table, which were determined by fitting Gaussians to the line profiles of each of the spectra. As the table shows, the HCO⁺ spectra typically had $T_R^* \sim 0.5$ K and line widths near 3.5 km s^{-1} . These line widths are somewhat broader than typically observed in comets for neutral molecules. For example, HCN had a line width of 2.3 km s^{-1} in the $J = 3 \rightarrow 2$ transition in comet Hale-Bopp (Ziurys et al. 1999).

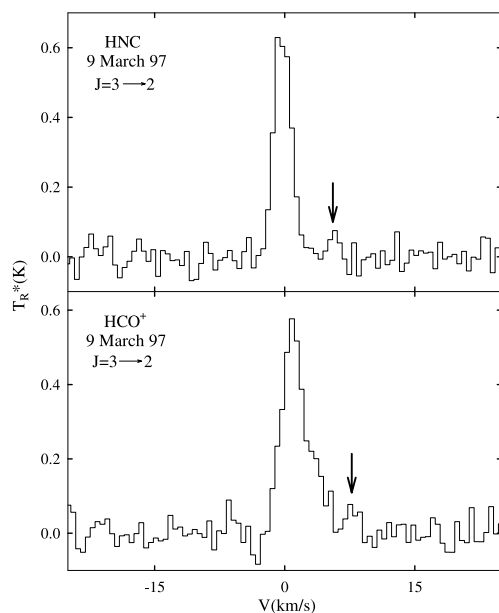


FIG. 1.—The $J = 3 \rightarrow 2$ transition of HCO⁺ at 267 GHz and the $J = 3 \rightarrow 2$ line of HNC at 272 GHz detected toward comet Hale-Bopp, using the 12 m telescope on 1997 March 9 with 500 kHz (0.55 km s^{-1}) resolution. A second velocity component appears to be present in both spectra, shifted by about 5 km s^{-1} from the main line, indicated by arrows. The HNC feature is at the nominal comet velocity, while that of HCO⁺ is redshifted by $\sim 1.2 \text{ km s}^{-1}$. The HCO⁺ profile also is asymmetric with a prominent redshifted line wing. Spectra are plotted in a cometocentric velocity frame.

Spectra obtained from comet Hale-Bopp are presented for each date observed in Figures 1 and 2. Figure 1 displays the spectra of the $J = 3 \rightarrow 2$ transition of HCO⁺ (integration time 48 minutes) and the $J = 3 \rightarrow 2$ transition of HNC (integration time 1 hr), both recorded on March 9. Figure 2 displays the $J = 2 \rightarrow 1$ transition of HCO⁺ on March 10 (integration time 1 hr 48 minutes) and March 20 (with 1 hr integration time). All figures are plotted in the cometocentric velocity frame. Each HCO⁺ transition displays a strong central peak shifted by $\sim 1.2 \text{ km s}^{-1}$ from the predicted geocentric comet velocity (cf. HNC velocity in Fig. 1). Also, the $J = 3 \rightarrow 2$ line of HCO⁺ shows an asymmetric profile with a redshifted tail, which is in the antisolar direction. This effect has been seen in other ion spectra (Lovell et al. 1998; Wright et al. 1998; Womack et al.

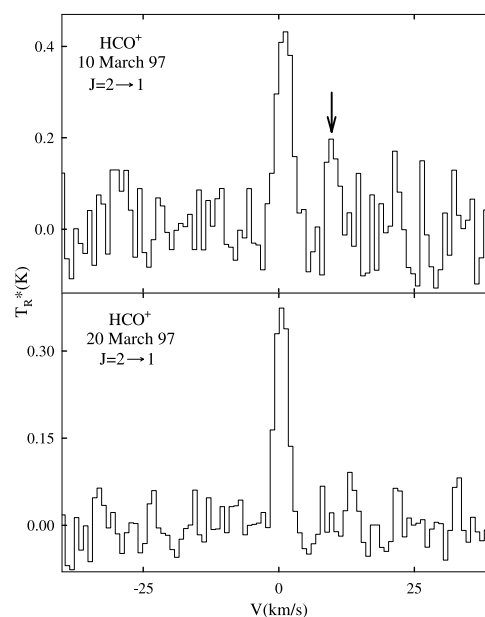


FIG. 2.—The $J = 2 \rightarrow 1$ transition of HCO⁺ at 178 GHz detected on 1997 March 10 and 20 toward comet Hale-Bopp, using 500 kHz resolution. A second component may be present in the March 10 data, as indicated by an arrow, but is not visible in the March 20 spectrum.

1999; Narayanan et al. 1997). The slight redward displacement and asymmetry likely arise from the antisolar motional force due to the solar wind interaction with the comet. Lovell et al. (1999) estimated the HCO⁺ acceleration to be $\sim 10 \text{ cm s}^{-2}$ in 1997 March.

In addition to the main emission-line feature, both the HNC and the HCO⁺ ($J = 3 \rightarrow 2$ and $J = 2 \rightarrow 1$) lines have weaker redshifted velocity components, displaced from the stronger lines by $\sim 7 \text{ km s}^{-1}$ (indicated by arrows in Figs. 1 and 2). These redshifted velocity components do not arise from extraneous background sources, nor are they likely caused by interaction with the solar wind, since the neutral (HNC) and ionic (HCO⁺) species both display the same velocity shifts and have similar primary-to-secondary intensity ratios. If associated with the comet, these redshifted velocity components may represent the first spectroscopic evidence for a distinct secondary coma source rich in volatile complex organic compounds. If so, the relatively high velocity can probably be explained by solar radiation pressure forces acting on submicron-sized grains rich in organic material. The velocities for the HNC and HCO⁺ line pairs associated with the secondary source, deprojected onto the solar radius vector, $v_{ss} \approx 10 \text{ km s}^{-1}$, are well in excess of the escape velocity from the comet nucleus, $v_{esc} \sim 15 \text{ m s}^{-1}$ (radius $r_n \sim 20 \text{ km}$). If the weak HCO⁺ component indicated in Figure 2 (top) is real, its deprojected velocity is $\sim 13 \text{ km s}^{-1}$, corresponding to an acceleration of the secondary source $a_{ss} \sim 0.05 \text{ m s}^{-2}$. This acceleration would require an antisolar force about 10 times the solar gravitational attraction.

4. ANALYSIS

4.1. Abundances of HCO⁺

Since the projected beam diameters of the 12 m telescope (see Fig. 3 and Table 1) at both observing frequencies are smaller than the collisionopause, it is most probable that the excitation of HCO⁺ is dominated by collisions with H₂O. The collisionopause of a comet is defined by the mean free path of a neutral molecule in a water-dominated coma (e.g., Wyckoff 1982). For Hale-Bopp, with $Q(\text{H}_2\text{O}) \sim 10^{31}$ molecules s^{-1} and an outflow velocity of $v \sim 1 \text{ km s}^{-1}$, the mean free path is $\sim 8 \times 10^4 \text{ km}$ for an assumed neutral-neutral collisional cross section of $\sigma \sim 10^{-15} \text{ cm}^2$ or a collisionopause of $r \sim 10^5 \text{ km}$ centered at the nucleus. The only other form of excitation is by solar radiation as the comet approaches perihelion, which can be estimated for comparison. This radiative rate g is defined as $g = (\pi e^2/mc^2) f F_\odot$, where $\pi e^2/mc^2 = 8.82 \times 10^{-13} \text{ cm}$, f is the absorption oscillator strength, and F_\odot is the solar flux (Weaver & Mumma 1984). Using this formula, g is calculated to be $\sim 10^{-6} \text{ s}^{-1}$ for HCO⁺. In contrast, the collision rate (with water) for excitation from the $J = 2$ level to the $J = 3$ level is $\sim 2 \times 10^{-5} \text{ s}^{-1}$, assuming a cross section of $\sigma = 10^{-14} \text{ cm}^2$ (Crovisier 1987), a density of $n_{\text{H}_2\text{O}} = 1.2 \times 10^5 \text{ cm}^{-3}$ (Dello Russo et al. 2000), and a kinetic temperature of 50 K. This value is significantly faster than the radiative rate.

Because collisional excitation is dominant, a rotational diagram was constructed to estimate the column density of HCO⁺. In such diagrams, the slope is inversely related to the rotational temperature T_{rot} and the y -intercept establishes the total column density, assuming that the gas is optically thin and in thermal equilibrium. Four data points were included in this analysis: the $J = 3 \rightarrow 2$ and $J = 2 \rightarrow 1$ transitions [$E_{\text{rot}}(J) = 12.84$ and 8.56 K] from this work and the $J = 3 \rightarrow 2$ and $J = 4 \rightarrow 3$ ($E_{\text{rot}} = 17.12 \text{ K}$) lines from the SMT observations

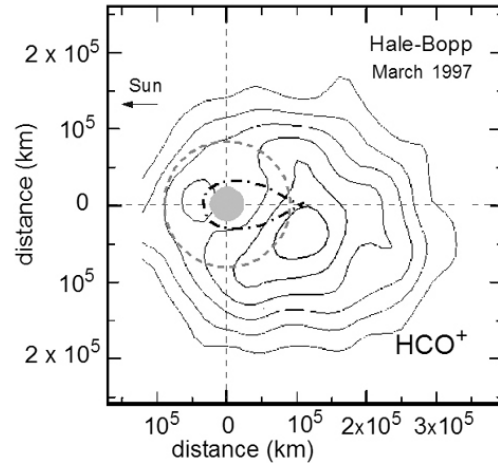


FIG. 3.—HCO⁺ emission distribution (isophotes adapted from Lovell et al. 1999) in comet Hale-Bopp. Projected beam size of 12 m telescope for $J = 2 \rightarrow 1$ transition, centered on nominal position of comet nucleus at position (0, 0), is indicated by the gray circle. Within the magnetic field-free ionopause (dot-dashed line; also called the diamagnetic cavity), HCO⁺ ions initially expand with neutrals at 1 km s^{-1} . Ion-molecule chemical reactions produce HCO⁺ over an extended region; a significant fraction is reacted outside the collisionopause (dashed circle with radius 80,000 km). The low intensity of HCO⁺ emission in the ionopause and the collisionopause regions is likely due to rapid destruction of these ions by dissociative recombination.

(Narayanan et al. 1997). These HCO⁺ lines were all detected at approximately the same heliocentric distance (March 5 through March 10). The equation used to determine an average HCO⁺ column density for these dates is

$$\log(3kT_R \Delta v_{1/2} / 8\pi^3 \nu S_{ij} \mu_0^2) = \log(N_{\text{tot}} / g_{\text{rot}}) - (\log e)(E_u / T_{\text{rot}}), \quad (1)$$

where ν is the frequency, S_{ij} is the line strength, μ_0 is the permanent dipole moment (4.0 D), g_{rot} is the rotational partition function, and N_{tot} is the total number of HCO⁺ ions observed in the beam.

The results of this analysis are shown in Figure 4. The data taken with the 12 m are shown by filled circles and that from the SMT by unfilled circles. As is apparent in Figure 4, the $J = 3 \rightarrow 2$ column density obtained with the 12 m telescope is consistent with the observations obtained with the SMT (Narayanan et al. 1997), and all four data points lie along a straight line, lending credibility to this analysis. The rotational temperature derived from the plot in Figure 4 is approximately 7 K, and the total column density is $N_{\text{tot}} = 1.1 \times 10^{12} \text{ cm}^{-2}$. This value is in close agreement with those reported by other authors. For example, Narayanan et al. (1997) estimated a column density from the $J = 3 \rightarrow 2$ and the $J = 4 \rightarrow 3$ transitions of $2.7 \times 10^{12} \text{ cm}^{-2}$. The column density reported here corresponds to a space density of 36 cm^{-3} , given a region with a radius of $r \sim 1.5 \times 10^{10} \text{ cm}$ (Lovell et al. 1999).

The $J = 2 \rightarrow 1$ line was also observed separately on March 20. To calculate a total column density on this date, the following formula was used, which assumes low optical depth:

$$N_{\text{tot}} = (3kT_R \Delta v_{1/2} / 8\pi^3 \nu S_{ij} \mu_0^2) g_{\text{rot}} / e^{-\Delta E / kT_{\text{rot}}}. \quad (2)$$

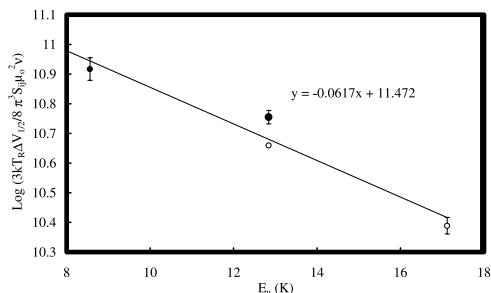


FIG. 4.—Rotational diagram for HCO^+ in comet Hale-Bopp (1997 March). Filled circles: Data presented from this study. Open circles: Data from Narayanan et al. (1997). The diagram indicates $N_{\text{tot}} = 1.1 \times 10^{12} \text{ cm}^{-2}$ and $T_{\text{rot}} = 7 \text{ K}$ for HCO^+ .

The symbols have identical meaning as in equation (1), and ΔE indicates the energy of the $J = 2$ level above ground state. A rotational temperature of 7 K was used, as indicated by the rotational diagram. The resulting column density for March 20 was calculated to be $N = 4.3 \times 10^{11} \text{ cm}^{-2}$, about a factor of 3 lower.

These equations, however, assume the Rayleigh-Jean limit, namely, $h\nu \ll kT_{\text{ex}}$, which may not be appropriate. For comparison, a column density was also calculated from the $J = 2 \rightarrow 1$ data without the Rayleigh-Jean approximation; $N_{\text{tot}} = 4.647 \times 10^{11} \text{ cm}^{-2}$ was derived. The two values differ by only 8%, and hence the former assumption is justified.

4.2. Chemical Schemes for HCO^+ Production and Destruction

The only plausible mechanism for creating HCO^+ in this very high production rate comet is by chemical reactions in the coma (e.g., Lovell et al. 1998, 1999; Irvine et al. 1998). Three reactions are possible for HCO^+ synthesis in the coma:

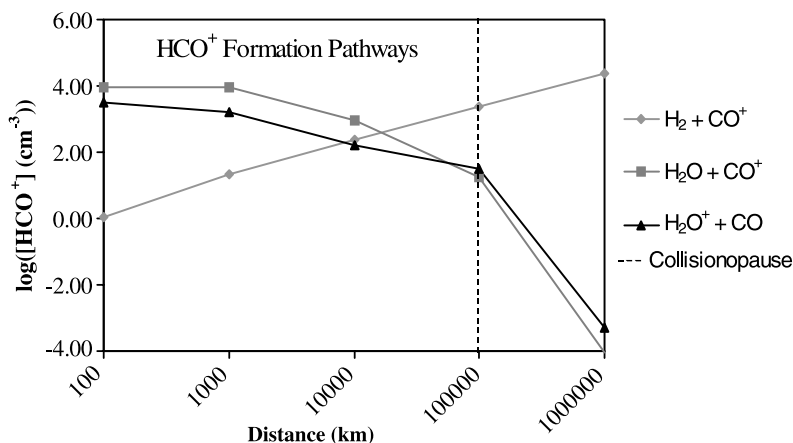
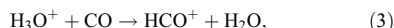
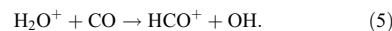


FIG. 5.—Plot illustrating the relative importance of the reactions $\text{H}_2\text{O}^+ + \text{CO}$, $\text{H}_2\text{O} + \text{CO}^+$, and $\text{CO}^+ + \text{H}_2$ in the production of HCO^+ . Inside the collisionopause (indicated by the dashed line at 10^5 km), water and H_2O^+ are the major precursors. However, near the edge of this region, the H_2 abundance has sufficiently risen to enable the pathway $\text{H}_2 + \text{CO}^+$ to dominate HCO^+ synthesis.



Reaction (4) cannot be significant because H_2O has a higher proton affinity than CO (Huntress et al. 1980). Irvine et al. (1998) suggest that reaction (5) is the likely source of HCO^+ , which is consistent with the broad distribution of CO^+ , which is consistent with the broad distribution of CO^+ predicted by models (Gombosi et al. 1999). The rate of this reaction is $k_5 = 8.8 \times 10^{-10} \text{ cm}^3 \text{ s}^{-1}$ (Le Teuff et al. 2000). The model by Gombosi et al. (1999) also predicts large abundances of H_2O^+ at the nucleus and throughout the comet tail. Given the high relative abundance of CO within the collisionopause in Hale-Bopp, reaction (6) is also a viable route to HCO^+ . This reaction has a rate of $k_6 = 5.0 \times 10^{-10} \text{ cm}^3 \text{ s}^{-1}$, which is comparable to that of reaction (5).

On the other hand, H_2O is rapidly destroyed by photodissociation within the collisionopause as predicted, for example, by the model of Lovell et al. (1999). The photodissociation of water leads mainly to H , OH , and O , but H_2 and H_2O^+ are also significant products (Huebner et al. 1992). Because a large amount of CO^+ exists beyond the collisionopause, another way to produce HCO^+ is



This reaction proceeds at a rate of $k_6 = 1.8 \times 10^{-9} \text{ cm}^3 \text{ s}^{-1}$ (Le Teuff et al. 2000), which is certainly competitive with the other HCO^+ formation rates.

A quantitative comparison of these three major production schemes of HCO^+ is illustrated by Figure 5, which displays the density of HCO^+ (in cm^{-3}) as a function of distance from the nucleus, calculated separately from reactions (5), (6), and (7). The density of water, CO , and CO^+ used in the computations was taken from Lovell et al. (1999), and that of H_2O^+ from Gombosi et al. (1999). To determine the density of H_2 , the branching ratios for the photodestruction of water by Huebner et al. (1992) were used (an average density of $\sim 10^6 \text{ cm}^{-3}$ was obtained). An outflow velocity of 1 km s^{-1} was also assumed. Figure 5 clearly shows that the reactions starting with H_2O and

H₂O⁺ are the dominant source of HCO⁺ within the collisionopause ($r_N \sim 1 \times 10^5$ km), but they become insignificant compared to the H₂ reaction outside of that region.

HCO⁺ is likely destroyed by photodissociation, proton transfer to H₂O, and dissociative electron recombination. Using the cross section of Koch et al. (1995), the photodissociation rate for HCO⁺ ($R = 1$ AU) is 4.18×10^{-8} ions s⁻¹, which corresponds to a lifetime of $\tau \sim 2.4 \times 10^7$ s or 277 days. Proton transfer via the reaction H₂O + HCO⁺ → CO + H₃O⁺ has a rate of 2.5×10^{-9} cm³ s⁻¹ (Le Teuff et al. 2000). Assuming that the HCO⁺ density is 36 cm⁻³, the lifetime for HCO⁺ with destruction by this reaction is $\tau \sim 1 \times 10^7$ s, or 129 days. In contrast, at 50 K, the electron recombination rate was calculated to be 5.22×10^{-8} cm³ s⁻¹ (Le Teuff et al. 2000). From the model of Lovell et al. (1999), the electron density falls in the range $n_e \sim 10^3$ – 10^5 cm⁻³ over the region traced by HCO⁺ (see Fig. 3). Therefore, the electron recombination rate for HCO⁺ is typically $\sim 5 \times 10^{-5}$ to 5×10^{-3} s⁻¹. Thus, the lifetime of this ion against dissociative electron recombination is about 3–300 minutes, making this pathway the primary destruction route by many orders of magnitude. This calculation also indicates that HCO⁺ is short lived and is likely formed in situ in the various cometary regions.

4.3. Origin of HNC and HCO⁺ in the High-Velocity Component

The stronger components in HNC and HCO⁺ (Figs. 1 and 2) arise from the nucleus region, since the line positions correspond to the nominal comet ephemeris positions, taking into account the solar wind-induced ion acceleration. The similar line intensity ratios of the two weaker components for HNC and HCO⁺, together with their identical redshifts relative to the main feature, constitute strong evidence that these lines are associated with a common secondary source. This redshifted coma component had not previously been reported for any comet, although other HCO⁺ spectra (e.g., Lovell et al. 1998; Lis et al. 1999) show a possible feature near 5 km s⁻¹ at about the same epoch. The main HCO⁺ and HNC lines (Fig. 1) have relatively high signal-to-noise ratios (~ 26), but for the weaker feature the ratio is about 3. The secondary source is not obvious in the March 20 spectra of HCO⁺ but may be present in the March 10 data (see Fig. 2), as noted above. No secondary velocity component was observed in HCN spectra, but this absence may be explained by masking of the hyperfine structure.

HNC, CO, and H₂CO are thought to be produced at least in part in the extended coma, not only the comet nucleus (Huebner et al. 1991; Cottin et al. 2001; Rodgers & Charnley 2001). For example, the map of HCN by Veal et al. (2000) on March 8 showed a nucleus-centered distribution extending $\sim 10^4$ km from the nucleus. In contrast, observations of HNC by Hirota et al. (1999) show a slightly more extended region than HCN (50'' vs. 38'', respectively). Blake et al. (1999) found that HCN and HNC arose from two distinct regions, leading to the suggestion that HNC arose from photodestruction of complex organic species or CHON particles when the comet was near the Sun, $R_h \sim 1$ AU (Rodgers & Charnley 1998; Rodgers et al. 2003).

As is the case for HNC, HCO⁺ is not a direct sublimation product. The primary component of HCO⁺ is probably created by ion-molecule reactions requiring an environment with significant collisional rates. Using the modeled number densities of Lovell et al. (1999), the ion-molecule reaction timescales in the ringlike region where HCO⁺ had peak abundances (Fig. 3 and Lovell et al. 1999) ranged from $\tau_{\text{im}} \sim 100$ s at a distance

from the nucleus $R_n \sim 10^3$ km to $\tau_{\text{im}} \sim 10^5$ s at $R_n \sim 10^5$ km. Consequently there is little question that most of the HCO⁺ was produced by ion-molecule reactions (and destroyed by electron recombination) in the dense inner coma. However, the high-velocity redshifted component of HCO⁺ may have been created in the same transient secondary source, which produced the HNC and presumably also made CO. Virtually all ($\sim 95\%$) of the H₂CO in Hale-Bopp arose from an extended coma source (Wink et al. 1999), perhaps from a formaldehyde polymer such as polyoxymethylene (POM; Huebner et al. 1991; Cottin et al. 2001). Destruction of POM material could also lead to HCO⁺.

4.4. Acceleration Mechanisms

Several mechanisms could accelerate small fragments from the vicinity of the nucleus preferentially in the antisolar direction. Comet Hale-Bopp had one of the highest levels of gas production ever observed in a comet and displayed activity at optical wavelengths (transient emission enhancements) over a large range in heliocentric distance ($R_h \sim 7$ AU). The comet was particularly active during the weeks before March as it approached perihelion (1997 April 1). Frequent outbursts, arcs, and jets of dust, OH, C₂, and CN were reported from January to August (e.g., Lederer et al. 1999; McCarthy et al. 1999; Schwarz et al. 1999). Jetlike structures were also noticeable in the HCN and HNC maps (Veal et al. 2000; Blake et al. 1999).

The nucleus mass ($m_n \sim 10^{16}$ kg) and rotation ($P_{\text{rot}} \sim 11.3$ hr) (e.g., Jewitt & Matthews 1999) set constraints on the dynamics of ejected fragments. A large fragment ejected by rotation from the comet nucleus would leave with a velocity $v_{\text{rot}} = 2\pi r_n / P_{\text{rot}} \sim 3$ m s⁻¹, less than the escape velocity $v_{\text{esc}} \sim 15$ m s⁻¹ for a nucleus radius $r_n \sim 20$ km (Weaver & Lamy 1999; Jewitt & Matthews 1999). The maximum size r_g for a small fragment lifted from the nucleus surface by sublimating gases with velocity $v_{\text{ej}} \sim 1$ km s⁻¹ ($R_h \sim 1$ AU) and gas production rate $\dot{Q} \sim 10^{31}$ molecules s⁻¹ may have been larger for Hale-Bopp than for most comets [$r_g(\text{max}) \sim 15$ cm] with a terminal velocity $v_t \sim 10$ m s⁻¹ (Harmon et al. 1999) because of the large gas production rate. Hence the combination of nucleus rotation plus gas drag could have ejected fragments with sizes ≤ 15 cm from the surface.

Large-grain production rates comparable to gas production rates have been inferred from detections of icy grain halos using radar techniques (Harmon et al. 1999). The large grains have centimeter size scales and have been observed surrounding several comet nuclei out to distances of $R_n \sim 10^2$ – 10^3 km (e.g., Harmon et al. 1999). Large-grain evaporation and fragmentation can explain spherical gas comae, distributed sources, and discrepancies between radar and radio-continuum observations (Harris et al. 1997; Jewitt & Matthews 1997; Harmon et al. 1999). To account for the HCO⁺ and HNC components comoving with a velocity ~ 10 km s⁻¹, we suggest a secondary source originating from the abrupt disintegration of a near-nucleus fragment initially drifting with a velocity ~ 10 m s⁻¹. Depending on the grain size distribution and ice content of the resulting debris field, the subfragments were subjected to a variety of antisolar-directed net forces, including sublimation recoil (dominant for the 1 mm to 1 cm sized “mini comets”), solar radiation pressure (dominant for the submicron grains), and electrostatic forces (dominant for grains < 0.1 μm ; Horanyi & Mendis 1991; Ip & Jorda 1998). For an observed acceleration $a_{\text{ss}} \sim 0.05$ m s⁻², the dust debris source was accelerated to 10 km s⁻¹ on timescales of days and was located on the antisolar side of the nucleus at a distance $R_n \sim 10^5$ – 10^6 km, coinciding with the observed locations of both HCO⁺

and HNC (Lovell et al. 1999; Wink et al. 1999; Blake et al. 1999).

Our observations set limits to the lifetime of the secondary source associated with the HCO⁺ and HNC high-velocity components. The time interval between the March 9 and the March 10 observations was ~ 15 hr, and no redshifted weak HCO⁺ line was observed in the March 20 spectrum. Therefore, the secondary source lifetime is set at $\tau_{ss} \sim 10^4$ – 10^6 s.

If a sublimation jet force biased in the antisolar direction accounted for part of the acceleration of large (centimeter sized) icy grain fragments associated with the secondary source of gas velocity (~ 10 km s⁻¹), their lifetimes had to exceed the destruction timescales from sublimation, fragmentation, and collisions. The sublimation lifetime for a 1 cm dirty ice grain is about 1 hr ($R_h \sim 1$ AU), and for pure ice ~ 1 day (Mukai 1986). For an icy grain moving away from the Sun because of a sublimation recoil force, the acceleration due to this jet effect is

$$a_j = v_{ej}(dm_g/dt)m_g^{-1}, \quad (7)$$

where v_{ej} is the gas ejection velocity and the grain mass is

$$m_g = 4\pi\rho_g r_g^3/3, \quad (8)$$

where ρ_g is the mean density. The mass-loss rate is then given by

$$(dm_g/dt) = 7.5 \times 10^{-4} r_g^2 \text{ kg s}^{-1}, \quad (9)$$

where a mass-loss rate per unit area $d\mu/dt = 1.2 \times 10^{-4}$ kg m⁻² s⁻¹ is assumed (Harmon et al. 1999). This gas mass-loss rate scaling is consistent with the Hale-Bopp nucleus gas mass-loss rate and with the mass-loss rates observed for centimeter-sized grains in other comets (Harmon et al. 1999). The solar gravitational acceleration at 1 AU is

$$a_s = GM_s d_h^{-2} \sim 5.9 \times 10^{-3} \text{ m s}^{-2}, \quad (10)$$

where G is the gravitational constant, M_s is the mass of the Sun, and d_h is the heliocentric distance. For a 1 cm ice grain with $v_{ej} \sim 1$ km s⁻¹ and $\rho_g \sim 300$ kg m⁻³, we find the net antisolar acceleration $a_{net} = a_j - a_s \sim 0.05$ m s⁻². Thus, the time required to accelerate a 1 cm grain by sublimation recoil to $v_{ss} \sim 10,000$ m s⁻¹ is

$$t_g \sim v_{ss}/2a_{net} \sim 1 \text{ day}. \quad (11)$$

This value is an order of magnitude longer than the sublimation lifetime for dirty ice (1 AU) but the same order as the lifetime for pure ice (Mukai 1986). Since the large grains surrounding comet nuclei probably arise from hierarchical fragmentation (e.g., Harris et al. 1997), the freshly exposed ices may have lifetimes longer than indicated by dirty ice models, possibly closer to those of pure ice. If it survives, the distance from the nucleus, R_n , reached by a 1 cm ice grain accelerated by a sublimation jet effect is

$$R_n \sim a_{net} t_g^2 / 2 \sim 10^5 \text{ km}. \quad (12)$$

This distance is comparable to the size of the collisionopause and within the region where ion-molecule chemistry is significant (see Fig. 4).

Although sublimation recoil may have contributed to the antisolar acceleration of small grains, their short sublimation

lifetimes require an additional acceleration mechanism to account for the observed redshifted HNC and HCO⁺ lines. We therefore suggest that rapid thermal decomposition (or possibly crystallization) of a fragment suddenly produced a swarm of organic-rich material with submicron size scales, such as CHON particles or organic-rich polymers. A swarm of such particles (parent material of the observed HNC and HCO⁺) could have been *selectively* accelerated (because of their grain sizes) to velocities of ~ 10 km s⁻¹ on timescales of days by solar radiation pressure and, possibly, electrostatic forces. If these submicron-sized refractory particles were volatile (e.g., DiSanti et al. 1999; Rodgers & Chamley 2001), they could have accounted for the secondary source giving rise to the redshifted HNC and HCO⁺ lines. Solar radiation pressure acceleration is given by

$$a_r = 3L_s Q_{pr} (16\pi d_h^2 c \rho_g r_g)^{-1}, \quad (13)$$

where L_s is the solar luminosity, Q_{pr} is the radiation interaction efficiency, and c is the velocity of light (e.g., Harris et al. 1997). For a grain with $r_g \sim 10^{-7}$ m at 1 AU, $\rho_g \sim 1000$ kg m⁻³, $L_s \sim 3.9 \times 10^{26}$ W, and $Q_{pr} \sim 1$, a_r is estimated to be ~ 0.03 m s⁻². For a dielectric grain such as olivine charged by solar UV radiation and the cometary plasma environment, the electrostatic acceleration a_e is ~ 0.03 m s⁻² for a grain with $r_g \sim 10^{-7}$ m at $d_h = 1$ AU (Horanyi & Mendis 1991). Thus a submicron-sized grain at 1 AU would require ~ 4 days to accelerate to a velocity of 10 km s⁻¹ by radiation pressure alone and would require ~ 2 days for a combination of radiation pressure and electrostatic acceleration, reaching distances on the antisolar side of the nucleus in the range $R_n \sim 10^5$ – 10^6 km. If the decomposition timescales of the parents of HNC and HCO⁺ were comparable to the time of flight of the putative submicron dust debris field, then the redshifted lines may be explained by such a scenario. We note that the 12 m telescope field of view projected at the comet distance was 24,000 and 36,000 km for the March 9 and 10 observations, respectively. Thus, the debris field could have been dispersed over a large area, yet represent an enhancement of HCO⁺ and HNC over the ambient coma.

5. DISCUSSION

5.1. A Model of HCO⁺ Formation in Comet Hale-Bopp

HCO⁺ emission in Hale-Bopp appears to be concentrated in a large shell-like region offset from the nominal comet nucleus position in the tailward direction ($r_N \sim 10^5$ km) and extending over several hundred thousand kilometers, as shown in Figure 3. This shell-like HCO⁺ distribution has density peaks in the sunward ($r_N \sim 5 \times 10^4$ km) and the antisolar ($r_N \sim 10^5$ km) directions. The sunward HCO⁺ peak may be caused by two effects: (1) a decrease in the HCO⁺ destruction rate (due to an increase in electron temperature beyond the collisionopause; e.g., Lovell et al. 1998), and (2) stagnation/reversal of the outward HCO⁺ outflow due to mass loading of the incoming solar wind plasma. Between the collisionopause ($r_c \sim 10^5$ km) and the bow shock ($r_N \sim 2 \times 10^6$ km) that has formed on the sunward side of the coma, mass loading of the incoming solar wind by the cometary pickup ions tends to decelerate and to redirect the coma ion outflow tailward (e.g., Gombosi et al. 1999). This ion stagnation and flow reversal enhances the column densities of ions on the sunward side of the coma (Lovell et al. 1998). A further enhancement of the ion densities would be expected from a sudden increase in electron temperature beyond the collisionopause, where the electrons are

no longer collisionally coupled to the ion and neutral outflow (e.g., Gombosi et al. 1999; Lovell et al. 1998). This sunward HCO⁺ peak may also be associated with the H₂O⁺ pileup region identified in comet Hale-Bopp (Bouchez et al. 1999). The HCO⁺ enhancement at $r_N \sim 10^5$ km tailward is probably caused by the focusing of the ion flow (Gombosi et al. 1999).

The distribution of HCO⁺ is beyond the outer boundaries of the collisionopause as well. The collisionopause is defined as the area where water is the main collisional partner; however, there are clearly other collisional partners (e.g., CO and H₂). The critical density for collisional excitation of HCO⁺ ($J = 1 \rightarrow 0$) is on the order of $\sim 10^6$ cm⁻³. For HCO⁺ ($J = 1 \rightarrow 0$) emission to be present, these densities must exist. They are certainly high enough to allow for significant collisions and to promote ion-molecule chemistry within the collisionopause.

For carbon monoxide and water, the overall coma abundance ratio was found to be $n(\text{CO})/n(\text{H}_2\text{O}) \sim 23\%$ (Bockelée-Morvan et al. 2000). The ion-molecule production rates of HCO⁺ for reactions (5) and (6) with this correlated abundance ratio give the production ratio of the two reactions as $Q_5/Q_6 \sim k_5 n(\text{H}_2\text{O})/k_6 n(\text{CO}) \sim 7.7$. Consequently, reaction (5) is probably the dominant pathway for producing HCO⁺ within the collisionopause of the comet coma. Once H₂O is destroyed, reaction (7) may become the dominant source, contributing to the extended region of HCO⁺ observed well beyond the collisionopause.

5.2. The High-Velocity Secondary Source

Split nuclei have occurred for a few percent of both short- and long-period comets, with roughly 40 events documented (Boehnhardt 2002). When near the Sun ($R_n < 2$ AU), individual fragments of split nuclei have well-defined comae and tails. The fragments of split nuclei generally fade away and disappear on rapid timescales (hours to weeks) or may survive many subsequent perihelion passages (e.g., Sekanina 1982; Weaver et al. 2001). Occasionally, but not always, cometary outbursts are correlated with observed fragmentation events. Only the splitting of the Sun-grazing comets and Shoemaker-Levy 9 have been attributed with any certainty to gravitational tidal disruption, and no correlation is evident between the occurrences of split nuclei and their perihelion distances. The disruption, splitting, and fragmentation of comet nuclei have been attributed to (1) gravitational tides by the Sun and planets, (2) subsurface sublimation, (3) rotation, (4) thermal stress, and (5) collisions (Ip 2003; Boehnhardt 2002; Sekanina & Chodas 2004). Evidence that comet nuclei are surrounded by debris fields with centimeter-sized fragments and larger has been mounting for years, culminating with observations of the bright comets Hyakutake (C/1996 B2) and Hale-Bopp (e.g., Harris et al. 1997; Sekanina 1998a, 1998b; Harmon et al. 1999).

The observed ratios of the secondary to the primary HNC and HCO⁺ integrated line intensities are

$$\int I(\text{HCO}^+)_{\text{ss}} / \int I(\text{HCO}^+)_{\text{ps}} = 0.063 \pm 0.026, \quad (14)$$

$$\int I(\text{HNC})_{\text{ss}} / \int I(\text{HNC})_{\text{ps}} = 0.054 \pm 0.032, \quad (15)$$

where the subscripts “ps” refer to the stronger HNC and HCO⁺ lines. As indicated by the HCO⁺ map in Figure 3, the observations on 1997 March 9 probed a line of sight in the 12 m field of view with diameter $\sim 10^4$ km (Table 1). The distribution of

HCO⁺ was shell-like, while the distribution of HNC was quite different at that time. Thus, the primary line components of these two species were averaged through quite different columns in the coma. We have argued that the secondary source producing the weaker lines of HNC and HCO⁺ was a localized region at a distance $R_n \sim 10^5$ – 10^6 km. Thus, it is quite remarkable that the ratios in equations (14) and (15) were roughly the same within the observational errors, indicative of chemical homogeneity in the primary and secondary sources of HCO⁺ and HNC.

The mass of the secondary source can be estimated assuming that the line intensity ratio between the primary and secondary line components, $s \sim 0.05$, is indicative of the local production rate Q_{ss} of the observed species, i.e., $Q_{\text{ss}} \sim sQ_{\text{ps}}$. For a monolithic spherical fragment, $r_{\text{ss}} \sim s^{1/2}r_n$ and $m_{\text{ss}} \sim s^{3/2}m_n$, where the mass of the nucleus $m_n \sim 10^{16}$ kg. For a source that is a debris field of small grains, the surface area-to-mass ratio for a grain relative to that for the comet nucleus scales as $(r_n/r_g)^{-1}$ (Harris et al. 1997). Therefore, very little total mass in the form of small grains is required to account for the secondary source HNC and HCO⁺ parent production. We estimate the total mass required for the secondary source to account for the observed line ratios in equations (14) and (15) to be roughly

$$m_{\text{ss}} \sim sm_n(r_n/r_g)^{-1} \sim 10^3 \text{ kg} \quad (16)$$

for 0.1 μm grains, where $r_n \sim 20$ km. The number of submicron-sized particles comprising the secondary source is then roughly $N \sim 3sm_{\text{ss}}(4\pi\rho_g r_g^3)^{-1} \sim 10^{20}$ grains for $\rho \sim 1000$ kg m⁻³.

5.3. Polymer Chemistry in the Secondary Source?

As mentioned previously, both HNC and HCO⁺ in the secondary source may arise directly from organic polymer material. As discussed by Rodgers & Charnley (2001), the HNC abundance in comet Lee cannot be reproduced by ion-molecule chemistry or by reactions of energetic H atoms with HCN, another possible route (Rodgers & Charnley 1998). Instead, these authors suggest that HNC arises from the photofragmentation of large organic HCN polymers in this comet, such as polyaminocyanomethylene.

HCO⁺ would require an oxygen-bearing polymer. Both CO and H₂CO have extended sources in several comets, including Halley and Hale-Bopp (Huebner et al. 1991; Wink et al. 1999). The proposed precursor for these two species is polyoxymethylene, a formaldehyde polymer with the formula $(-\text{CH}_2\text{O}-)_n$, or POM (Cottin et al. 2001). Because of photodestruction, this compound leads to H₂CO and CO, as well as CH₂ and CH (Huebner et al. 1991); HCO is another likely product. HCO⁺ could then be created by direct photoionization of HCO. Photoionization of this molecule has two possible sets of products, H+CO and HCO⁺, with a branching ratio of 2:1. Hence, the production of HCO⁺ from neutral HCO is a viable pathway. Quiet-Sun photofragmentation of H₂CO directly into HCO⁺ has a branching ratio of 1:1400 (Huebner et al. 1992), so it is also a possible pathway, depending on the relative abundances of HCO and H₂CO.

6. CONCLUSIONS

Observations of HCO⁺ toward comet Hale-Bopp conducted with the 12 m telescope indicate a large abundance of this species (~ 36 molecules cm⁻³) and the possibility of a secondary emission source composed of small fragments. This

secondary component was also observed at the same date in HNC emission. HCO^+ and HNC are products of ion-molecule chemistry in the primary source, although maps of these molecules show that HCO^+ is far more extended in its spatial distribution relative to the comet nucleus than HNC. HCO^+ is in fact present well beyond the collisionopause, suggesting that it is produced by reactants that are photodissociation products of H_2O , rather than H_2O itself. Calculations indicate that the process $\text{CO}^+ + \text{H}_2 \rightarrow \text{HCO}^+ + \text{H}$ is the major source of HCO^+ beyond the collisionopause, where almost all the water has been photodissociated. The secondary, high-velocity line components of HCO^+ and HNC can probably be explained by an ensemble of organic-rich, volatile grains accelerated by radiation pressure and, possibly, electrostatic forces. Destruction

of polymer-like material in these grains may be creating both species. The variations in spatial distributions and the possible presence of secondary sources all indicate that the chemistry in comets, at least high production rate ones, is far more complex than the simple parent/daughter model. A wide variety of chemical and dynamical processes are obviously occurring on very short timescales that have only begun to be evaluated.

This research is supported by NASA through the NASA Astrobiology Institute under cooperative agreement CAN-02-OSS-02 issued through the Office of Space Science.

REFERENCES

- A'Hearn, M. F., Hoban, S., Birch, P. V., Bowers, C., Martin, R., & Klinglesmith, D. A. 1986, *Nature*, 324, 649
- Arpigny, C., Jehin, E., Manfroid, J., Hutsemekers, D., Schulz, R., Stuwe, J., Zucconi, J.-M., & Ilyin, I. 2003, *Science*, 301, 1522
- Blake, G. A., Qi, C., Hogerheide, M. R., Gurwell, M., & Muhleman, D. 1999, *Nature*, 398, 213
- Bockelée-Morvan, D., et al. 2000, *A&A*, 353, 1101
- Boehnhardt, H. 2002, *Earth Moon Planets*, 89, 91
- Bouchez, A. H., Brown, M. E., Spinrad, H., & Misch, A. 1999, *Icarus*, 137, 62
- Charnley, S. B., Rodgers, S. D., Kuan, Y. J., & Huang, H. C. 2002, *Adv. Space Res.*, 30, 1419
- Cottin, H., Gazeau, M. C., Benilan, Y., & Raulin, F. 2001, *ApJ*, 556, 417
- Crovisier, J. 1987, *A&AS*, 68, 223
- Crovisier, J., & Bockelée-Morvan, D. 1999, *Space Sci. Rev.*, 90, 19
- Crovisier, J., & Encrenaz, T. 2000, *Comet Science: The Study of Remnants from the Birth of the Solar System* (transl. Stephen Lyle; Cambridge: Cambridge Univ. Press)
- Dello Russo, N., Mumma, M. J., DiSanti, M. A., Magee-Sauer, K., Novak, R., & Rettig, T. W. 2000, *Icarus*, 143, 324
- Desvoivres, E., et al. 1999, *MNRAS*, 303, 826
- DiSanti, M. A., Mumma, M. J., Dello Russo, N., Magee-Sauer, K., Novak, R., & Rettig, T. W. 1999, *Nature*, 399, 662
- Eberhardt, P. 1999, *Space Sci. Rev.*, 90, 45
- Gombosi, T., Hansen, K., DeZeeuw, D., Combi, M., & Powell, K. 1999, *Earth Moon Planets*, 79, 179
- Gunnarsson, M., et al. 2003, *A&A*, 402, 383
- Harmon, J. K., Campbell, D. B., Ostro, S. J., & Nolan, M. C. 1999, *Planet. Space Sci.*, 47, 1409
- Harris, W. M., Combi, M. R., Honeycutt, R. K., Mueller, B., & Schloerb, F. 1997, *Science*, 277, 676
- Hirota, T., Yamamoto, S., Kawaguchi, K., Sakamoto, A., & Ukita, N. 1999, *ApJ*, 520, 895
- Horanyi, M., & Mendis, A. 1991, in *Comets in the Post-Halley Era*, ed. R. L. Newburn, Jr., M. Neugebauer, & J. Rahe (Dordrecht: Kluwer), 1093
- Huebner, W. F., Boice, D. C., Schmidt, H. U., & Wegmann, R. 1991, in *Comets in the Post-Halley Era*, ed. R. L. Newburn, Jr., M. Neugebauer, & J. Rahe (Dordrecht: Kluwer), 907
- Huebner, W. F., Boice, D. C., & Sharp, C. M. 1987, *ApJ*, 320, L149
- Huebner, W. F., Keady, J. J., & Lyon, S. P. 1992, *Ap&SS*, 195, 1
- Huntress, W. T., McEwan, M. J., Karpas, Z., & Anicich, V. G. 1980, *ApJS*, 44, 481
- Ip, W.-H. 2003, *Celest. Mech. Dyn. Astron.*, 87, 197
- Ip, W.-H., & Jorda, L. 1998, *ApJ*, 496, L47
- Irvine, W. M., et al. 1998, *Faraday Discuss.*, 109, 475
- Jewitt, D. C., & Matthews, H. E. 1997, *AJ*, 113, 1145
- . 1999, *AJ*, 117, 1056
- Koch, A., van Hemert, M. C., & van Dishoeck, E. F. 1995, *J. Chem. Phys.*, 103, 7006
- Lederer, S. M., Campins, H., Osip, D. J., & Schleicher, D. G. 1999, *Earth Moon Planets*, 78, 131
- Le Teuff, Y. H., Millar, T. J., & Markwick, A. J. 2000, *A&AS*, 146, 157
- Lis, D. C., et al. 1999, *Earth Moon Planets*, 78, 13
- Lovell, A. J., Schloerb, F. P., Bergin, E. A., Dickens, J. E., De Vries, C. H., Senay, M. C., & Irvine, W. M. 1999, *Earth Moon Planets*, 77, 253
- Lovell, A. J., Schloerb, F. P., Dickens, J. E., De Vries, C. H., Senay, M. C., & Irvine, W. M. 1998, *ApJ*, 497, L117
- McCarthy, D., et al. 1999, *Earth Moon Planets*, 78, 243
- Mukai, T. 1986, *A&A*, 164, 397
- Narayanan, G., et al. 1997, *IAU Circ.*, 6591, 1
- Owens, A., Oosterbroek, T., Orr, A., Parmar, A. N., Schulz, R., & Tozzi, G. P. 1999, *Earth Moon Planets*, 77, 293
- Rodgers, S. D., Butner, H. M., Charnley, S. B., & Ehrenfreund, P. 2003, *Adv. Space Res.*, 31, 2577
- Rodgers, S. D., & Charnley, S. B. 1998, *ApJ*, 501, L227
- . 2001, *MNRAS*, 323, 84
- Schwarz, G., et al. 1999, *Earth Moon Planets*, 78, 189
- Sekanina, Z. 1982, in *Comets*, ed. L. L. Wilkening (Tucson: Univ. Arizona Press), 251
- . 1998a, *ApJ*, 494, L121
- . 1998b, *ApJ*, 509, L133
- Sekanina, Z., & Chodas, P. W. 2004, *ApJ*, 607, 620
- Sekanina, Z., & Farrell, J. A. 1980, *AJ*, 85, 1538
- Veal, J. M., et al. 1997, *IAU Circ.*, 6575, 1
- . 2000, *AJ*, 119, 1498
- Weaver, H. A., & Lamy, P. L. 1999, *Earth Moon Planets*, 79, 17
- Weaver, H. A., & Mumma, M. J. 1984, *ApJ*, 276, 782
- Weaver, H. A., et al. 2001, *Science*, 292, 1329
- Whipple, F. L. 1950, *ApJ*, 111, 375
- . 1999, *Planet. Space Sci.*, 47, 301
- Wink, J., et al. 1999, *Earth Moon Planets*, 78, 63
- Womack, M., Homich, A., Festou, M. C., Mangum, J., Uhl, W. T., & Stern, S. A. 1999, *Earth Moon Planets*, 77, 259
- Wright, M. C. H., et al. 1998, *AJ*, 116, 3018
- Wyckoff, S. 1982, in *Comets*, ed. L. L. Wilkening (Tucson: Univ. Arizona Press), 3
- Ziurys, L. M., Savage, C., Brewster, M. A., Apponi, A. J., Pesch, T. C., & Wyckoff, S. 1999, *ApJ*, 527, L67

APPENDIX B

THE $^{12}\text{C}/^{13}\text{C}$ ISOTOPE GRADIENT DERIVED FROM MILLIMETER TRANSITIONS
OF CN: THE CASE FOR GALACTIC CHEMICAL EVOLUTION

S.N. Milam, C. Savage, M.A. Brewster, L.M. Ziurys, & S. Wyckoff 2005, *Astrophys. J.*,
634, 1126-1132.

Reproduced by permission of the AAS.

THE $^{12}\text{C}/^{13}\text{C}$ ISOTOPE GRADIENT DERIVED FROM MILLIMETER TRANSITIONS OF CN: THE CASE FOR GALACTIC CHEMICAL EVOLUTION

S. N. MILAM, C. SAVAGE,¹ M. A. BREWSTER,² AND L. M. ZIURYS

Department of Chemistry, Department of Astronomy, and Steward Observatory, 933 North Cherry Avenue,
 University of Arizona, Tucson, AZ 85721

AND

S. WYCKOFF

Department of Physics and Astronomy, Arizona State University, Tempe, AZ 85287

Received 2005 April 8; accepted 2005 August 16

ABSTRACT

New measurements of $^{12}\text{C}/^{13}\text{C}$ ratios in Galactic molecular clouds have been conducted using the $N = 1 \rightarrow 0$ transition of the CN radical. This species is unique in that it has extensive hyperfine structure that can be accurately used to correct for line saturation effects. Combined with the past observations of Savage and coworkers, the ratios derived from CN are the most extensive data set to date for molecular clouds, and they include sources that lie in the range of 0.09–16.41 kpc in distance from the Galactic center (D_{GC}). The ratios derived from CN indicate a gradient with Galactic distance of $^{12}\text{C}/^{13}\text{C} = 6.01D_{\text{GC}} + 12.28$. This gradient agrees rather closely with those derived from measurements of CO and H_2CO . The least-squares fit to all data points for the three molecules is $^{12}\text{C}/^{13}\text{C} = 6.21D_{\text{GC}} + 18.71$. CO, CN, and H_2CO are synthesized from quite varied reactions, and any ^{13}C fractionation must follow different pathways for these three species. The relatively good agreement between the $^{12}\text{C}/^{13}\text{C}$ ratios of the three molecules, as well as their lack of correlation with gas kinetic temperature, suggests that chemical fractionation and isotope-selective photodissociation both do not play a substantial role in influencing such ratios. Therefore, the $^{12}\text{C}/^{13}\text{C}$ gradient found in the Galaxy is a true indicator of Galactic chemical evolution. The apparent discrepancy between the solar system ($^{12}\text{C}/^{13}\text{C} = 89$) and local interstellar medium values ($^{12}\text{C}/^{13}\text{C} \approx 68$) of this ratio may be a result of ^{13}C enrichment since the formation of the solar system, as predicted by recent models.

Subject headings: astrochemistry — Galaxy: evolution — ISM: abundances — ISM: clouds — radio lines: ISM — stars: AGB and post-AGB

1. INTRODUCTION

Observations of isotopic abundances in the interstellar medium provide an avenue for a quantitative assessment of stellar nucleosynthesis and therefore Galactic chemical evolution (GCE). For example, the $^6\text{Li}/^7\text{Li}$ ratio places constraints on the formation of lithium after the big bang, as well as providing insight into the destruction mechanisms of these isotopes (Aoki et al. 2004). The $^{12}\text{C}/^{13}\text{C}$ isotope ratio is also considered an important tracer, because it reflects the relative degree of primary to secondary processing in stars. ^{12}C is predicted to be formed in the triple alpha reaction (Timmes et al. 1995); in massive stars, extremely high temperatures due to gravitational collapse initiate the formation of carbon through the fusion of three alpha particles. ^{13}C is a reaction intermediate in the carbon-nitrogen-oxygen (CNO) cycle, which occurs in asymptotic giant branch (AGB) stars (Pagel 1997). These objects have a carbon/oxygen core surrounded by helium- and hydrogen-burning shells. As nuclear burning takes place in each shell, they eventually become unstable due to the loss of fuel, leading to gravitational collapse followed by rapid expansion, otherwise known as “helium flashes.” Once the helium shell becomes convectively unstable, processed material from the core of the star is pulled to the surface; this convective mixing is known as the “third dredge-up” (e.g., Herwig & Austin 2004). In the course of this dredge-up, the intermediate

product, ^{13}C , is mixed into the expanding atmosphere of the star, where it is then ejected into the interstellar medium (ISM). The dredge-up properties of AGB stars are not well understood (Herwig & Austin 2004), but obviously have a significant impact on interstellar isotope abundances.

Numerous studies of the $^{12}\text{C}/^{13}\text{C}$ ratio have been conducted toward molecular clouds throughout the Galaxy (e.g., Wilson & Rood 1994; Penzias 1980; Langer & Penzias 1990; Henkel et al. 1983; Gardner & Whiteoak 1979). One of the most common methods of measuring the ratio is to compare line intensities of the ^{12}C and ^{13}C isotopomers of common molecules such as CO, H_2CO , and HCO^+ . However, favorable transitions of very abundant molecules are often saturated, and therefore relative line intensities are not necessarily an accurate indicator of isotope ratios (e.g., Langer & Penzias 1990). In the past, this problem has been dealt with by using molecular line modeling or the double isotope ratios. Possible effects of chemical fractionation may also be influencing $^{12}\text{C}/^{13}\text{C}$ isotope ratios. For example, some molecules such as CO are thought to be preferentially enriched in ^{13}C , because the bond in ^{13}CO is slightly stronger than that in ^{12}CO . Despite these difficulties, molecular line measurements taken over a period of several decades indicate that the $^{12}\text{C}/^{13}\text{C}$ ratio steadily increases with distance from the Galactic center (e.g., Wilson & Rood 1994). These studies have also suggested that values established from CO serve as a lower limit to the “true” $^{12}\text{C}/^{13}\text{C}$ isotope ratio gradient, while those from H_2CO reflect the upper range (Wilson & Rood 1994).

In order to further examine $^{12}\text{C}/^{13}\text{C}$ ratios, we have conducted new observations of ^{12}CN and ^{13}CN toward Galactic molecular

¹ Current address: JILA, NIST, and University of Colorado, Boulder, CO 80309.

² Current address: Sfyri, Inc., P. O. Box 19742, Seattle, WA 98109.

$^{12}\text{C}/^{13}\text{C}$ ISOTOPE GRADIENT

1127

TABLE 1
COMPARISON OF $^{12}\text{C}/^{13}\text{C}$ RATIOS OBSERVED IN MOLECULAR CLOUDS FROM CN, CO, AND H_2CO

SOURCE	l (deg)	b (deg)	D_{GC} (kpc)	D_z (kpc)	T_k (K)	$\tau_{\text{total}}^{\text{a}}$	T_{ex}^{a} (K)	$^{12}\text{C}/^{13}\text{C}$			
								CN ^b	CO ^c	$\text{H}_2\text{CO}^{\text{d}}$	Average
Sgr B2(OH).....	0.662	-0.041	0.1	-0.01	30	$\geq 18_{-6}^{\text{e}}$	24 ± 1	10	17
G29.9.....	29.930	-0.050	4.1	-0.01	20	2.55 ± 0.92	5.10 ± 0.72	63 ± 27	...	45 ± 5	54
G49.2.....	49.204	-0.345	6.3	-0.04	20	$\geq 33_{-13}^{\text{f}}$...	58 ± 4	46
W33.....	12.799	-0.209	4.1	-0.02	25	$37 \pm 8^{\text{e}}$	$39 \pm 1, 43 \pm 4^{\text{g}}$	100	55
G19.6.....	19.608	-0.235	4.3	-0.02	20	4.24 ± 0.89	3.39 ± 0.08	71 ± 17	...	41 ± 4	56
W31.....	10.150	-0.340	3.1	-0.03	18	1.42 ± 0.34	6.95 ± 0.85	20 ± 6	...	37 ± 6	29
G34.3.....	34.258	0.153	5.1	0.01	25	$28 \pm 4^{\text{e}}$...	58 ± 5	43
G35.2.....	35.194	-1.750	5.7	-0.09	20	2.78 ± 1.00	4.49 ± 0.40	64 ± 24	...	55 ± 5	60
W51M.....	49.490	-0.387	6.1	-0.04	30	$35 \pm 12^{\text{e}}$	45 ± 2	...	40
W49.....	43.170	0.011	7.8	0.01	35	$44 \pm 22^{\text{e}}$	49 ± 6	74 ± 20	56
DR 21(OH).....	81.720	0.570	8.	0.03	25	$36 \pm 3^{\text{e}}$	53 ± 2	66	52
Orion A.....	208.992	-19.385	8.3	-0.16	80	$43 \pm 7^{\text{e}}$	79 ± 7	...	61
NGC 2024.....	206.557	-16.361	8.3	-0.12	40	$65 \pm 12^{\text{e}}$...	68 ± 11	67
Orion Bar.....	209.050	-19.382	8.3	-0.16	50	$70 \pm 11^{\text{e}}$	$75 \pm 9^{\text{h}}$...	73
NGC 7538.....	111.542	0.776	8.9	0.03	24	$56 \pm 10^{\text{e}}$	56
W3(OH).....	133.950	1.064	9.6	0.04	20	$63 \pm 16^{\text{e}}$	$66 \pm 4, 85 \pm 15^{\text{g}}$	91 ± 16	76
S156.....	110.110	0.050	10.9	0.01	20	1.03 ± 0.49	6.57 ± 1.59	78 ± 44	78
WB89 391.....	125.807	3.050	16.4	0.56	16	3.20 ± 0.75	2.90 ± 0.03	134 ± 43	134

^a Total optical depth (τ_{total}) and excitation temperatures (T_{ex}) derived from CN (see text).

^b Derived from the $N = 1 \rightarrow 0$ transition.

^c Derived from the $J = 1 \rightarrow 0$ transition by Langer & Penzias (1990) except where indicated.

^d Derived from the $J_{K_a, K_c} = 1_{10} \rightarrow 1_{11}$ and the $J_{K_a, K_c} = 2_{11} \rightarrow 2_{12}$ transitions by Henkel et al. (1980, 1982, 1983, 1985).

^e From Savage et al. (2002).

^f Calculated in the thin limit.

^g From Wouterloot & Brand (1996).

^h From Keene et al. (1998).

clouds. This work is an extension of a study previously carried out by Savage et al. (2002). CN is a unique tracer of this ratio, because the hyperfine structure present within a given rotational transition enables an accurate assessment of the line opacity (Savage et al. 2002). Thus, more accurate values of the $^{12}\text{C}/^{13}\text{C}$ isotope ratio can be determined. In this paper we present the latest results of millimeter observations of the $N = 1 \rightarrow 0$ transitions of ^{12}CN and ^{13}CN , which include measurements at the far edges of the Galaxy. In conjunction with the past data of Savage et al. (2002), the ratio has been measured over the entire range of 0.1–16.4 kpc from the Galactic center. Here we present our results, compare them with ratios derived from other molecules, and discuss the implications for GCE.

2. OBSERVATIONS

Measurements of the $N = 1 \rightarrow 0$ rotational transitions of ^{12}CN and ^{13}CN were carried out during the period 2002 September–2004 June. The observations were made using the Kitt Peak 12 m telescope of the Arizona Radio Observatory (ARO).³ The receivers used were dual-channel SIS mixers operated in single-sideband mode with image rejection around 20 dB. The back ends employed were filter banks with 100 kHz, 250 kHz, 500 kHz, or 1 MHz resolutions, depending on the source. The observing frequencies used were 113490.98 MHz for ^{12}CN and 108780.2 MHz for ^{13}CN ; the telescope beam size was $58''$ – $59''$ at these frequencies. The temperature scale is given in terms of T_R^* , which is the chopper-wheel antenna temperature corrected for forward spillover losses (η_{fss}). The radiation temperature

is then determined using η_c , the corrected beam efficiency, where $T_R = T_R^*/\eta_c$. All data were taken in position-switching mode with an off position $30'$ west in azimuth. To ensure positional accuracy, periodic pointing and focusing on planets was conducted.

3. RESULTS AND ANALYSIS

3.1. $^{12}\text{C}/^{13}\text{C}$ Isotope Ratios from CN

The observations of the $N = 1 \rightarrow 0$ transitions of ^{12}CN and ^{13}CN were made toward seven molecular clouds across the Galaxy. Such clouds generally have low kinetic temperatures. In these objects, emission is thought to arise from the cold extended material. The new sources and those of Savage et al. (2002) are listed in Table 1, along with their Galactic (l , b) coordinates, kinetic temperatures, and distances to the Galactic center D_{GC} (assuming a solar distance of 7.9 kpc; McNamara et al. 2000). These clouds were chosen based on their strategic locations throughout the Galaxy. These new data expand the original set of Savage et al. (2002) by including sources between 0 and 6 kpc and beyond 10 kpc. A total of 18 self-consistent data points are consequently available for examining a Galactic gradient from CN—more than previous sets of CO and H_2CO data (see Wilson & Rood 1994). The details of these measurements will be given in a later paper (S. N. Milam et al. 2005, in preparation).

An example of the observational data is shown in Figure 1, which presents spectra observed toward the molecular cloud S156. The $N = 1 \rightarrow 0$ rotational transitions of both ^{12}CN (*top*: $J = 3/2 \rightarrow 1/2$ spin component) and ^{13}CN (*bottom*: $F_1 = 1 \rightarrow 0$, $F_2 = 2 \rightarrow 1$ spin component) are displayed. Each transition is further split into hyperfine components, whose relative intensities are plotted beneath the observed spectra. As shown in Figure 1, this transition of ^{12}CN consists of five individual hyperfine

³ The Kitt Peak 12 m telescope is currently operated by the Arizona Radio Observatory, at Steward Observatory (University of Arizona), with partial support from the Research Corporation.

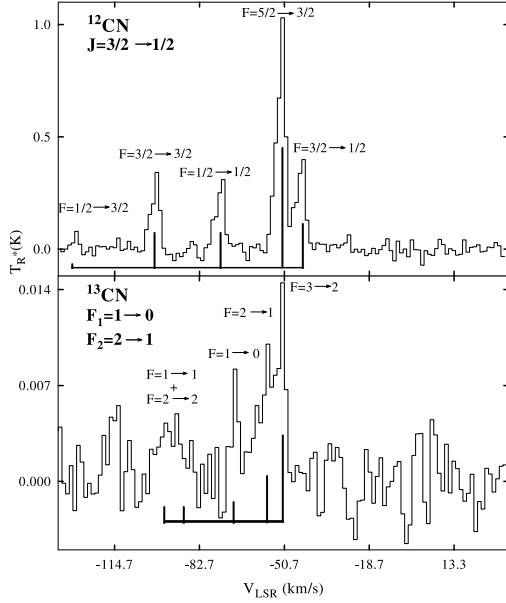


FIG. 1.—Representative spectra of the $N = 1 \rightarrow 0$ transition of ^{12}CN (top: $J = 3/2 \rightarrow 1/2$ spin component) at 113 GHz and ^{13}CN (bottom: $F_1 = 1 \rightarrow 0$, $F_2 = 2 \rightarrow 1$ spin component) at 109 GHz observed toward the molecular cloud S156 using the ARO 12 m telescope. The spectra were recorded with 500 kHz resolution (1.32 km s^{-1}). The positions and intensities of the hyperfine components, indicated by quantum number F , are shown under the spectra. The hyperfine structure in CN is a direct measure of the opacity in these lines.

(hf) components, indicated by the quantum number F , which were all resolved in the spectrum. The hf structure arises from the nuclear spin of nitrogen ($I = 1$). The same transition in ^{13}CN also consists of five hyperfine components, but these lie closer in frequency, and hence some are blended together. They also have considerably weaker brightness temperatures. Furthermore, the ^{13}CN spectrum is more complicated, because the ^{13}C nucleus has a spin of $I = 1/2$. Hence, two spins are coupled to the rotational motion to generate quantum numbers F_1 , F_2 , and F . The lines shown here correspond to $N = 1 \rightarrow 0$, $F_1 = 1 \rightarrow 0$, and $F_2 = 2 \rightarrow 1$.

The $^{12}\text{C}/^{13}\text{C}$ isotope ratio is directly evaluated by comparing the line intensities of the $N = 1 \rightarrow 0$ transitions of ^{12}CN to those of ^{13}CN , corrected for the relative intensities of the hf components, provided the lines are optically thin. The line intensities and their uncertainties were determined by Gaussian fits to the spectral profiles. Low opacities are indicated by line intensities that match the theoretical predictions, of which the spectra from S156 are an example. Some of the ^{12}CN transitions, however, are saturated, as indicated by the less-favored hyperfine lines, which exhibit higher intensities than predicted relative to the main hf feature. To correct for these saturation effects, the relative intensities of the hyperfine components can be compared to determine τ , the optical depth, for that particular source by using the relationship (Savage et al. 2002)

$$\frac{T_R^*(\text{hf})}{T_R^*(\text{hf}_{\text{main}})} = \frac{1 - e^{-R_{\text{hf}}\tau}}{1 - e^{-\tau}}. \quad (1)$$

Here T_R^* is the observed line intensity for a particular hf component and R_{hf} is its theoretical relative intensity. When a given transition is saturated, the line intensity is not an accurate measurement of the amount of ^{12}CN . In this case, the opacity and excitation temperature are used instead to determine the quantity of ^{12}CN (see Savage et al. 2002 for a complete discussion).

One molecular cloud (G49.2) showed evidence of self-absorption in its ^{12}CN spectrum. In this case, the intensity of the weakest hf component ($F = 1/2 \rightarrow 3/2$, 1.23%) of ^{12}CN had to be used to estimate the ratio in the thin limit. However, even this component could be slightly self-reversed; therefore, only a lower limit to the true ratio could be determined.

Table 1 lists the opacity τ , excitation temperature T_{ex} (K), distance to the Galactic center D_{GC} (kpc), distance above/below the Galactic plane D_z (kpc), and $^{12}\text{C}/^{13}\text{C}$ isotope ratios derived from CN, CO, and H_2CO . The $^{12}\text{C}/^{13}\text{C}$ isotope ratios from CN include those from Savage et al. (2002). The average $^{12}\text{C}/^{13}\text{C}$ ratios were also derived from the three molecules toward a given source.

3.2. The Galactic $^{12}\text{C}/^{13}\text{C}$ Gradient

The complete set of $^{12}\text{C}/^{13}\text{C}$ ratios established from CN is plotted as a function of distance from the Galactic center D_{GC} and is shown in Figure 2. The gray squares are the new values presented in this paper, while the black diamonds are those from Savage et al. (2002). Errors are 1σ . A linear fit to the combined CN data is indicated by the solid black line. (G49.2 was not included in this fit, because the ratio is only a lower limit.) The y -intercept is $^{12}\text{C}/^{13}\text{C} \sim 12$. A positive Galactic gradient is apparent in the isotope ratios.

Also shown in Figure 2 are the gradients determined for CO and H_2CO . The CO isotope data (*gray dashed line*) are from Langer & Penzias (1990, 1993), Keene et al. (1998), and Wouterloot & Brand (1996), while the H_2CO values (*black dash-dotted line*) are from Henkel et al. (1980, 1982, 1983, 1985), Gardner & Whiteoak (1979), and Güsten et al. (1985). These molecular species show a positive Galactic gradient as well. Unweighted least-squares fits to these individual data sets yield

$$\text{CN}, \quad ^{12}\text{C}/^{13}\text{C} = 6.01(1.19)D_{\text{GC}} + 12.28(9.33), \quad (2)$$

$$\text{CO}, \quad ^{12}\text{C}/^{13}\text{C} = 5.41(1.07)D_{\text{GC}} + 19.03(7.90), \quad (3)$$

$$\text{H}_2\text{CO}, \quad ^{12}\text{C}/^{13}\text{C} = 7.60(1.79)D_{\text{GC}} + 18.05(10.88). \quad (4)$$

The least-squares fit to all data points for these three molecules using all available data from the literature, shown by the gray dotted line, is

$$^{12}\text{C}/^{13}\text{C} = 6.21(1.00)D_{\text{GC}} + 18.71(7.37). \quad (5)$$

The CO fit was determined primarily from surveys conducted by Langer & Penzias (1990, 1993), but other data points were included. Wouterloot & Brand (1996), however, have determined a lower limit to the $^{12}\text{C}/^{13}\text{C}$ ratio from CO in the outer Galaxy at 13.7 kpc toward WB89 437. If this limit of $^{12}\text{C}/^{13}\text{C} \geq 201 \pm 15$ is included in the CO data, the resulting fit yields

$$\text{CO}, \quad ^{12}\text{C}/^{13}\text{C} = 10.63(2.32)D_{\text{GC}} - 12.01(18.58). \quad (6)$$

This fit varies quite significantly from the previous ones, and the value of the y -intercept is negative and hence not physical.

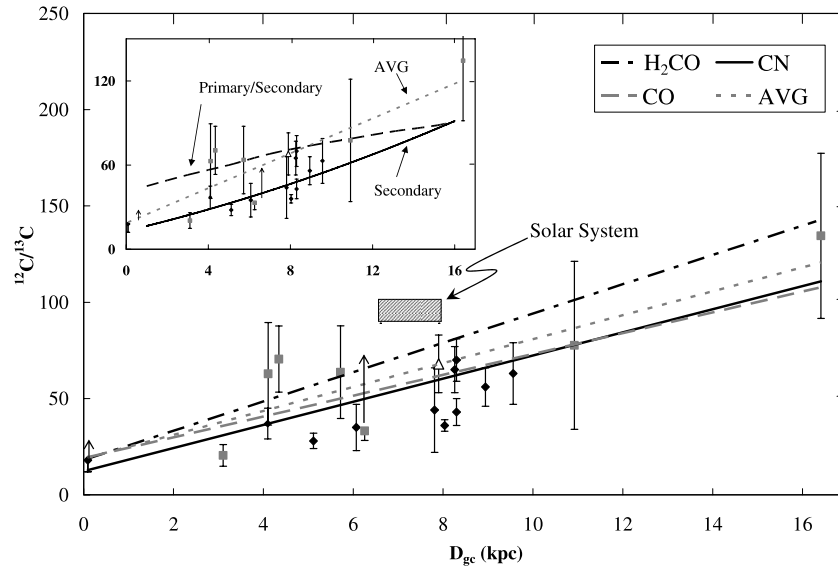


FIG. 2.—Plot of $^{12}\text{C}/^{13}\text{C}$ isotope ratios as a function of distance to the Galactic center, D_{GC} (kpc). The solar distance to the Galactic center is assumed to be 7.9 kpc. The gray squares are values of $^{12}\text{C}/^{13}\text{C}$ ratios derived in the current work, and the black diamonds are values from Savage et al. (2002), both from CN $N = 1 \rightarrow 0$ measurements conducted at the ARO 12 m telescope. A linear fit of the ratios derived from CN is plotted as a solid black line. The isotope gradient derived from CO is indicated by the gray dashed line, and the black dash-dotted line represents that resulting from H_2CO data. The gray dotted line represents the least-squares fit to all data points from the three molecules. The hatched box represents the range of $^{12}\text{C}/^{13}\text{C}$ isotope ratios for the solar system (89 meteorite organics, 100 solar wind lunar regoliths, 6.6 kpc initial Sun orbit, and 7.9 kpc current Sun galactocentric distance). The open triangle represents the average local ISM carbon isotope ratio of 68 ± 15 (this study; S. N. Milam et al. 2005, in preparation). The inset shows the $^{12}\text{C}/^{13}\text{C}$ isotope ratios from CN as a function of D_{GC} along with the model by Prantzos et al. (1996). The dashed black line represents the calculation of the ratio assuming that ^{13}C has a mixed primary and secondary source, while the solid line displays the calculations with a purely secondary ^{13}C source. The gray dotted line continues to represent the average for all three molecules: CO, CN, and H_2CO (see text).

Therefore, this data point was not included in the analysis. Obviously, additional ratios are needed for sources with $D_{GC} > 12$ kpc.

4. DISCUSSION

4.1. A Comparison of $^{12}\text{C}/^{13}\text{C}$ Gradients from CO, H_2CO , and CN

As shown in Figure 2, the $^{12}\text{C}/^{13}\text{C}$ isotope ratios determined from CN are in reasonable agreement with those of CO and H_2CO . CO and CN display a lower limit of the $^{12}\text{C}/^{13}\text{C}$ isotope ratio, and H_2CO seemingly provides an upper limit. However, the average fit from all three species does not significantly deviate from the individual fits. For example, within the quoted errors, the slopes and y-intercepts from the three fits agree with each other. All fits also provide a Galactic center value of $^{12}\text{C}/^{13}\text{C} \sim 20$. It should additionally be noted that only the CN data set provides ratios beyond 10 kpc.

4.2. Effects of Isotope-selective Photodissociation

Isotope-selective photodissociation, which occurs when a large UV flux is present near a molecular cloud (Savage et al. 2002), can potentially influence the $^{12}\text{C}/^{13}\text{C}$ ratio. Molecules containing ^{12}C are more abundant than those with ^{13}C and hence are self-shielding to photodissociation, unlike their ^{13}C counterparts. The $^{12}\text{C}/^{13}\text{C}$ ratio should therefore increase in regions of high UV radiation. Most giant molecular clouds are near H II regions and thus are subject to such fields. In photon-dominated regions (PDRs) this effect is particularly pronounced, and these sources should consequently exhibit higher $^{12}\text{C}/^{13}\text{C}$ ratios. Two such PDRs, the

Orion Bar and NGC 2024, have been included in this survey. They do not appear, however, to exhibit particularly high ratios relative to other sources.

The $N = 1 \rightarrow 0$ transition of CN, in addition, has a critical density on the order of $\sim 2 \times 10^5 \text{ cm}^{-3}$ for collisional excitation, whereas the $J = 1 \rightarrow 0$ transition of CO requires a density of merely $\sim 1000 \text{ cm}^{-3}$. The CN emission observed must arise from dense gas, where UV flux can only partially penetrate. In contrast, CO is present in the more diffuse material; it is also 10,000 times more abundant than CN. Consequently, the ratios derived from CO should show a marked increase relative to those established from CN. However, the ratios found from these two molecules in this study are in good agreement, even toward the PDR sources. The isotope-selective photodissociation therefore cannot be significantly influencing the $^{12}\text{C}/^{13}\text{C}$ ratios.

4.3. Fractionation in Carbon Isotope Ratios?

In order to examine the relative chemistries of CN, CO, and H_2CO , a qualitative chemical network has been created for these species and is shown in Figure 3. This network has been compiled from the reactions of Prasad & Huntress (1980a, 1980b) and has been updated using the UMIST database (Le Teuff et al. 2000). The diagram illustrates that each molecular species used in determining carbon isotope ratios has a different major formation pathway. Formaldehyde is created by the neutral-neutral reaction of CH_3 and atomic oxygen; CN is also formed in a neutral-neutral reaction with CH and atomic nitrogen; and multiple reactions, both ion-molecule and neutral-neutral processes, lead to CO. There is no favorable route from CO to CN.

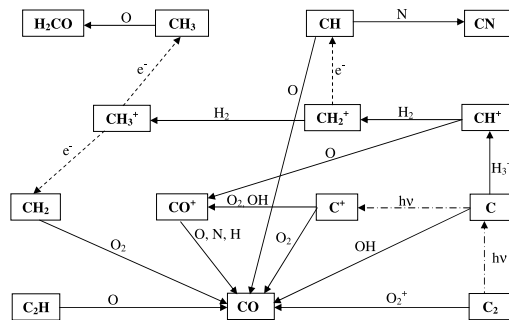
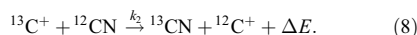
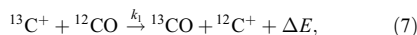


FIG. 3.—Formation pathways leading to CN, H₂CO, and CO in molecular clouds. As the figure illustrates, the reaction networks leading to the three molecules are quite different, suggesting that the ¹³C enrichment from fractionation should vary considerably between the three species.

Chemical fractionation is postulated to affect values of the ¹²C/¹³C isotope ratios. For simple carbon-containing molecules, fractionation is predicted to occur through the isotopic exchange reactions (Penzias 1980; Langer 1992)



Here ΔE is the zero-point energy difference between the ¹²C and ¹³C isotopomers. The reaction involving CO has been studied at 300 K, where the rate has been established to be $k_1 = 2 \times 10^{-10} \text{ cm}^3 \text{ s}^{-1}$ and $\Delta E = 35 \text{ K}$ (Watson et al. 1976). The second process has not been studied experimentally, but ΔE has been determined to be 34 K based on the vibrational energy level ($v = 0$) differences (see Langer 1992). Hence, at low temperatures the 34–35 K differences in zero-point energies should favor ¹³CO and ¹³CN over their ¹²C isotopomers, provided the rates of the exchange reactions given above are fast at such temperatures. For formaldehyde, this simplistic treatment does not apply, because the carbon in this molecule is bonded to three other atoms. Thus, ¹²C cannot be simply exchanged via a reaction with ¹³C⁺. ¹³C enrichment in H₂CO must occur via an earlier precursor, perhaps CH⁺ (see Fig. 3). It should also be noted that one direct route to CO is via C⁺. In contrast, C⁺ does not appear to be a significant precursor to CN. All three molecules should therefore trace ¹²C/¹³C ratios that are not correlated with each other.

Given the variations in the respective reaction pathways leading to CO, CN, and H₂CO and the differences in mechanisms of ¹³C enrichment, the effects of fractionation should vary significantly between the three molecules. Langer et al. (1984) in fact predict that due to chemical fractionation, the ¹²C/¹³C ratio derived from CO should be anticorrelated with those obtained from other molecules. This effect results from the fact that CO has a very high abundance relative to the other species, such that it becomes a “sink” of ¹³C. The ratio derived from CO is predicted to be the lowest as a consequence. Looking at the gradients plotted in Figure 2, the ratio derived from CO may reflect a lower limit at large Galactic distances. However, the gradients established independently from CO, CN, and H₂CO are remarkably similar, even though their formation pathways are independent. The gradient from H₂CO lies only slightly above those of CO

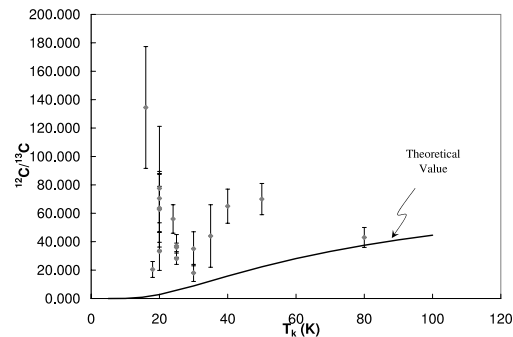


FIG. 4.—Graph of the ¹²C/¹³C isotope ratios derived from CN plotted against gas kinetic temperature of the respective sources, shown by gray squares. The black curve is the theoretical prediction of ¹³C enrichment arising from fractionation at equilibrium, from a ¹²C/¹³C reservoir of 89. There is little correlation between the actual and predicted value.

and CN, even though its formation pathway does not involve C⁺. The similarity of all three gradients suggests that chemical fractionation cannot be a dominant effect. Otherwise, the gradients should agree less favorably.

To examine the extent of chemical fractionation, a simple time-dependent model has been constructed involving C, C⁺, CN, and CO and two reactions, equations (7) and (8). Initial relative abundances of the reactants used in the model are C:C⁺:CO:CN = 18:8:74:0.0074 based on Kramer et al. (2004) and our CN data. The initial isotopic composition was assumed to be ¹²C/¹³C = 89. For reactions (7) and (8), a rate of $2 \times 10^{-10} \text{ cm}^3 \text{ s}^{-1}$ was used, as measured for CO (Watson et al. 1976), and reverse rates were estimated from the Gibb’s free energy of formation of the respective species. Fractionation of CO and CN was assumed to occur only through C⁺. The calculations were carried out for a typical lifetime of a molecular cloud, 10⁶ yr.

These calculations show that for timescales of molecular clouds, chemical fractionation by the C⁺ mechanism is negligible, given a temperature range of $T_k = 10\text{--}100 \text{ K}$. For example, the ¹²C/¹³C ratio at 10⁵ yr for a cloud at 50 K, derived from both CO and CN, is 89. In fact, the isotope ratio did not vary significantly from 89 over the whole temperature range for both CO and CN. At 10⁶ yr, only a 1.7% decrease in the ¹²CO/¹³CO ratio at 30 K and lower was found in both molecules.

Further evidence that fractionation is negligible is illustrated in Figure 4. Here the ¹²C/¹³C ratios derived from CN are plotted against gas kinetic temperature, T_k , for the molecular clouds studied, denoted by gray squares. Kinetic temperatures (Table 1) were obtained from Mangum et al. (1991, 1999), van der Werf et al. (1996), Carral & Welch (1992), White et al. (1982), Jaffe et al. (1989), Apponi et al. (1999), Churchwell et al. (1992), Lis & Goldsmith (1991), Wouterloot & Brand (1996), Langer & Penzias (1990), Henkel et al. (1980, 1985), Dickel et al. (1981), Goldsmith & Mao (1983), and Blitz et al. (1982). There is no obvious correlation between the ratio and T_k . In fact, a wide range of ratios is found around $T_k \sim 20\text{--}30 \text{ K}$. For comparison, the expected ¹²C/¹³C ratio at chemical equilibrium for CN is also plotted versus kinetic temperature, assuming a zero-point energy difference of 34 K and a ¹²C/¹³C reservoir of 89. This ratio is shown by the black curve, which predicts significant enrichment in ¹³C at $T_k \leq 60 \text{ K}$. There is little correlation between the curve and the observed ratios. Although chemistry in the interstellar

medium is not necessarily at equilibrium, the contrast between the predicted and observed values is striking.

4.4. Implications for Galactic Chemical Evolution

Changes in the ISM carbon isotope abundance ratios occur over Galactic timescales as a function of (1) galactocentric distance and (2) time. The distance- $^{12}\text{C}/^{13}\text{C}$ abundance correlation evident in Figure 2 confirms previous studies (Langer & Penzias 1990, 1993; Wilson & Rood 1994; Savage et al. 2002) and matches expectations of simple theories of nucleosynthesis and GCE (e.g., Prantzos & Aubert 1995; Prantzos et al. 1996; Pagel 1997).

The primary source of interstellar ^{12}C is thought to be massive stars ($M > 6 M_{\odot}$) that evolve through core collapse to become Type II supernovae (SNe II). Additional, steadily increasing contributions of ^{12}C to the ISM are postulated to arise from (1) C/O white dwarfs that accrete material from binary companions and evolve into Type Ia supernovae (SNe Ia), and (2) AGB stars that eject nucleosynthesis products in stellar winds and planetary nebulae. Roughly half the observed ^{12}C is thought to have been expelled from SNe II, and half ejected by AGB stars (e.g., Iben & Renzini 1983, 1984; Boothroyd & Sackmann 1999; Clayton 2003). Stellar evolutionary timescales are steep functions of initial masses. Stars with masses $M > 6 M_{\odot}$ become SNe II on rapid timescales ($< 10^8$ yr) and contribute freshly synthesized elements to the ISM at early Galactic epochs, while ^{12}C contributions from smaller mass (1.5–6 M_{\odot}) AGB stars and SNe Ia are delayed due to the longer stellar evolutionary timescales ($> 10^8$ yr). Low- to intermediate-mass stars ($M < 6 M_{\odot}$) evolve to the AGB third dredge-up stage or become SNe Ia on timescales $> 10^8$ yr (e.g., Clayton 1983). Low-mass stars ($M < 1.5 M_{\odot}$) have barely had sufficient time to evolve to the AGB stage (timescale $\sim 10^{10}$ yr) and so contribute negligibly to the ISM enrichment.

Nearly all of the observed ^{13}C is thought to be produced directly from ^{12}C in the CN cycle and is ejected from intermediate-mass (1.5–6 M_{\odot}) AGB stars (Iben & Renzini 1983; Clayton 2003). The onset of the ^{13}C contribution to the ISM is speculated to be delayed from the initial Galactic epochs, because this isotope is probably produced predominantly in low- to intermediate-mass AGB stars, which have long evolutionary timescales relative to the age of the Galaxy. Since star formation tracks the regions of highest gas density, the increase of the $^{12}\text{C}/^{13}\text{C}$ ratio with galactocentric distance can be understood as gradual depletion of ^{12}C and enrichment of ^{13}C resulting from the cycling of interstellar gas through stars of all masses over the lifetime of the Galaxy (provided ^{13}C is not purely a primary product; e.g., Prantzos et al. 1996). Although subject to a variety of uncertainties, this simple theory accounts well for the overall distance- $^{12}\text{C}/^{13}\text{C}$ and age- $^{12}\text{C}/^{13}\text{C}$ trends observed here and by others (e.g., Prantzos et al. 1996), as illustrated by the inset in Figure 2. Here the model predictions by Prantzos et al. (1996, their Fig. 3) are displayed against the $^{12}\text{C}/^{13}\text{C}$ ratios plotted as a function of distance to the Galactic center. The dashed line indicates the calculations where ^{13}C is assumed to be a mixed product of primary and secondary stellar processing, while the solid line depicts the results of a purely secondary ^{13}C contribution. Although there is sufficient scatter such that neither model can be ruled out, the results from the purely secondary calculations follow the observational gradient more closely.

An age-carbon isotope abundance effect is expected in the sense that the ISM $^{12}\text{C}/^{13}\text{C}$ decreases with time. The carbon iso-

tope ratio was locked into the solar system 4.6 Gyr ago and represents the ISM abundance at that Galactic epoch in the region where the Sun formed. From equation (5), the average local present-day carbon isotope ratio is $^{12}\text{C}/^{13}\text{C} = 68 \pm 15$ at the Sun's distance, $D_{\text{GC}} = 7.9$ kpc (Fig. 2). This value is in agreement with very recent optical measurements of CH^+ , which yield 78 ± 2 (Casassus et al. 2005). The hatched box (Fig. 2) represents the ranges in the (1) observed solar system $^{12}\text{C}/^{13}\text{C}$ abundance ratios and (2) calculated drift in galactocentric distance for the Sun over the past 4.6 Gyr (Wielen et al. 1996; Wielen & Wilson 1997). The abundance ratio range is set by the bulk values found for meteorites, comets, and interplanetary dust particles (IDPs), $^{12}\text{C}/^{13}\text{C} = 89 \pm 1$ (Clayton & Nittler 2004). The Sun's outward drift in galactocentric distance as a result of orbital diffusion over the past 4.6 Gyr can account for the Sun's overabundance in metals, $[\text{Fe}/\text{H}] = +0.17 \pm 0.04$, relative to the average metallicity of nearby F and G stars (Wielen et al. 1996). If the solar system were formed at 6.6 kpc, not 7.9 kpc, then the age-carbon isotope abundance difference is a 1σ effect in the sense that the local ISM $^{12}\text{C}/^{13}\text{C}$ ratio has decreased by $\sim 30\%$ over the past 4.6 Gyr (see Fig. 2), presumably due largely to ^{13}C enrichment of the ISM by AGB stars (Prantzos et al. 1996).

The dispersion in the $^{12}\text{C}/^{13}\text{C}$ abundance ratio for the sources observed in Figure 2 is roughly a factor of 2. At this level of significance we find no evidence for chemical fractionation effects. Since the Sun's metal abundance exceeds that of nearby stars, yet is about the same as metal abundances observed in local molecular clouds now forming stars in the Orion nebula, clearly an intrinsic dispersion in carbon isotope abundances exists, requiring more complex models of Galaxy formation and evolution to account for the intrinsic spread in Figure 2. Several possible explanations have been suggested to account for deviations from the basic simple GCE model (e.g., Olive & Schramm 1982; Pagel 1997; Binney & Merrifield 1998; Goswami & Vanhala 2000); among them are (1) cloud-to-cloud variations in molecular abundances due to initial chemical inhomogeneities (e.g., ejecta from local SNe or AGB stars) or differences in cloud chemistry and (2) Galactic dynamical effects such as cloud mergers, orbital diffusion, or radial gas streaming.

5. CONCLUSIONS

An independent measure of the $^{12}\text{C}/^{13}\text{C}$ isotope ratio has been measured across the Galaxy using the CN radical and its isotope. These ratios are in good agreement with past values derived from CO and H_2CO . These three molecules are formed by different chemical pathways; hence, fractionation effects in each species will occur via different mechanisms. The good agreement between $^{12}\text{C}/^{13}\text{C}$ ratios obtained from CO, CN, and H_2CO provides evidence against significant fractionation or isotope-selective photodissociation in molecular clouds. These measurements will help further establish the Galactic gradient and therefore enable more accurate models of GCE.

This research is supported by NASA through the NASA Astrobiology Institute under cooperative agreement CAN-02-OSS-02 issued through the Office of Space Science. The authors would like to thank Mark A. Smith, Department of Chemistry at the University of Arizona, for insight on how kinetic temperature affects the isotope ratio.

REFERENCES

- Aoki, W., Inoue, S., Kawanomoto, S., Ryan, S. G., Smith, I. M., Suzuki, T. K., & Takada-Hidai, M. 2004, *A&A*, 428, 579
- Apponi, A. J., Pesch, T. C., & Ziurys, L. M. 1999, *ApJ*, 519, L89
- Binney, J., & Merrifield, M. 1998, *Galactic Astronomy* (Princeton: Princeton Univ. Press)
- Blitz, L., Fich, M., & Stark, A. A. 1982, *ApJS*, 49, 183
- Boothroyd, A. I., & Sackmann, I.-J. 1999, *ApJ*, 510, 232
- Carral, P., & Welch, W. J. 1992, *ApJ*, 385, 244
- Casassus, S., Stahl, O., & Wilson, T. L. 2005, *A&A*, 441, 181
- Churchwell, E., Walmsley, C. M., & Wood, D. O. S. 1992, *A&A*, 253, 541
- Clayton, D. D. 1983, *Principles of Stellar Evolution and Nucleosynthesis* (Chicago: Univ. Chicago Press)
- . 2003, *Handbook of Isotopes in the Cosmos* (Cambridge: Cambridge Univ. Press)
- Clayton, D. D., & Nittler, L. R. 2004, *ARA&A*, 42, 39
- Dickel, H. R., Dickel, J. R., & Wilson, W. J. 1981, *ApJ*, 250, L43
- Gardner, F. F., & Whiteoak, J. B. 1979, *MNRAS*, 188, 331
- Goldsmith, P. F., & Mao, X.-J. 1983, *ApJ*, 265, 791
- Goswami, J. N., & Vanhala, H. A. T. 2000, in *Protostars and Planets IV*, ed. V. Mannings, A. P. Boss, & S. S. Russell (Tucson: Univ. Arizona Press), 963
- Güsten, R., Henkel, C., & Batrla, W. 1985, *A&A*, 149, 195
- Henkel, C., Güsten, R., & Gardner, F. F. 1985, *A&A*, 143, 148
- Henkel, C., Walmsley, C. M., & Wilson, T. L. 1980, *A&A*, 82, 41
- Henkel, C., Wilson, T. L., & Bieging, J. 1982, *A&A*, 109, 344
- Henkel, C., Wilson, T. L., Walmsley, C. M., & Pauls, T. 1983, *A&A*, 127, 388
- Hervig, F., & Austin, S. M. 2004, *ApJ*, 613, L73
- Iben, I., Jr., & Renzini, A. 1983, *ARA&A*, 21, 271
- . 1984, *Phys. Rep.*, 105, 329
- Jaffe, D. T., Genzel, R., Harris, A. I., Lugten, J. B., Stacey, G. J., & Stutzki, J. 1989, *ApJ*, 344, 265
- Keene, J., et al. 1998, *ApJ*, 494, L107
- Kramer, C., Jakob, H., Mookerjee, B., Schneider, N., Brüll, M., & Stutzki, J. 2004, *A&A*, 424, 887
- Langer, W. D. 1992, in *IAU Symp. 150, Astrochemistry of Cosmic Phenomena*, ed. P. D. Singh (Dordrecht: Kluwer), 193
- Langer, W. D., Graedel, T. E., & Armentrout, P. B. 1984, *ApJ*, 277, 581
- Langer, W. D., & Penzias, A. A. 1990, *ApJ*, 357, 477
- . 1993, *ApJ*, 408, 539
- Le Teuff, Y. H., Millar, T. J., & Markwick, A. J. 2000, *A&AS*, 146, 157
- Lis, D. C., & Goldsmith, P. F. 1991, *ApJ*, 369, 157
- Mangum, J. G., Wootten, A., & Barsony, M. 1999, *ApJ*, 526, 845
- Mangum, J. G., Wootten, A., & Mundy, L. G. 1991, *ApJ*, 378, 576
- McNamara, D. H., Madsen, J. B., Barnes, J., & Ericksen, B. F. 2000, *PASP*, 112, 202
- Olive, K., & Schramm, D. 1982, *ApJ*, 257, 276
- Pagel, B. 1997, *Nucleosynthesis and Chemical Evolution of Galaxies* (Cambridge: Cambridge Univ. Press)
- Penzias, A. A. 1980, *Science*, 208, 663
- Prantzos, N., & Aubert, O. 1995, *A&A*, 302, 69
- Prantzos, N., Aubert, O., & Audouze, J. 1996, *A&A*, 309, 760
- Prasad, S. S., & Huntress, W. T., Jr. 1980a, *ApJS*, 43, 1
- . 1980b, *ApJ*, 239, 151
- Savage, C., Apponi, A. J., Ziurys, L. M., & Wyckoff, S. 2002, *ApJ*, 578, 211
- Timmes, F. X., Woosley, S. E., & Weaver, T. A. 1995, *ApJS*, 98, 617
- van der Werf, P. P., Stutzki, J., Sternberg, A., & Krabbe, A. 1996, *A&A*, 313, 633
- Watson, W. D., Anicich, V. G., & Huntress, W. T., Jr. 1976, *ApJ*, 205, L165
- White, G. J., Phillips, J. P., Beckman, J. E., & Cronin, N. J. 1982, *MNRAS*, 199, 375
- Wielen, R., Fuchs, B., & Dettbarn, C. 1996, *A&A*, 314, 438
- Wielen, R., & Wilson, T. 1997, *A&A*, 326, 139
- Wilson, T. L., & Rood, R. T. 1994, *ARA&A*, 32, 191
- Wouterloot, J. G. A., & Brand, J. 1996, *A&AS*, 119, 439

APPENDIX C

FORMALDEHYDE IN COMETS C/1995 O1 (HALE-BOPP), C/2002 T7 (LINEAR)
AND C/2001 Q4 (NEAT): INVESTIGATING THE COMETARY ORIGIN OF H₂CO

Stefanie N. Milam, Anthony J. Remijan, Maria Womack, Leif Abrell, L. M. Ziurys, Susan Wyckoff, A. J. Apponi, D. N. Friedel, L. E. Snyder, J. M. Veal, Patrick Palmer, L. M. Woodney, Michael F. A'Hearn, J. R. Forster, M. C. H. Wright, I. de Pater, S. Choi, & M. Gesmundo 2006, *Astrophys. J.*, **649**, 1169-1177.

Reproduced by permission of the AAS.

FORMALDEHYDE IN COMETS C/1995 O1 (HALE-BOPP), C/2002 T7 (LINEAR), AND C/2001 Q4 (NEAT):
 INVESTIGATING THE COMETARY ORIGIN OF H₂CO

STEFANIE N. MILAM,¹ ANTHONY J. REMIJAN,^{2,3,4,5} MARIA WOMACK,⁶ LEIF ABRELL,⁷ L. M. ZIURYS,¹ SUSAN WYCKOFF,⁸
 A. J. APPONI,¹ D. N. FRIEDEL,² L. E. SNYDER,² J. M. VEAL,^{2,9} PATRICK PALMER,¹⁰ L. M. WOODNEY,¹¹
 MICHAEL F. A'HEARN,¹² J. R. FORSTER,¹³ M. C. H. WRIGHT,¹³
 I. DE PATER,¹³ S. CHOI,⁶ AND M. GESMUNDO⁶

Received 2006 March 16; accepted 2006 June 2

ABSTRACT

Observations of formaldehyde (H₂CO) have been conducted toward comets C/1995 O1 (Hale-Bopp), C/2001 Q4 (NEAT), and C/2002 T7 (LINEAR) using the Arizona Radio Observatory (ARO) 12 m telescope at 1.2 and 2 mm. Aperture synthesis maps of H₂CO at 3 mm were made using the Berkeley-Illinois-Maryland Association (BIMA) interferometer toward comet Hale-Bopp. These data indicate that the production rate of H₂CO is $\sim 3.7 \times 10^{28} \text{ s}^{-1}$ at ~ 1 AU in comet Hale-Bopp, using a simple Monte Carlo model, if a nuclear origin for the molecule is assumed. However, maps of H₂CO in Hale-Bopp, in comparison with CO, show an extended distribution ($r_s \sim 15,000$ km) with small-scale structure oriented roughly along the comet-Sun direction. This result suggests a source of H₂CO other than the comet nucleus. The extended source of formaldehyde is probably grains composed of a mixture of silicates and organic material. The production rate for H₂CO increases to $Q \sim 1.4 \times 10^{29} \text{ s}^{-1}$ assuming such an extended grain source. This value implies a $Q/Q(\text{H}_2\text{O}) \sim 1.4\%$, which is similar to the production rate ratio of $Q/Q(\text{H}_2\text{O}) \sim 4\%$ derived from in situ measurements of H₂CO in comet Halley. Production rates for H₂CO toward comets C/2002 T7 (LINEAR) and C/2001 Q4 (NEAT) are 1.4×10^{27} and $5.6 \times 10^{26} \text{ s}^{-1}$, respectively, modeled using the extended grain source. The spectra of H₂CO measured toward comet C/2002 T7 (LINEAR) show evidence for a second velocity component, most likely arising from comet fragmentation.

Subject headings: astrobiology — comets: individual (Hale-Bopp (C/1995 O1), NEAT (C/2001 Q4), LINEAR (C/2002 T7)) — radio lines: solar system — techniques: interferometric

1. INTRODUCTION

The close approach of comet C/1995 O1 (Hale-Bopp) provided an observational flourish of molecular lines, including detections of over 10 new cometary species. These molecules ranged from simple diatomics to complex organic compounds, for example, sulfur monoxide (SO), hydrogen sulfide (H₂S), formic acid (HCOOH), formamide (NH₂CHO), and ethylene

glycol (HOCH₂CH₂OH; see Bockelée-Morvan et al. 2000; Woodney et al. 1996; Crovisier et al. 2004; Lis et al. 1999). These successes were partly due to the fact that comet Hale-Bopp was visible for a record 569 days and reached a peak visual magnitude of -1 .

In the spring of 2004, two long-period comets crossed the sky with peak visual magnitudes of ~ 2 : comets C/2001 Q4 (NEAT) and C/2002 T7 (LINEAR). Comet C/2001 Q4 (NEAT) was originally discovered in August of 2001. However, H₂O was not detected in this comet until 2004 March 6.6 (UT) by Lecacheux et al. (2004). The measured production rate of $Q(\text{H}_2\text{O}) \sim 1.3 \times 10^{29} \text{ s}^{-1}$ at a heliocentric distance of $R_h \sim 1.5$ AU was found to be similar to that of comet Halley (Mumma et al. 1986). Comet C/2002 T7 (LINEAR) was first discovered in 2002 mid-October and reached perihelion on 2004 April 23. This comet was a dynamically new Oort cloud object, as evidenced by its slightly hyperbolic orbit at perihelion. From 2004 April 10 to 17, Howell et al. (2004) observed the 18 cm OH lines, which are good tracers of H₂O production. Their average measured OH production rate was $Q(\text{OH}) \sim 2.5 \times 10^{29} \text{ s}^{-1}$ ($R_h \sim 0.6$ AU), again similar to that of comet Halley at perihelion. In both comets, a variety of other molecules were observed as well, predominantly in 2004 May. Species such as hydrogen cyanide (HCN), hydrogen isocyanide (HNC), carbon monosulfide (CS), formaldehyde (H₂CO), methanol (CH₃OH), and carbon monoxide (CO) were detected in both objects, by single-dish and aperture synthesis techniques (Küppers et al. 2004; Friedel et al. 2005; Remijan et al. 2006; Magee-Sauer et al. 2004).

As these observations, as well as others, have demonstrated, a vast number of cometary molecules found are organic, including CH₃OH, H₂CO, NH₂CHO, and HOCH₂CH₂OH. Both CH₃OH

¹ NASA Astrobiology Institute, Department of Chemistry, Department of Astronomy, and Steward Observatory, 933 North Cherry Avenue, University of Arizona, Tucson, AZ 85721; stemil@as.arizona.edu, lziurys@as.arizona.edu, aapponi@as.arizona.edu.

² Department of Astronomy, University of Illinois, 1002 West Green Street, Urbana, IL 61801; friedel@astro.uiuc.edu, snyder@astro.uiuc.edu.

³ NASA Goddard Space Flight Center, Computational and Information Sciences and Technologies Office, Code 606, Greenbelt, MD 20771.

⁴ National Research Council Resident Research Associate.

⁵ Current address: National Radio Astronomy Observatory, 520 Edgemont Road, Charlottesville, VA 22903; aremijan@nrao.edu.

⁶ Department of Physics and Astronomy, St. Cloud State University, St. Cloud, MN 56301; mwomack@stcloudstate.edu.

⁷ Department of Chemistry, NASA Astrobiology Institute, University of Arizona, 1306 East University Boulevard, Tucson, AZ 85721; abrell@u.arizona.edu.

⁸ Department of Physics and Astronomy, Arizona State University, Tempe, AZ 85287.

⁹ Current address: Southwestern College, 900 Otay Lakes Road, Chula Vista, CA 91910; jveal@swc.cc.ca.us.

¹⁰ Department of Astronomy and Astrophysics, University of Chicago, Chicago, IL 60637; ppalmer@oskar.uchicago.edu.

¹¹ Department of Physics, California State University, San Bernardino, CA 92407; woodney@csusb.edu.

¹² Department of Astronomy, University of Maryland, College Park, MD 20742-2421; ma@astro.umd.edu.

¹³ Department of Astronomy, University of California, Berkeley, CA 94720; rforster@astro.berkeley.edu, wright@astro.berkeley.edu, imke@floris.berkeley.edu.

TABLE I
OBSERVATIONS AND ABUNDANCES OF H₂CO AND CO TOWARD HALE-BOPP, Q4 NEAT, AND T7 LINEAR

Comet	Line	Telescope	Transition	UT Date	ν (MHz)	θ_b (arcsec)	D (km)	η_c	T_R^* (K)	$\Delta v_{1/2}$ (km s ⁻¹)	R_R (AU)	Δ (AU)
Hale-Bopp.....	H ₂ CO	12 m	2 _{1,2} → 1 _{1,1}	1997 Mar 11.99	140839.5	45	44648	0.78	0.18 ± 0.03	2.0 ± 0.9	1.0	1.4
		12 m	2 _{0,2} → 1 _{0,1}	1996 May 31.45	145603.0	43	107315	0.76	0.04 ± 0.02	0.8 ± 0.5	4.2	3.4
		12 m	2 _{1,1} → 1 _{1,0}	1996 May 28.28	150498.3	42	106799	0.75	0.02 ± 0.01	4.4 ± 2.0	4.3	3.5
	CO	12 m ^a	3 _{1,2} → 2 _{1,1}	1997 Mar 28.60	225697.8	28	27009	0.53	0.75 ± 0.34	2.0 ± 0.6	0.9	1.3
		BIMA	1 _{0,1} → 0 _{0,0}	1997 Mar 24.83	72838.0	...	10499	...	1.10 ± 0.32 ^c	1.0 ± 0.5	0.9	1.3
		12 m ^a	2 → 1	1997 Apr 7.61	230538.0	27	27611	0.5	0.66 ± 0.33	1.7 ± 0.3	0.9	1.4
Q4 NEAT.....	H ₂ CO	BIMA	1 → 0	1997 Apr 7.93	115271.2	...	8181	...	2.35 ± 0.49 ^c	1.8 ± 0.5	0.9	1.4
		12 m	3 _{1,3} → 2 _{1,2}	2004 May 26.19	211211.4	30	14883	0.57	0.04 ± 0.02	0.9 ± 0.7	1.0	0.7
		12 m	3 _{0,3} → 2 _{0,2}	2004 May 15.03	218222.2	29	8729	0.55	0.02 ± 0.01	1.4 ± 0.7	1.0	0.4
T7 LINEAR.....	H ₂ CO	12 m	3 _{1,3} → 2 _{1,2}	2004 May 25.01	211211.4	30	7724	0.57	0.04 ± 0.02	1.6 ± 0.7	0.9	0.4
		12 m	3 _{0,3} → 2 _{0,2}	2004 May 15.60	218222.2	29	6794	0.55	0.09 ± 0.02	2.1 ± 0.7	0.8	0.3
		12 m	3 _{1,2} → 2 _{1,1}	2004 May 15.73	225697.8	28	6559	0.53	0.08 ± 0.02	2.0 ± 0.7	0.8	0.3

^a OTF map data.

^b Synthesized beam for BIMA observations of H₂CO (11^h2 × 10^h4) and CO (8^h8 × 6^h1).

^c Intensity given in Jy beam⁻¹, which corresponds to 2.2 K for H₂CO and 4.02 K for CO in these observations.

and H₂CO are considered to be interstellar precursors to the diose, glycolaldehyde (CH₂OHCHO; e.g., Halfen et al. 2006; Sorrell 2001). Terrestrially, CH₂OHCHO is a precursor to the aldopentose ribose, which is a key component to ribonucleic acid (RNA). In the interstellar medium, CH₂OHCHO has been detected in the extended regions surrounding the high-mass star-forming region Sgr B2(N) (Hollis et al. 2001, 2004; Halfen et al. 2006). The detection of this complex species may indicate that some part of the synthesis of large prebiotic organic molecules originated in the interstellar medium. Furthermore, the detection of these large compounds in comets may support planetary “seeding” through the disruption of cometary bodies at they approach perihelion, thus ejecting prebiotic material into planetary atmospheres.

As part of an ongoing investigation to establish the contribution of molecular clouds to prebiotic synthesis, we have been conducting observations of simple organic molecules in cometary gases. Because of its importance in the formation of ribose via the formose reaction, measurements have focused on H₂CO. This molecule is also of interest because it is speculated that it may originate from a polymer, polyoxymethylene [(CH₂O)_{*n*}, *n* = 2, 3, 4, ...] in comets. Here we report detections of the $J = 1 \rightarrow 0$, $J = 2 \rightarrow 1$, and $J = 3 \rightarrow 2$ transitions of H₂CO and the $J = 1 \rightarrow 0$ and $J = 2 \rightarrow 1$ lines of CO toward comet C/1995 O1 (Hale-Bopp), using the former National Radio Astronomy Observatory (NRAO) Kitt Peak 12 m telescope, now run by the Arizona Radio Observatory (ARO), and the Berkeley-Illinois-Maryland Association (BIMA) interferometer. In addition, the $J = 3 \rightarrow 2$ transitions of H₂CO were observed toward comets C/2002 T7 (LINEAR) and C/2001 Q4 (NEAT) with the ARO 12 m telescope. From these data, column densities and production rates have been determined for H₂CO and CO for each comet. Using the BIMA observations, a comparison of the distributions for these molecules around the nucleus of Hale-Bopp has also been made. Here we present our analysis and discuss the origin of H₂CO in cometary material.

2. OBSERVATIONS

2.1. Arizona Radio Observatory 12 m

Observations of H₂CO and CO toward comet C/1995 O1 (Hale-Bopp) (hereafter, comet Hale-Bopp) were taken during two observing runs in 1996 May and 1997 March using the former

NRAO 12 m telescope on Kitt Peak, AZ.¹⁴ Observations of H₂CO toward comets C/2002 T7 (LINEAR) (hereafter, comet T7 LINEAR) and C/2001 Q4 (NEAT) (hereafter, comet Q4 NEAT) were conducted from 2004 May to June, also using the 12 m telescope, now run by ARO. Dual-channel SIS mixers were used for the 2 and 1.2 mm bands, operated in single-sideband mode with ~20 dB image rejection. Back ends used for these observations were individual filter banks with 100, 250, or 500 kHz resolutions, as well as the millimeter autocorrelator (MAC) with resolutions of 791 or 98 kHz. The spectral temperature scale was determined by the chopper-wheel method, corrected for forward spillover losses, given in terms of T_R^* (in K). The radiation temperature, T_R , is then derived from the corrected beam efficiency, η_c , where $T_R = T_R^*/\eta_c$. A two-body ephemeris program was used to determine the comet’s position using the orbital elements provided by D. Yeomans (1996 and 2004, private communication) of JPL (Jet Propulsion Laboratory). Focus and positional accuracy were checked periodically on nearby planets or masers. Data were taken in position-switched mode with the off position 30′ west in azimuth.

On-the-fly maps of H₂CO and CO toward comet Hale-Bopp were also conducted at the ARO 12 m telescope from 1997 mid-March to early April. The 250 kHz resolution filter bank was principally employed for these measurements. The images have the following sample spacings, or angular separation of the dish beam size projected onto the sky per sample output, in R.A. and decl.: CO, (10^h7, 7^h9); and H₂CO, (10^h6, 7^h9). Observing frequencies, dates, beam size (θ_b), diameter of the projected beam size on the comet (D), and comet distances at the times of measurements are listed in Table 1.

2.2. BIMA Array

Comet Hale-Bopp was observed using the “soft” C configuration of the BIMA array¹⁵ from 1997 March to April. Data were acquired in interferometric (cross-correlation) mode with nine antennas. The minimum baseline for these observations was ~15 m,

¹⁴ The National Radio Astronomy Observatory is a facility of the National Science Foundation operated under cooperative agreement by the Associated Universities, Inc. The Kitt Peak 12 m telescope is currently operated by the Arizona Radio Observatory (ARO), Steward Observatory, University of Arizona, with partial funding from the Research Corporation.

¹⁵ Operated by the University of California, Berkeley, the University of Illinois, and the University of Maryland with support from the National Science Foundation.

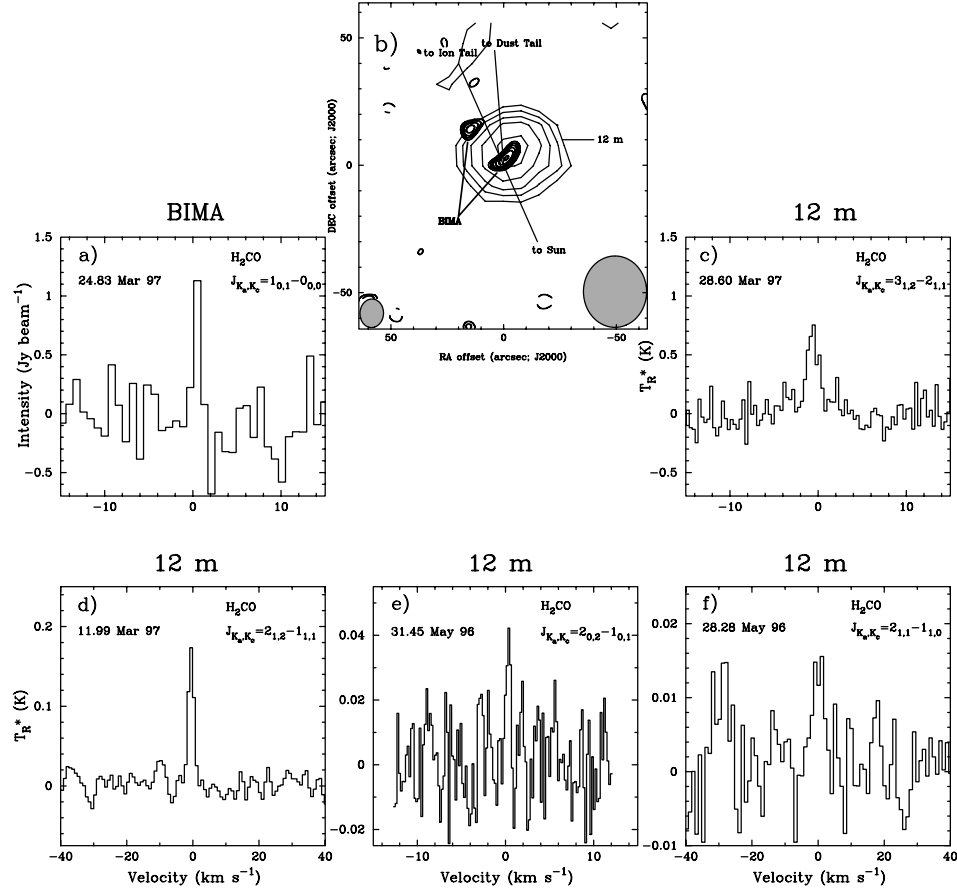


FIG. 1.—Comet C/1995 O1 (Hale-Bopp) single-field H₂CO images and spectra taken with the BIMA array and ARO 12 m radio telescope. The observation date is located at the top left corner of each spectrum. (a) H₂CO $J_{K_a, K_c} = 1_{0,1} \rightarrow 0_{0,0}$ cross-correlation spectrum of the distribution in (b) at 72.838 GHz taken with the BIMA array; the ordinate is flux density per beam (Jy beam^{-1} , $1 \sigma \sim 0.3 \text{ Jy beam}^{-1}$). (b) Hale-Bopp emission contours (*bold*) from the BIMA array of the $J_{K_a, K_c} = 1_{0,1} \rightarrow 0_{0,0}$ transition of H₂CO and emission contours (*normal*) from the ARO 12 m of the $J_{K_a, K_c} = 3_{1,2} \rightarrow 2_{1,1}$ transition. The bold contour levels are $-0.825, 0.750, 0.825, 0.900, 0.975, 1.050,$ and $1.125 \text{ Jy beam}^{-1}$. The normal contour levels are 0.9, 1.2, 1.5, 1.8, and 2.1 K, for $\int T_R dV$. Image coordinates (in arcseconds) are offsets relative to the predicted position of the nucleus. The synthesized beam ($11''.22 \times 10''.41$) of the BIMA array is in the lower left. The beam size ($28''$) of the ARO 12 m is in the lower right. The line segments show the directions to the ion and dust tails and toward the Sun. (c) H₂CO $J_{K_a, K_c} = 3_{1,2} \rightarrow 2_{1,1}$ center spectrum of the distribution in (b) at 225.698 GHz taken at the ARO 12 m with 250 kHz resolution; the ordinate is the chopper wheel antenna temperature, T_R^* (K, $1 \sigma \sim 0.3 \text{ K}$). (d) H₂CO $J_{K_a, K_c} = 2_{1,2} \rightarrow 1_{1,1}$ spectrum at 140.840 GHz taken at the ARO 12 m with 391 kHz resolution at $\sim 1 \text{ AU}$ ($1 \sigma \sim 0.03 \text{ K}$). (e) H₂CO $J_{K_a, K_c} = 2_{0,2} \rightarrow 1_{0,1}$ spectrum at 145.603 GHz taken at the ARO 12 m with 100 kHz resolution at $\sim 4 \text{ AU}$ ($1 \sigma \sim 0.02 \text{ K}$). (f) H₂CO $J_{K_a, K_c} = 2_{1,1} \rightarrow 1_{1,0}$ spectrum at 150.498 GHz taken at the ARO 12 m with 500 kHz resolution at $\sim 4 \text{ AU}$ ($1 \sigma \sim 0.01 \text{ K}$). All spectra are plotted in a cometocentric velocity frame.

and the maximum baseline was $\sim 139 \text{ m}$. The synthesized beamwidths in R.A. and decl. for CO and H₂CO are ($8''.8, 6''.1$) and ($11''.2, 10''.4$), respectively. Typical system temperatures ranged from $\sim 200 \text{ K}$ at high elevations to $\sim 400 \text{ K}$ at low elevations. The spectral windows containing these transitions had a bandwidth of 25 MHz and were divided into 256 channels for a spectral resolution of $0.1 \text{ MHz channel}^{-1}$. However, to increase the signal-to-noise ratio in each window, the data were averaged over two channels, giving an effective spectral resolution of $0.2 \text{ MHz channel}^{-1}$, which corresponds to $\sim 0.52 \text{ km s}^{-1}$ for CO and $\sim 0.80 \text{ km s}^{-1}$ for H₂CO.

Table 1 also lists the parameters for the BIMA array observations. The source used to calibrate the antenna-based gains was

0102+584 for both H₂CO and CO observations, with a 0.30 and 0.40 Jy beam^{-1} channel rms, respectively. Intensities of H₂CO and CO were 2.2 and 4.2 Jy beam^{-1} , which are equivalent to 2.20 and 4.02 K in these observations. The absolute amplitude calibration of these sources was based on planetary observations and is accurate to within $\sim 20\%$. All data were corrected to JPL ephemeris reference orbit 139. The data were combined and imaged using the MIRIAD software package (Sault et al. 1995).

3. RESULTS

Formaldehyde is a slightly asymmetric top species with C_{2v} symmetry with an a -dipole moment of $\mu_a = 2.3 \text{ D}$ (Shoolery & Sharbaugh 1951). Consequently, transitions in H₂CO follow

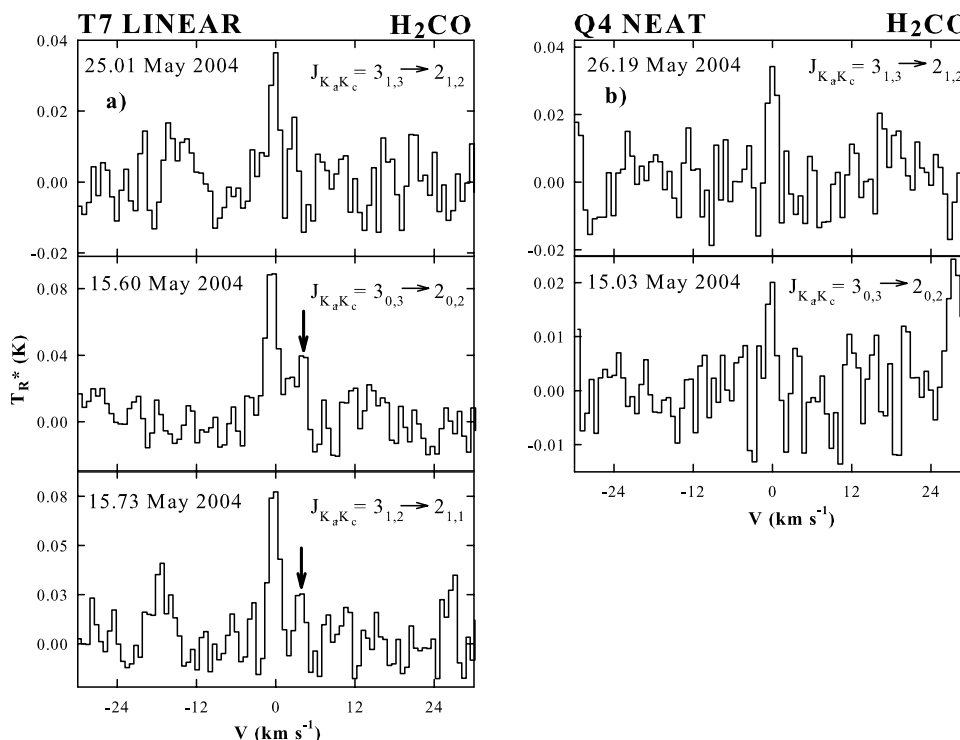


FIG. 2.—(a) Comet C/2002 T7 (LINEAR) observations of H₂CO $J_{K_a K_c} = 3_{1,3} \rightarrow 2_{1,2}$, $3_{0,3} \rightarrow 2_{0,2}$, and $3_{1,2} \rightarrow 2_{1,1}$ transitions from the ARO 12 m telescope in 2004 May. A second velocity component is present in the 2004 May 15 data at approximately 4 km s⁻¹. (b) Comet C/2001 Q4 (NEAT) observations of H₂CO $J_{K_a K_c} = 3_{1,3} \rightarrow 2_{1,2}$ and $3_{0,3} \rightarrow 2_{0,2}$ transitions from the ARO 12 m telescope in 2004 May. All spectra are plotted in a cometocentric velocity frame with 500 kHz resolution.

a -dipole selection rules of $\Delta J = 0, \pm 1$; $\Delta K_a = 0$; and $\Delta K_c = \pm 1$. Therefore, the $J = 1 \rightarrow 0$, $J = 2 \rightarrow 1$, and $J = 3 \rightarrow 2$ transitions each consist of several asymmetry components. Most of these components were observed for each transition.

Figure 1 displays the maps and spectra of H₂CO observed toward comet Hale-Bopp, plotted in a cometocentric velocity frame. The UT date of each observed transition is located in the top left corner of the plotted spectrum. Figure 1d shows the $J_{K_a K_c} = 2_{1,2} \rightarrow 1_{1,1}$ transition of H₂CO detected toward comet Hale-Bopp at the 12 m, as it approached perihelion. It is quite strong compared to the other two $J = 2 \rightarrow 1$ transitions (Figs. 1e and 1f) observed in 1996 May, almost a year before perihelion. This difference likely arises from the variation in heliocentric distance of the comet during the respective observations (see Table 1). However, these spectra definitively establish the presence of H₂CO toward comet Hale-Bopp, as all three asymmetry components of the $J = 2 \rightarrow 1$ transition were detected.

Figure 1b shows the map of the $J_{K_a K_c} = 1_{0,1} \rightarrow 0_{0,0}$ line of H₂CO toward comet Hale-Bopp, made with the BIMA array (*bold contours*), overlaid with the on-the-fly (OTF) map of the $J_{K_a K_c} = 3_{1,2} \rightarrow 2_{1,1}$ transition from the 12 m (*normal contours*). The spectra for the distributions in Figure 1b, measured by BIMA and the 12 m, are plotted with a cometocentric velocity frame in Figures 1a and 1c, respectively. The $J = 3 \rightarrow 2$ emission from the 12 m indicates a somewhat extended source (cf. beam sizes on

map), while the $J = 1 \rightarrow 0$ emission is centered on two distinct clumps. One clump is virtually outside the contour of the $J = 3 \rightarrow 2$ emission. These differences probably arise from the variation in beam sizes, measurement techniques (single dish vs. interferometer), and excitation conditions of the two lines. (The $J = 3 \rightarrow 2$ transition traces higher densities than the $J = 1 \rightarrow 0$ line.) In addition, the formaldehyde emission shows slight horizontal asymmetry around the cometary nucleus in the 12 m map; this is more apparent in the map derived on 1997 April 6.6, which had twice the integration time (see Womack et al. 2000). In the BIMA map, made with $\sim 10''$ resolution, the nuclear component is asymmetric with an elongation similar to that of the 12 m. The separated second component lies tailward of the nucleus.

Figure 2 displays the H₂CO detections toward comets Q4 NEAT and T7 LINEAR from the ARO 12 m telescope. The $J = 3 \rightarrow 2$ transition toward comet T7 LINEAR was observed in all three asymmetry components (Fig. 2a), while only two components were measured toward comet Q4 NEAT due to time constraints and weather (Fig. 2b). Detection of multiple transitions confirms the presence of H₂CO in these comets. In addition, the comet T7 LINEAR data also appear to exhibit a possible second velocity component ~ 4 km s⁻¹ redward of the main line in the $J_{K_a K_c} = 3_{0,3} \rightarrow 2_{0,2}$ transition on 2004 May 16. The $J_{K_a K_c} = 3_{1,2} \rightarrow 2_{1,1}$ transition, although it has a lower signal-to-noise ratio, supports the presence of the second component observed the

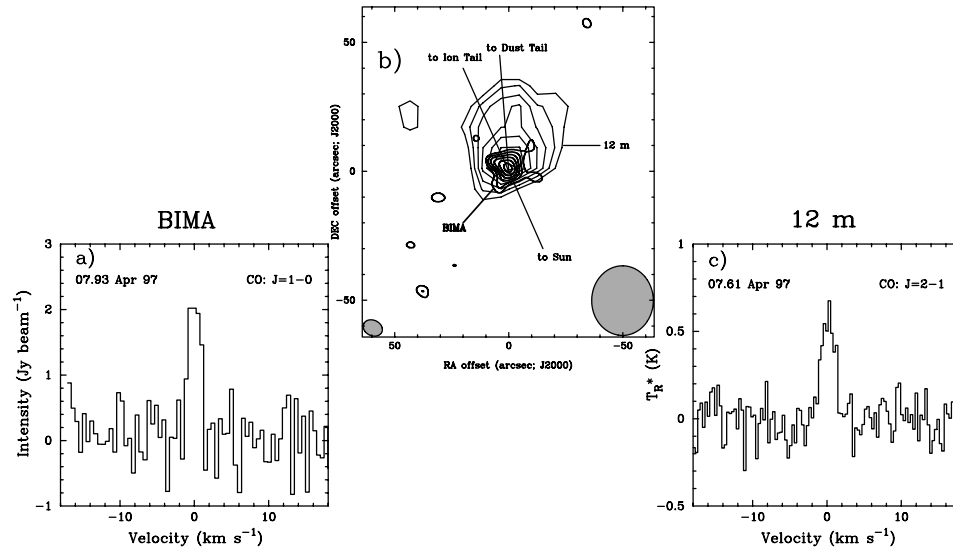


FIG. 3.—Comet C/1995 O1 (Hale-Bopp) single-field CO images and spectra taken with the BIMA array and ARO 12 m radio telescope. The observation date is located at the top left corner of each spectrum. (a) CO $J = 1 \rightarrow 0$ cross-correlation spectrum of distribution in (b) at 115.271 GHz taken with the BIMA array; the ordinate is flux density per beam (Jy beam^{-1} , $1 \sigma \sim 0.5 \text{ Jy beam}^{-1}$). (b) Hale-Bopp emission contours (*bold*) from the BIMA array of the $J = 1 \rightarrow 0$ transition of CO and emission contours (*normal*) from the ARO 12 m of the $J = 2 \rightarrow 1$ transition. The bold contour levels are $-0.8, 0.6, 0.8, 1.0, 1.2, 1.4,$ and 1.6 Jy beam^{-1} . The normal contour levels are $1.05, 1.20, 1.35, 1.50, 1.65, 1.80,$ and 1.95 K , for $\int T_R dV$. Image coordinates (in arcseconds) are offsets relative to the predicted position of the nucleus. The synthesized beam ($8''6 \times 6''1$) of the BIMA array is in the lower left. The beam size ($27''$) of the ARO 12 m is in the lower right. The line segments show the directions to the ion and dust tails and toward the Sun. (c) CO $J = 2 \rightarrow 1$ center spectrum from distribution in (b) at 230.538 GHz taken at the ARO 12 m with 250 kHz resolution; the ordinate is the chopper wheel antenna temperature, T_R^* (K, $1 \sigma \sim 0.2 \text{ K}$). Both spectra are plotted in a cometocentric velocity frame.

same day. This result is similar to that found for comet Hale-Bopp, where a second velocity component was also observed in HCO⁺ and HNC with a velocity shift of 7 km s^{-1} relative to the main feature (Milam et al. 2004).

For comparison, observations of CO toward comet Hale-Bopp were conducted with both facilities. Figure 3 shows the maps and spectra of the $J = 1 \rightarrow 0$ and $J = 2 \rightarrow 1$ transitions of CO toward comet Hale-Bopp. In Figure 3b, the BIMA data of the $J = 1 \rightarrow 0$ transition near 115 GHz (*bold contours*) are overlaid on the 12 m OTF map of the $J = 2 \rightarrow 1$ transition near 230 GHz (*normal contours*). Figures 3a and 3c show the spectra for each map with a cometocentric velocity frame. The emission is more extended than the projected beam sizes for each facility, and a tailward “wing” is present in the 12 m data. The 12 m OTF map of CO shows elongation toward the dust tail, possibly associated CO emission with dust particles. This extension was not observed in the BIMA data. It was most likely resolved out due to the higher spatial resolution of the interferometer.

4. DISCUSSION

4.1. Column Densities, Production Rates, and Abundances

Abundances were derived for H₂CO and CO assuming that the source filled the beams of both telescopes. The formalism for calculating column densities using BIMA array data can be found in Friedel et al. (2005). The column density for 12 m observations was calculated from

$$N_{\text{tot}} = (3kT_R \Delta v_{1/2} \zeta_{\text{rot}}) / \left(8\pi^3 \nu S_{ij} \mu_0^2 e^{-\Delta E/kT_{\text{rot}}} \right), \quad (1)$$

where ν is the frequency, T_R is the line temperature corrected for efficiency, $\Delta v_{1/2}$ is the FWHM line width, S_{ij} is the line strength, μ_0 is the permanent dipole moment, ζ_{rot} is the rotational partition function, and N_{tot} is the total number of molecules observed in the beam. The rotational temperature, T_{rot} , was assumed to be 50 K for $R_h \sim 1 \text{ AU}$ and 15 K for $R_h \sim 4 \text{ AU}$, based on the values derived for CH₃OH from Biver et al. (1997). This value is somewhat lower than that determined from Biver et al. (2002), because H₂CO has a larger dipole moment than CH₃OH. Hence, its rotational temperature should be lower. This rotational temperature may not apply to CO, which, in contrast, has a smaller dipole moment relative to CH₃OH; however, for consistency in the calculations it was assumed. Line widths for all three comets were typically $1\text{--}2 \text{ km s}^{-1}$, within the quoted errors.

The column densities derived for CO and H₂CO are listed in Table 2. There is some scatter among these values, because they were measured on different dates and with varying beam sizes. The values for H₂CO are slightly higher in comet Hale-Bopp ($N_{\text{tot}} \sim 7.4 \times 10^{13} \text{ cm}^{-2}$, $\sim 1 \text{ AU}$) compared to comets T7 LINEAR ($N_{\text{tot}} \sim 2 \times 10^{12} \text{ cm}^{-2}$) and Q4 NEAT ($N_{\text{tot}} \sim 5 \times 10^{11} \text{ cm}^{-2}$). This result is expected because of the higher water production rate of comet Hale-Bopp. The CO column densities for comet Hale-Bopp are 2.1×10^{16} and $1.4 \times 10^{15} \text{ cm}^{-2}$ for the $J = 1 \rightarrow 0$ and $J = 2 \rightarrow 1$ transitions, respectively. The difference in column density values, which vary by a factor of 15, is expected because the brightness distribution is centrally peaked and different beam sizes were used.

Table 2 also summarizes the production rates of the molecules observed toward the three comets. The photodissociation rates from Huebner et al. (1992), as well as the abundance ratio with

TABLE 2
COLUMN DENSITIES, PHOTODESTRUCTION RATES, AND PRODUCTION RATES FOR H₂CO AND CO

COMET	LINE	TELESCOPE	TRANSITION	R_h (AU)	N_{tot} (cm ⁻²)	ν_{pd} (s ⁻¹)	Q (s ⁻¹)		$Q/Q(\text{H}_2\text{O})$ (%)	
							Parent	Grain	Parent	Grain
Hale-Bopp	H ₂ CO	12 m	2 _{1,2} → 1 _{1,1}	1.0	5.9 ± 2.8 × 10 ¹²	2.8 × 10 ⁻⁴	2.66 × 10 ²⁸	9.06 × 10 ²⁸	0.3 ^a	0.9 ^a
			2 _{0,2} → 1 _{0,1}	4.2	1.8 ± 1.4 × 10 ¹¹	...	2.68 × 10 ²⁶	1.24 × 10 ²⁷	0.3 ^b	1.2 ^b
		12 m	2 _{1,1} → 1 _{1,0}	4.3	4.8 ± 3.2 × 10 ¹¹	...	6.94 × 10 ²⁶	3.06 × 10 ²⁷	0.7 ^b	3.1 ^b
	CO	12 m (OTF)	3 _{1,2} → 2 _{1,1}	0.9	1.5 ± 0.8 × 10 ¹³	...	2.82 × 10 ²⁸	9.67 × 10 ²⁸	0.3 ^a	1.0 ^a
			BIMA 1 _{0,1} → 0 _{0,0}	0.9	2.0 ± 1.2 × 10 ¹⁴	...	5.64 × 10 ²⁸	2.19 × 10 ²⁹	0.6 ^a	2.2 ^a
		12 m (OTF)	2 → 1	0.9	1.4 ± 0.7 × 10 ¹⁵	1.2 × 10 ⁻⁶	3.25 × 10 ²⁹	2.54 × 10 ²⁹	3.2 ^a	2.5 ^a
Q4 NEAT	H ₂ CO	12 m	3 _{1,3} → 2 _{1,2}	1.0	3.5 ± 3.0 × 10 ¹¹	2.8 × 10 ⁻⁴	2.09 × 10 ³⁰	1.50 × 10 ³⁰	20.9 ^a	15.0 ^a
			12 m	3 _{0,3} → 2 _{0,2}	1.0	5.8 ± 4.1 × 10 ¹¹	...	1.79 × 10 ²⁶	6.51 × 10 ²⁶	0.1 ^c
		12 m	3 _{1,3} → 2 _{1,2}	0.9	6.2 ± 4.1 × 10 ¹¹	2.8 × 10 ⁻⁴	1.09 × 10 ²⁶	4.61 × 10 ²⁶	0.1 ^c	0.4 ^c
T7 LINEAR	H ₂ CO	12 m	3 _{1,3} → 2 _{1,2}	0.9	6.2 ± 4.1 × 10 ¹¹	2.8 × 10 ⁻⁴	1.03 × 10 ²⁶	4.36 × 10 ²⁶	0.1 ^d	0.2 ^d
			12 m	3 _{0,3} → 2 _{0,2}	0.8	3.9 ± 1.6 × 10 ¹²	...	6.63 × 10 ²⁶	2.69 × 10 ²⁷	0.2 ^d
		12 m	3 _{1,2} → 2 _{1,1}	0.8	1.6 ± 0.7 × 10 ¹²	...	2.52 × 10 ²⁶	1.04 × 10 ²⁷	0.1 ^d	0.3 ^d

^a $Q(\text{H}_2\text{O}) \sim 1 \times 10^{31} \text{ s}^{-1}$ at $R_h \sim 1$ AU from Harris et al. (2002).

^b $Q(\text{H}_2\text{O}) \sim 1 \times 10^{29} \text{ s}^{-1}$ at $R_h \sim 4$ AU from Biver et al. (1997).

^c $Q(\text{H}_2\text{O}) \sim 1.3 \times 10^{29} \text{ s}^{-1}$ at $R_h \sim 1.5$ AU from Lecacheux et al. (2004).

^d $Q(\text{OH}) \sim 3.2 \times 10^{29} \text{ s}^{-1}$ at $R_h \sim 0.6$ AU from Howell et al. (2004).

respect to water (in percent), are listed in this table. Assuming H₂CO and CO are parent species, production rates were determined from a Monte Carlo model. The Monte Carlo model traces the trajectories of molecules, within the telescope beam, ejected from the comet surface. The observed column density is then matched for an output molecular production rate, Q . The CO production rate for comet Hale-Bopp in this case was $\sim 1 \times 10^{30} \text{ s}^{-1}$ (1 AU), based on both observed transitions, implying $Q/Q(\text{H}_2\text{O}) \sim 12\%$. These values are reasonably consistent with those measured by Bockelée-Morvan et al. (2000), who found $Q/Q(\text{H}_2\text{O}) \sim 23\%$. The average H₂CO production rate for comet Hale-Bopp, derived from the Monte Carlo model, was $\sim 3.7 \times 10^{28} \text{ s}^{-1}$ with a $Q/Q(\text{H}_2\text{O})$ of 0.4% at ~ 1 AU. In comparison, Bockelée-Morvan et al. (2000) predict a $Q/Q(\text{H}_2\text{O})$ for H₂CO of 1.1% with their Haser model assuming a nuclear source.

The Hale-Bopp production rate for H₂CO was also calculated using a modified Monte Carlo model, based on the work by Combi & Fink (1997). Here it is assumed that all the H₂CO is released from small ($\sim 0.2 \mu\text{m}$) organic refractory particles (such as CHON grains), which are expanding with a constant velocity from the nucleus. A single grain radius and velocity are assumed to represent the average of an ensemble of particles constituting the expanding grain halo. Such grains decouple collisionally from the inner coma gas ~ 300 km from the nucleus at a terminal velocity $v_g \sim 0.5 \text{ km s}^{-1}$ at 1 AU (Gombosi & Horanyi 1986). The grains then become superheated to temperatures ~ 500 K (Lamy & Perrin 1988; Combi & Fink 1997; Kolokolova et al. 2004), releasing gaseous H₂CO from the grains directly into the coma, with no intermediate dissociation or thermal degradation assumed. Each H₂CO molecule is then released from a grain in a random direction with a constant velocity $v_d = v_0 R_h^{-1/4}$, where $v_0 = 0.6 \text{ km s}^{-1}$ (Combi & Fink 1997). The radial extent of the distributed grain halo inferred from the observed H₂CO spatial distribution at 1 AU is $R_{\text{gh}} \sim 10^4 \text{ km}$ (see Fig. 1). Thus, the estimated CHON-like grain lifetime is $\tau_g = R_{\text{gh}}/v_g \sim 2 \times 10^4 \text{ s}$.

Following Combi & Fink (1997), it was assumed that the size of each grain decreases linearly with time (since the grain evaporation rate and the surface area are both assumed to scale with the square of the grain radius). Each H₂CO molecule is released from a grain after some time interval, t_i , given by the probability distribution, $P = (1 - t_i/\tau_g)^2$ (Combi & Fink 1997). Using

Monte Carlo precepts, this release time can be expressed as $t_i = \tau_g [1 - (1 - R_i)^{1/2}]$, where R_i is a random number in the interval 0–1. Each H₂CO molecule subsequently photodissociates in the solar UV radiation field on the usual randomized exponential timescale, $t_d = -\tau_d \ln(1 - R_i)$ (Combi & Fink 1997; Combi & Smyth 1988), where τ_d is the H₂CO photodissociation timescale, scaled to the appropriate heliocentric distance (Huebner et al. 1992).

This grain model yields an average production rate for H₂CO toward comet Hale-Bopp at ~ 1 AU of $Q(\text{H}_2\text{CO}) \sim 1.4 \times 10^{29} \text{ s}^{-1}$ (see Table 2) with $Q/Q(\text{H}_2\text{O}) \sim 1.4\%$. An increase of about a factor of 4 is therefore found. This model was also used for determining the CO production rate, which was found to be $Q(\text{CO}) \sim 8.8 \times 10^{29} \text{ s}^{-1}$ with $Q/Q(\text{H}_2\text{O}) \sim 9\%$. The grain model results do not increase the production rate from the nuclear model for CO ($Q \sim 1 \times 10^{30} \text{ s}^{-1}$), indicating that the CO lifetime is too long for a significant variation between models. The large difference in the H₂CO and CO production rates derived here for comet Hale-Bopp confirms that H₂CO cannot be an important source of CO in the comet.

4.2. Spatial Distribution of H₂CO versus CO

The H₂CO and CO maps (Figs. 1b and 3b) show extended spatial distributions for the observations near 1 AU. Extended sources for both species in this comet have been suggested from previous observations for heliocentric distances $R_h < 1.5$ AU (Bockelée-Morvan et al. 2000). The transitions observed here are likely to be collisionally excited. Water and CO are the primary collision partners for neutral species within the coma collision radius, $r_c \sim 10^5 \text{ km}$, of Hale-Bopp (1 AU). The CO number density within the collision radius of Hale-Bopp at 1 AU was $n(r) > 10^4 \text{ cm}^{-3}$, although it should drop off roughly as r^{-2} with distance from the nucleus r . Because of its low dipole moment (0.1 D), densities of only $(1-10) \times 10^3 \text{ cm}^{-3}$ are needed to excite the $J = 1 \rightarrow 0$ and $J = 2 \rightarrow 1$ transitions of CO. In addition, the photodestruction rate of this molecule is only $1.2 \times 10^{-6} \text{ molecules s}^{-1}$, i.e., the molecule is fairly robust against photodestruction by solar radiation. On the other hand, H₂CO has a larger dipole moment (2.3 D), and collisional excitation requires densities on the order of $\sim 10^6 \text{ cm}^{-3}$ for the $J = 1 \rightarrow 0$ and $J = 3 \rightarrow 2$ lines. Moreover, the photodissociation rate is

2.8×10^{-4} molecules s^{-1} , almost 2 orders of magnitude higher than that of CO. In addition, the production rate ratio $Q(\text{CO})/Q(\text{H}_2\text{CO})$ is ≥ 10 . For all of these reasons, CO should be far more extended than H₂CO; yet the 12 m maps indicate that these two molecules have roughly the same extent (see Figs. 1 and 3). The estimate source size scale of H₂CO is $r_s \sim 15,000$ km, similar to that of CO, $r_s \sim 19,000$ km.

As discussed, the interferometer map showed a secondary source of H₂CO, 20'' away from the comet nucleus in the tailward direction. This source may be caused by a large fragmentation event. The 12 m OTF map, observed 4 days later, also shows extended (and perhaps asymmetric) emission, although the beam size is likely contributing to this effect. The elongation, however, may be related to the second component seen in the BLMA data.

The extended distribution and differing structure of the H₂CO emission compared to CO may support independent formation mechanisms for these two species within 1 AU. Observations at 6 AU (Womack et al. 1997; Biver et al. 1997) also indicate different distributions for CO and H₂CO. Feldman et al. (2004) has suggested that the sunward-directed CO emission-line velocities of ~ 0.3 – 0.4 km s^{-1} were too high to be explained by sublimation of exposed surface CO ice, but might be explained by a phase change in water ice from amorphous to crystalline states. On the other hand, the H₂CO expansion velocity at 6 AU was nucleus centered, possibly indicative of release from icy grains (Feldman et al. 2004). Asymmetric expansions are typical of comets in which the redward versus blueward line wings do not necessarily have the same outflow velocity, such as, for example, in CH₃OH toward comet Hale-Bopp (Ikeda et al. 2002).

The data collected in the coma of P1/Halley (~ 1 AU) by the Ion Mass Spectrometer (IMS-HIS) aboard *Giotto* indicate that both CO and H₂CO arose in part from extended sources. Approximately half of the CO and most of the H₂CO were released from distributed coma sources with size scales of $\sim 10^4$ and 5000 km respectively (Eberhardt 1999; Meier et al. 1993). The IMS-HIS spectrometer showed an increasing protonated formaldehyde ion (CH₂OH⁺) concentration as the spacecraft moved away from the nucleus of comet Halley. At 1500 km from the nucleus, inside the coma contact surface, the CH₂OH⁺ abundance was calculated to be 1% of water and increased to a few percent of water at the ionopause—apparently due to an extended source (Geiss et al. 1991; ion velocity and two incidence angles affected mass/charge information; therefore, laboratory calibration was required for fitting).

4.3. An Origin in POM?

Since the first radio detection of H₂CO toward comet Halley, it has been proposed that this molecule arises generally from a source 10^3 – 10^4 km from the nucleus (Snyder et al. 1989). Missions to comet Halley also detected an extended production region of H₂CO and CO up to a few times 10^4 km from the nucleus (Festou 1999). The extended source of H₂CO was predicted to have a scale length of approximately 1.2 times the photodissociative scale length of H₂CO at 1 AU (~ 5000 km) for comet Halley, roughly 10^4 km from the nucleus (Meier et al. 1993).

The origin of the extended source of H₂CO in comets has been in debate since the Halley era. The first proposed parent of H₂CO was a polymer called polyoxymethylene or ‘‘POM’’ (Wickramasinghe 1975). The evidence for POMs was suggested in the 1986 *Giotto* mission encounter with comet Halley, which carried five sensor instruments used to analyze volatile material in the coma. Three of these instruments were ‘‘magnetic mass spectrometers,’’ NMS (neutral mass spectrometer), IMS-HERS (ion mass spectrometer–high energy range spectrometer), and IMS-HIS (IMS–high intensity mass spectrometer), and two were

energy analyzers, RPA-PICCA (Reme plasma analyzer–positive ion cluster composition analyzer) and the NMS energy analyzer. Together these instruments were able to measure neutral molecules of mass 12–50 amu and ion molecules and clusters of mass 12–100 amu with limited mass resolution and different integrities at distances of ~ 2000 , 10,000, and 60,000 km from the comet nucleus (Altwegg et al. 1999). In addition, the Halley *Vega* missions carried dust particle impact TOF (time of flight) mass spectrometers (PUMAs) to measure positive atomic and molecular ions released by dust particles. Forty-three ‘‘suitable’’ spectra were cumulatively evaluated for predominant, vibrationally cold, desorption molecular ions.

POM was invoked to explain the RPA-PICCA ion data, where an ordered series of mass groups centered at 31, 45, 61, 75, 90, and 105 amu was found (Korth et al. 1986; Mitchell et al. 1987; Huebner 1987). The mass groups could be explained by H₂CO chain-type molecules. Mitchell et al. (1992), with a more detailed analysis of 30 RPA-PICCA ‘‘molecular ion mass spectra’’ from *Giotto*, later noted that the spectra were admittedly different from those obtained by PUMA on board *Vega 1*. Other interpretations of the NMS data also disagreed with the POM identification (Meier et al. 1993). Mitchell et al. (1992) finally explained this ordered series of mass groups in their spectra as arising from a natural abundance of ion molecules composed of all possible combinations of C, H, O, and N (similar experimental results were found by Schutte et al. 1993).

Observations of a large number of comets now indicate that cometary dust grains consist predominantly of silicates (crystalline and amorphous) intimately mixed with a significant organic refractory component (e.g., Jessberger 1999; Hanner & Bradley 2004). CHON grains, which are plausible sources of radicals such as CN and C₂, long observed in comets (e.g., A’Hearn et al. 1986; Combi & Fink 1997), were discovered from the organic component samples by in situ experiments in comet Halley. H₂CO could also be released directly from these volatile organic-rich coma grains. POM is not a likely source of H₂CO because (1) a relatively large abundance of POM is required (1%–16% of the mass of the grains; Fray et al. 2004) and (2) the possible chemical pathways for producing the POM in interstellar and early solar system environments are not efficient (e.g., Allamandola et al. 1999). Instead, H₂CO is likely to be embedded in volatile grain matrices and released directly into the coma upon vaporization by solar heating, as suggested for C₂ by others (e.g., A’Hearn et al. 1986; Combi & Fink 1997).

4.4. Comet T7 LINEAR’s Second Velocity Component?

As discussed, a second component seems to be apparent in the H₂CO data at $v_{ss} \sim 4.5 \pm 0.8$ km s^{-1} and $v_{ss} \sim 4.0 \pm 0.7$ km s^{-1} with line temperatures of ~ 0.04 and 0.03 K for the $J_{K_a, K_c} = 3_{0,3} \rightarrow 2_{0,2}$ and $J_{K_a, K_c} = 3_{1,2} \rightarrow 2_{1,1}$ transitions, respectively. This component was apparently observed in OH as well. Howell et al. (2004) reported an OH excess from Arecibo observations in 2004 mid-April, of 10%–20% around a $+3$ km s^{-1} cometocentric velocity. Second velocity components have also been observed in HCO⁺ and HNC toward comet Hale-Bopp and are believed to be due to cometary fragmentation of submicron grains (Milam et al. 2004). Such grains were detected toward comet T7 LINEAR at 3.5 AU by Kawakita et al. (2004) and were believed to consist of water ice grains and silicate grains. These dirty ices could possibly also bear H₂CO and other volatile material that would be released as the grain material reaches a thermal degradation limit. The second velocity component, however, was not observed in the third line, detected almost 10 days later, indicating that the putative grain source had become inactive. The second component found

in HCO⁺ observations toward Hale-Bopp also disappeared 1–2 days later (Milam et al. 2004).

Fragmentation events in comets and/or other solar system bodies such as asteroids may play a key role in understanding the origins of prebiotic material (see review by Ehrenfreund et al. 2002). Molecules such as H₂O, H₂CO, and other organics known to be ubiquitous in comets could have detached from a cometary body and perhaps seeded planets or other objects that interact with planetary systems. These fragmentations occur multiple times over a comet orbit and can occur many times before the comet is completely destroyed. Enough material could have been ejected from these icy bodies and onto planetary surfaces to help initiate the formation of prebiotic material.

4.5. Comparison Among Various Comets

The H₂CO production rates are fairly consistent for the three comets included in this study, as well as for comet Halley, having typical $Q(\text{H}_2\text{CO})/Q(\text{H}_2\text{O})$ ratios of 0.1%–2% at ~1 AU. Even though these values were determined from an extended source model, the results are still in good agreement with others. The multiple-comet study by Biver et al. (2002) found the $Q(\text{H}_2\text{CO})/Q(\text{H}_2\text{O})$ ratio in 13 comets to be between 0.13% and 1.3%. These values were determined from a distributed source with a Haser equivalent density distribution (Biver et al. 2002). These results suggest that there is some chemical homogeneity among the comets, at least for H₂CO.

Observations of H₂CO at 4 AU indicate a higher $Q(\text{H}_2\text{CO})/Q(\text{H}_2\text{O})$ ratio of ~2% for a grain source, or 0.5% for a parent species, indicating a non-water-driven chemistry at large heliocentric distances. These results are in good agreement with the long-term chemical evolution studies of Hale-Bopp conducted by Biver et al. (2002) and Womack et al. (1997). The steep dependence of the formaldehyde production rate on R_h is also confirmed.

5. CONCLUSIONS

Observations of H₂CO toward comet Hale-Bopp demonstrate that this molecule has an extended distribution, indicating that it

originates at least in part from a source other than the comet nucleus. A likely source of H₂CO in comets may be coma grains composed of an organic-dominated silicate-organic matrix. These grains are released from the nucleus and are vaporized or thermally degraded by solar heating, ejecting organic molecules into the expanding coma. Hence, organic molecules with short photodissociation lifetimes (<10⁴ km) such as H₂CO can be found much farther from the comet nucleus than their photodestruction rates would suggest. A grain source for H₂CO may also explain structure observed in the BIMA maps of this molecule, as well as secondary velocity components observed in other comets such as comet T7 LINEAR. Fragmentation of comet dust in the coma, as well as material rich in carbon (e.g., C₂ and C₃) released from jets (A'Hearn et al. 1986), may contribute significantly to the carbon that is thought to have been deposited in the Earth's atmosphere over the centuries, as suggested by Ehrenfreund et al. (2002). Results also confirm that H₂CO cannot be a significant source of CO in Hale-Bopp, since the production rates differ by a factor of ≥10.

We thank D. K. Yeomans for ephemerides assistance and G. Engargiola, T. Helfer, W. Hoffman, R. L. Plambeck, and M. W. Pound for invaluable technical contributions. This material is based on work supported by the National Aeronautics and Space Administration through the NASA Astrobiology Institute under Cooperative Agreement CAN-02-OSS-02 issued through the Office of Space Science. S. N. M. would like to thank the Phoenix Chapter of ARCS, specifically Mrs. Scott L. Libby, Jr. endowment, for partial funding. This work was partially funded by NASA NAG5-4292, NAG5-4080, NAG5-8708, and NGT5-0083; NSF AST 96-13998, AST96-13999, AST96-13716, AST96-15608, and AST99-81363; and the Universities of Illinois, Maryland, and California, Berkeley. M. W. was funded by NSF AST 9625360, AST 9796263, and AST 0098583 and NASA NAG5-4349. L. A. was partially supported by NSF 0216226.

REFERENCES

- A'Hearn, M. F., Hoban, S., Birch, P. V., Bowers, C., Martin, R., & Klinglesmith, D. A. 1986, *Nature*, 324, 649
- Allamandola, L. J., Bernstein, M. P., Sandford, S. A., & Walker, R. L. 1999, *Space Sci. Rev.*, 90, 219
- Altwegg, K., Balsiger, H., & Geiss, J. 1999, *Space Sci. Rev.*, 90, 3
- Biver, N., et al. 1997, *Science*, 275, 1915
- . 2002, *Earth Moon Planets*, 90, 5
- Bockelée-Morvan, D., et al. 2000, *A&A*, 353, 1101
- Combi, M. R., & Fink, U. 1997, *ApJ*, 484, 879
- Combi, M. R., & Smyth, W. H. 1988, *ApJ*, 327, 1026
- Crovisier, J., et al. 2004, *A&A*, 418, 1141
- Eberhardt, P. 1999, *Space Sci. Rev.*, 90, 45
- Ehrenfreund, P., et al. 2002, *Rep. Prog. Phys.*, 65, 1427
- Feldman, P. D., Cochran, A. L., & Combi, M. R. 2004, in *Comets II*, ed. M. C. Festou, H. U. Keller, & H. A. Weaver (Tucson: Univ. Arizona Press), 425
- Festou, M. C. 1999, *Space Sci. Rev.*, 90, 53
- Fray, N., Benilan, Y., Cottin, H., & Gazeau, M.-C. 2004, *J. Geophys. Res. Planets*, 109, E07S12
- Friedel, D. N., et al. 2005, *ApJ*, 630, 623
- Geiss, J., et al. 1991, *A&A*, 247, 226
- Gombosi, T. I., & Horanyi, M. 1986, *ApJ*, 311, 491
- Halfen, D. T., et al. 2006, *ApJ*, 639, 237
- Hanner, M. S., & Bradley, J. P. 2004, in *Comets II*, ed. M. C. Festou, H. U. Keller, & H. A. Weaver (Tucson: Univ. Arizona Press), 555
- Harris, W. M., Scherb, F., Mierkiewicz, E., Oliverson, R., & Morgenthaler, J. 2002, *ApJ*, 578, 996
- Hollis, J. M., Jewell, P. R., Lovas, F. J., & Remijan, A. 2004, *ApJ*, 613, L45
- Hollis, J. M., Vogel, S. N., Snyder, L. E., Jewell, P. R., & Lovas, F. J. 2001, *ApJ*, 554, L81
- Howell, E. S., Lovell, A. J., & Schloerb, F. P. 2004, *IAU Circ.*, 8329, 2
- Huebner, W. F. 1987, *Science*, 237, 628
- Huebner, W. F., Keady, J. J., & Lyon, S. P. 1992, *Ap&SS*, 195, 1
- Ikeda, M., Kawaguchi, K., Takakuwa, S., Sakamoto, A., Sunada, K., & Fuse, T. 2002, *A&A*, 390, 363
- Jessberger, E. K. 1999, *Space Sci. Rev.*, 90, 91
- Kawakita, H., et al. 2004, *ApJ*, 601, L191
- Kolokolova, L., Hanner, M. S., Levasseur-Regourd, A.-Ch., & Gustafson, B. Å. S. 2004, in *Comets II*, ed. M. C. Festou, H. U. Keller, & H. A. Weaver (Tucson: Univ. Arizona Press), 577
- Korth, A., et al. 1986, *Nature*, 321, 335
- Küppers, M., Hartogh, P., & Villanueva, G. 2004, *AAS Planet. Sci. Meet. Abs.*, 36, 25.05
- Lamy, P. L., & Perrin, J. M. 1988, *Icarus*, 76, 100
- Lecacheux, A., Biver, N., Crovisier, J., & Bockelée-Morvan, D. 2004, *IAU Circ.*, 8304, 2
- Lis, D. C., et al. 1999, *Earth Moon Planets*, 78, 13
- Magée-Sauer, K., Dello Russo, N., DiSanti, M. A., Bonev, B., Gibb, E. L., & Mumma, M. J. 2004, *AAS Planet. Sci. Meet. Abs.*, 36, 25.03
- Meier, R., Eberhardt, P., Krankowsky, D., & Hodges, R. R. 1993, *A&A*, 277, 677
- Milam, S. N., Savage, C., Ziurys, L. M., & Wyckoff, S. 2004, *ApJ*, 615, 1054
- Mitchell, D., Lin, R., Carlson, C., Korth, A., Reme, H., & Mendis, D. 1992, *Icarus*, 98, 125
- Mitchell, D., et al. 1987, *Science*, 237, 626
- Mumma, M. J., Weaver, H. A., Larson, H. P., Davis, D. S., & Williams, M. 1986, *Science*, 232, 1523
- Remijan, A., et al. 2006, *ApJ*, 643, 567
- Sault, R. J., Teuben, P. J., & Wright, M. C. H. 1995, in *ASP Conf. Ser. 77*, *Astronomical Data Analysis Software and Systems IV*, ed. R. A. Shaw, H. E. Payne, & J. J. E. Hayes (San Francisco: ASP), 433

- Schutte, W. A., Allamandola, L. J., & Sandford, S. A. 1993, *Icarus*, 104, 118
Shoolery, J. N., & Sharbaugh, A. H. 1951, *Phys. Rev.*, 82, 95
Snyder, L. E., Palmer, P., & de Pater, I. 1989, *AJ*, 97, 246
Sorrell, W. H. 2001, *ApJ*, 555, L129
Wickramasinghe, N. C. 1975, *MNRAS*, 170, 11P
Womack, M., Festou, M. C., & Stern, S. A. 1997, *AJ*, 114, 2789
Womack, M., Pinnick, D. A., Mangum, J. G., Festou, M. C., & Stern, S. A. 2000, in *ASP Conf. Ser. 217, Imaging at Radio through Submillimeter Wavelengths*, ed. J. G. Mangum & S. J. E. Radford (San Francisco: ASP), 82
Woodney, L. M., et al. 1996, *IAU Circ.*, 6408, 2

APPENDIX D

CHEMICAL COMPLEXITY IN THE WINDS OF THE OXYGEN-RICH
SUPERGIANT STAR VY CANIS MAJORIS

L.M. Ziurys, S.N. Milam, A.J. Apponi, & N.J. Woolf 2007, *Nature*, **447**, 1094-1097.

**NATURE PUBLISHING GROUP LICENSE
TERMS AND CONDITIONS**

Dec 09, 2007

This is a License Agreement between Stefanie N Milam ("You") and Nature Publishing Group ("Nature Publishing Group"). The license consists of your order details, the terms and conditions provided by Nature Publishing Group, and the payment terms and conditions.

License Number	1845120593293
License date	Dec 09, 2007
Licensed content publisher	Nature Publishing Group
Licensed content publication	Nature
Licensed content title	Chemical complexity in the winds of the oxygen-rich supergiant star VY Canis Majoris
Licensed content author	L. M. Ziurys, S. N. Milam, A. J. Apponi, N. J. Woolf
Volume number	
Issue number	
Pages	
Year of publication	2007
Portion used	Full paper
Requestor type	Student
Type of Use	Thesis / Dissertation
PO Number	
Total	\$0.00
Terms and Conditions	

Terms and Conditions for Permissions

Nature Publishing Group hereby grants you a non-exclusive license to reproduce this material for this purpose, and for no other use, subject to the conditions below:

1. NPG warrants that it has, to the best of its knowledge, the rights to license reuse of this material. However, you should ensure that the material you are requesting is original to Nature Publishing Group and does not carry the copyright of another entity (as credited in the published version). If the credit line on any part of the material you have requested indicates that it was reprinted or adapted by NPG with permission from another source, then you should also seek permission from that source to reuse the material.
2. Permission granted free of charge for material in print is also usually granted for any electronic version of that work, provided that the material is incidental to the work as a whole and that the electronic version is essentially equivalent to, or substitutes for, the print version. Where print permission has been granted for a fee, separate permission must be obtained for any additional, electronic re-use (unless, as in the

case of a full paper, this has already been accounted for during your initial request in the calculation of a print run). NB: In all cases, web-based use of full-text articles must be authorized separately through the 'Use on a Web Site' option when requesting permission.

3. Permission granted for a first edition does not apply to second and subsequent editions and for editions in other languages (except for signatories to the STM Permissions Guidelines, or where the first edition permission was granted for free).
4. Nature Publishing Group's permission must be acknowledged next to the figure, table or abstract in print. In electronic form, this acknowledgement must be visible at the same time as the figure/table/abstract, and must be hyperlinked to the journal's homepage.
5. The credit line should read:

Reprinted by permission from Macmillan Publishers Ltd: [JOURNAL NAME]
(reference citation), copyright (year of publication)

For AOP papers, the credit line should read:

Reprinted by permission from Macmillan Publishers Ltd: [JOURNAL NAME],
advance online publication, day month year (doi: 10.1038/sj.[JOURNAL
ACRONYM].XXXXXX)

6. Adaptations of single figures do not require NPG approval. However, the adaptation should be credited as follows:

Adapted by permission from Macmillan Publishers Ltd: [JOURNAL NAME]
(reference citation), copyright (year of publication)

7. Translations of 401 words up to a whole article require NPG approval. Please visit <http://www.macmillanmedicalcommunications.com> for more information. Translations of up to a 400 words do not require NPG approval. The translation should be credited as follows:

Translated by permission from Macmillan Publishers Ltd: [JOURNAL NAME]
(reference citation), copyright (year of publication).

We are certain that all parties will benefit from this agreement and wish you the best in the use of this material. Thank you.

v1.1

LETTERS

Chemical complexity in the winds of the oxygen-rich supergiant star VY Canis Majoris

L. M. Ziurys^{1,2,3,4}, S. N. Milam^{1,2,4}, A. J. Apponi^{1,2,4} & N. J. Woolf^{1,2}

The interstellar medium is enriched primarily by matter ejected from old, evolved stars^{1,2}. The outflows from these stars create spherical envelopes, which foster gas-phase chemistry^{3–5}. The chemical complexity in circumstellar shells was originally thought to be dominated by the elemental carbon to oxygen ratio⁶. Observations have suggested that envelopes with more carbon than oxygen have a significantly greater abundance of molecules than their oxygen-rich analogues⁷. Here we report observations of molecules in the oxygen-rich shell of the red supergiant star VY Canis Majoris (VY CMa). A variety of unexpected chemical compounds have been identified, including NaCl, PN, HNC and HCO⁺. From the spectral line profiles, the molecules can be distinguished as arising from three distinct kinematic regions: a spherical outflow, a tightly collimated, blue-shifted expansion, and a directed, red-shifted flow. Certain species (SiO, PN and NaCl) exclusively trace the spherical flow, whereas HNC and sulphur-bearing molecules (amongst others) are selectively created in the two expansions, perhaps arising from shock waves. CO, HCN, CS and HCO⁺ exist in all three components. Despite the oxygen-rich environment, HCN seems to be as abundant as CO. These results suggest that oxygen-rich shells may be as chemically diverse as their carbon counterparts.

Circumstellar envelopes are unique chemical laboratories. Molecules are thought to form near the hot, dense stellar photosphere by a combination of equilibrium and non-equilibrium (that

is, shocks and stellar photodissociation) processes⁸. As the gas flows from the star, molecular abundances ‘freeze-out’ until the outer edge, where the chemistry is further modified by interstellar ultraviolet radiation^{3,4}. Chemical compounds in these shells apparently survive thousands of years as the star evolves to its final stage⁵.

Oxygen is typically more abundant than carbon on the surface of main sequence stars, with a roughly solar ratio of C/O = 0.5 (refs 6, 9). Stars in a certain mass range, however, pass through the asymptotic giant branch (AGB), where they undergo substantial convection. ‘Dredge-up’ events mix carbon from the interior helium-burning shell to the surface such that the C/O ratio becomes >1 (ref. 6), resulting in ‘carbon-rich’ as opposed to ‘oxygen-rich’ envelopes, which vary in chemical complexity. The C-rich envelope of the AGB star IRC+10216, for example, contains over 60 different chemical compounds, including unusual carbon chain radicals⁵. In contrast, only 10–12 compounds have been identified in the most chemically interesting oxygen-rich evolved stars, such as IK Tau¹⁰.

VY Canis Majoris (VY CMa) is an oxygen-rich¹¹ supergiant (~25 solar masses, 25M_⊙) star with a luminosity of 500,000 times that of the Sun and an effective temperature near 3,000 K (ref. 12). The mass loss rate of VY CMa is substantial (~2 × 10⁻⁴ M_⊙ yr⁻¹), resulting in a clumpy envelope consisting of arcs, knots and jets on the scale of 10³ (~15,000 AU), evident in Hubble Space Telescope images¹² (Fig. 1). Molecular line observations trace a shell expanding at a velocity of ~40 km s⁻¹ (ref. 13). Aperture synthesis maps of CO and maser

Table 1 | Molecular abundances in VY Canis Majoris

Molecule*	Source radius (arcsec)		Abundance relative to H ₂		
	Spherical wind	Red/blue flow	Spherical wind	Red-shifted flow	Blue-shifted flow
CN	6	8.5	2 × 10 ⁻⁸	3 × 10 ⁻⁸	1 × 10 ⁻⁸
CO	6	8.5	5 × 10 ⁻⁵	6 × 10 ⁻⁵	8 × 10 ⁻⁵
CS	0.5	0.7	1 × 10 ⁻⁷	4 × 10 ⁻⁸	1 × 10 ⁻⁷
H ₂ O	0.1		4 × 10 ⁻⁴ †		
H ₂ S	6	8.5	7 × 10 ⁻⁸	2 × 10 ⁻⁷	1 × 10 ⁻⁷
HNC	3	3.5	8 × 10 ⁻⁵	4 × 10 ⁻⁵	4 × 10 ⁻⁵
HCO ⁺	6	8.5	2 × 10 ⁻⁸	2 × 10 ⁻⁸	2 × 10 ⁻⁸
HNC		0.7		2 × 10 ⁻⁸	2 × 10 ⁻⁸
NaCl	0.25		8 × 10 ⁻⁹		
NH ₃				4 × 10 ⁻⁶ ‡	4 × 10 ⁻⁶ ‡
NS		8.5		1 × 10 ⁻⁸ ‡	6 × 10 ⁻⁹ ‡
OH				maser	maser
PN	0.5		4 × 10 ⁻⁸		
SiO	6		~1 × 10 ⁻⁵		
SiS	0.5	0.7	7 × 10 ⁻⁶	2 × 10 ⁻⁶	7 × 10 ⁻⁷
SO		8.5		5 × 10 ⁻⁸	4 × 10 ⁻⁸
SO ₂		8.5		4 × 10 ⁻⁷	3 × 10 ⁻⁷

Abundances are relative to H₂. Abundances and source sizes were derived by modelling the line profiles, assuming an appropriate geometry and mass loss rate. In almost all cases, at least two transitions were simultaneously fitted to establish abundances. Collisional excitation was assumed. See Supplementary Information for details.

* Bold denotes first time observed towards VY CMa.

† Ref. 28.

‡ Ref. 29.

¹NASA Astrobiology Institute, ²Department of Astronomy/Steward Observatory, ³Arizona Radio Observatory, University of Arizona, 933 North Cherry Avenue, ⁴Department of Chemistry, University of Arizona, 1306 East University Boulevard, Tucson, Arizona 85721, USA.

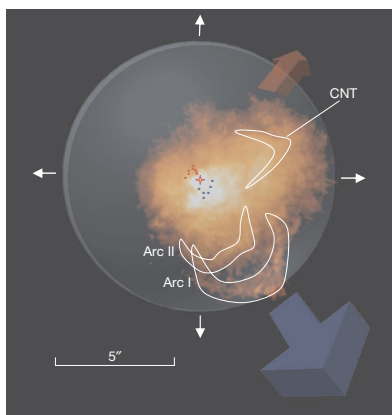


Figure 1 | Model of the molecular outflows in VY CMa, superimposed on the HST infrared image. The spherical wind is represented by the white arrows and the semi-transparent circle, whereas the two directed expansions are indicated by the (large) blue and red arrows. Positions of the red- and blue-shifted OH masers are shown (small rectangles) relative to the central star (red diamond), as well as the locations of the infrared features Arc I and Arc 2, located to the southwest, and the Curved Nebulous Tail (CNT), which appears northwest of the star¹². The blue-shifted flow is slightly inclined relative to the line of sight, following the orientation of the masers. The arcs seem to follow the blue-shifted expansion. The red-shifted flow is oriented at a larger angle relative to the line of sight, roughly in the direction of the CNT. These infrared features probably trace shocks associated with the two expansions.

emission from OH, H₂O and SiO indicate structure of the order of an arcsecond, suggesting the presence of a tilted, expanding disk or a bipolar outflow^{14,15}.

Oxygen-rich circumstellar shells have never been studied in equivalent detail to the carbon-rich counterparts. Therefore, we began a spectral survey of VY CMa at wavelengths of 1, 2 and 3 mm (75–270 GHz) using the 12-m telescope and the Sub-millimeter Telescope (SMT) of the Arizona Radio Observatory. In the course of our observations, seven molecules new to this source were discovered (NaCl, HCO⁺, PN, CS, NS, HNC and SiS), bringing to 17 the total number of chemical compounds found in the envelope of VY CMa (Table 1).

The spectral-line profiles varied between species. SiO and PN were found to have roughly triangular line shapes (Fig. 2), tracing a spherical wind concentrated in the plane of the sky, with line widths $\Delta v_{1/2}$ (full-width at half-maximum) near 40 km s^{-1} . NaCl exhibited a much narrower line profile ($\Delta v_{1/2} \approx 14 \text{ km s}^{-1}$), and arises from the interior region where the maximum outflow velocity has not yet been attained. SO₂ and SO display asymmetric horn-shaped profiles, with distinct blue- and red-shifted components near -7 km s^{-1} and 42 km s^{-1} , respectively. The horned profile in SO₂ is strikingly similar to that found in the OH 1,612 MHz maser transition¹⁴, as shown in Fig. 2. SO₂, however, exhibits the same line shape in multiple transitions over a wide range of energies, consistent with a Boltzmann distribution with temperature $T \approx 50 \text{ K}$. Furthermore, the blue-shifted feature in both molecules is almost identical in shape, suggesting a collimated flow close to the line of sight. In

disappears before the terminal outflow velocity is achieved. SO₂ and the OH maser profiles (f and g) are remarkably similar, suggesting that these species are linked chemically and dynamically. The narrow spike that appears in the CO spectrum near 25 km s^{-1} in LSR velocity arises from background gas. Spectral resolution for all data except the OH line is 1 MHz.

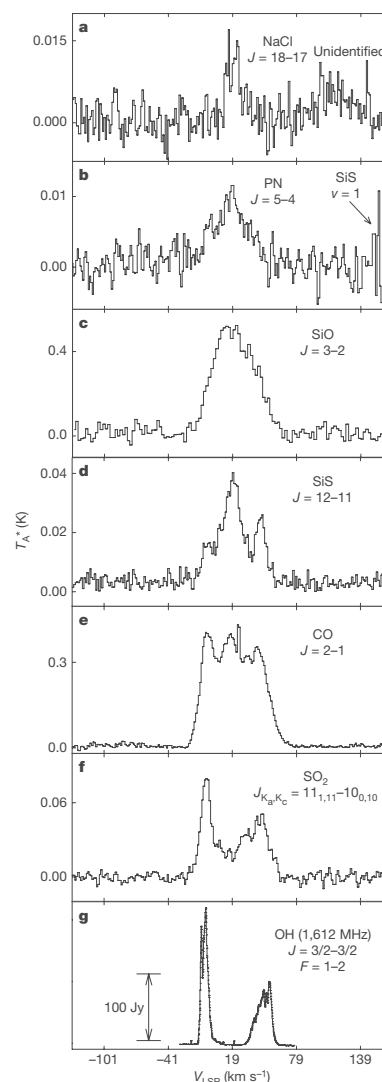


Figure 2 | Sample molecular spectra from VY CMa, measured with the Arizona Radio Observatory's Sub-millimeter Telescope (SMT), showing the variation in line profiles. The receiver used for these observations was an ALMA Band 6 prototype system³⁰, which produced exceptional total system temperatures (single sideband) of $T_{\text{sys}} \approx 120\text{--}140 \text{ K}$ on the sky. Various rotational transitions of molecules measured in the 1–2-mm wavelength region are shown (a–f), as well as the OH 1,612 MHz maser emission from ref. 14 (g). The spectrum in e was obtained with the 12-m telescope. The spectra are plotted in terms of intensity (T_A^* , in K) versus velocity with respect to the local standard of rest (V_{LSR} in km s^{-1}). The intensity scale for the OH data are in Janskys (Jy). The quantum numbers of the particular rotational transition displayed are given to the right of each spectrum. As these data illustrate, NaCl (a), PN (b) and SiO (c) exclusively trace the spherical wind, whereas the two directed outflows are prominent in SO₂ (f), SiS (d) and CO (e) are found in all three regions. The NaCl line is particularly narrow because this molecule

contrast, the red-shifted emission in SO_2 lies at lower projected expansion velocities than the terminal value indicated by this species itself and the maser emission. This difference indicates that the bulk of the red-shifted material is moving at a substantial angle relative to the line of sight. Many species, including SiS, HCN, H_2S , CO and CS, are present in all three flows. Comparison with previous CO and HCN data suggests that these regions extend to radii $6''$ – $8''$ from the central star^{16,17}.

The similarity of the OH and SO_2 line profiles indicate that the blue-shifted outflow is oriented to the southwest, like the masers, and encompasses the infrared dust features Arc 1 and Arc 2 (see Fig. 1). Potassium emission lines from Arc 1 also show a strong, blue-shifted feature with a velocity almost identical to that of the molecular spectra^{18,19}, suggesting that the arcs trace shocks created in the flow. Atomic absorption lines from the 'Curved Nebulous Tail' (CNT) have the same peak velocities as the red-shifted molecular lines. The red-shifted outflow therefore probably lies to the northwest, with the masers on the eastern edge. These two expansions seem to be unrelated; they exhibit different line shapes and molecular rotational temperatures. Large convective cells²⁰, as observed in the supergiant Betelgeuse²¹, could be their origin.

The chemistry in the envelope of VY CMa differs with physical location. NaCl is present only in the spherical flow close to the photosphere, and probably condenses into grains at a radius near $0.25''$. NaCl has previously been observed in the carbon-rich shells of two AGB stars²², but is more abundant in VY CMa. SiO, in contrast, survives well into the spherical flow, reaching the terminal velocity. The abundance of this species is estimated to be $\sim 10^{-5}$, relative to H_2 , in a $12''$ region. (Abundances quoted here are relative to H_2 , unless stated otherwise; see Supplementary Information.) A large fraction of the elemental silicon is therefore in gas-phase SiO, as opposed to silicate particles. SiS has a narrower line width than its oxide counterpart ($\sim 25 \text{ km s}^{-1}$ versus $\sim 42 \text{ km s}^{-1}$), suggesting that it condenses out or reacts to form other species, well before SiO. Modelling of the observed SiS transitions indicates a source size of $1''$, consistent with an early disappearance, and an abundance of 7×10^{-6} (Supplementary Information). Unlike SiO, however, SiS also appears in the red- and blue-shifted expansions. PN exists exclusively in the inner part of the spherical flow with a $1''$ source size and an abundance of $\sim 4 \times 10^{-8}$. These observations are the first conclusive identification of PN in circumstellar gas²³.

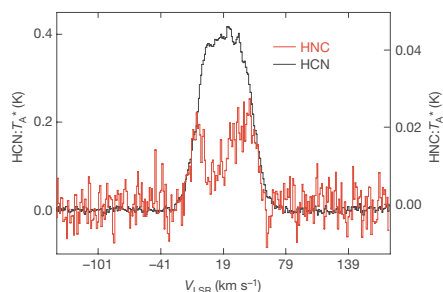


Figure 3 | Comparison of spectra for the metastable isomers HCN and HNC in VY CMa. The $J = 3 \rightarrow 2$ rotational transitions of both species are shown in the figure. The HNC spectrum is displayed in red, whereas that for HCN is plotted in black. HNC shows only the red- and blue-shifted flows, whereas HCN has a contribution from the spherical wind as well. The HNC/HCN ratio is roughly 0.001 for the directed flows, indicating high temperature formation²⁶, perhaps due to shocks. The spectra were measured in the 1-mm wavelength band using the SMT. The scale on the left-hand side of the spectra applies to the HCN data, whereas that on the right is for HNC. Spectral resolution for both lines is 1 MHz.

Six carbon-bearing species are present in VY CMa: CO, HCN, HNC, CN, CS and HCO^+ . Shock and 'mixed' chemistry models have predicted the synthesis of HCN and CS in O-rich environments^{8,17,24}, and these species indeed are observed in several O-rich shells^{17,25}. The models compute an HCN abundance at least a factor of ten less than CO, whereas observations have found $\text{HCN}/\text{CO} < 1/100$. In contrast, CO and HCN in VY CMa seem to have comparable abundances in all three flows, roughly 5×10^{-5} (Table 1). The appearance of HCO^+ is completely unexpected; this molecular ion had not been identified previously in circumstellar gas, and its existence in such material is not predicted by 'mixed' chemistry models^{8,17}. HNC, the metastable isomer of HCN (ref. 26), is also an unusual species for O-rich shells²⁵. This molecule is present exclusively in the directed flows, probably generated by the shock dissociation of HCN as the expansions drive into the spherical wind (Fig. 3).

SO_2 , NS and SO predominantly exist in the red- and blue-shifted outflows. The similarity of their line profiles to OH suggests these species are related dynamically. Models have predicted that the creation of OH quickly leads to SO and SO_2 , provided there is available sulphur^{13,27}. Sulphur may arise from the dissociation of CS and SiS, and OH is a shock product of H_2O . Nitrogen for NS is probably produced from dissociated HCN. For both SiS and HNC, the red-shifted component seems to have stronger emission, whereas the blue-shifted wing is dominant in SO_2 , SO and NS, showing chemical variation and suggesting shock differences in the two expansions.

Molecular production in VY CMa and its associated morphology cannot be explained by the usual spherical models of circumstellar synthesis, even when modified by non-equilibrium or 'mixed' chemistries. Shock waves and grain sputtering are likely to be influencing abundances. The diverse chemistry of VY CMa may be characteristic of red supergiant stars, induced by their complex process of mass loss.

Received 15 March; accepted 4 May 2007.

- Marvel, K. B. No methane here. The HCN puzzle: Searching for CH_3OH and C_2H in oxygen-rich stars. *Astron. J.* **130**, 261–268 (2005).
- Wilson, L. A. Mass loss from cool stars: Impact on the evolution of stars and stellar populations. *Annu. Rev. Astron. Astrophys.* **38**, 573–611 (2000).
- McCabe, E. M., Smith, R. C. & Clegg, R. E. S. Molecular abundances in IRC+10216. *Nature* **281**, 263–266 (1979).
- Glassgold, A. E. Circumstellar photochemistry. *Annu. Rev. Astron. Astrophys.* **34**, 241–278 (1996).
- Ziurys, L. M. The chemistry in circumstellar envelopes of evolved stars: Following the origin of the elements to the origin of life. *Proc. Natl Acad. Sci. USA* **103**, 12274–12279 (2006).
- Iben, I. & Renzini, A. Asymptotic giant branch evolution and beyond. *Annu. Rev. Astron. Astrophys.* **21**, 271–342 (1983).
- Olofsson, H. Molecules in envelopes around AGB-stars. *Astrophys. Space Sci.* **251**, 31–39 (1997).
- Cherchneff, I. A chemical study of the inner winds of asymptotic giant branch stars. *Astron. Astrophys.* **456**, 1001–1012 (2006).
- Anders, E. & Grevesse, N. Abundances of the elements: Meteoritic and solar. *Geochim. Cosmochim. Acta* **53**, 197–214 (1989).
- Duari, D., Cherchneff, I. & Willacy, K. Carbon molecules in the inner wind of the oxygen-rich Mira IK Tauri. *Astron. Astrophys.* **341**, L47–L50 (1999).
- Wallerstein, G. & Gonzalez, G. The spectrum of VY Canis Majoris in 2000 February. *Publ. Astron. Soc. Pacif.* **113**, 954–956 (2001).
- Smith, N. et al. The asymmetric nebula surrounding the extreme red supergiant VY Canis Majoris. *Astron. J.* **121**, 1111–1125 (2001).
- Sahai, R. & Wannier, P. G. SO and SO_2 in mass-loss envelopes of red giants: Probes of nonequilibrium circumstellar chemistry and mass-loss rates. *Astrophys. J.* **394**, 320–339 (1992).
- Bowers, P. F., Johnston, K. J. & Spencer, J. H. Circumstellar envelope structure of late-type stars. *Astrophys. J.* **274**, 733–754 (1983).
- Muller, S. et al. The molecular envelope around the red supergiant VY CMa. *Astrophys. J.* **656**, 1109–1120 (2007).
- Kemper, F. et al. Mass loss and rotational CO emission from asymptotic giant branch stars. *Astron. Astrophys.* **407**, 609–629 (2003).
- Nercessian, E., Guilloteau, S., Omont, A. & Benayoun, J. J. HCN emission and nitrogen-bearing molecules in oxygen-rich circumstellar envelopes. *Astron. Astrophys.* **210**, 225–235 (1989).
- Humphreys, R. M., Davidson, K., Ruch, G. & Wallerstein, G. High-resolution, long-slit spectroscopy of VY Canis Majoris: The evidence for localized high mass loss events. *Astron. J.* **129**, 492–510 (2005).
- Smith, N. Spatially extended K I $\lambda 7699$ emission in the nebula of VY CMa: kinematics and geometry. *Mon. Not. R. Astron. Soc.* **349**, L31–L35 (2004).

20. Schwarzschild, M. On the scale of photospheric convection in red giants and supergiants. *Astrophys. J.* **195**, 137–144 (1975).
21. Lim, J., Carilli, C. L., White, S. M., Beasley, A. J. & Marson, R. G. Large convective cells as the source of Betelgeuse's extended atmosphere. *Nature* **392**, 575–577 (1998).
22. Highberger, J. L., Thomson, K. J., Young, P. A., Arnett, D. & Ziurys, L. M. The salty scrambled egg: Detection of NaCl toward CRL 2688. *Astrophys. J.* **593**, 393–401 (2003).
23. Cernicharo, J., Guelin, M. & Kahane, C. A λ 2 mm molecular line survey of the C-star envelope IRC+10216. *Astron. Astrophys.* **142** (Suppl.), 181–215 (2000).
24. Szczerba, R., Schmidt, M. R. & Pulecka, M. Mixed chemistry phenomenon during late stages of stellar evolution. *Balt. Astron.* **16**, 134–141 (2007).
25. Bujarrabal, V., Fuente, A. & Omont, A. Molecular observations of O- and C-rich circumstellar envelopes. *Astron. Astrophys.* **285**, 247–271 (1994).
26. Schilke, P. *et al.* A study of HCN, HNC and their isotopomers in OMC-1. *Astron. Astrophys.* **256**, 595–612 (1992).
27. Nejad, L. A. M. & Millar, T. J. Chemical modeling of molecular sources – VI. Carbon-bearing molecules in oxygen-rich circumstellar envelopes. *Mon. Not. R. Astron. Soc.* **230**, 79–86 (1988).
28. Zubko, V., Li, D., Lim, T., Feuchtgruber, H. & Harwit, M. Observations of water vapour outflow from NML Cygnus. *Astrophys. J.* **610**, 427–435 (2004).
29. Monnier, J. D., Danchi, W. C., Hale, D. S., Tuthill, P. G. & Townes, C. H. Mid-infrared interferometry on spectral lines. III. Ammonia and silane around IRC+10216 and VY Canis Majoris. *Astrophys. J.* **543**, 868–879 (2000).
30. Lauria, E. F. *et al.* First Astronomical Observations with an ALMA Band 6 (211–275 GHz) Sideband-Separating SIS Mixer-preamp (ALMA Memo No. 553); (www.alma.nrao.edu/memos/) (2006).

Supplementary Information is linked to the online version of the paper at www.nature.com/nature.

Acknowledgements We thank the National Radio Astronomy Observatory for the loan of the ALMA Band 6 mixer system, and A. Lichtenberger and the University of Virginia Microfabrication Laboratory for supplying the mixer junctions. This research is partly supported by the NSF Astronomy and NASA Astrobiology programmes.

Author Information Reprints and permissions information is available at www.nature.com/reprints. The authors declare no competing financial interests. Correspondence and requests for materials should be addressed to L.M.Z. (lziurys@as.arizona.edu).

APPENDIX E

DETECTION OF NaCl TOWARDS IK Tau AND VY CMa: OXYGEN-RICH MASS
LOSS WITH A PINCH OF SALT

S.N. Milam, A.J. Apponi, N.J. Woolf, & L.M. Ziurys 2007, *Astrophys. J.*, **668**, L131-
L134.

Reproduced by permission of the AAS.

OXYGEN-RICH MASS LOSS WITH A PINCH OF SALT: NaCl IN THE CIRCUMSTELLAR GAS
 OF IK TAURI AND VY CANIS MAJORIS

S. N. MILAM, A. J. APPONI, N. J. WOOLF, AND L. M. ZIURYS

Department of Chemistry, Department of Astronomy, NASA Astrobiology Institute, and Steward Observatory, University of Arizona,
 933 North Cherry Avenue, Tucson, AZ 85721; stemil@as.arizona.edu, aapponi@as.arizona.edu,
 nwoolf@as.arizona.edu, lziurys@as.arizona.edu

Received 2007 June 30; accepted 2007 August 31; published 2007 October 4

ABSTRACT

The NaCl molecule has been observed in the circumstellar envelopes of VY Canis Majoris (VY CMa) and IK Tauri (IK Tau)—the first identifications of a metal refractory in oxygen-rich shells of evolved stars. Five rotational transitions of NaCl at 1 and 2 mm were detected toward VY CMa and three 1 mm lines were observed toward IK Tau, using the telescopes of the Arizona Radio Observatory. In both objects, the line widths of the NaCl profiles were extremely narrow relative to those of other molecules, indicating that sodium chloride has not reached the terminal outflow velocity in either star, likely a result of early condensation onto grains. Modeling the observed spectra suggests abundances, relative to H₂, of $f \sim 5 \times 10^{-9}$ in VY CMa and $f \sim 4 \times 10^{-9}$ in IK Tau, with source sizes of 0.5" and 0.3", respectively. The extent of these sources is consistent with the size of the dust acceleration zones in both stars. NaCl therefore appears to be at least as abundant in O-rich shells as compared to C-rich envelopes, where $f \sim (0.2\text{--}2) \times 10^{-9}$, although it appears to condense out earlier in the O-rich case. Chemical equilibrium calculations indicate that NaCl is the major carrier of sodium at $T \sim 1100$ K for oxygen-rich stars, with predicted fractional abundances in good agreement with the observations. These measurements suggest that crystalline salt may be an important condensate for sodium in both C- and O-rich circumstellar shells.

Subject headings: astrochemistry—radio lines: stars—stars: chemically peculiar—
 stars: individual (VY Canis Majoris, IK Tauri, IRC +10216)

1. INTRODUCTION

Molecular material has been known for decades to exist in the envelopes of both carbon- and oxygen-rich evolved stars, primarily in the form of CO, SiO, and HCN. However, chemical complexity has been usually associated with C-rich asymptotic giant branch (AGB) stars and their successors, protoplanetary nebulae (Pardo et al. 2007). For example, in the shell of the AGB star IRC +10216, where $C > O$, over 60 molecular species have been detected, including sodium-, magnesium-, and aluminum-bearing compounds, as well as silicon and carbon chain compounds (Cernicharo & Guélin 1987; Turner et al. 1994; Kawaguchi et al. 1993; Ziurys et al. 1994, 1995, 2002).

Some of the exotic types of species found in carbon-rich envelopes are those containing sodium. In IRC +10216, for example, two sodium-bearing molecules have been detected: NaCl and NaCN (Cernicharo & Guélin 1987; Turner et al. 1994). These species have been found to have a condensed, inner-envelope distribution in this object, with a source size of $\theta_s \sim 5''$, corresponding to a radius of ~ 86 stellar radii, or $86R_*$ (Guélin et al. 1996). More recently, NaCl and NaCN have been detected in CRL 2688 as well. These sodium-containing species are thought to be produced by equilibrium chemistry near the stellar photosphere (Tsuji 1973), although additional chemical effects exist in CRL 2688 because the object is undergoing a second, enhanced phase of mass loss (Highberger & Ziurys 2003; Highberger et al. 2003).

Here we present the first detections of NaCl in oxygen-rich circumstellar envelopes. Sodium chloride has been observed in the supergiant star VY Canis Majoris (VY CMa) and the Mira variable IK Tauri (IK Tau). This species has been identified via measurements of multiple rotational transitions at $\lambda = 1$ and 2 mm using the Arizona Radio Observatory (ARO). The spectra suggest a strictly inner-envelope distribution, within $50R_*$. The original detection of NaCl toward VY CMa

was mentioned in a previous publication (Ziurys et al. 2007). In this Letter we present the results for NaCl in detail and discuss their implications for circumstellar sodium chemistry.

2. OBSERVATIONS

Observations at 1 mm were conducted at the ARO with the Submillimeter Telescope (SMT) on Mount Graham, Arizona, and measurements at 2 mm with the 12 m telescope at Kitt Peak, Arizona, during the period from 2006 February to 2007 March. The receiver at the SMT was an image-separating Atacama Large Millimeter Array (ALMA) Band 6 mixer; the lower sideband was used for the measurements (Lauria et al. 2006). Rejection for the image, in this case, upper sideband, was typically >20 dB. The back end employed was a 2048 channel, 1 MHz filter bank. At the 12 m, a dual-channel SIS receiver was used, operated in single sideband mode with image rejection >18 dB. Spectrometer back ends utilized at this facility were 1 and 2 MHz resolution filter banks, configured in parallel mode for the two receiver channels. The temperature scale at the SMT is T_A^* and at the 12 m, T_R^* . Conversion to radiation temperature is then $T_R = T_A^*/\eta_B$ and $T_R = T_R^*/\eta_C$, where η_B is the main-beam efficiency and η_C is the beam efficiency corrected for forward spillover losses. Observations were conducted in beam-switching mode with a subreflector throw of $\pm 2'$ toward VY CMa (B1950.0: $\alpha = 07^h20^m54.7^s$, $\delta = -25^\circ40'12''$) and IK Tau (B1950.0: $\alpha = 03^h50^m43.6^s$, $\delta = 11^\circ15'32''$). Supporting measurements were additionally carried out toward IRC +10216 (B1950.0: $\alpha = 09^h45^m14.8^s$, $\delta = 13^\circ30'40''$) at 1 and 2 mm. Pointing and focus corrections were established by frequent observations of planets. Frequencies and telescope parameters are given in Table 1.

TABLE 1
OBSERVATIONS OF NaCl TOWARD VY CMA, IK TAU, AND IRC +10216

Source	Transition	Frequency (MHz)	θ_b (arcsec)	η_r or η_b	T_A^* (K)	V_{LSR} (km s $^{-1}$)	$\Delta V_{1/2}$ (km s $^{-1}$)
VY CMa ^a	$J = 11 \rightarrow 10$	143237.37	44	0.76	0.003 ± 0.001^d	18.0 ± 2.1	18.8 ± 2.1
	$J = 17 \rightarrow 16$	221260.11	34	0.78	0.008 ± 0.004	17.7 ± 2.7	15.0 ± 2.7
	$J = 18 \rightarrow 17$	234251.87	32	0.78	0.013 ± 0.005	17.4 ± 2.6	14.1 ± 2.6
	$J = 19 \rightarrow 18$	247239.59	30	0.78	0.014 ± 0.005	16.7 ± 2.4	14.5 ± 2.4
IK Tau ^b	$J = 20 \rightarrow 19$	260223.06	29	0.78	0.014 ± 0.010	16.0 ± 3.5	18.4 ± 3.5
	$J = 18 \rightarrow 17$	234251.87	32	0.78	0.005 ± 0.004	28.0 ± 2.6	6.4 ± 2.6
	$J = 19 \rightarrow 18$	247239.59	30	0.78	0.006 ± 0.004	27.9 ± 2.4	4.2 ± 2.4
IRC +10216 ^c	$J = 20 \rightarrow 19$	260223.06	29	0.78	0.006 ± 0.003	29.5 ± 2.4	5.7 ± 2.4
	$J = 10 \rightarrow 9$	130223.68	48	0.80	0.026 ± 0.006	-27.7 ± 4.6	19.1 ± 4.6
	$J = 17 \rightarrow 16$	221260.11	34	0.78	0.023 ± 0.008	-26.1 ± 2.8	19.6 ± 2.8
	$J = 18 \rightarrow 17$	234251.87	32	0.78	0.028 ± 0.013	-27.6 ± 2.6	21.6 ± 2.6
	$J = 19 \rightarrow 18$	247239.59	30	0.78	0.026 ± 0.008	-26.3 ± 2.4	19.1 ± 2.4
$J = 20 \rightarrow 19$	260223.06	29	0.78	0.062 ± 0.034	-26.7 ± 2.3	19.0 ± 2.3	

^a $\alpha = 07^{\text{h}}20^{\text{m}}54.7^{\text{s}}$, $\delta = -25^{\circ}40'12''$ (B1950.0).

^b $\alpha = 03^{\text{h}}50^{\text{m}}43.6^{\text{s}}$, $\delta = 11^{\circ}15'32''$ (B1950.0).

^c $\alpha = 09^{\text{h}}45^{\text{m}}14.8^{\text{s}}$, $\delta = 13^{\circ}30'40''$ (B1950.0).

^d Intensity scale was corrected from T_R to T_A^* ; $\eta_{\text{bs}} = 0.68$.

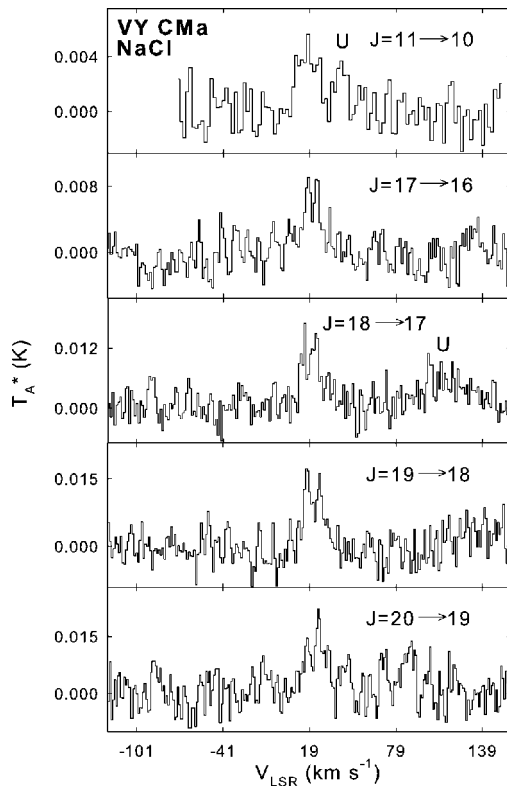


FIG. 1.—Spectra of the five rotational transitions of NaCl observed toward VY CMA using the ARO 12 m and SMT telescopes at 143, 221, 234, 247, and 260 GHz, respectively. Spectral resolution is 1 MHz, and the temperature scale is T_A^* . (The 12 m data, $J = 11 \rightarrow 10$, have been converted to T_A^* from T_R .) The assumed LSR velocity is 19 km s^{-1} . The line profiles, which are unusually narrow for this object, suggest a confined source where gas-phase NaCl disappears before the terminal velocity of the outflow is achieved. The features marked ‘U’ are unidentified.

3. RESULTS

Five rotational transitions of NaCl were detected toward VY CMA: four lines at 1 mm measured with the SMT ($J = 17 \rightarrow 16$ through $J = 20 \rightarrow 19$) and an additional transition at 2 mm ($J = 11 \rightarrow 10$) observed at the 12 m telescope. These data are presented in Figure 1. As the figure shows, the intensities are consistent among these five lines detected ($T_A^* \sim 4\text{--}14 \text{ mK}$), and the LSR velocities are all $V_{\text{LSR}} \sim 18 \text{ km s}^{-1}$ —typical for VY CMA (Ziurys et al. 2007). Furthermore, each transition has a somewhat flat-topped profile, indicating the source of NaCl was not resolved in VY CMA, even with the smallest beam size of $\theta_b \sim 29''$ at the SMT. An unresolved source is also consistent with the observed line widths. As listed in Table 1, typical line widths (FWHM) for NaCl in VY CMA are $\Delta V_{1/2} \sim 15 \text{ km s}^{-1}$, which are considerably smaller than those measured for CO ($\sim 33 \text{ km s}^{-1}$), HCN ($\sim 33 \text{ km s}^{-1}$), and SiO (43 km s^{-1}) in this object (Kemper et al. 2003; Ziurys et al. 2007). This finding suggests that NaCl has not yet reached the terminal velocity in VY CMA, estimated to be $V_{\text{exp}} \geq 21 \text{ km s}^{-1}$ (Ziurys et al. 2007; Muller et al. 2007).

Three transitions of NaCl ($J = 18 \rightarrow 17$, $J = 19 \rightarrow 18$, and $J = 20 \rightarrow 19$) were detected toward IK Tau (see Fig. 2); observed line parameters are also listed in Table 1. The spectra show a consistent velocity of $V_{\text{LSR}} \sim 29 \text{ km s}^{-1}$, and intensities near $T_A^* \sim 0.006 \text{ K}$. As for VY CMA, the line widths of these three transitions are significantly less than those of other known molecular species in this object, with $\Delta V_{1/2} \sim 5 \text{ km s}^{-1}$, as compared to CO and HCN ($\Delta V_{1/2} \sim 23 \text{ km s}^{-1}$; S. N. Milam et al. 2007, in preparation; Nerecessian et al. 1989).

In order to obtain a consistent data set for comparison, five transitions of NaCl were additionally measured toward IRC +10216. Line parameters for these spectra are also listed in Table 1.

4. DISCUSSION

4.1. Abundance and Spatial Distribution

The fractional abundance of NaCl, relative to H_2 (all fractional abundances are relative to H_2), was modeled with a radiative transfer circumstellar code developed by Bieging & Tafalla (1993) for a spherical distribution. Collisional excitation was assumed, using cross sections of SiO, corrected for the mass difference. The dis-

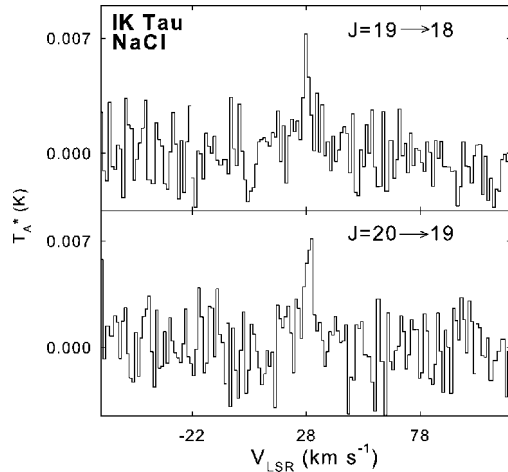


FIG. 2.—The $J = 19 \rightarrow 18$ and $J = 20 \rightarrow 19$ transitions of NaCl in IK Tau, measured with the SMT telescope of the ARO. Spectral resolution is 1 MHz, and the assumed velocity is $V_{\text{LSR}} = 34.5 \text{ km s}^{-1}$. As found in VY CMa, the narrow line widths observed indicate that NaCl does not remain in the gas phase long enough to reach the terminal outflow velocity.

tance to VY CMa was set at 1500 pc with a mass-loss rate of $\sim 10^{-4} M_{\odot} \text{ yr}^{-1}$ and a stellar temperature of $T_{\star} \sim 3368 \text{ K}$ (see Ziurys et al. 2007; Humphreys et al. 2007). A mass-loss rate of $4.5 \times 10^{-6} M_{\odot} \text{ yr}^{-1}$, distance of 270 pc, and $T_{\star} \sim 2100 \text{ K}$ were assumed for IK Tau (Marvel 2005; Duari et al. 1999). The temperature law used in the modeling was $T \propto r^{-0.7}$, based on other codes written for evolved stars (Kemper et al. 2003; Keady et al. 1988). However, the model results did not significantly change with a constant temperature profile (appropriate only in the inner-shell region) or a $r^{-0.58}$ dependence, as used in other models for the acceleration zone (Justtanont et al. 1994). A r^{-2} dependence was assumed for the density profile, with the initial density derived from a constant mass-loss rate, assuming an expansion velocity of $V_{\text{exp}} \sim 5 \text{ km s}^{-1}$ (VY CMa) or $\sim 3 \text{ km s}^{-1}$ (IK Tau), i.e., half the observed NaCl line width. Calculations were also conducted with an increased density (factor of 5) through the dust acceleration zone, for comparison, to account for additional density enhancements prior to achieving the terminal outflow velocity. This situation was not the case for IRC +10216, where NaCl attained the full expansion velocity, as indicated by the line profiles.

The model was used to reproduce the observed line profiles by varying two parameters: the molecular abundance and source size. For VY CMa, a source size of $0.5''$ with a fractional abundance relative to H_2 of $\sim 5 \times 10^{-9}$ was derived from a fit to all five lines, using the r^{-2} density law (see Table 2). This value is consistent with the size of the dust acceleration zone in VY CMa ($r \sim 0.5''$; Monnier et al. 1999) and the narrow line profiles. However, for IK Tau, the source size could not be constrained by the observational data because the three lines observed were very close in energy. Instead, the source size was estimated from that of the inner dust shell ($d \sim 0.2''$) obtained by Hale et al. (1997), as well as the expansion velocity deduced from the line width. Based on the dynamical model of Bujarrabal et al. (1989), an expansion velocity of $\sim 2.5 \text{ km s}^{-1}$ is achieved in IK Tau at a radius of $5 \times 10^{14} \text{ cm}$, or $\theta \sim 0.3''$. A source size of $0.3''$ was therefore assumed, resulting in a fractional abundance relative to H_2 toward

TABLE 2
OBSERVED FRACTIONAL ABUNDANCES OF CIRCUMSTELLAR
SODIUM-BEARING MOLECULES

Molecule	IRC +10216	CRL 2688	VY CMa	IK Tau
NaCl	2.0×10^{-9}	1.6×10^{-10} ^a	5.0×10^{-9}	4.0×10^{-9}
NaCN	2.3×10^{-8} ^a	5.2×10^{-9} ^a	$< 1 \times 10^{-8}$...
NaOH	$< 3 \times 10^{-9}$...
NaF	$< 9 \times 10^{-10}$...

^a From Highberger et al. (2003).

IK Tau of 4×10^{-9} , for the r^{-2} density dependence. For the enhanced density calculations, the fractional abundance in both sources decreased by a factor of ~ 5 . Because the molecular envelopes of VY CMa and IK Tau extend well beyond $10''$ – $20''$, as indicated by HCN and CO observations (Guélin et al. 1996; Nersessian et al. 1989; Ziurys et al. 2007), NaCl is likely incorporated into grains early in the condensation process.

A rotational diagram analysis was also done for comparison. For a source size of $\theta_s \sim 0.5''$, the total column density of $2.4 \times 10^{14} \text{ cm}^{-2}$ was obtained with $T_{\text{rot}} \sim 92 \text{ K}$ for VY CMa, corresponding to a fractional abundance of $f \sim 4 \times 10^{-9}$. This value is in excellent agreement with the model results. This analysis was also conducted for IK Tau, assuming a source size of $\sim 0.3''$. The total column density of NaCl derived was $N_{\text{rot}} = 2.5 \times 10^{14} \text{ cm}^{-2}$ with $T_{\text{rot}} \sim 70 \text{ K}$, or $f \sim 4 \times 10^{-9}$.

4.2. Comparison with Chemical Models

To gain further understanding of refractory abundances, a chemical equilibrium model was used to predict the key Na-bearing species found in the O-rich envelopes (adapted from Tsuji 1973). Figure 3 displays the results of these calculations for a range of temperatures with $\text{C/O} = 0.5$ (solar abundance) and $n \sim 10^{11} \text{ cm}^{-3}$. NaCl is clearly the main carrier of sodium in an oxygen-rich environment for the temperature range 500–1250 K, with $f \sim 10^{-7}$ to 10^{-10} , with NaOH reaching a peak fractional abundance near $T \sim 500 \text{ K}$ at $f \sim 10^{-9}$. NaO, surprisingly, never attains a fractional abundance above $f \sim 10^{-15}$ at any temperature.

Observational results for both oxygen-rich envelopes agree qualitatively with model predictions at $T \sim 1100 \text{ K}$ (see Table 2 for a summary of fractional abundances). This temperature implies formation at a radius of $\sim 5R_{\star}$ for VY CMa and $\sim 3R_{\star}$ for IK Tau, given the assumed $r^{-0.7}$ dependence and the stellar temperatures of 3368 K (VY CMa) and 2100 K (IK Tau). Presumably, these LTE abundances “freeze out” as the molecules flow from the hotter regions, as predicted by chemical models (McCabe et al. 1979), thus explaining the observed source sizes of $\sim 40R_{\star}$ (VY CMa) and $\sim 30R_{\star}$ (IK Tau). Rotational temperatures of 70–92 K are consistent with this scenario as well, considering the high dipole moment of NaCl (9.0 D). It should also be noted that NaCN and NaOH were not observed in VY CMa with upper limits of $f \leq 10^{-8}$ (see Table 2). These limits, however, are not sufficiently low to constrain the model.

4.3. Salt in Carbon- versus Oxygen-rich Envelopes

For comparison, the LTE model was also run for the C-rich case ($\text{C/O} = 1.5$) with identical densities and temperatures. As shown in Figure 3, the most noticeable distinction between the two models is the importance of NaCN in carbon-rich gas. This species is at least three orders of magnitude more abundant than in the O-rich case, reaching a peak concentration near 10^{-7} at $T \sim 700 \text{ K}$. The abundance of NaCl roughly follows that of

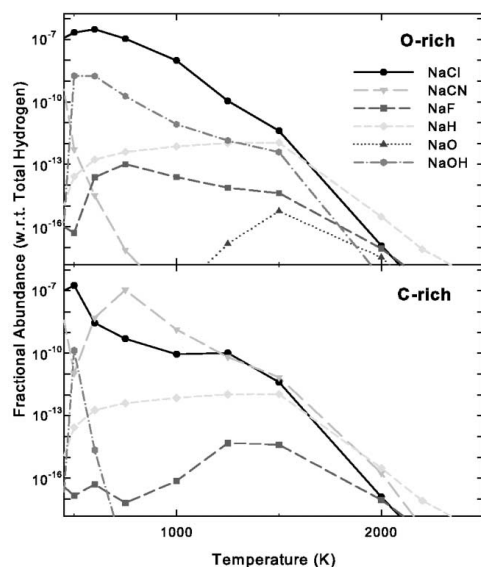


FIG. 3.—Thermodynamic equilibrium calculations of major sodium-bearing species in circumstellar shells that are O-rich (solar composition; *top*) and C-rich (C/O = 1.5; *bottom*) at densities $n \sim 10^{11} \text{ cm}^{-3}$ (based on Tsuji 1973). Fractional abundances are plotted with respect to total hydrogen for various temperatures. Abundances determined at $T \sim 1100 \text{ K}$ are in good agreement with the results obtained for VY CMa and IK Tau.

NaCN as a function of temperature, except at 700–1000 K, where NaCN is more abundant than NaCl by about factors of 10–100.

The fractional abundances derived from observations of the C-rich shells IRC + 10216 and CRL 2688 are in good agreement with the models (see Table 2). For IRC + 10216, the abundances of NaCl and NaCN are well predicted by the model at $T \sim 700 \text{ K}$, with $f(\text{NaCl}) \sim 2 \times 10^{-9}$ and $f(\text{NaCN}) \sim 2 \times$

10^{-8} . For CRL 2688, the best fit is for $T \sim 1000 \text{ K}$. These formation temperatures are consistent with the photosphere temperatures of 2320 and 6600 K for IRC + 10216 and CRL 2688. Considering a $r^{-0.7}$ profile, this temperature implies a formation radius of $r \sim 2 \times 10^{14} \text{ cm}$ or $\sim 3R_*$ for IRC + 10216. For CRL 2688, the formation radius is much larger ($\sim 11R_*$), although it is unlikely that the temperature profile is so simple in this object. The larger radius, however, is consistent with shock formation induced by the second stage of mass loss, as found by Highberger et al. (2003b).

Despite the chemical differences, NaCl appears to have a distribution close to the star in both oxygen- and carbon-rich envelopes, with a maximum radius of $\sim (6\text{--}10) \times 10^{15} \text{ cm}$, corresponding to $\sim 41R_*$ and $172R_*$ for VY CMa and IRC + 10216. In IRC + 10216, however, the molecule does not reach the terminal velocity of the envelope—not the situation for either VY CMa or IK Tau. The condensed distribution of sodium chloride in both types of objects implies that it condenses onto grains. Lodders & Fegley (1999) suggest that NaCl (i.e., crystalline salt) may be a major carrier of sodium in the solid state in C-rich envelopes. These data suggest it could be equally important for O-rich environments, as opposed to sodalite $[\text{Na}_4(\text{AlSi}_3\text{O}_4)_3\text{Cl}]$. The amount of sodium contained in crystalline salt must be controlled by the chlorine abundance, which is Cl/H $\sim 3.2 \times 10^{-7}$, as opposed to Na/H $\sim 2.1 \times 10^{-6}$, assuming solar composition—an order of magnitude difference. (It should also be noted that sodium may be enriched by hot bottom burning in AGB stars; Izzard et al. 2007.) In O-rich shells, another important condensate for sodium is albitite, $\text{NaAlSi}_3\text{O}_8$. This alternative is probably not as prevalent in carbon-rich environments, and may explain why NaCl remains longer in the gas phase for C stars such as IRC + 10216.

This research was supported by NSF grant AST 06-07803 and based on work supported by the National Aeronautics and Space Administration through the NASA Astrobiology Institute under cooperative agreement CAN-02-OSS-02 issued through the Office of Space Science. S. N. M. would like to thank the Phoenix Chapter of ARCS, specifically the Mrs. Scott L. Libby, Jr., endowment, for partial funding.

REFERENCES

- Biegging, J. H., & Tafalla, M. 1993, *AJ*, 105, 576
 Bujarrabal, V., Gómez-González, J., & Planesas, P. 1989, *A&A*, 219, 256
 Cernicharo, J., & Guélin, M. 1987, *A&A*, 183, L10
 Duari, D., Cherchneff, I., & Willacy, K. 1999, *A&A*, 341, L47
 Guélin, M., Lucas, R., & Neri, R. 1996, in *CO: Twenty-Five Years of Millimeter Wave Spectroscopy*, ed. W. B. Latter et al. (Dordrecht: Kluwer), 359
 Hale, D. D. S., et al. 1997, *ApJ*, 490, 407
 Highberger, J. L., Thomson, K. J., Young, P. A., Arnett, D., & Ziurys, L. M. 2003, *ApJ*, 593, 393
 Highberger, J. L., & Ziurys, L. M. 2003, *ApJ*, 597, 1065
 Humphreys, R. M., Helton, L. A., & Jones, T. J. 2007, *AJ*, 133, 2716
 Izzard, R. G., Lugaro, M., Karakas, A. I., Iliadis, C., & van Raaij, M. 2007, *A&A*, 466, 641
 Justtanont, K., Skinner, C. J., & Tielens, A. G. G. M. 1994, *ApJ*, 435, 852
 Kawaguchi, K., Kagi, E., Hirano, T., Takano, S., & Saito, S. 1993, *ApJ*, 406, L39
 Keady, J. J., Hall, D. N. B., & Ridgway, S. T. 1988, *ApJ*, 326, 832
 Kemper, F., Stark, R., Justtanont, K., de Koter, A., Tielens, A. G. G. M., Waters, L. B. F. M., Cami, J., & Dijkstra, C. 2003, *A&A*, 407, 609
 Lauria, E. F., Kerr, A. R., Reiland, G., Freund, R. F., Lichtenberger, A. W., Ziurys, L. M., Metcalf, M., & Forbes, D. 2006, First Astronomical Observations with an ALMA Band 6 (211–275 GHz) Sideband-Separating SIS Mixer-preamp (ALMA Memo 553), <http://www.alma.nrao.edu/memos>
 Lodders, K., & Fegley, B. 1999, in *IAU Symp. 191, Asymptotic Giant Branch Stars*, ed. T. Le Bertre, A. Lébre, & T. Waelkens (Dordrecht: Kluwer), 279
 Marvel, K. B. 2005, *AJ*, 130, 261
 McCabe, E. M., Common Smith, R., & Clegg, R. E. S. 1979, *Nature*, 281, 263
 Monnier, J. D., Tuthill, P. G., Lopez, B., Cruzalebes, P., Danchi, W. C., & Haniff, C. A. 1999, *ApJ*, 512, 351
 Muller, S., Dinh-V-Trung, Lim, J., Hirano, N., Muthu, C., & Kwok, S. 2007, *ApJ*, 656, 1109
 Nercissian, E., Guilloteau, S., Omont, A., & Benayoun, J. J. 1989, *A&A*, 210, 225
 Pardo, J. R., Cernicharo, J., Goicoechea, J. R., Guélin, M., & Asensio Ramos, A. 2007, *ApJ*, 661, 250
 Tsuji, T. 1973, *A&A*, 23, 411
 Turner, B. E., Steimle, T. C., & Meerts, L. 1994, *ApJ*, 426, L97
 Ziurys, L. M., Apponi, A. J., Guélin, M., & Cernicharo, J. 1995, *ApJ*, 445, L47
 Ziurys, L. M., Apponi, A. J., & Phillips, T. G. 1994, *ApJ*, 433, 729
 Ziurys, L. M., Milam, S. N., Apponi, A. J., & Woolf, N. J. 2007, *Nature*, 447, 1094
 Ziurys, L. M., Savage, C., Highberger, J. L., Apponi, A. J., Guélin, M., & Cernicharo, J. 2002, *ApJ*, 564, L45

APPENDIX F

CONSTRAINING PHOSPHORUS CHEMISTRY IN CARBON- AND OXYGEN-RICH
CIRCUMSTELLAR ENVELOPES: OBSERVATIONS OF PN, HCP, AND CP

S. N. Milam, D. T. Halfen, E. D. Tenenbaum, A. J. Apponi, N. J. Woolf, & L. M. Ziurys
2007, *Astrophys. J.*, submitted.

**Constraining Phosphorus Chemistry in Carbon- and
Oxygen-Rich Circumstellar Envelopes: Observations of PN,
HCP, and CP**

S. N. Milam,
D. T. Halfen¹,
E. D. Tenenbaum²,
A. J. Apponi,
N. J. Woolf,
and

L. M. Ziurys

Department of Chemistry
Department of Astronomy
NASA Astrobiology Institute
Arizona Radio Observatory

and

Steward Observatory
933 N. Cherry Avenue
The University of Arizona
Tucson, Arizona 85721

stemil, halfendt, emilyt, aapponi, nwoolf, & lziurys@as.arizona.edu

¹ NSF Astronomy and Astrophysics Postdoctoral Fellow

² NSF Graduate Research Fellow

ABSTRACT

Millimeter-wave observations of PN, CP, and HCP have been carried out towards circumstellar envelopes of evolved stars using the Arizona Radio Observatory (ARO). HCP and PN have been identified in the carbon-rich source CRL 2688 via observations at 1 mm using the Sub Millimeter Telescope (SMT) and 2-3 mm with the Kitt Peak 12m. An identical set of measurements were carried out towards IRC +10216, as well as observations of CP at 1 mm. PN was also observed towards VY Canis Majoris (VY CMa), an oxygen-rich supergiant star. The PN and HCP line profiles in CRL 2688 and IRC +10216 are roughly flat-topped, indicating unresolved, optically thin emission; CP, in contrast, has a distinct “U”-shape in IRC +10216. Modeling of the line profiles suggests abundances, relative to H₂, of $f(\text{PN}) \sim 3\text{-}5 \times 10^{-9}$ and $f(\text{HCP}) \sim 2 \times 10^{-7}$ in CRL 2688 - about an order of magnitude higher than in IRC +10216. In VY CMa, $f(\text{PN})$ is $\sim 4 \times 10^{-8}$. The data in CRL 2688 and IRC +10216 are consistent with LTE formation of HCP and PN in the inner envelope, as predicted by calculations, with CP a photodissociation product at larger radii. The observed abundance of PN in VY CMa is a factor of 100 higher than LTE predictions. In IRC +10216, the chemistry of HCP/CP mimics that of HCN/CN and suggests an N₂ abundance of $f \sim 1 \times 10^{-7}$. The chemistry of phosphorus appears active in both carbon- and oxygen-rich envelopes of evolved stars.

Subject Headings: astrochemistry --- astrobiochemistry --- line: identification --- stars: abundances --- stars: individual (VY CMa; CRL 2688; IRC +10216) --- stars: chemically peculiar

1. INTRODUCTION

Phosphorus plays a major role in biochemistry, being relevant to replication, metabolism, and structure in living systems (Pasek & Lauretta 2005). Yet, it is not a particularly prevalent element, with a cosmic abundance, relative to hydrogen, of $P/H \sim 2.8 \times 10^{-7}$ (Grevesse & Sauval 1998) – less than that of iron, magnesium, sodium, calcium, and aluminum. Despite this fact, phosphorus is a frequent constituent in meteorites, where the common form is in a iron-nickel-phosphide compound called schreibersite ($[(Fe,Ni)_3P]$). Because of its concentrated presence in meteorites, there is some thought that phosphorus needed for living systems was brought to Earth via meteoritic impact (Pasek & Lauretta 2005; Maciá 2005).

The history of phosphorus in interstellar gas is far less certain. This element is thought to be formed in massive stars ($M > 15 M_{\odot}$) during hydrostatic-shell C- and Ne-burning (Arnett 1996). It is released into the interstellar medium as these objects become supernovae. The rarity of high mass stars has a direct effect on the low (solar) P abundance as compared to other “biotic” elements such as C, N and O (Maciá 2005), which are all formed in a larger stellar population. In diffuse clouds, gas-phase phosphorus has been found to have an abundance that is consistent with minimal depletion into a solid form, based on P II observations (Lebouteiller, Kuassivi & Ferlet 2005). In dense gas, on the other hand, large depletions have been claimed because the only phosphorus-bearing gas-phase molecule observed thus far has been PN (Ziurys 1987; Turner & Bally 1987; Turner et al. 1990). However, it could be that phosphorus exists in other, as yet undiscovered, gaseous molecular forms.

In circumstellar envelopes, the state of phosphorus chemistry, until recently, has been similar to that in molecular clouds. CP had been the only species observed, and only in one object, IRC +10216 (Guélin et al. 1990). However, HCP has now been definitively detected in

IRC +10216, along with a tentative identification of PN, based on one clean and one blended transition (Agúndez, Cernicharo & Guélin 2007). Furthermore, PN and PO have recently been observed in the shell of the oxygen-rich red supergiant, VY Canis Majoris (VY CMa; Ziurys et al. 2007; Tenenbaum, Woolf & Ziurys 2007). Thus, four P-bearing compounds have now been identified in circumstellar gas.

Here we present observations of phosphorus-bearing molecules in another circumstellar source, the carbon-rich post Asymptotic Giant Branch (AGB) star, CRL 2688. PN and HCP have been conclusively detected in this object. An additional transition of PN has also been observed in IRC +10216, confirming the presence of this species towards this star, as well as several lines of HCP. The HCP data were discovered independently of Agúndez et al. (2007), and were in preparation for submission when their detection was published. Several transitions of PN in VY CMa and CP in IRC +10216 have been measured as well for comparison. In this paper we present our observations, derive molecular abundances, and discuss their implications for phosphorus chemistry in circumstellar envelopes.

2. OBSERVATIONS

The measurements were conducted during the period 2006 October through 2007 June at 1, 2 and 3 mm using the facilities of the Arizona Radio Observatory (ARO): the Kitt Peak 12m and Submillimeter Telescope (SMT) at Mt. Graham, AZ. The 1 mm observations were carried out at the SMT with a dual-channel ALMA Band 6 receiver system employing sideband-separating mixers with an image rejection of typically 15-20 dB. The backend was a 2048 channel 1 MHz filterbank, used in parallel (2 x 1024) mode. The temperature scale at the SMT is T_A^* ; radiation temperature is then defined as $T_R = T_A^*/\eta_b$, where η_b is the main-beam efficiency. The 2 and 3 mm observations were conducted at the 12m using dual-channel SIS

5

mixers, operated in single-sideband mode with the image rejection ≥ 20 dB. Filterbanks with 512 channels of 1 and 2 MHz resolutions were used simultaneously in parallel mode for the measurements, along with an autocorrelator with 782 kHz resolution. The intensity scale of the 12m is the chopper-wheel corrected antenna temperature, T_R^* , including forward spillover losses, which is converted to radiation temperature by $T_R = T_R^*/\eta_c$, where η_c is the corrected beam efficiency. Data was taken in beam-switching mode with a subreflector throw of $\pm 2'$. Pointing and focus was monitored regularly by observations of nearby planets and quasars. Source coordinates, rest frequencies, telescope efficiencies, and beam sizes are given in Table 1.

3. RESULTS

The data obtained for CRL 2688 are presented in Figure 1. As shown, three rotational transitions were detected individually for HCP and PN towards this object. The $J=2 \rightarrow 1$ and $3 \rightarrow 2$ lines of PN and $J=4 \rightarrow 3$ transition of HCP were measured at the 12m, while the $J=5 \rightarrow 4$ and $6 \rightarrow 5$ lines of HCP, as well as the $J=5 \rightarrow 4$ transition of PN, were observed at the SMT. As shown in Table 1, all features have LSR velocities in the range -34 to -37 km s^{-1} , and linewidths of ~ 35 km s^{-1} , typical parameters for CRL 2688 (e.g. Sopka et al. 1989; Young et al. 1992). The intensities are also consistent among the transitions. The HCP line profiles are roughly flat-topped with evidence of a slight “U”-shape, with stronger emission on the blue-shifted side. This profile indicates unresolved, or partially resolved, optically-thin emission. Observations of other molecules in CRL 2688 suggest a roughly spherical, AGB “remnant” flow of $\sim 20''$ - $30''$ in size (Rieu, Graham & Bujarrabal 1984; Fukasaku et al. 1994; Highberger et al. 2003). The three transitions of HCP were measured with a beam size of $\leq 39''$, consistent with the extent of the remnant wind. Slight asymmetries are also present in line profiles from species arising in this flow, such as NaCl, NH_3 , and HC_7N . Some of these asymmetries may result from the additional

6

outflows present in CRL 2688, caused by an erratic, second phase of mass-loss, which distorts the remnant AGB wind (e.g. Cox et al. 1997, 2000). The PN profiles are also flat-topped in shape, although there is again evidence of a “U” in the $J=5\rightarrow 4$ line, observed with the smallest beam of $32''$. The $J=3\rightarrow 2$ transition of PN is unfortunately blended with $^{30}\text{SiC}_2$ at 140956.2 MHz, with the $J_{K_a, K_c}=9_{3,6}\rightarrow 8_{3,5}$ transition of NaCN nearby at 140937.8 MHz.

In Figure 2, the same transitions of PN and HCP are shown for IRC +10216. The $J=3\rightarrow 2$ transition of PN is contaminated by $^{30}\text{SiC}_2$, as in CRL 2688, but the $J=5\rightarrow 4$ line is clean and confirms the presence of this species in IRC +10216. The LSR velocities and linewidths found for these molecules are characteristic of this object (see Table 1: Cernicharo, Guélin, & Kahane 2000). The data from this source display the classic, flat-topped profile, suggesting that the emission is unresolved and optically thin. Agúndez et al. (2007) found slight “U”-shapes in corresponding HCP spectra obtained with the IRAM 30m telescope. These authors derived a source of roughly $12''$ - $30''$, consistent with the ARO beam sizes at these frequencies for unresolved emission.

Figure 3 displays the $J=3\rightarrow 2$, $5\rightarrow 4$, and $6\rightarrow 5$ transitions of PN towards VY CMa. All three lines of this molecule appear to exhibit somewhat triangular line profiles, likely coming from an ellipsoidal wind that is elongated in the plane of the sky (see Ziurys et al. 2007). PN is the first phosphorus-bearing species identified in an oxygen-rich, as opposed to carbon-rich, envelope. The initial detection of phosphorus nitride in this source was mentioned briefly in Ziurys et al. (2007), where the $J=5\rightarrow 4$ spectra was presented.

For comparison, observations of the $N=5\rightarrow 4$ lines of CP were also carried out towards IRC +10216; see Figure 4. This radical was originally detected by Guélin et al. (1990) in this source, who measured several transitions. In Figure 4, the two fine structure components of the

N=5→4 transition are shown. Each component consists of two hyperfine lines, but these are separated at most by 1.5 channels in the resolution displayed, and therefore do not affect the line shape. While the J=5.5→4.5 feature is blended with the spin-rotation doublets of $^{13}\text{CCCCCH}$ (top panel), the J=4.5→3.5 component is uncontaminated (lower panel), and appears to be somewhat “U”-shaped. Guélin et al. (1990) had suggested that this line was flat-topped, but the signal-to-noise is better in the current data shown here. Additional observations would help clarify this issue. If real, the “U”-shape would again indicate a resolved, optically-thin distribution and hence a source size of $\sim 32''$.

A complete summary of line parameters for all spectra is given in Table 1. These values include the measured antenna temperature (T_A^* for the SMT and T_R^* for the 12m), the FWHM linewidth, the LSR velocity, and the integrated intensity.

4. ANALYSIS

For IRC +10216, the same transitions of CP, PN, and HCP were measured with two different telescopes, the IRAM 30m and the ARO SMT or 12m, allowing for an independent estimate of the source distributions for the three molecules of interest. Comparison of the HCP profiles suggests a source size for this species of $\theta_s \sim 22''$ considering a spherical distribution. Radiative transfer calculations by Agúndez et al. (2007) indicate a spherical source of HCP with a radius between $r \sim 6''$ and $15''$, in relatively good agreement. Similarly, the source size estimated for PN, based on the J=2→1 transition, is $\theta_s \sim 38''$ assuming a spherical geometry, consistent with the “U”-shaped profile observed by Guélin et al. (2000). For CP, only older data is available from IRAM, and it is not consistent with the spectrum recently measured from the SMT. Based on the observed “U”-shaped profile, the distribution of CP is $\theta_s \sim 32''$. For VY

CMa and CRL 2688, source sizes were derived based on radiative transfer modeling of the multiple transitions observed, as no other comparative data was available.

The radiative transfer code used to model the line profiles was that of Biegging and Tafalla (1993), where a set of statistical equilibrium equations are solved for populating rotational levels of a given molecule assuming a spherically expanding circumstellar shell. Input parameters necessary for the modeling are distance to the object, outflow velocity, mass-loss rate, and temperature and density profiles. The gas temperature profile was modeled as:

$$T_{Kin} = T_{Kin0} \left(\frac{r}{r_{Kin0}} \right)^{-0.7} \quad (1),$$

The initial temperature, T_{kin0} , was assumed to be the effective temperature of the star and r_{kin0} was defined as the stellar radius. The exponent value of -0.7 was chosen on the basis of other profiles from evolved stars (see Kemper et al. 2003 & Keady et al. 1988). A density distribution dependence of r^{-2} was used for all calculations, and the outflow velocity was established individually from the line profiles for a given species. Collisional cross-sections for PN have been recently measured by Tobiła et al. (2007) and were incorporated into the model. Cross-sections for HCP or CP are not known; thus, values for HCN and PN were used, respectively.

The model was used to reproduce the observed line profiles by varying two parameters: the molecular abundance and the source radius. The source radius was defined as the position from the star where the abundance decreased by $1/e$, assuming a spherical distribution. Three rotational transitions per molecule were simultaneously fit, in most cases, to constrain these variables, except where there was severe line contamination.

Because independent estimates of source sizes were available for IRC +10216, these data were modeled first. The fitting parameters assumed for IRC +10216 were a mass-loss rate of $3 \times 10^{-5} M_{\odot} \text{ yr}^{-1}$, an effective stellar temperature of $T_{\text{eff}} \sim 2320 \text{ K}$, a stellar radius of $R_{*} \sim 6.5 \times 10^{13}$

cm, and a distance of 150 pc (Agúndez & Cernicharo 2006). A fit to 8 observed profiles of HCP (4 transitions, SMT; 4 transitions IRAM) yielded a source size of $22''$, assuming a spherical geometry, and a fractional abundance, relative to H_2 , of $f \sim 3 \times 10^{-8}$. For PN, 3 spectral profiles were fit ($J=2 \rightarrow 1$, IRAM and 12m; $J=5 \rightarrow 4$, SMT), yielding a source size of $\sim 36''$ for a spherical distribution and a fractional abundance of $f \sim 3 \times 10^{-10}$. Shell geometries were also attempted in the analysis of the HCP and PN profiles, but were not as successful in reproducing these spectra. In the case of CP, only one transition could be reliably modeled: the $J=4.5 \rightarrow 3.5$ component of the $N=5 \rightarrow 4$ line. The other lines of CP observed in this work or by Guélin et al. (1990) were contaminated. In this case, both the IRAM and SMT data were modeled with a shell distribution. The shell source is consistent with the predictions of Agúndez et al. (2007) and the “U”-shape observed at the SMT. The best fit to the two data sets suggests that CP arises from a shell approximately $18''$ wide, with a peak abundance of $f \sim 5 \times 10^{-9}$ at a radius of $r \sim 13''$.

Using these source sizes, rotational diagrams were used to estimate column densities for HCP and PN towards IRC +10216. For HCP, the quantity derived is $N_{\text{tot}} \approx 1.0 \times 10^{14} \text{ cm}^{-2}$ with $T_{\text{rot}} \sim 111 \text{ K}$, using the ARO data alone. These values change slightly to $N_{\text{tot}} \sim 1.4 \times 10^{14} \text{ cm}^{-2}$ and $T_{\text{rot}} \sim 81 \text{ K}$ if the IRAM data is incorporated in the analysis. Including the $J=2 \rightarrow 1$ transition from the 30m with the ARO spectra (Guélin et al. 2000), the column density derived for PN is $N_{\text{tot}} \sim 6.3 \times 10^{12} \text{ cm}^{-2}$ and $T_{\text{rot}} \sim 11 \text{ K}$. The lower rotational temperature here reflects the higher dipole moment of PN (2.75 D). The column density for CP, based on one transition from the SMT, is $5.0 \times 10^{12} \text{ cm}^{-2}$, assuming $T_{\text{rot}} \sim 50 \text{ K}$ and a filling factor of unity.

For CRL 2688, the model parameters employed in the analysis are a distance of 1000 pc, $R_* \sim 9 \times 10^{12} \text{ cm}$, $T_{\text{eff}} \sim 6500 \text{ K}$ and a mass-loss rate of $1.7 \times 10^{-4} M_{\odot} \text{ yr}^{-1}$ (Skinner et al. 1997; Truong-Bach et al. 1990). The spectra for both PN and HCP were constrained as flat-topped

profiles with a spherical distribution. The best fit to the data for HCP yielded an abundance of $f \sim 2 \times 10^{-7}$ and $\theta_s \sim 8''-12''$ and $f \sim 3-5 \times 10^{-9}$ with $\theta_s \sim 12''-20''$ for PN. Using these source sizes, the rotational diagram analysis gave $N_{\text{tot}} \sim 0.6-1.4 \times 10^{15} \text{ cm}^{-2}$ and $T_{\text{rot}} \sim 31-32 \text{ K}$ for HCP and $0.5-2.8 \times 10^{13} \text{ cm}^{-2}$ with $T_{\text{rot}} \sim 16-18 \text{ K}$ for PN.

In the case of VY CMa, the distance was set at 1500 pc, with a mass-loss rate of $\sim 10^{-4} M_{\odot} \text{ yr}^{-1}$, $T_{\text{eff}} \sim 3368 \text{ K}$, and a stellar radius of $R_* \sim 1.36 \times 10^{14} \text{ cm}$ (Humphreys, Helton & Jones 2007). The total mass-loss rate in this object is $2-4 \times 10^{-4} M_{\odot} \text{ yr}^{-1}$ (Monnier et al. 1999), but PN only appears in one of the three flows that contribute to the loss of material (see Ziurys et al. 2007). A fit to three transitions of PN resulted in $f \sim 4 \times 10^{-8}$ for a source size of $1''$. The column density for PN is $N_{\text{tot}} \sim 3.4 \times 10^{15} \text{ cm}^{-2}$ with $T_{\text{rot}} \sim 17 \text{ K}$.

The derived source sizes, column densities, and fractional abundances are listed in Table 2. The dipole moments used for PN, HCP and CP were 2.75 D, 0.39 D and 0.86 D, respectively (Pickett et al. 1998; Müller et al. 2005; Rohlfsing & Almlöf 1988).

5. DISCUSSION

5.1. Active Phosphorus Chemistry in Circumstellar Envelopes

The detection of HCP and PN in another circumstellar envelope, CRL 2688, coupled with the results in IRC +10216 (CP, PN, HCP: Guélin et al. 1990; Agúndez et al. 2007) and VY CMa (PN, PO: Ziurys et al. 2007; Tenenbaum et al. 2007), suggest that gas-phase phosphorus chemistry in these types of objects may be relatively complex. Phosphorus as an element is not particularly abundant, as mentioned, and it is thought to be refractory, as suggested by condensation models (Lodders & Fegley 1999). Moreover, this element is formed primarily in neon-burning of massive stars, where it is released during Type II SNe (Clayton 2003). Therefore, there should be little overproduction of phosphorus in IRC +10216 or CRL 2688.

Because VY CMa is quite massive, and is thought to be on the track to becoming a supernova (Richards, Yates & Cohen 1998), there may be some enhancement of this element in this object, depending on the degree of dredge-up. Measurements of the $^{12}\text{C}/^{13}\text{C}$ ratio towards this source imply a ratio near 7 (Milam, Ziurys and Woolf, in preparation), suggesting that considerable mixing from the stellar interior may have occurred. How this process affects the phosphorus abundance is unknown.

Assuming solar abundance ($\text{P}/\text{H} \sim 3 \times 10^{-7}$), and neglecting the possible presence of other P-bearing species, about 11% of the available phosphorus is in gas-phase molecules towards IRC +10216, but about 80% in CRL 2688. In VY CMa, the percentage is $\sim 43\%$. The higher amounts of gas-phase phosphorus in CRL 2688 and VY CMa may result from the energetic outflows present in both these sources (Humphreys et al. 2007; Skinner et al. 1997), which could be destroying phosphorus-bearing grains. Both PN and PO, however, appear to arise from the more quiescent wind in VY CMa, as opposed to the red- and blue-shifted flows which apparently correlate with sporadic mass-loss events (see Ziurys et al. 2007). In CRL 2688, the suggestion of asymmetries in the profiles of HCP and PN may link these species in part to some of the fast winds in this object, but higher sensitivity spectra and/or maps are needed to examine this possibility more thoroughly. Alternatively, IRC +10216 may contain additional but unknown molecular forms of phosphorus. Further observations may yield additional species that raise the gas-phase component of this element.

5.2. Theoretical Predictions of Phosphorus-Bearing Molecules

The current models of circumstellar phosphorus chemistry available in the literature use the same approach: certain species are formed at LTE near the stellar photosphere, as “parent molecules”; as these compounds flow into the outer envelope, photochemistry creates radicals

and ions. In the oxygen-rich model of Willacy and Millar (1997), LTE chemistry produces a single important parent molecule, PH_3 , which then reacts to create PH , PH_2 , P , P^+ and finally PO at radii of $r \sim 10^{16}$ - 10^{17} cm. PH_3 and P^+ remain the most abundant species, with $f \sim 3 \times 10^{-8}$, relative to H_2 . The peak abundance for PO is $f \sim 3 \times 10^{-10}$. The computations of MacKay and Charnley (2001) consider both the carbon- and oxygen-rich cases. For the C-rich envelope, these authors predict HCP as the exclusive parent species, which photodissociates to create CP , P and P^+ again at radii of 10^{16} - 10^{17} cm. In the O-rich scheme, the only major parent molecule is PS , which leads to the photodissociation products P , P^+ and PO at similar radii. The maximum abundance of PO is $f \sim 10^{-9}$ at $r \sim 2 \times 10^{16}$ cm.

A more recent model by Agúndez et al. (2007) predicts a somewhat different set of abundances. In the O-rich case, PO is the most prevalent species at ~ 2 stellar radii (R_*) with $f \sim 10^{-7}$, and PS attaining an equivalent abundance at $\sim 3 R_*$. Beyond a radius of $\sim 4 R_*$, P_4O_6 becomes the only significant phosphorus carrier. The abundance of PN never exceeds $f \sim 10^{-10}$. In the carbon-rich scenario, the Agúndez et al. (2007) model predicts HCP to be the major phosphorus-bearing species at $r \leq 10 R_*$, with $f \sim 10^{-7}$. Following the chemistry through the envelope, HCP gradually reacts to form CP , HC_3P , and PN at radii of 10^{16} - 10^{17} cm, with $f(\text{CP}) \sim 3 \times 10^{-9}$ and $f(\text{PN}) \sim 2 \times 10^{-9}$. The abundance of HCP then drops to $f \sim 10^{-8}$. All molecules are photodissociated at $r \sim 10^{17}$ cm.

For comparison, LTE abundance calculations for P-containing species were carried out in this work, using an updated model of Tsuji (1973). The computations were done for O-rich (solar: $\text{C}/\text{O} \sim 0.5$) and C-rich ($\text{C}/\text{O} \sim 1.5$) abundances, over the range of temperatures from 600-3000 K with a particle density of $n \sim 10^{11} \text{ cm}^{-3}$. The results of these calculations are presented in Figure 5. The condensation temperature of schreibersite ($[\text{Fe},\text{Ni}]_3\text{P}$), the main solid-state carrier

of phosphorus, is ~ 1800 K at these pressures (Lodders & Fegley 1999). At this temperature, carbon-rich LTE chemistry predicts $f(\text{HCP}) \sim 10^{-8}$, with $f(\text{CP}) \sim f(\text{PN}) \sim 3 \times 10^{-10}$. In the O-rich model, PO is the main phosphorus species with $f \sim 5 \times 10^{-8}$, followed by PN and PS, both with $f \sim 5 \times 10^{-10}$.

5.3. Comparison with Observations

In IRC +10216, the behaviours of both HCP and CP are well-predicted by the model of Agúndez et al. (2007). The observed abundance of HCP is $f \sim 3 \times 10^{-8}$, with $r \sim 11''$ or 2.5×10^{16} cm ($\sim 380 R_*$), while $f(\text{CP}) \sim 4 \times 10^{-9}$, having a shell distribution with $r \sim 13''$ (3×10^{16} cm). On the other hand, PN has $f \sim 3 \times 10^{-10}$ – about an order of magnitude less than the Agúndez et al. (2007) prediction. However, this abundance matches the LTE value calculated here at 1800 K (see Figure 5). This result suggests that PN is not produced by non-equilibrium photochemistry in the outer envelope of IRC +10216, but instead is created close to the star under LTE conditions. The abundance then “freezes out” until the molecule is photodissociated or condensed. The PN line profiles are consistent with a spherical distribution, supporting the “freeze-out” scenario.

In CRL 2688, the abundances of PN and HCP are both about one order of magnitude higher than in IRC +10216, but the PN/HCP ratio is roughly the same (~ 0.01 - 0.02). Both HCP and PN have extended distributions with radii of $\sim 1.3 \times 10^{17}$ cm ($1.3 \times 10^4 R_*$), consistent with an older, larger shell. To a first approximation, the chemistry of these two species mimics that of IRC +10216, with LTE formation, but at a lower condensation temperature of ~ 1600 K instead of 1800 K (see Figure 5). The shock activity in this post-AGB envelope may be keeping material from condensing onto grains longer than in IRC +10216, lowering the effective condensation temperature. However, the PN abundance from the model at the lower temperature

is still about an order of magnitude too low. Perhaps a more active photochemistry is also contributing to the formation of PN in CRL 2688, caused by the more advanced stage of mass-loss, which has exposed a hotter star.

In VY CMa, PN and PO have abundances of 4×10^{-8} and 9×10^{-8} in a 1'' region. At the distance of this object, this distribution corresponds to a radius of $r \sim 10^{16}$ cm, or $\sim 75 R_*$. The abundance of PO in VY CMa is very well predicted by the LTE model at 1800 K (see Figure 5). However, the prediction of PN is about two orders of magnitude too low. Even at its maximum calculated value at 1000 K, the abundance of PN only reaches $\leq 10^{-9}$ – about a factor of 15 less than that observed.

Given the assumed solar abundance of 3×10^{-7} , not all the phosphorus in VY CMa is confined to PO. According to the LTE calculations, PS is the next important sink for this element. Yet, this radical has yet to be observed in VY CMa. SiS is quite abundant in the spherical wind of this object, with $f \sim 10^{-6}$ (Ziurys et al. 2007). Along with CS, it may be consuming the majority of the gas-phase sulfur, with little remaining for PS. As a consequence, phosphorus is available to create additional PN. A sensitive astronomical search for PS in VY CMa would certainly help in understanding the complete phosphorus chemical network.

5.4. Phosphorus vs. Nitrogen Chemistry

To a first approximation, the chemistry of phosphorus and nitrogen should be fairly similar in circumstellar shells; phosphorus lies directly below nitrogen in the same column of the periodic table, with similar chemical properties. However, the refractory nature of phosphorus may also affect the comparative gas-phase chemistries between the two atoms.

A comparison of HCP/CP and HCN/CN might be enlightening. The distribution of HCN and CN in IRC +10216 has been mapped in detail by Dayal and Bieging (1995) with the BIMA

interferometer. These authors then modeled the observed distributions and determined fractional abundances for both species. The HCN distribution has a peak abundance of $f \sim 3.1 \times 10^{-5}$ and a source radius of $\sim 11''$, while CN has a maximum concentration of $f \sim 3.9 \times 10^{-6}$ and a peak radius of $r \sim 12.5''$. In comparison, the distributions for HCP and CP correspond to radii of $r \sim 11''$ and $r \sim 13''$, respectively, using the same radiative transfer model. Furthermore, the CN/HCN abundance ratio is 0.13 (Dayal & Bieging 1995), while that for CP/HCP is ~ 0.17 . These results suggest that the chemistry of phosphorus is similar to that of nitrogen, at least in IRC +10216.

It should also be noted that the solar P/N ratio ~ 0.003 and the HCP/HCN ratio in IRC +10216 is ~ 0.001 . The relatively close agreement between the two ratios implies a lack of major nitrogen enrichment in this object. Therefore, PN may represent an avenue by which to estimate the N_2 abundance. Assuming $PN/N_2 \sim P/N$, the N_2 abundance in IRC +10216 is $\sim 1 \times 10^{-7}$. LTE models have predicted higher values of $f(N_2) \sim 10^{-5}$ - 10^{-4} (McKay & Charnley 2001; Lafont, Lucas & Omont 1982). The lower value inferred from PN suggests that the majority of the nitrogen in IRC +10216 is locked into HCN.

6. CONCLUSIONS

Phosphorus chemistry appears to be relatively active in both O- and C-rich circumstellar envelopes. Several new species have been found that are not obviously present in molecular clouds, despite the low abundance of phosphorus. While CP is primarily the photodissociation product of HCP in carbon-rich shells, the abundance of PN may principally reflect LTE chemistry in the inner envelope. In the O-rich case, PO appears to be the dominant carrier of phosphorus, although PN is fairly abundant as well. A wider range of sources clearly needs to be

investigated for phosphorus-bearing compounds, as well as observations of possible new P-containing species.

Acknowledgements: We would like to thank the ARO operators and engineering staff for enabling these observations. Additionally, we would like to acknowledge J.H. Biegging and M. Tafalla for use of their radiative transfer code. This research was supported by NSF grant ASF 0607803 and based on work supported by the National Aeronautics and Space Administration through the NASA Astrobiology Institute under Cooperative Agreement CAN-02-OSS-02 issued through the Office of Space Science. DTH is supported by an NSF Astronomy and Astrophysics Postdoctoral Fellowship under award AST-0602282. EDT acknowledges financial support from the NSF Graduate Research Fellowship Program.

REFERENCES

- Agúndez, M. & Cernicharo, J. 2006, ApJ, 650, 374
- Agúndez, M., Cernicharo, J., & Guélin, M. 2007, ApJ, 662, L91
- Arnett, D. 1996, *Supernovae and Nucleosynthesis*, (Princeton: Princeton University Press)
- Biegging, J.H. & Tafalla, M. 1993, AJ, 105, 576
- Cernicharo, J., Guélin, M., & Kahane, C. 2000, A&AS, 142, 181
- Clayton, D. 2003, *Handbook of Isotopes in the Cosmos*, (Cambridge: Cambridge University Press)
- Cox, P., Lucas, R., Huggins, P.J., Forveille, T., Bachiller, R., Guilloteau, S., Maillard, J.P., & Omont, A. 2000, A&A, 353, L25
- Cox, P., et al. 1997, A&A, 321, 907
- Dayal, A. & Biegging, J.H. 1995, ApJ, 439, 996

- Fukasaku, S., Hirahara, Y., Masuda, A., Kawaguchi, K., Ishikawa, S., Kaifu, N., & Irvine, W.M. 1994, *ApJ*, 437, 410
- Grevesse, N. & Sauval, A.J. 1998, *SSRv*, 85, 161
- Guélin, M., Cernicharo, J., Paubert, G., & Turner, B.E. 1990, *A&A*, 230, L9
- Guélin, M., Muller, S., Cernicharo, J., Apponi, A.J., McCarthy, M.C., Gottlieb, C.A., & Thaddeus, P. 2000, *A&A*, 363, L9
- Highberger, J.L., Thomson, K.J., Young, P.A., Arnett, D., & Ziurys, L.M. 2003, *ApJ*, 593, 393
- Humphreys, R.M., Helton, L.A., & Jones, T.J. 2007, *AJ*, 133, 2716
- Keady, J.J., Hall, D.N.B., & Ridgway, S.T. 1988, *ApJ*, 326, 832
- Kemper, F., Stark, R., Justtanont, K., de Koter, A., Tielens, A.G.G.M., Waters, L.B.F.M., Cami, J., & Dijkstra, C. 2003, *A&A*, 407, 609
- Lafont, S., Lucas, R., & Omont, A. 1982, *A&A*, 106, 201
- Lebouteiller, V., Kuassivi, & Ferlet, R. 2005, *A&A*, 443, 509
- Lodders, K. & Fegley Jr., B. 1999, in *IAU Symp. 191, Asymptotic Giant Branch Stars*, ed. T. Le Bertre, A. Lèbre, & C. Waelkens (San Francisco: ASP), 279
- Maciá, E. 2005, *Chem. Soc. Rev.* 34, 691
- MacKay, D.D.S. & Charnley, S.B. 2001, *MNRAS*, 325, 545
- Monnier, J.D., Tuthill, P.G., Lopez, B., Cruzalebes, P., Danchi, W.C., & Haniff, C.A. 1999, *ApJ*, 512, 351
- Müller, H.S.P., Schlöder, F., Stutzki, J., & Winnewisser, G. 2005, *J. Mol. Struct.*, 742, 215
- Pasek, M.A. & Lauretta, D.S. 2005, *Astrobiology*, 5, 515
- Pickett, H.M., Poynter, R.L., Cohen, E.A., Delitsky, M.L., Pearson, J.C., & Müller, H.S.P. 1998, *J. Quant. Spectrosc. & Rad. Transfer*, 60, 883

- Richards, A.M.S., Yates, J.A., & Cohen, R.J. 1998, MNRAS, 299, 319
- Rieu, N.-Q., Graham, D., & Bujarrabal, V., 1984, A&A, 138, L5
- Rohlfing, C.M. & Almlöf, J. 1988, Chem. Phys. Lett., 147, 258
- Skinner, C.J., et al. 1997, A&A, 328, 290
- Sopka, R.J., Olofsson, H., Johansson, L.E.B., Nguyen, Q.-Rieu, & Zuckerman, B. 1989, A&A, 210, 78
- Tenenbaum, E.D., Woolf, N.J., & Ziurys, L.M. 2007, ApJ, in press
- Toboła, R., Kłos, J., Lique, F., Chałasiński, G., & Alexander, M.H. 2007, A&A, 468, 1123
- Truong-Bach, Morris, D., Nguyen-Q-Rieu, & Deguchi, S. 1990, A&A, 230, 431
- Tsuji, T. 1973, A&A, 23, 411
- Turner, B.E. & Bally, J. 1987, ApJ, 321, L75
- Turner, B.E., Tsuji, T., Bally, J., Guélin, M., & Cernicharo, J. 1990, ApJ, 365, 569
- Willacy, K. & Millar, T.J. 1997, A&A, 324, 237
- Young, K., Serabyn, G., Phillips, T.G., Knapp, G.R., Guesten, R., & Schulz, A. 1992, ApJ, 385, 265
- Ziurys, L.M. 1987, ApJ, 321, L81
- Ziurys, L.M., Milam, S.N., Apponi, A.J., & Woolf, N.J. 2007, Nature, 447, 1094

FIGURE CAPTIONS

Figure 1: Spectra obtained for PN and HCP towards CRL 2688, using the ARO 12m and SMT telescopes. The right panel displays the $J=4\rightarrow 3$, $6\rightarrow 5$, and $7\rightarrow 6$ transitions of HCP at 160, 240, and 280 GHz, which all display a slight asymmetric “U”-shape. The left panel shows the $J=2\rightarrow 1$, $3\rightarrow 2$, and $5\rightarrow 4$ transitions of PN at 94, 141, and 235 GHz. The $J=3\rightarrow 2$ line of PN is contaminated by $^{30}\text{SiC}_2$, but the other two transitions are fairly flat-topped, considering the signal-to-noise ratios. The PN $J=2\rightarrow 1$ and $J=3\rightarrow 2$ as well as the HCP $J=4\rightarrow 3$ lines were obtained with the 12m telescope, while the other spectra were measured at the SMT. All spectra were obtained with 1 MHz resolution. These measurements are clear evidence that these two P-bearing compounds are present towards CRL 2688.

Figure 2: The identical set of spectra as in Figure 1, but observed towards IRC +10216. In this source, all lines display a flat-topped profile indicating optically thin, unresolved emission. The $J=3\rightarrow 2$ line of PN (left panel) appears as a shoulder on the $^{30}\text{SiC}_2$ feature. All data were taken with 1 MHz resolution.

Figure 3: Spectra of the $J=5.5\rightarrow 4.5$ (top panel) and the $J=4.5\rightarrow 3.5$ (lower panel) fine structure components of the $N=5\rightarrow 4$ transition of CP observed with the SMT at 238 GHz towards IRC +10216. Each component consists of two hyperfine lines which are split by no more than 3 MHz, and hence do not impact the line profiles. The $J=5.5\rightarrow 4.5$ line is severely contaminated by the two fine structure components of $^{13}\text{CCCCCH}$, as indicated by the arrows. The $J=4.5\rightarrow 3.5$ line profile appears “U”-shaped, indicating thin, resolved emission. These data were measured with 1 MHz filters and smoothed to a 2 MHz resolution.

Figure 4: Spectra of PN observed towards VY CMa. The $J=5\rightarrow 4$ and $6\rightarrow 5$ transitions were measured with the SMT at 235 and 282 GHz, respectively, with a resolution of 1 MHz. The $J=3\rightarrow 2$ line at 141 GHz was obtained at the 12m and observed with 2 MHz resolution. The line profiles are triangular shaped, tracing a roughly ellipsoidal wind in VY CMa. (The $J=5\rightarrow 4$ spectrum was previously published in Ziurys et al. (2007).)

Figure 5: LTE abundances relative to the total hydrogen ($H_2 + H + H^+$) as a function of temperature for the phosphorus chemical network, predicted using a modified version of the model by Tsuji (1973). Calculations were made for the O-rich ($C/O \sim 0.5$; top panel) and C-rich ($C/O \sim 1.5$; lower panel) cases at a density of $n \sim 10^{11} \text{ cm}^{-3}$. At the phosphorus condensation temperature of 1800 K, HCP is the dominant species in the carbon-rich model, while PO is for the oxygen-rich prediction.

Table 1: Observations of Phosphorus Species Towards Circumstellar Envelopes^{a)}

Source	Molecule	Transition	Frequency (MHz)	η_b or η_c	θ_b (")	T_A^* or T_R^* (K)	$\Delta V_{1/2}$ (km s ⁻¹)	V_{LSR} (km s ⁻¹)	$\int T_A^* \Delta V_{1/2}$ (K km s ⁻¹)
CRL 2688 ^{c)}	PN	J = 2→1	93979.8	0.88	67	0.004 ± 0.003	31.9 ± 6.4	-36.8 ± 6.2	0.054
		J = 3→2 ^{b)}	140967.8	0.76	44	0.007 ± 0.003	35.7 ± 6.4	-37.6 ± 6.4	0.090
		J = 5→4	234935.7	0.78	32	0.007 ± 0.005	32.0 ± 2.6	-37.4 ± 2.6	0.197
HCP	J = 4→3	159802.6	0.72	39	0.009 ± 0.006	37.6 ± 3.8	-34.0 ± 3.8	0.255	
	J = 6→5	239693.8	0.78	31	0.015 ± 0.009	35.0 ± 2.5	-35.9 ± 2.5	0.361	
	J = 7→6	279634.7	0.78	27	0.022 ± 0.010	35.3 ± 3.2	-34.4 ± 3.2	0.591	
IRC+10216 ^{e)}	PN	J = 2→1	93979.8	0.88	67	0.006 ± 0.001	28.7 ± 6.4	-27.5 ± 6.4	0.156
		J = 3→2 ^{b)}	140967.8	0.76	44	0.008 ± 0.004	34.0 ± 8.5	-24.0 ± 8.5	0.168
		J = 5→4	234935.7	0.78	32	0.008 ± 0.003	29.4 ± 2.6	-27.3 ± 2.6	0.179
HCP	J = 4→3	159802.6	0.72	39	0.007 ± 0.003	24.5 ± 3.8	~27	~27	0.168
	J = 5→4	199749.4	0.78	38	0.008 ± 0.005	~27	~27	~27	0.188
	J = 6→5	239693.8	0.78	31	0.016 ± 0.005	27.5 ± 2.2	-26.6 ± 2.2	0.428	
CP	N = 5→4	J = 7→6	279634.7	0.78	27	0.022 ± 0.008	27.9 ± 2.1	-27.1 ± 2.1	0.593
		J = 5.5→4.5 ^{d)}	238856.5	0.78	32	0.009 ± 0.002	37.5 ± 7.5	-27.4 ± 7.5	0.390
		J = 4.5→3.5	238303.1	0.78	32	0.005 ± 0.002	27.6 ± 5.0	-27.2 ± 2.5	0.154
VY CMa ^{d)}	PN	J = 3→2	140967.8	0.76	44	0.002 ± 0.001	~40	~40	0.255
		J = 5→4	234935.7	0.78	32	0.009 ± 0.004	37.1 ± 5.1	16.7 ± 5.1	0.369
		J = 6→5	281914.1	0.78	27	0.011 ± 0.006	34.1 ± 4.2	18.6 ± 4.2	0.380

^{a)} All data measured with the SMT except the J=2→1, 3→2 lines of PN and the J=4→3 line of HCP, which were observed with the 12m.

^{b)} η_b and T_A^* for SMT measurements and η_c and T_R^* for 12m data.

^{c)} $\alpha = 21^h02^m18.7^s$, $\delta = 36^\circ41'38''$ (B1950.0).

^{d)} Blended feature (see text).

^{e)} $\alpha = 09^h45^m14.8^s$, $\delta = 13^\circ30'40''$ (B1950.0).

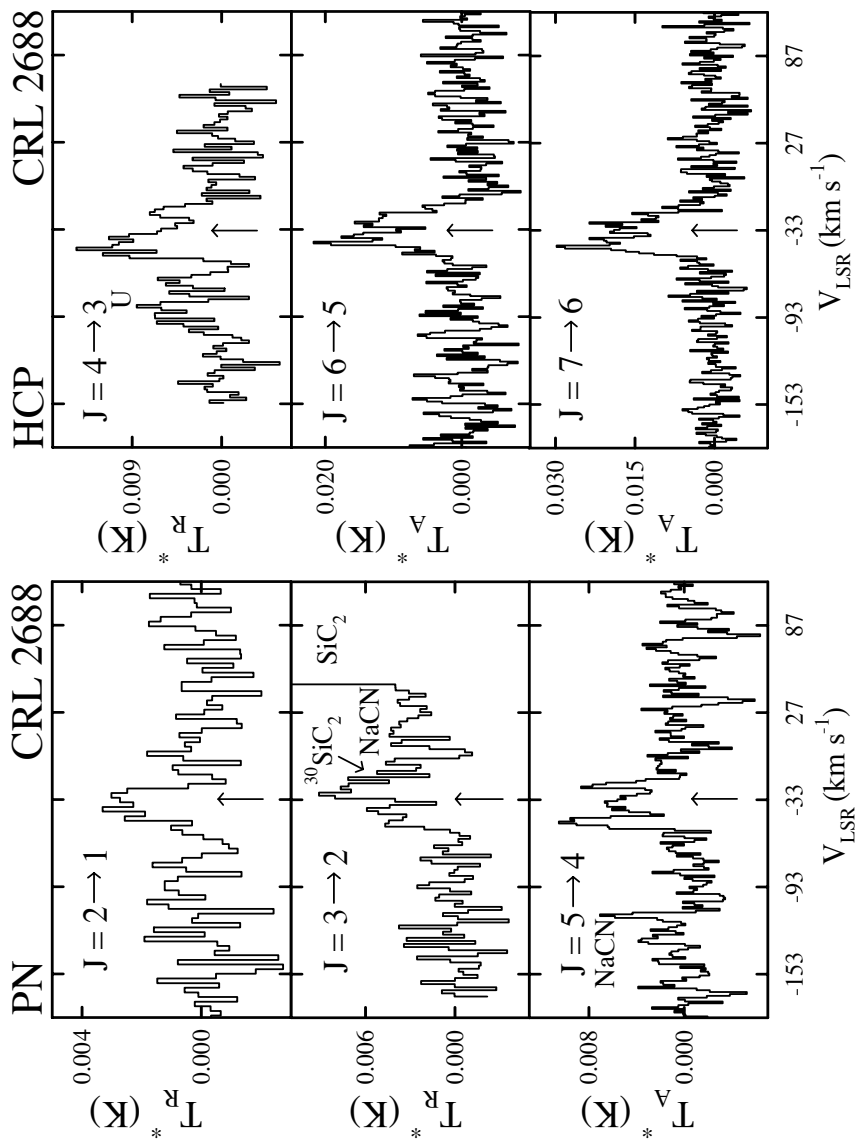
^{f)} $\alpha = 07^h20^m54.7^s$, $\delta = -25^\circ40'12''$ (B1950.0).

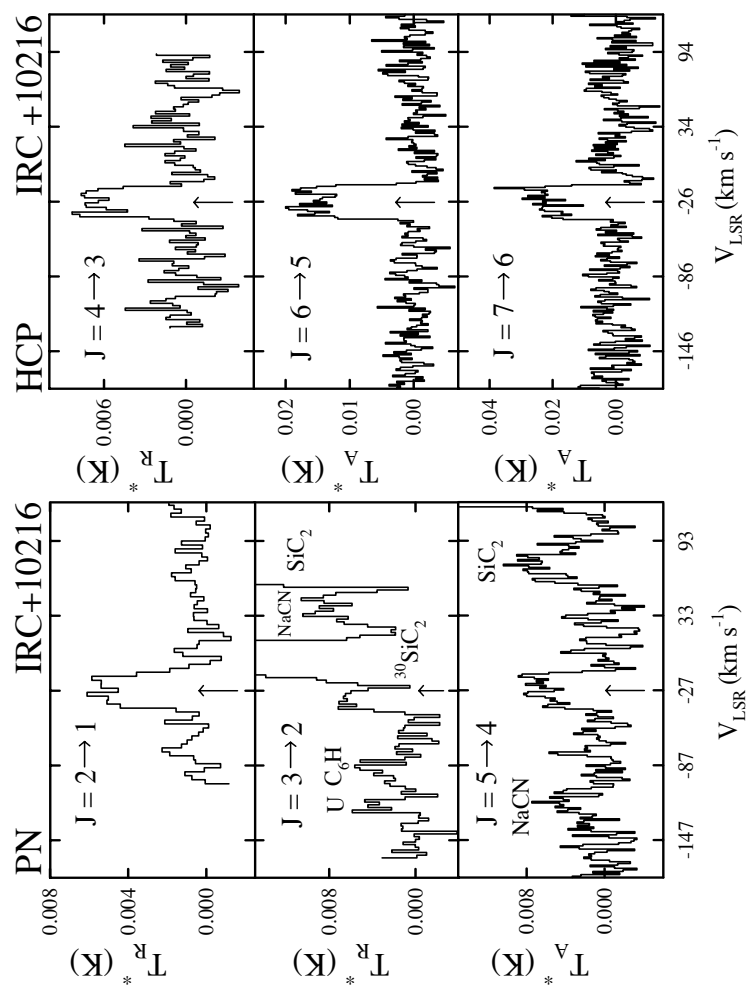
Table 2: Column Densities and Abundances of Circumstellar Phosphorus-Bearing Molecules

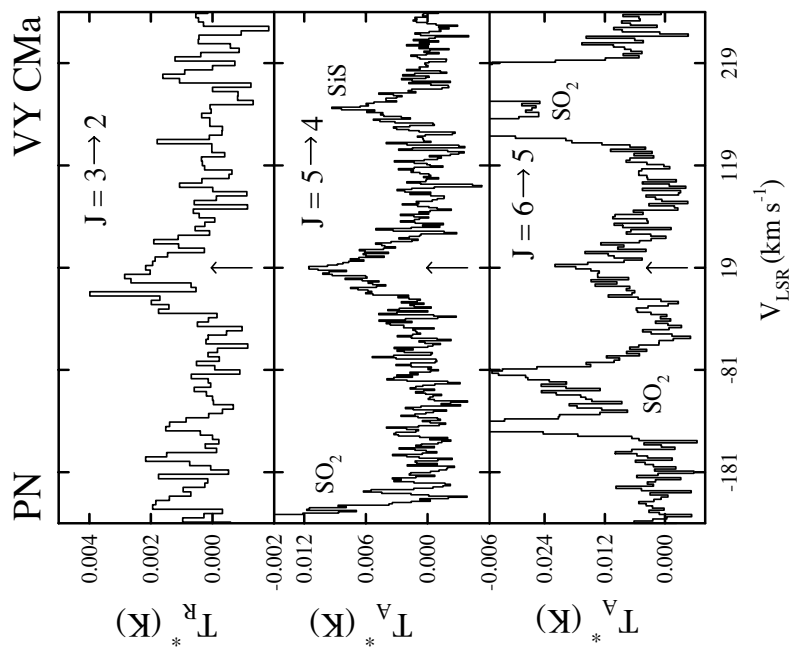
Source	Molecule	θ_s (")	N_{rot} (cm^{-2})	T_{rot} (K)	f (X/H ₂)
VY CMa	PN	1	3.4×10^{15}	17	4×10^{-8}
	PO	1	2.8×10^{15}	45	9×10^{-8}
CRL 2688	PN	8-20	$0.5\text{-}2.8 \times 10^{13}$	16-18	$3\text{-}5 \times 10^{-9}$
	HCP	8-12	$0.6\text{-}1.4 \times 10^{15}$	31-32	2×10^{-7}
IRC +10216	PN	36	6.3×10^{12}	11	3×10^{-10}
	HCP	22	$1.0\text{-}1.4 \times 10^{14}$	81-111	3×10^{-8}
	CP	26 (shell) ^{a)}	5×10^{12}	50 ^{b)}	5×10^{-9}

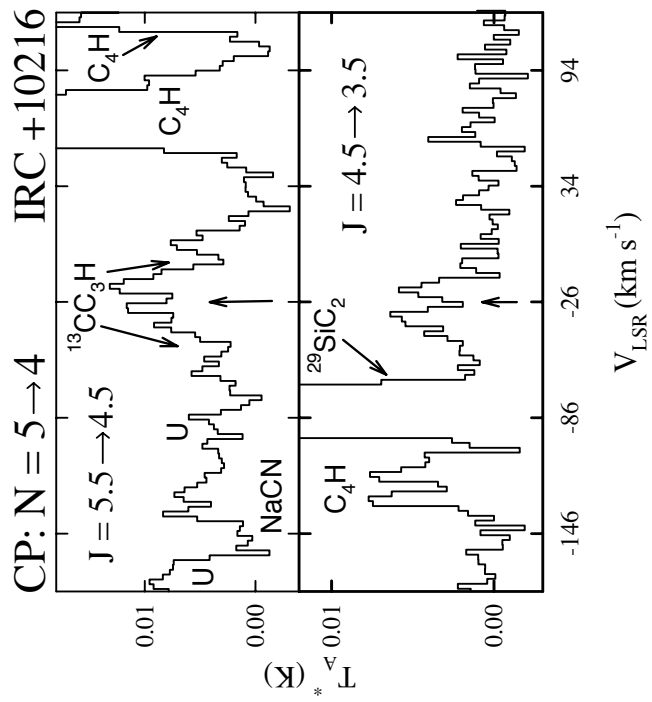
^{a)} Inner radius $r \sim 4''$ and outer radius $r \sim 22''$.

^{b)} Assumed T_{rot} .









APPENDIX G

THE DISTRIBUTION, EXCITATION AND FORMATION OF COMETARY
MOLECULES: METHANOL, METHYL CYANIDE AND ETHYLENE GLYCOL

Anthony J. Remijan, Stefanie N. Milam, Maria Womack, A. J. Apponi, L. M. Ziurys, Susan Wycoff, M. F. A'Hearn, S. Choi, Imke de Pater, J. R. Forster, D. N. Friedel, C. Kraybill, Patrick Palmer, L. E. Snyder, J. M. Veal, L. M. Woodney, & M. C. H. Wright
2007, *Astrophys. J.*, submitted.

**THE DISTRIBUTION, EXCITATION AND FORMATION OF
COMETARY MOLECULES: METHANOL, METHYL
CYANIDE AND ETHYLENE GLYCOL**

Anthony J. Remijan¹, Stefanie N. Milam², Maria Womack³, A. J. Apponi², L. M. Ziurys²,
Susan Wycoff⁴, M. F. A'Hearn⁵, S. Choi³, Imke de Pater⁶, J. R. Forster⁶, D. N. Friedel⁷, C.
Kraybill⁶, Patrick Palmer⁸, L. E. Snyder⁷, J. M. Veal^{7,9}, L. M. Woodney¹⁰, & M. C. H.
Wright⁶

ABSTRACT

We present an interferometric and single dish study of cometary molecules toward comets C/1995 O1 (Hale-Bopp) and C/2002 T7 (LINEAR) using the Berkeley-Illinois-Maryland Association (BIMA) interferometer at 3 mm and the Arizona Radio Observatory (ARO) 12 m telescope at 2 mm. For Comet Hale-Bopp, both the single-dish and interferometer observations indicate an excitation

¹National Radio Astronomy Observatory, 520 Edgemont Road, Charlottesville, VA 22901
email: aremijan@nrao.edu.

²NASA Astrobiology Institute, Department of Chemistry, Department of Astronomy, and Steward Observatory, 933 North Cherry Avenue, University of Arizona, Tucson, AZ 85721; email: stemil@as.arizona.edu, lziurys@as.arizona.edu, aapponi@as.arizona.edu.

³Department of Physics and Astronomy, St. Cloud State University, St. Cloud, MN 56301; mwomack@stcloudstate.edu.

⁴Department of Physics and Astronomy, Arizona State University, Tempe AZ 85287; wycoff@asu.edu.

⁵Department of Astronomy, University of Maryland, College Park MD 20742-2421 email: ma@astro.umd.edu

⁶Department of Astronomy, University of California, Berkeley, CA 94720 email: imke@floris.berkeley.edu, rforster@astro.berkeley.edu, ckraybill@astro.berkeley.edu, wright@astro.berkeley.edu

⁷Department of Astronomy, 1002 W. Green St., University of Illinois, Urbana IL 61801 email: friedel@astro.uiuc.edu, snyder@astro.uiuc.edu

⁸Department of Astronomy and Astrophysics, University of Chicago, Chicago, IL 60637 email: ppalmer@oskar.uchicago.edu

⁹Current address: Southwestern College, 900 Otay Lakes Road, Chula Vista, CA 91910; jveal@swc.cc.ca.us.

¹⁰Department of Physics, California State University, San Bernardino, CA 92407; woodney@csusb.edu.

– 2 –

temperature of CH₃OH of 105(10) K and a total column density of $9(1)\times 10^{14}$ cm⁻² from the BIMA array data and $2.4(1)\times 10^{14}$ cm⁻² from the 12 m data. Using a Monte Carlo solution to the Haser model assuming a nuclear origin for CH₃OH, we find a total CH₃OH production rate of $\sim 5.9(1)\times 10^{29}$ s⁻¹ from the BIMA array data and $\sim 1.5(1)\times 10^{29}$ s⁻¹ from the 12 m data at ~ 1 AU. Furthermore, from the aperture synthesis observations of CH₃OH, we find the distribution of CH₃OH is well described by a spherical outflow with an increase in column density and production closer to the cometary nucleus. Also, the maps show no evidence of enhanced production of CH₃OH in the extended coma or from jets. For the single-dish observations of Comet LINEAR we find an excitation temperature of CH₃OH of 35(5) K and a total column density of $2.2(1)\times 10^{13}$ cm⁻² for a total CH₃OH production rate of $\sim 2.0(1)\times 10^{27}$ s⁻¹ at ~ 0.3 AU which is nearly an order of magnitude smaller than what was determined by Remijan et al. (2006). We find similar results for the excitation and distribution of cometary CH₃CN. For Comet Hale-Bopp, the single-dish observations indicate an excitation temperature of CH₃CN of 200(10) K and a total column density of $2.6(1)\times 10^{12}$ cm⁻² for a total CH₃CN production rate of $\sim 1.7(1)\times 10^{27}$ s⁻¹ at ~ 1 AU. The observations of both these species suggest a nuclear origin of CH₃OH and CH₃CN. Finally, the non-detection of a previously identified transition of cometary (CH₂OH)₂ toward Comet Hale-Bopp with the 12 m telescope indicates a compact distribution of emission on the order of $<9''$ (<8500 km). This supports the hypothesis that the cometary production of (CH₂OH)₂ is direct sublimation off cometary ices from the nucleus. Furthermore, if the production of CH₂OHCHO is from direct dissociation of (CH₂OH)₂, this would imply an extended distribution of CH₂OHCHO in the outer coma of comets similar to the distribution of H₂CO. Thus, high resolution ($<10''$) observations would detect the emission from (CH₂OH)₂ but would be insensitive to the more extended distribution of CH₂OHCHO. Our data continue to support the theories that CH₃OH, CH₃CN and (CH₂OH)₂ are parent nuclear species and that CH₂OHCHO would be a daughter species present in the extended coma from direct dissociation of (CH₂OH)₂.

Subject headings: astrobiology - comets: individual (HALE BOPP (C/1995 01), LINEAR (C/2002 T7)) - molecular processes - techniques: interferometric - radio lines: solar system

– 3 –

1. INTRODUCTION

Over the last several years, complementary observations of comets with both single-dish telescopes and interferometric arrays have shed new light on the abundance, production rate, distribution and formation of molecules in cometary comae. Milam et al. (2006) started this investigation by searching for the origins of cometary formaldehyde (H_2CO) by comparing observations with both the former NRAO 12m single-dish telescope and the Berkeley-Illinois-Maryland Association (BIMA) array. From this investigation toward Comet C/1995 O1 (Hale-Bopp), the authors clearly showed that the distribution and abundance of H_2CO must be coming from a source other than the comet nucleus. The extended source of H_2CO may be due to an enhanced production of H_2CO from grains consisting of silicates and organic material or possibly from the photodissociation of a larger parent species such as methanol (CH_3OH) (Hudson, Moore & Cook 2005). Furthermore, toward Comet C/2002 T7 (LINEAR), a second velocity component of H_2CO was found further suggesting comet fragmentation and an enhanced production of H_2CO in the outer coma. (Milam et al. 2006). These complementary observations, however, are very difficult to attain as most of the molecular observations toward comets are performed using solely single-dish telescopes or interferometric arrays depending on the telescope available at the time as the comet approaches the inner solar system and perigee.

As an example, Remijan et al. (2006) performed an interferometric survey of several molecular species, including large organic molecules, toward Comet LINEAR and Comet C/2001 Q4 (NEAT) using solely the BIMA array. In this case, the authors were successful in detecting one transition and mapping the distribution of cometary CS and CH_3OH toward Comet LINEAR and CH_3OH toward Comet NEAT. Using $3(1,3)-4(0,4)$ A⁺ transition of CH_3OH near 107.0 GHz and adopting a temperature of 115 K from observations by other authors (DiSanti et al. 2004; Magee-Sauer et al. 2004; Küppers et al. 2004), Remijan et al. (2006) found a total CH_3OH column density of $1.4(3)\times 10^{14}$ cm^{-2} , a production rate of $7.5(15)\times 10^{27}$ s^{-1} for a total production rate ratio with respect to H_2O of $3.8(8)\times 10^{-2}$. Based on this lone observation of CH_3OH toward Comet LINEAR, it was designated as a Comet Hale-Bopp class comet which is overly rich in both HCN and CH_3OH . As previous observations of Comet Hale-Bopp have clearly demonstrated, it was unique in not only its rich molecular complexity (see e.g. Bockelée-Morvan et al. 2000; Crovisier et al. 2004) but also in the abundance and production rate of complex molecular species. Thus, to observe a comet in the same class as Hale-Bopp based on the CH_3OH production rate was quite encouraging and yet the search for other complex molecules, clearly detected in Comet Hale-Bopp, in Comet LINEAR yielded all negative results (Remijan et al. 2006). Therefore, it appears that the production rate of CH_3OH determined by Remijan et al. (2006) was overestimated, however no other observations of CH_3OH or any other large molecular species were available.

– 4 –

Attempts to detect rotational transitions of large cometary molecules have taken place since the 1970's. The first attempt to detect rotational transitions of cometary CH_3OH was done toward Comet Kohoutek by Mango et al. (1974) between 22.2 and 25.2 GHz using the 26 m radio telescope of the U.S. Naval Research Lab at Maryland Point Observatory. They searched for the 7(2,5)-7(1,6) E transition at 25.1 GHz and the 2(2,0)-2(1,1) E transition at 24.9 GHz. No detection of either transition was made, but they calculated an upper limit to the column density of $N_T < 9 \times 10^{14} \text{ cm}^{-2}$ and a production rate of $Q_o < 1 \times 10^{29} \text{ s}^{-1}$ for a destruction radius of 10^4 km . (For $r_o = 10^5 \text{ km}$, $Q_o < 2 \times 10^{28} \text{ s}^{-1}$). Colom et al. (1990) reported the first millimeter detection of cometary CH_3OH towards Comet Brorsen-Metcalf (1989 o) and Comet Austin (1989 c1). The $J=3-2$ transition complex of CH_3OH near 145.1 GHz was detected using the IRAM 30m radio telescope. Similarly, the first reported, yet unconfirmed, detection of cometary methyl cyanide (CH_3CN) was by Ulich & Conklin (1974) toward Comet Kohoutek, in the $\nu_8=1$ vibrationally excited state. Bockelée-Morvan et al. (1987) attempted to confirm the existence of cometary CH_3CN using the IRAM 30m telescope toward Comets P/Giacobini-Zinner 1984e and P/Halley 1982i. No detection was made and an upper limit to the column density of $N_T < 3.3 \times 10^{10} \text{ cm}^{-2}$ and production rate of $Q_o < 1.6 \times 10^{26} \text{ s}^{-1}$ was reported. The first confirmed detection of cometary CH_3CN was toward Comet Hale-Bopp (Biver et al. 2002). Finally, the only detection of cometary ethylene glycol $[(\text{CH}_2\text{OH})_2]$ was toward Comet Hale-Bopp (Crovisier et al. 2004). With an abundance of 0.25% with respect to water, it is the third most abundant molecule in cometary comae after CH_3OH and H_2CO . However, given the fact that most of the H_2CO is coming from an extended source in the outer coma, $(\text{CH}_2\text{OH})_2$ can be considered the second most abundant molecule contained in cometary ices after CH_3OH .

Each of these complex molecular species are believed to be parent species which are directly sublimated off the cometary ices in the nucleus. Bockelée-Morvan et al. (1987) comment that from the upper limits of CH_3CN and HC_3N , both species are not more abundant than HCN in cometary comae. Also, CH_3CN and HC_3N may be parent species that would add to the abundance of the CN radical as well as C_2 in the coma. The authors point out however, that the upper limits to the observations do not preclude the possibility of CH_3CN and HC_3N having their own parent species. In addition, the high abundance of $(\text{CH}_2\text{OH})_2$ observed in Comet Hale-Bopp at high spatial resolution also strongly suggests a nuclear origin. However, no complementary observations of either CH_3CN or $(\text{CH}_2\text{OH})_2$ were available to follow-up on the claimed distribution of these species in the coma and their possible formation pathways.

In this paper, we report on complementary observations of cometary CH_3OH , CH_3CN and $(\text{CH}_2\text{OH})_2$ taken with the Berkeley-Illinois-Maryland Association (BIMA) array near

– 5 –

Hat Creek, California¹¹ and the former NRAO 12 m telescope on Kitt Peak, AZ. From these observations, we continued to investigate the abundance, production rate, distribution and formation of organic species in comets by directly comparing the observations taken of common molecular species with different telescopes. We were successful in confirming the hypothesis that CH₃OH, CH₃CN and (CH₂OH)₂ are primarily parent species by direct sublimation of cometary ices contained in the nucleus. We also posit the existence of cometary glycolaldehyde (CH₂OHCHO) as well as the type of experiment needed to confirm its presence in cometary comae and why it eluded detection using the IRAM 30 m (Crovisier et al. 2004).

2. OBSERVATIONS

2.1. BIMA Array

Our observations of Comet Hale-Bopp with the BIMA array constitute the earliest detection and measurements of cometary CH₃OH with an interferometer. The CH₃OH observations were taken using the “soft” C configuration of the BIMA array from 1997 March 24 to April 03. Data were acquired in the interferometric (cross-correlation) mode with nine antennas. The minimum baseline for these observations was ~ 15 m and the maximum baseline was ~ 139 m. The average resulting full width half power synthesized beam size was $\sim 8'' \times 10''$ for all the observations. Table 1 lists the observational parameters of the BIMA array observations. The first column lists rest frequency (GHz). The second column lists the sources used to calibrate the antenna based gains. The absolute amplitude calibration of these sources was based on planetary observations and is accurate to within $\sim 20\%$. The third column lists the observation date. The fourth and fifth columns list the geocentric distance and heliocentric distance of Comet Hale-Bopp (AU). The sixth column gives the average beamsize ($'' \times ''$) for the observation. The final column lists the approximate 1σ channel rms noise level (Jy beam⁻¹) in the window containing the CH₃OH transition. The spectral windows containing the transitions had a bandwidth of 25 MHz and was divided into 256 channels for a spectral resolution of 0.1 MHz per channel. This channel rms reported in table 1 is based on this observing setup. However, to increase the signal-to-noise ratio in each window, the data were averaged over two channels giving an effective spectral resolution of 0.2 MHz per channel. All data were first corrected to JPL ephemeris reference orbit 139. The

¹¹Operated by the University of California, Berkeley, the University of Illinois, and the University of Maryland with support from the National Science Foundation. 121°28'8".0 West, 40°49'4".1 North; altitude 1033 m

– 6 –

data were then combined and imaged using the MIRIAD software package (Sault, Teuben & Wright 1995). To include all the data from the comet with multiple tracks, the data were inverted in u - v space. The resulting synthesized beamsize was determined from the combined dataset.

2.2. Arizona Radio Observatory 12 m

Observations of CH_3OH , CH_3CN and $(\text{CH}_2\text{OH})_2$ toward Comet Hale-Bopp were taken during three observing runs on 1997 Mar 10, 11, and 20 using the former NRAO 12 m telescope on Kitt Peak, AZ¹². Observations of CH_3OH toward Comet LINEAR were conducted on 2004 May 20 also using the 12 m telescope, now operated by the ARO. Dual-channel SIS mixers were used for the 2 mm observations, operated in single-sideband mode with ~ 20 dB image rejection. The backend used for the presented observations were individual filter banks with 500 kHz resolution. The spectral temperature scale was determined by the chopper-wheel method, corrected for forward spillover losses, given in terms of T_R^* (K). The radiation temperature, T_R , is then derived from the corrected beam efficiency, η_c , where $T_R = T_R^*/\eta_c$. A two body ephemeris program was used to determine the comet’s position using the orbital elements provided by D. Yeomans (1996, private communication) of JPL. Focus and positional accuracy were checked periodically on nearby planets or maser sources. Data were taken in the position-switched mode with the off position 30’ west in azimuth. Observing frequencies (GHz), dates, comet distances (AU), beam size (θ_b), the diameter of the projected beam size on the comet (km), and the corrected main beam efficiency (η_c) at the times of observations are listed in Table 2, respectively.

Table 3 lists the transitions and molecular line parameters of CH_3OH , CH_3CN and $(\text{CH}_2\text{OH})_2$ selected for this survey. The first column lists the molecule; the second column, the transition; the third column, the calculated rest frequency and its 2σ standard deviation; the fourth column, the product of the line strength and the square of the relevant dipole moment; and the fifth column, the upper state energy level of each transition. All spectral line data were taken from the Spectral Line Atlas of Interstellar Molecules (SLAIM) available at www.splatalogue.net and the Cologne Database for Molecular Spectroscopy (Müller et al. 2005).

¹²The National Radio Astronomy Observatory is a facility of the National Science Foundation operated under cooperative agreement by the Associated Universities, Inc. The Kitt Peak 12 m telescope is currently operated by Arizona Radio Observatory (ARO), Steward Observatory, University of Arizona, with partial funding from the Research Corporation.

- 7 -

3. RESULTS

Figure 1 shows the maps and spectra of CH₃OH taken toward Comet Hale-Bopp with the BIMA array. Figure 1(a) shows the map of the 2(0,2)-1(0,1) E transition of methanol in contours averaged over 2 days, 1997 March 27 and 31. Notice that the CH₃OH emission is larger than the synthesized beam of the BIMA Array (located at the bottom left of each map) and follows the general position angle of the synthesized beam. The line segment in the image is the projection from the predicted location of the cometary nucleus toward the sun. The coordinates are given in offset arcseconds centered on the comet nucleus. Figure 1(b) shows the spectra of 4 methanol transitions near 96.7 GHz (Table 3) including the 2(0,2)-1(0,1) E transition. The spectrum has been hanning smoothed over 3 channels and the resulting 4 transitions are located at velocities of \sim -43, -10, 0 and 7 km s⁻¹. The rms noise level is \sim 0.05 Jy beam⁻¹ (indicated by the vertical bar at the left of the spectrum). The spectral line labels correspond to the rest frequency located at the top left of the spectral window for a cometocentric velocity of 0 km s⁻¹. The dashed line is centered on this velocity. Figure 1(c) shows the map of the 3(1,3)-4(0,4) A⁺ transition of methanol in contours averaged over 3 days, 1997 March 26 and April 2-3. Figure 1(d) shows the spectrum of this methanol transition near 107.0 GHz (Table 3). Note that the two CH₃OH emission contours shown in figures (a) and (c) are centered on the predicted location of the comet nucleus with no apparent offset. The maps are similar to each other and similar to the average of the March HCN BIMA Array contours given by Veal et al. (2000), but without the pronounced evidence for the jets as observed in HCN, beyond the 3 σ detection level (§4.2). Furthermore, from figures 1(b) and (d), there is no apparent second velocity component of CH₃OH nor is the emission offset from the cometocentric rest velocity of 0 km s⁻¹. Figure 2 shows the spectra of the five 2 mm transition of CH₃OH detected toward Comet Hale-Bopp with the ARO 12 m telescope (Table 3). The UT date and spectral line quantum numbers of each observed transition are located in the top left corner of the plotted spectrum. As in the BIMA spectra, the spectral line labels correspond to the rest frequency of that transition for a cometocentric velocity of 0 km s⁻¹. The CH₃OH detections reported here are all E-type transitions. Similarly, Figure 3 shows the spectrum of a cluster of E-type transitions of CH₃OH centered around 157.3 GHz toward Comet LINEAR with the ARO 12 m telescope. In both the single dish Hale-Bopp and LINEAR data, there is no apparent second velocity component of CH₃OH. However, unlike the BIMA array Hale-Bopp data, the 12 m Hale-Bopp data are shifted to lower frequencies by \sim -0.45 MHz (\sim +0.9 km s⁻¹). This may indicate a red-shifted acceleration of the cometary CH₃OH in the outer coma with respect to the comet's velocity or that there was a small error in the ephemeris correction at the time of the observations. Finally, Figure 4 shows the spectrum of the $J = 8 - 7$ ($K=0 - 7$) transitions of the symmetric top species methyl cyanide (CH₃CN) toward Comet

– 8 –

Hale-Bopp taken with the ARO 12 m telescope. However, the spectral line labels of the $K=5-7$ transitions should be viewed with some caution (§4.1). CH_3CN and other symmetric tops have properties that make them ideal probes of physical conditions of astronomical environments (see e.g. Araya et al. 2005; Remijan et al. 2004; Hofner et al. 1996). Similar to the CH_3OH emission, there is no apparent additional velocity components of CH_3CN and the emission is offset from the cometocentric rest velocity by ~ -0.45 MHz ($\sim +0.9$ km s $^{-1}$).

Table 4 lists the molecular species that were searched for toward Comets Hale-Bopp and LINEAR at or near the cometocentric velocity (0 km s $^{-1}$). Least square Gaussian fits were made for each spectral line in order to obtain the peak intensities and line-widths for the detected transitions or the 1σ rms noise level is given for those transitions not detected. In table 4, the first column lists the molecule; the second column, the associated transition. The fourth and fifth column list the fitted line intensities and full power line widths at half maximum intensities, respectively. Finally, the first entries in column six list the total beam averaged column density of the molecular species listed in column two based on ALL the detected transitions of that species. Columns seven and eight list the production rate of each molecular species and the relative production rate ratio with respect to water, respectively, based on the column density measurement listed in column six. The formalism for determining column densities and production rates are described in §4.1.

4. ANALYSIS AND DISCUSSION

4.1. EXCITATION, ABUNDANCES AND PRODUCTION RATES

Determining the best temperature, column density, and production rates of cometary molecules are important because they are essential to understanding the formation of cometary species including the role of grains in molecule formation and whether warm or cold gas phase chemistry is important to the production of daughter species in the coma. In order to determine the temperatures and column densities of the region of the coma that contains the CH_3OH and CH_3CN emission, we assume that each region has uniform physical conditions, that the populations of the energy levels can be characterized by a Boltzmann distribution and finally, that the emission is optically thin. We did not utilize the rotational temperature diagram method because even small errors in the intensities and widths of inherently weak spectral lines can cause large errors in determining the temperature and total column density (see e.g. Snyder et al. 2005). Therefore, it is better to generate a model spectrum using the above conditions by varying the temperature and total column density and then comparing the model fit to the observed data.

– 9 –

From Remijan et al. (2003), the total beam-averaged column density obtained with an interferometer is:

$$N_T = 1.22 \times \frac{\int \Delta I dv}{B \theta_a \theta_b} \frac{Q_r e^{(E_u/T_{ex})}}{\nu^3 S \mu^2} \times 10^{20} \text{ cm}^{-2}. \quad (1)$$

Equation (1) can then be solved for $\int \Delta I dv$ which is the product of the spectral line intensity (Jy beam⁻¹) and line width (km s⁻¹). The variables that need to be input into Equation (1) to evaluate the spectral line integrated intensity include the total beam-averaged column density, N_T and the excitation temperature, T_{ex} . Also, Q_r is the rotational partition function; $S \mu^2$ is the product of the transition line strength and the square of the dipole moment (Debye²); and E_u is the upper rotational energy level (K). Finally, θ_a and θ_b are the FWHM beam widths (arcsec) (Table 1) and $B = \Omega_S / [\Omega_B + \Omega_S]$ is the beam filling factor where Ω_B is the solid angle subtended by the synthesized beam of the interferometer and Ω_S is the solid angle subtended by the source emission. In the extreme case where the source emission is much greater than the synthesized beam, $B=1$.

For the ARO 12 m observations, following the formalism outlined by Milam et al. (2006), the total beam-averaged column density of a molecular species obtained with a single element radio telescope is given by:

$$N_T = (1.8 \times 10^{14}) \frac{Q_r e^{E_u/T_{ex}}}{B \nu S \mu^2} \frac{\left\{ \frac{\Delta T_A^* \Delta V}{\eta_c} \right\}}{\left\{ 1 - \frac{(e^{(4.8 \times 10^{-5}) \nu / T_{ex}} - 1)}{(e^{(4.8 \times 10^{-5}) \nu / T_{bg}} - 1)} \right\}} \text{ cm}^{-2}. \quad (2)$$

In both equations, the line shapes are assumed to be Gaussian. In equation 2, η_c is the telescope beam efficiency (Table 2); $\Delta T_A^* \Delta V$ is once again the integrated line intensity and is the product of the spectral line intensity (mK) and line width (km s⁻¹) and T_{bg} is assumed to be 2.7 K, the cosmic background temperature.

Figure 5 shows the results of the model fit (red trace) applied to the CH₃OH BIMA array data (blue sawtooth). The BIMA array data are well fit by an excitation temperature of $T_{ex}=105(5)$ K and a total beam-averaged column density of $N_T=9(1) \times 10^{14} \text{ cm}^{-2}$ assuming that the CH₃OH emission is extended beyond the 10."33 \times 8."46 average synthesized beam of the BIMA array. Similarly, Figure 6 shows the results of the model fit applied to the CH₃OH ARO 12 m data. These data are also well fit by an excitation temperature, $T_{ex}=105(5)$ K but a lower total beam-averaged column density of $N_T=2.4(1) \times 10^{14} \text{ cm}^{-2}$. In nearly all cases, the estimated excitation temperature and column densities for each instrument, match the observational data. Using a Monte Carlo solution to the Haser model assuming a nuclear

– 10 –

origin for CH₃OH, we find a total CH₃OH production rate of $\sim 5.9(1) \times 10^{29} \text{ s}^{-1}$ from the BIMA array data and $\sim 1.5(1) \times 10^{29} \text{ s}^{-1}$ from the 12 m data at $\sim 1 \text{ AU}$. In Figure 6, there is a slight discrepancy between the CH₃OH lines at 151.86 GHz where the model predicts a higher line intensity than what is actually observed and the model underestimates the line intensity at 148.11 GHz and 145.76 GHz. However, given the S/N ratio of all the passbands where these lines are observed, the model does a very good job in predicting the expected line intensity of each CH₃OH transition observed with the ARO 12 m telescope. The same cannot be said for the BIMA array data, however. In Figure 5, the 96.7445 GHz, 2(0,2)-1(0,1) E CH₃OH transition is clearly underestimated from our model fit. Moreover, we have varied the temperature and column density predictions over many decades of values to try and match the relative line intensity ratios between the CH₃OH transitions observed at 96 and 107 GHz but no combination of temperature and column density can account for the higher observed intensity of the 96.7445 GHz, 2(0,2)-1(0,1) E transition. In addition, there is no reason the other CH₃OH transitions detected should have a higher optical depth or that the 96.7445 GHz CH₃OH transition should have a higher line intensity due to some maser process. Also, given the S/N ratio in the passband, the higher observed intensity cannot be explained by random fluctuations in the noise. Thus, it appears this transition must be contaminated by a spectral feature from an unknown molecule.

To evaluate the spectral line profiles of the 96.7 GHz CH₃OH transitions taken with the BIMA array, we compared the observed Hale-Bopp spectrum to the spectrum of the Orion KL Compact Ridge also using the BIMA array. Figure 7 shows the spectrum of the 96.7 GHz CH₃OH transitions taken toward the Orion KL Compact Ridge. In this case, the 96.7445 GHz, 2(0,2)-1(0,1) E transition is NOT observed at a greater intensity relative to the other detected transitions. The red trace is the model spectra of these data generated from a best fit by an excitation temperature, $T_{ex}=190(10) \text{ K}$ and a total beam-averaged column density, $N_T=1.3(1) \times 10^{17} \text{ cm}^{-2}$. This is once again assuming that the CH₃OH emission is much greater than the $12'' \times 10''$ synthesized beam of the BIMA array and a FWHM line width of 3.3 km s^{-1} . Thus, there is no contaminating emission feature from any known interstellar molecular species that is adding to the intensity of the 2(0,2)-1(0,1) E transition. Searching the publically available spectral line catalogs, the only transition of a well known cometary molecule that has been unambiguously detected toward Comet Hale-Bopp that could interfere with the line intensity of the CH₃OH transition is the 20(5,16) $v=0$ -19(6,13) $v=0$ transition of (CH₂OH)₂ at a rest frequency of 96.745 GHz (Müller et al. 2005). In order to add to the emission from the CH₃OH transition at 96.7445 GHz, the (CH₂OH)₂ would need to be shifted to a lower frequency by 0.5 MHz (or a higher velocity of 1.6 km s^{-1}). Yet there is no indication of any velocity shift of any other transitions of (CH₂OH)₂ toward comet Hale-Bopp (Crovisier et al. 2004) and this would be the first detection of the *gGg* form of (CH₂OH)₂

– 11 –

ever detected in an astronomical environment. Thus, further scrutiny to the nature of the anomalously high emission detected from the $2(0,2)-1(0,1)$ E CH_3OH transition is necessary but we cannot rule out the emission from $(\text{CH}_2\text{OH})_2$ at this time.

To compare the excitation of CH_3OH to other molecular species, Figure 8 shows the best model fit to the $J = 8 - 7$ ($K=0 - 4$) transitions of methyl cyanide (CH_3CN) toward Comet Hale-Bopp taken with the ARO 12 m telescope near 147.2 GHz. In addition, these data overlap with the $(\text{CH}_2\text{OH})_2$ IRAM 30 m survey of Crovisier et al. 2004. From that survey, the detected transitions of $15(7,9) v=0-14(7,8) v=1$ and $15(7,8) v=0-14(7,7) v=1$ at 147.13 GHz are nearly frequency coincident and show up as one feature given the resolution of their passband. Also, the detected transitions have an overall line intensity equal to that of the $J = 8(4) - 7(4)$ transition of CH_3CN . From the ARO 12 m data, we identify many of the same spectral features present in the IRAM 30 m survey but we do not detect any emission feature from the two transitions of $(\text{CH}_2\text{OH})_2$ beyond the 1σ detection limit. Once again, the red trace is the model of the CH_3CN data which is best fit by an excitation temperature, $T_{ex}=200(10)$ K and a total beam-averaged column density, $N_T=2.6(1) \times 10^{12} \text{ cm}^{-2}$. In this case, the $K = 7$ line is not detected beyond the 1σ detection limit which indicates that the chance coincidence of the emission feature near the $K = 7$ rest frequency is due to random noise in the passband. The $K = 6$ line is detected but only at the 1σ level and the $K = 5$ and 4 lines appear to be underestimated from our model fit but it is clear from this spectrum, and from the IRAM 30 m spectrum, that there are more lines of other molecular species in this passband in addition to CH_3CN . Moreover, given the noise level, the $K = 4$ line can clearly have a contribution to noise adding to its intensity. Using the Haser model assuming a nuclear origin for CH_3CN , we find a production rate of $\sim 1.7(1) \times 10^{27} \text{ s}^{-1}$ at ~ 1 AU. From the CH_3CN , CH_3OH and $(\text{CH}_2\text{OH})_2$ 12 m data, it is clear we are probing different physical environments in the coma of Comet Hale-Bopp. A discussion of the distribution of these molecular species is in §4.2.

Finally, Figure 9 shows the best model fit to the cluster of E-type transitions of CH_3OH centered around 157.26 GHz toward Comet LINEAR with the ARO 12 m telescope. There have been very few molecule observations toward Comet LINEAR. The most complete survey of molecular species toward Comet LINEAR was by Remijan et al. (2006) using the BIMA array. From that survey, the authors detected the $3(1,3)-4(0,4)$ A^+ transition of CH_3OH with a synthesized beam size of $22.''3 \times 16.''9$. Using an excitation temperature of 115 K (DiSanti et al. 2004; Magee-Sauer et al. 2004; Küppers et al. 2004), they determined a total beam-averaged column density of $N_T=1.4(3) \times 10^{14} \text{ cm}^{-2}$. However, from figure 9, the 12 m CH_3OH data are best fit by an excitation temperature of $T_{ex}=35(5)$ K and a total beam-averaged column density of $N_T=2.2(1) \times 10^{13} \text{ cm}^{-2}$ and thus, a production rate of $\sim 2.0(1) \times 10^{27} \text{ s}^{-1}$ at 0.3 AU. Therefore, to reassess the column density measurement determined by Remijan

– 12 –

et al. (2006), we used the best model fit parameters of temperature and column density from the 12 m data to predict the line intensity of the 3(1,3)-4(0,4) A⁺ transition detected by the BIMA array. Figure 10 shows the results of this analysis. Figure 10(a) is the hanning smoothed data and figure 10(b) is the raw data. These data are the same that are plotted in figure 1 of Remijan et al. (2006) for Comet LINEAR. It is quite clear that assuming an excitation temperature of 115 K for CH₃OH was incorrect and the determined column density and production rate of CH₃OH toward Comet LINEAR was overestimated by almost an order of magnitude in that survey. This is once again assuming that the CH₃OH emission is much greater than the 22."3 × 16."9 synthesized beam of the BIMA array and a FWHM line width of 2.0 km s⁻¹.

4.2. DISTRIBUTION OF MOLECULAR SPECIES

We present two complementary sets of data from Comet Hale-Bopp that give great insights into the distribution of cometary CH₃OH, CH₃CN and (CH₂OH)₂. First, it is quite clear from the data presented in Figures 5 and 6 that despite the drastic change in the telescope beam sizes between the BIMA array and the ARO 12 m, we are still sampling a region of the coma that is thermalized to ~105 K. The ratio of areas subtended by the 12 m beam compared to the BIMA array synthesized beam is ~21 × which corresponds to a change in the physical sampled size scale from ~40000 km with the 12 m telescope to ~8500 km with the BIMA array. From a comparison of the CH₃OH data from the BIMA array and 12 m, there is an enhancement of the column density and thus production of CH₃OH at smaller coma radii. This is further supported by the BIMA array maps of CH₃OH shown in Figure 1. Figure 11(a) once again shows the distribution of the 3(1,3)-4(0,4) A⁺ transition of CH₃OH around Comet Hale-Bopp. In figure 11(b), is a model fit to the data shown in (a). The model was generated assuming a spherical Haser model of parent species sublimating off the comet's nucleus. From the data in (a), the scale length of the distribution of CH₃OH around the nucleus is measured to be ~10". Using this scale length and the MIRIAD task IMGGEN, a Haser model distribution of CH₃OH was generated which was then convolved with the synthesized beam of the BIMA array (shown at the bottom left of each panel in figure 11). The residuals obtained by subtracting the model from the data are shown in figure 11(c). While it appears that there may be a more extended distribution of CH₃OH based on the residual data, it is important to note that the contour levels shown in (a) and (b) are 3, 4, 5 and 6 σ ($\sigma=0.05$ Jy beam⁻¹) whereas the data shown in (c), are 1 and 1.5 σ . So, even though there is evidence for a larger distribution of CH₃OH, the data presented in (c) should be viewed with some caution given the relative intensity levels. It also appears that the BIMA array data are well fit by the Haser model so using the VTOV model described

– 13 –

by Friedel et al. (2005) to generate a similar map to compare to the data will be an excellent test of the VTOV model. This analysis is still ongoing.

From the 12 m observations of CH_3CN and the non-detection of $(\text{CH}_2\text{OH})_2$, it appears that the CH_3CN is tracing higher temperature and higher density gas than CH_3OH . In general, because CH_3CN has a larger dipole moment than CH_3OH , its measured rotational temperature should be lower. However, if the overall distribution of CH_3CN is closer to the coma than CH_3OH , then we would measure a higher excitation temperature where it is well known that the temperature of the coma increases with decreasing coma radii (see e.g. Biver et al. 1999). Furthermore, this would also imply that CH_3CN is also a parent species (§4.3). The observed distribution and excitation CH_3CN is very different than that of an extended source of molecular emission which should display a lower temperature from both telescopes as the temperature will fall off from the coma due to adiabatic expansion of the gas. This is further supported by comparing the relative line intensities between the $K=3$ and 4 transitions of CH_3CN from the IRAM 30 m data and what is measured from the ARO 12 m. In general, the 30 m emission features from CH_3CN are 5-10 \times stronger than what is observed from the 12 m. Like the comparison with the BIMA array/12 m data, this implies an enhancement of the CH_3CN column density, and thus production rate, of CH_3CN at smaller coma radii. Finally, from the non-detection of $(\text{CH}_2\text{OH})_2$ in the 12 m observations, it is also apparent that the distribution of $(\text{CH}_2\text{OH})_2$ must also be compact in the cometary coma. Given the line strength of $(\text{CH}_2\text{OH})_2$ in the 30 m spectrum of ~ 0.09 K and a 1σ line intensity of ~ 0.01 K in the 12 m passband, the emission from $(\text{CH}_2\text{OH})_2$ must be on the order of $< 9''$ to not be detected in the 12 m observations, corresponding to a physical size of < 8500 km. High sensitivity, high resolution interferometer observations are necessary to confirm this predicted source size however. Not only does this measurement imply the cometary formation of $(\text{CH}_2\text{OH})_2$ is due to direct sublimation off cometary ices, but also gives insight into the formation and distribution of the related aldehyde species, glycolaldehyde (CH_2OHCHO), in cometary comae (§4.3).

4.3. FORMATION OF COMETARY METHANOL AND OTHER MOLECULAR SPECIES

Given the data presented herein, it is apparent that the combination of single dish and array observations are painting a clearer picture of the formation of molecular species in cometary comae. From the high resolution methanol observations of the BIMA array, it is quite clear that the CH_3OH is either sublimating directly off the cometary ices contained in the nucleus or is formed very deep in the cometary coma. Given the composition of

– 14 –

cometary ices, CH_3OH in the nucleus would be a remnant from the formation of the presolar nebula and, as such, the abundance of methanol in cometary ices is a direct correlation of its formation in interstellar environments. Currently, there are two accepted formation pathways to the production of methanol including the radiative association of $\text{CH}_3^+ + \text{H}_2\text{O} \rightarrow \text{CH}_3\text{OH}_2^+$; followed by recombination with an electron to produce CH_3OH and H and grain surface reactions that involve the repeated hydrogenation of $\text{CO} \rightarrow \text{H} + \text{CO} \rightarrow \text{HCO} + \text{H} \rightarrow \text{H}_2\text{CO}$ which eventually leads to CH_3O and CH_3OH . In either formation pathway, the abundance of cometary CH_3OH would be dominated from the native interstellar environments as our observations show there is no enhancement in the production of CH_3OH in the outer coma as the comet enters the inner solar system. The same argument can be applied to CH_3CN . The accepted route to the formation of CH_3CN in interstellar environments is when CH_3^+ collides with HCN , a collision complex is formed that equilibrates to $\text{CH}_3\text{CNH}^+ + \nu$; then CH_3CNH^+ combines with an electron to form $\text{CH}_3\text{CN} + \text{H}$. Our observations of CH_3CN compared to the complimentary observations from the 30 m support a higher abundance and production rate of CH_3CN closer to the cometary nucleus indicating direct sublimation off cometary ices.

Finally, the non-detection of $(\text{CH}_2\text{OH})_2$ with the ARO 12 m gives tremendous insight into the formation of $(\text{CH}_2\text{OH})_2$ as well as the possibility of detecting CH_2OHCHO . In §4.2, the predicted distribution of $(\text{CH}_2\text{OH})_2$ toward Comet Hale-Bopp was calculated to be $<9''$ (<8500 km). This, once again, suggests direct sublimation of $(\text{CH}_2\text{OH})_2$ off cometary ices or an enhanced production in the inner coma. The evidence for direct sublimation is further supported by the high abundance of $(\text{CH}_2\text{OH})_2$ with respect to CH_3OH and H_2O in cometary ices. However, the question still remains as to how $(\text{CH}_2\text{OH})_2$ gets embedded into icy grain mantles. Currently, there is no accepted gas phase formation mechanism that can lead to the production of $(\text{CH}_2\text{OH})_2$. However, there are several formation pathways using surface chemistry. For example, the formose reaction which can occur on carbonaceous meteorites is a possible pathway to the formation of sugars and sugar alcohols. To form $(\text{CH}_2\text{OH})_2$ and CH_2OHCHO , formaldehyde (H_2CO) reacts with itself in aqueous solution and CH_2OHCHO is produced which can then be hydrogenated to form $(\text{CH}_2\text{OH})_2$ (e.g., see Walker 1975). Charnley (2001) predicts that $(\text{CH}_2\text{OH})_2$ and CH_2OHCHO could be formed by direct hydrogenation reactions starting from ketene (CH_2CO) on grain surfaces. Finally, Hudson & Moore (2000) showed that proton irradiated CH_3OH on icy grain mantles can lead to the formation of $(\text{CH}_2\text{OH})_2$. Thus, there appear to be several ways to form and embed $(\text{CH}_2\text{OH})_2$ into cometary ices so if one or many of these surface reaction networks are correct, the distribution of $(\text{CH}_2\text{OH})_2$ in cometary comae is due to direct sublimation. Once $(\text{CH}_2\text{OH})_2$ is ejected into the coma, it can undergo photodissociation as alcohols, in general, can dissociate into aldehydes. Hudson, Moore & Cook (2005) showed that CH_3OH

– 15 –

can dissociate into H_2CO . Similarly, $(\text{CH}_2\text{OH})_2$ would dissociate into CH_2OHCHO . These dissociation processes could then lead to enhanced abundances of the aldehydes H_2CO and CH_2OHCHO in the outer coma. Evidence for this is overwhelming. It is well known that the bulk of the emission from H_2CO is from an extended source and there are several different theories as to the cause of this enhancement (Milam et al. 2006). Furthermore, H_2CO is only a fraction of the constituent of cometary ices (Crovisier et al. 2004). Thus, if CH_2OHCHO is formed by dissociation of $(\text{CH}_2\text{OH})_2$ in the extended cometary coma, it is not surprising that CH_2OHCHO eluded detection by the 30m or high resolution array observations. Conversely, $(\text{CH}_2\text{OH})_2$ would likely ONLY be detected with large single dish telescopes with small primary beams or high resolution arrays. The best chance of detecting CH_2OHCHO in cometary comae, if it is formed by dissociation of $(\text{CH}_2\text{OH})_2$, is with high sensitivity, moderately sized single-dish observations at high frequencies or by large single-dish telescopes operating at low frequencies. Of course, this can only be tested with observations of new comets with a dedicated search for CH_2OHCHO transitions.

In summary, we presented an interferometric and single dish study of cometary molecules toward comets C/1995 O1 (Hale-Bopp) and C/2002 T7 (LINEAR) using the Berkeley-Illinois-Maryland Association (BIMA) interferometer at 3 mm and the Arizona Radio Observatory (ARO) 12 m telescope at 2 mm. Furthermore, from the combination of the single-dish and aperture synthesis observations of CH_3OH , we find the distribution of CH_3OH toward Comet Hale-Bopp is well described by a spherical outflow with an increase in column density and production closer to the cometary nucleus. Also, the array maps show no evidence of enhanced production of CH_3OH in the extended coma or from jets. The single-dish observations from the ARO 12 m and the IRAM 30 m of CH_3CN also indicate an enhanced abundance and production at smaller coma radii. The observations of both these species suggest a nuclear origin of CH_3OH and CH_3CN . From the single-dish observations of CH_3OH in Comet LINEAR, we find that the total column density and production rate reported by Remijan et al. (2006) is overestimated by nearly an order of magnitude. Finally, the non-detection of a previously identified transition of cometary $(\text{CH}_2\text{OH})_2$ toward Comet Hale-Bopp with the ARO 12 m telescope indicates a compact distribution of emission on the order of $<9''$ (<8500 km). This supports the hypothesis that the cometary production of $(\text{CH}_2\text{OH})_2$ is direct sublimation off cometary ices from the nucleus. Furthermore, if the production of CH_2OHCHO is from direct dissociation of $(\text{CH}_2\text{OH})_2$, this would imply an extended distribution of CH_2OHCHO in the outer coma of comets similar to the distribution of H_2CO . Only with high sensitivity, high resolution interferometer observations can the distribution of $(\text{CH}_2\text{OH})_2$ be truly measured and only through observations of new comets and a dedicated search for CH_2OHCHO transitions can the formation route of both species be determined.

– 16 –

REFERENCES

- Araya, E., Hofner, P., Kurtz, S., Bronfman, L., & DeDeo, S. 2005, *ApJS*, 157, 279
- Biver, et al. 2002, *Earth, Moon, and Planets*, 90, 1, 5
- Bockelée-Morvan, D., Crovisier, J., Despois, D., Forveille, T., Gerard, E., Schraml, J., & Thum, C. 1987, *A&A*, 180, 253
- Bockelée-Morvan, D., et al. 2000, *A&A*, 353, 1101
- Charnley, S. B. 2001, in *The Bridge between the Big Bang and Biology*, ed. F. Giovannelli (Special Vol.; Rome: Consiglio Naz. Ric.), 139
- Colom, P., Despois, D., Bockelée-Morvan, D., Crovisier, J., & Paubert, G. 1990, In *Southwest Research Inst., Workshop on Observations of Recent Comets*, 80
- Crovisier, J., Bockelée-Morvan, D., Biver, N., Colom, P., Despois, D., & Lis, D. 2004, *A&A*, 418, L35
- DiSanti, M. A., Reuter, D. C., Mumma, M. J., Dello Russo, N., Magee-Sauer, K., Gibb, E. L., Bonev, B., & Anderson, W. M. 2004, *DPS Meeting 36*, 23.08
- Hudson, R. L., Moore, M. H., & Cook, A. M. 2005, *Adv. in Space Research*, 36, 183
- Hudson, R. L. & Moore, M. H. 2000, *Icarus*, 145, 661
- Hofner, P., Kurtz, S., Churchwell, E., Walmsley, C. M., & Cesaroni, R. 1996, *ApJ*, 460, 359
- Küppers, M., Hartogh, P., & Villanueva, G. 2004, *DPS Meeting 36*, 25.05
- Magee-Sauer, K., Mumma, M. J., DiSanti, M. A., Russo, N. D., & Rettig, T. W. 1999, *Icarus*, 142, 498
- Mango, S. A., Johnston, K. J., Chui, M. F., Cheung, A. C., & Matsakis, D. 1974, *Icarus*, 23, 590
- Milam et al. 2006, *ApJ*, 649, 1169
- Müller, H. S. P., Schloder, F., Stutzki, J., & Winnewisser, G. 2005, *J. Mol. Struct.*, 742, 215
- Remijan et al. 2006, *ApJ*, 643, 567
- Remijan, A., Sutton, E. C., Snyder, L. E., Friedel, D. N., Liu, S.-Y., & Pei, C.-C. 2005, *ApJ*, 606, 917

– 17 –

- Remijan, A., Snyder, L. E., Friedel, D. N., Liu, S.-Y., & Shah, R. Y. 2003, *ApJ*, 590, 314
- Sault, R. J., Teuben, P. J., & Wright, M. C. H. 1995, *ASP Conf. Ser. 77: Astronomical Data Analysis Software and Systems IV*, 77, 433
- Snyder, L. E., et al. 2005, *ApJ*, 619, 914
- Veal, J. M., Snyder, L. E., Wright, M., Woodney, L. M., Palmer, P., Forster, J. R., de Pater, I., A'Hearn, M. F., & Kuan, Y.-J. 2000, *AJ*, 119, 1498
- Ulich, B. L., & Conklin, E. K. 1974, *Nature*, 248, 121
- Walker, J. F. 1975, *Formaldehyde* (3d. ed.; Huntington: Robert E. Krieger), chap. 8

- 18 -

Table 1. Observational Parameters - BIMA array

Frequency (GHz)	Gain calibrator	Observation date	Δ (AU)	r (AU)	beam ("×")	chan rms (Jy beam ⁻¹)
96.741	0102+584	1997 Mar 27	1.323	0.919	10.8×8.2	0.21
	0102+584	1997 Mar 31	1.344	0.914	9.8×7.8	0.20
107.014	0102+584	1997 Mar 26	1.320	0.921	19.3×6.8	0.43
	0102+584	1997 Apr 02	1.359	0.914	11.7×6.6	0.15
	0102+584	1997 Apr 03	1.367	0.915	16.0×6.4	0.30

– 19 –

Table 2. Observational Parameters - ARO 12m

Frequency (GHz)	Observation date	Δ (AU)	r (AU)	beam (")	D (km)	η_c
Comet Hale-Bopp						
145.766	1997 Mar 20.94	1.318	0.940	43	41105	0.76
147.105 ^a	1997 Mar 20.66	1.318	0.940	43	41105	0.76
148.112	1997 Mar 11.89	1.368	0.989	42	41672	0.76
150.142	1997 Mar 10.71	1.377	0.996	42	41946	0.75
151.860	1997 Mar 20.92	1.318	0.940	41	39193	0.74
157.049	1997 Mar 21.54	1.316	0.936	40	38179	0.72
Comet LINEAR						
157.261 ^b	2004 May 21.80	0.284	0.865	40	8239	0.72

^aThis is an average of the observing frequencies between the $K=7$ and $K=0$ lines of CH_3CN .

^bThis is an average of the observing frequencies of the CH_3OH lines detected in the same spectral passband.

– 20 –

Table 3. Molecular Line Parameters

Molecule	Transition	Frequency (MHz)	$\langle S_{i,j}\mu^2 \rangle$ (Debye ²)	E_u (K)
CH ₃ OH ^a	2(-1,2)-1(-1,1) E	96,739.363(3)	1.2	12.6
	2(0,2)-1(0,1) A ⁺	96,741.377(3)	1.6	7.0
	2(0,2)-1(0,1) E	96,744.549(3)	1.6	20.1
	2(1,1)-1(1,0) E	96,755.507(3)	1.2	28.0
	3(1,3)-4(0,4) A ⁺	107,013.770(13)	3.0	28.4
	16(0,16)-16(-1,16) E	145,766.163(27)	7.0	327.9
	15(0,15)-15(-1,15) E	148,111.919(24)	7.3	290.9
	14(0,14)-14(-1,14) E	150,141.593(22)	7.5	256.3
	13(0,13)-13(-1,13) E	151,860.170(20)	7.6	223.9
	6(0,6)-6(-1,6) E	157,048.586(13)	5.7	61.9
	4(0,4)-4(-1,4) E	157,246.041(14)	4.2	36.4
	1(0,1)-1(-1,1) E	157,270.818(15)	1.5	15.5
	3(0,3)-3(-1,3) E	157,272.320(14)	3.3	27.1
	2(0,2)-2(-1,2) E	157,276.004(14)	2.4	20.1
	CH ₃ CN ^a	8(6)-7(6)	147,072.608(2)	13.7
8(5)-7(5)		147,103.741(1)	19.2	210.5
8(4)-7(4)		147,129.232(1)	23.5	146.2
8(3)-7(3)		147,149.068(1)	27.0	96.1
8(2)-7(2)		147,163.243(1)	29.4	60.4
8(1)-7(1)		147,171.750(1)	31.0	38.9
8(0)-7(0)		147,174.587(1)	31.3	31.8
(CH ₂ OH) ₂ ^b	15(7,9) v=0-14(7,8) v=1	147,131.814(36)	2.5	83.1
	15(7,8) v=0-14(7,7) v=1	147,132.412(36)	2.7	83.1

^aMolecular line parameters of CH₃OH and CH₃CN taken from SLAIM at www.splatalogue.net. $Q_r=1.2T_r^{\frac{3}{2}}$ for CH₃OH and $Q_r=3.9T_r^{\frac{3}{2}}$ for CH₃CN.

^aMolecular line parameters of (CH₂OH)₂ taken from CDMS (Müller et al. 2005).

- 21 -

Table 4. Comet Hale-Bopp and Comet LINEAR Molecular Line Identifications

ν (MHz)	Species	Transition	ΔI	dv (km s ⁻¹)	N_T (cm ⁻²)	Q_p (s ⁻¹)	Q_X/Q_{H_2O}
Comet Hale-Bopp							
BIMA Array (ΔI units of Jy beam ⁻¹)							
96,739.4	CH ₃ OH	2 ₋₁ -1 ₋₁ E	0.31(5)	2.4(2)	9(1)×10 ¹⁴	5.9(1)×10 ²⁹	5.9(1)×10 ^{-2?}
96,741.4	CH ₃ OH	2 ₀ -1 ₀ A+	0.52(5)	2.0(2)			
96,744.5	CH ₃ OH	2 ₀ -1 ₀ E	0.60(5)	2.1(2)			
96,755.5	CH ₃ OH	2 ₁ -1 ₁ E	0.29(5)	3.2(2)			
107,013.8	CH ₃ OH	3 ₁ -4 ₀ A+	1.12(5)	1.9(2)			
ARO 12m (ΔI units of K)							
147,129.2	CH ₃ CN	8(4)-7(4)	0.019(1)	1.6(8)	2.6(1)×10 ¹²	1.7(1)×10 ²⁷	1.7(1)×10 ⁻⁴
147,149.0	CH ₃ CN	8(3)-7(3)	0.054(1)	2.8(8)			
147,163.2	CH ₃ CN	8(2)-7(2)	0.034(1)	3.2(8)			
147,171.7	CH ₃ CN	8(1)-7(1)	0.049(1)	2.4(8)			
147,174.5	CH ₃ CN	8(0)-7(0)	0.051(1)	2.4(8)			
145,766.2	CH ₃ OH	16(0,16)-16(-1,16) E	0.03(2)	2.0(8)	2.4(1)×10 ¹⁴	1.5(1)×10 ²⁹	1.5(1)×10 ⁻²
148,111.9	CH ₃ OH	15(0,15)-15(-1,15) E	0.04(2)	3.0(8)			
150,141.6	CH ₃ OH	14(0,13)-14(-1,14) E	0.04(1)	1.9(8)			
151,860.2	CH ₃ OH	13(0,13)-13(-1,13) E	0.05(1)	2.5(8)			
157,048.6	CH ₃ OH	6(0,6)-6(-1,6) E	0.23(1)	2.4(8)			
147,131.8	(CH ₂ OH) ₂	15(7,*) v=0-14(7,*) v=1	<0.01				
Comet LINEAR							
ARO 12m (ΔI units of K)							
157,246.1	CH ₃ OH	6(0,6)-6(-1,6) E	0.087(1)	1.9(10)	2.2(1)×10 ¹³	2.0(1)×10 ²⁷	6.7(1)×10 ⁻³
157,270.9	CH ₃ OH	1(0,1)-1(-1,1) E	0.051(1)	1.9(10)			
157,272.3	CH ₃ OH	3(0,3)-3(-1,3) E	0.101(1)	1.9(10)			
157,276.0	CH ₃ OH	2(0,2)-2(-1,2) E	0.058(1)	1.9(10)			

– 22 –

Fig. 1.— CH₃OH Survey toward Comet Hale-Bopp with the BIMA array. (a) Emission contours from the 2(0,2)-1(0,1) E transition of CH₃OH at 96.741 GHz. Contours indicate the location of the 2(0,2)-1(0,1) E CH₃OH emission. The contour levels are -0.2, 0.4, 0.6, 0.8, 1.0, and 1.2 Jy beam⁻¹. The synthesized beam of 10''3 × 8''5 is indicated at the bottom left corner. (b) CH₃OH spectrum toward Comet Hale-Bopp (Hanning smoothed over three channels). The rms noise level is ~0.1 Jy beam⁻¹ (indicated by the vertical bar at the left of the spectrum). The spectral line labels correspond to the rest frequency located at the top left of the spectral window for a velocity of 0 km s⁻¹. The dashed line is centered on this velocity. The ordinate of the spectrum ranges from -0.4-1.0 Jy beam⁻¹. (c) Emission contours from the 3(1,3)-4(0,4) A⁺ transition of CH₃OH at 107.014 GHz. Contours indicate the location of the CH₃OH emission averaged between -2 km s⁻¹ and 2 km s⁻¹. The contour levels are -0.05, 0.20, 0.30, 0.40, 0.50, and 0.60 Jy beam⁻¹. The synthesized beam of 10''8 × 7''2 is indicated at the bottom left corner. (d) CH₃OH spectrum toward Comet Hale-Bopp. The rms noise level is ~0.1 Jy beam⁻¹ (indicated by the vertical bar at the left of the spectrum). The spectral line label is the same as in (b).

Fig. 2.— CH₃OH Survey toward Comet Hale-Bopp with the 12 m telescope

Fig. 3.— CH₃OH Survey toward Comet LINEAR with the 12 m telescope

Fig. 4.— CH₃CN Survey toward Comet Hale-Bopp with the 12 m telescope

Fig. 5.— CH₃OH transitions from Comet Hale-Bopp (blue sawtooth) and the model fit to the data (red trace) from the BIMA array data.

Fig. 6.— CH₃OH transitions from Comet Hale-Bopp (blue sawtooth) and the model fit to the data (red trace) from the 12 m data.

Fig. 7.— CH₃OH transitions near 96.7 GHz from Orion KL (blue sawtooth) and the model fit to the data (red trace) from the BIMA array data.

Fig. 8.— CH₃CN transitions from Comet Hale-Bopp (blue sawtooth) and the model fit to the data (red trace) from the 12 m data. The dashed line is centered on the rest frequency of the (CH₂OH)₂ transition detected by the 30 m telescope.

Fig. 9.— CH₃OH transitions from Comet LINEAR (blue sawtooth) and the model fit to the data (red trace) from the 12 m data.

Fig. 10.— CH₃OH transitions from Comet LINEAR (blue sawtooth) and the model fit to the data (red trace) from the BIMA array data.

- 23 -

Fig. 11.— CH_3OH model fit to the BIMA array data.

- 24 -

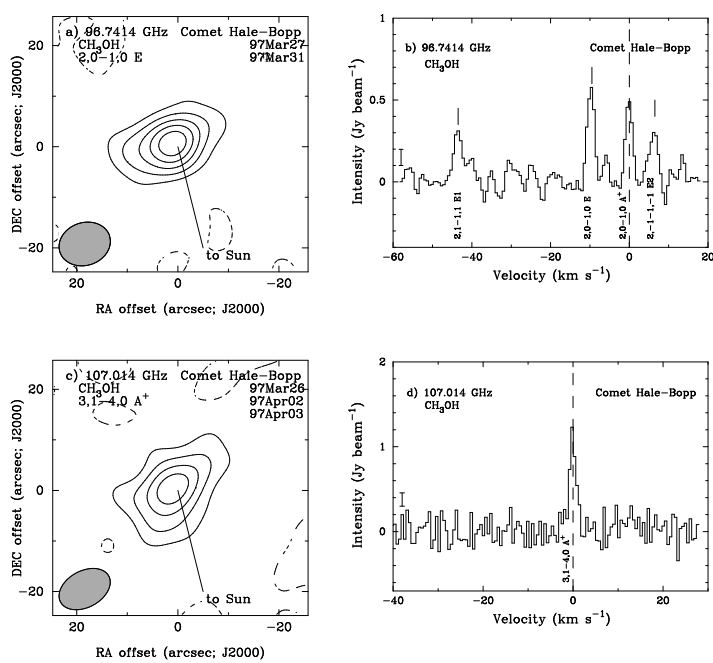


Figure 1.

- 25 -

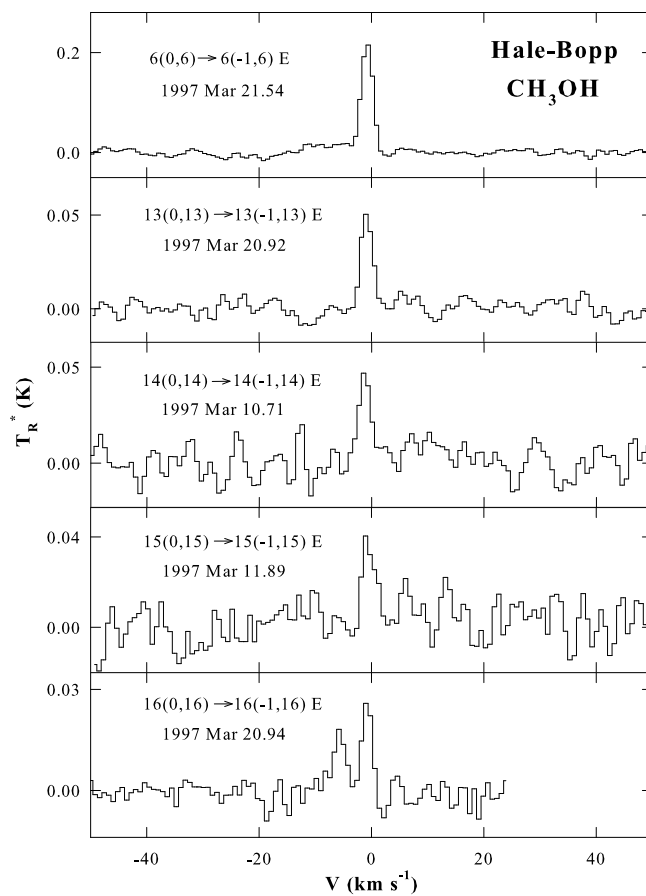


Figure 2.

- 26 -

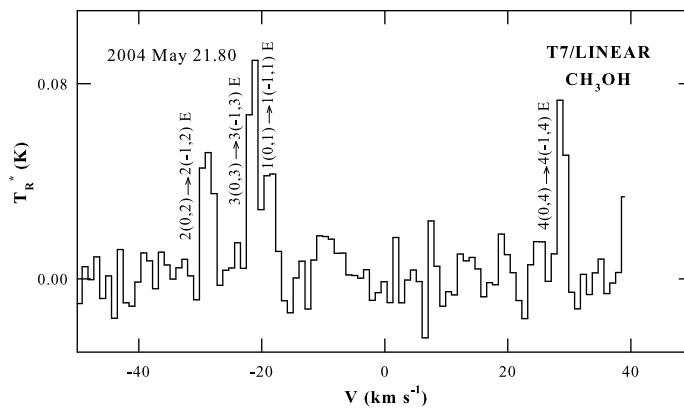


Figure 3.

- 27 -

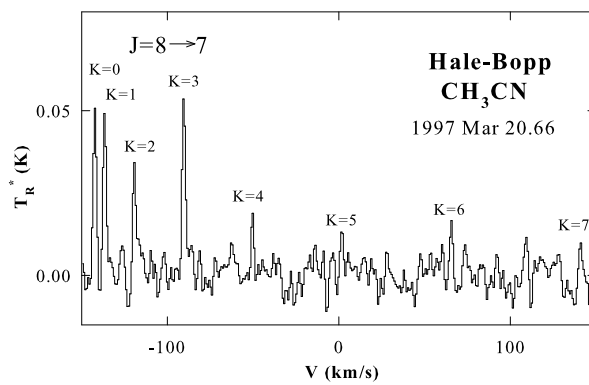


Figure 4.

- 28 -

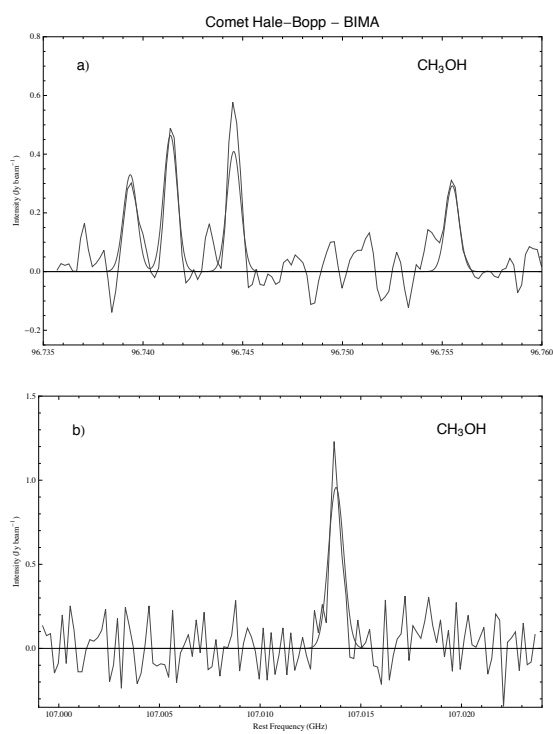


Figure 5.

- 29 -

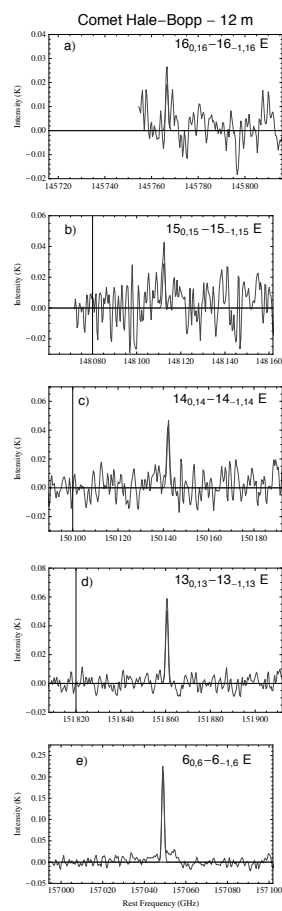


Figure 6.

- 30 -

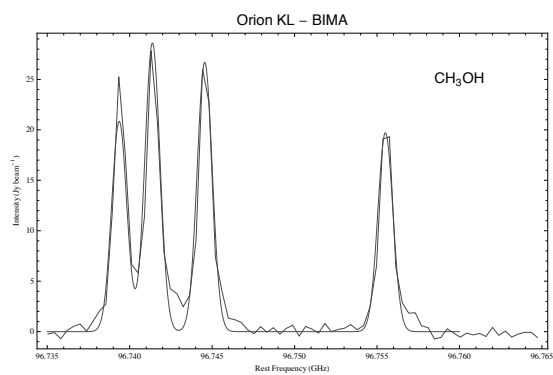


Figure 7.

- 31 -

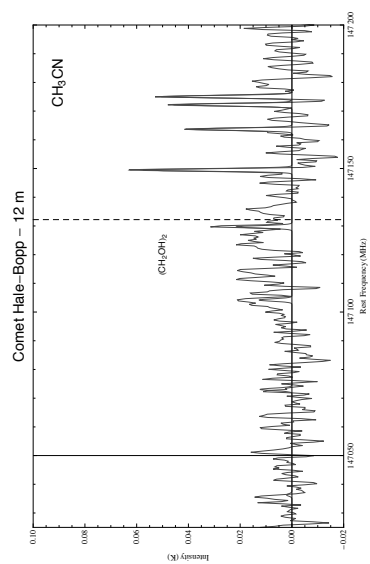


Figure 8.

- 32 -

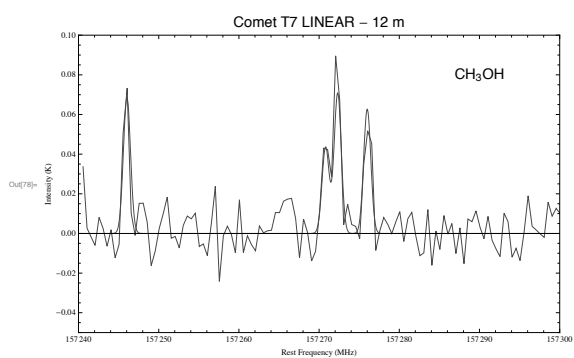


Figure 9.

- 33 -

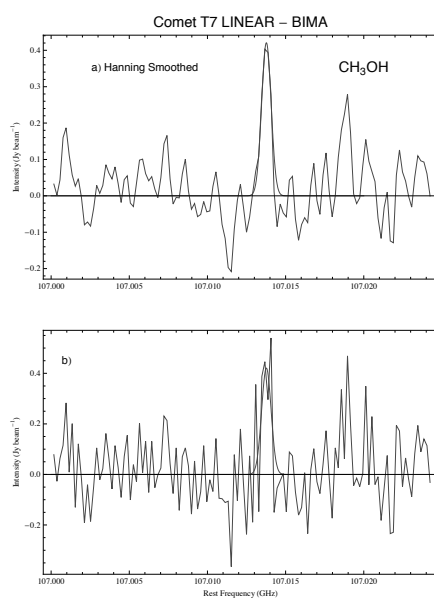


Figure 10.

- 34 -

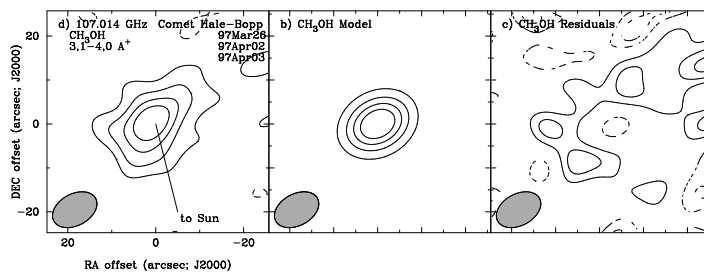


Figure 11.

APPENDIX H

A SURVEY OF CIRCUMSTELLAR $^{12}\text{C}/^{13}\text{C}$ ISOTOPE RATIOS DERIVED FROM CN
AND CO: NUCLEOSYNTHESIS IN VARIOUS TYPES OF STARS

S.N. Milam, N.J. Woolf, & L.M. Ziurys 2007, *Astrophys. J.*, submitted.

**A Survey of Circumstellar $^{12}\text{C}/^{13}\text{C}$ Isotope Ratios Derived from CN and CO:
Nucleosynthesis in Various Types of Stars**

S. N. Milam,

N. J. Woolf,

and

L. M. Ziurys

Department of Chemistry

Department of Astronomy

NASA Astrobiology Institute

and

Steward Observatory

933 N. Cherry Avenue

The University of Arizona

Tucson, Arizona 85721

stemil, nwoolf, and lziurys@as.arizona.edu

ABSTRACT

A self consistent study of the $^{12}\text{C}/^{13}\text{C}$ ratio towards circumstellar envelopes of various chemistry, age, and mass has been conducted at millimeter and submillimeter wavelengths. The ratio was obtained by measuring multiple transitions of CO and CN isotopologs. Values derived from these measurements are in good agreement to previous results and are the first ratios for multiple objects included in this survey. For carbon-rich circumstellar envelopes the ratios were $^{12}\text{C}/^{13}\text{C} \approx 25-90$, oxygen-rich shells have values of 10-35, S-type star ($\text{C}/\text{O} \sim 1$) $^{12}\text{C}/^{13}\text{C} \sim 33$, supergiants yield ratios of $\sim 3-13$, carbon-rich proto-planetary nebulae have $^{12}\text{C}/^{13}\text{C} \sim 30-66$, and oxygen-rich proto-planetary nebulae derive ratios of 3-10. All ratios obtained in this study are ≤ 89 , the solar value, suggesting substantial carbon-13 enrichment to the local interstellar medium. The observed values are modeled by two simple nucleosynthetic processes known to occur during and after the Red Giant Branch: hydrogen-shell burning and helium-shell burning/dredge-up events. These two phenomena effectively lower the $^{12}\text{C}/^{13}\text{C}$ ratio for an oxygen-rich envelope, which then evolves into a carbon-rich shell where the carbon-12 is enhanced. There are a few exceptional cases that are not explained by this mechanism, and should be further investigated. Results presented in this study will improve stellar yield models as well as contribute to the understanding of Galactic chemical evolution.

Subject Headings: astrochemistry --- astrobiology --- stars: AGB and post-AGB --- nucleosynthesis --- radio lines (stars) --- line: profiles

1. INTRODUCTION

Establishing various isotope ratios, for elements heavier than lithium, throughout the Galaxy is considered to be significant for tracing Galactic chemical evolution or the past star formation rate and the stellar mass function. The interstellar medium (ISM) is influenced by products of nearby stars, where atoms are created via nucleosynthesis and transformed into molecular material ejected during the latter stages of stellar evolution. The $^{12}\text{C}/^{13}\text{C}$ isotope ratio is highly dependent upon stellar mass and age as well as the amount of recycled material involved in the formation of a particular object. Carbon-12 is predicted to be formed in the triple alpha reaction; in massive stars, extremely high temperatures due to gravitational collapse initiate the formation of carbon through the fusion of three alpha particles. Carbon-13 is a reaction intermediate in the carbon-nitrogen-oxygen (CNO)-cycle, which occurs in Red Giant branch stars. The $^{12}\text{C}/^{13}\text{C}$ ratio reflects the degree of primary to secondary processing that has occurred in stars and is therefore significant to Galactic chemical evolution models.

Determining the $^{12}\text{C}/^{13}\text{C}$ isotope ratio towards high mass-loss objects can be difficult due to the large dust and molecular opacities obscuring most optical and infrared radiation. This is overcome by employing rotational spectra of molecules to represent the atomic composition. Molecular ratios are believed to reflect the true isotope ratio (see Schoier & Olofsson 2000). In addition, the molecular ratio will also determine the direct enrichment from circumstellar envelopes (CSEs) to the local ISM since molecular gas will trace the colder material being expelled by the stellar wind.

Over the last few decades, the $^{12}\text{C}/^{13}\text{C}$ isotope ratio has been studied in numerous molecular clouds via isotopologs of various species (e.g. Wilson & Rood 1994; Penzias 1980; Milam et al. 2005). Observations of CO, H₂CO and HCO⁺ were traditionally used to obtain this

ratio; however, large opacities of these molecules yield unrealistic abundances and therefore inaccurate $^{12}\text{C}/^{13}\text{C}$ isotope ratios (Schoier & Olofsson 2000). Typically, modeling the line profiles and/or using double isotope ratios are employed to compensate for the high optical depths. Another mechanism recently employed to gain further understanding of the $^{12}\text{C}/^{13}\text{C}$ ratio is by observing the ^{12}CN and ^{13}CN radicals (see Savage et al. 2002; Milam et al. 2005). These isotopologs have hyperfine structure (hf), splitting each rotational transition into multiple features of various strengths. The observed relative intensities can be compared to the equilibrium values to establish the line opacity directly. The work by Milam et al. (2005) verified the accuracy of the $^{12}\text{CN}/^{13}\text{CN}$ ratio and agreement with other molecular tracers. These authors found a gradient in the $^{12}\text{C}/^{13}\text{C}$ ratio, from CO, H_2CO and CN molecular tracers, as a function of distance to the Galactic center; ranging from $^{12}\text{C}/^{13}\text{C} \sim 20$ at 0.1 kpc to 130 at 16 kpc (Milam et al. 2005). The three species gave comparable results and are therefore all useful tracers of the $^{12}\text{C}/^{13}\text{C}$ ratio. The enhancement found towards the Galactic center denotes a higher degree of CNO-processing has occurred there.

To gain further understanding of the Galactic gradient, observations of the $^{12}\text{C}/^{13}\text{C}$ isotope ratio towards circumstellar envelopes have been conducted to investigate the chemical evolution of the Galaxy and the nucleosynthetic processes that occur in various types of stars. These studies have been primarily focused towards carbon-rich CSEs since these type of stars were once considered the primary source of carbon in the ISM (e.g. Kahane et al. 1992; Lambert et al. 1986; Schoier & Olofsson 2000). However, recent results towards the oxygen-rich supergiant star VY CMa have suggested that not only is this object varied in molecular composition, but that the carbon chemistry is also significant (Ziurys et al. 2007; Ziurys, Milam, Tenenbaum & Woolf, in preparation). Molecular $^{12}\text{C}/^{13}\text{C}$ ratios in O-rich envelopes are rare in

that these observations were typically constrained to CO for a few objects – assuming that all the carbon in an oxygen shell is locked into CO. HCN was employed for one study, though saturation effects may play a role in the $^{12}\text{C}/^{13}\text{C}$ values obtained in this study (Nercessian et al. 1989). Optical and infrared results suggest low ratios indicative of CNO processing and substantial mixing of the core with the outer layers of these stars (Geballe et al. 1972). Should this hold true to the outer envelopes of such objects with high mass loss rates, their contribution to carbon isotope enrichment in the ISM could be substantial.

Here we present a self-consistent study of the $^{12}\text{C}/^{13}\text{C}$ isotope ratio towards CSEs of various chemistries and evolutionary status. The ratio has been established from observations of multiple transitions of ^{12}CO , ^{13}CO , ^{12}CN , and ^{13}CN at millimeter/sub-millimeter wavelengths. These values are then compared to those found in the literature to establish a defined $^{12}\text{C}/^{13}\text{C}$ ratio for each object. Results and implications for Galactic chemical evolution and nucleosynthesis are discussed.

2. OBSERVATIONS

The measurements were conducted during the period 2003 October through 2007 June at 1 and 3 mm using the facilities of the Arizona Radio Observatory (ARO): the Kitt Peak 12 m and Submillimeter Telescope (SMT) on Mt. Graham, AZ. The 1 mm observations were carried out at the SMT with the 1.2 mm dual-channel SSB receiver or the new dual-channel ALMA Band 6 receiver system (Lauria et al. 2006) employing sideband-separating mixers with an image rejection of typically 15-20 dB. The backend was a 2048 channel 1 MHz filterbank, used in parallel (2×1024) mode. The temperature scale at the SMT is T_A^* ; radiation temperature is then defined as $T_R = T_A^*/\eta_b$, where η_b is the main-beam efficiency. The 3 mm observations were conducted at the 12 m using dual-channel SIS mixers, operated in single-sideband mode with the

image rejection ≥ 20 dB. Filterbanks with 512 channels of 1 and 2 MHz resolutions were used simultaneously in parallel mode for the measurements, along with an autocorrelator with 782 kHz resolution. The intensity scale of the 12 m is the chopper-wheel corrected antenna temperature, T_R^* , including forward spillover losses ($\eta_{\text{fss}} \sim 0.68$), which is converted to radiation temperature by $T_R = T_R^*/\eta_c$, where η_c is the corrected beam efficiency. All data was taken in beam-switching mode with a subreflector throw of $\pm 2'$. Pointing and focus corrections were monitored regularly by observations of nearby planets and quasars. Frequencies, telescope efficiencies, relative intensities of each transition and source coordinates are given in Tables 1 and 2.

3. RESULTS

Observations of the $^{12}\text{CO}/^{13}\text{CO}$ ratio proved difficult in many objects due to Galactic contamination. The alternative and more analytical species, CN, was then searched for even though the abundance of this molecule can be orders of magnitude lower than CO. However, CN was not detected in every object, in which upper limits were obtained for either one or more of the isotopologs. In objects where CN was not observed, CO emission is generally quite weak and hence likely to be optically thin. Thus, CO measurements should, in these cases, yield more accurate ratios.

The data obtained for the CO isotopologs are presented online in Figure 1 (*a-u*), sample spectra of CIT 6, χ Cyg, and VY CMa are shown. The $J=1 \rightarrow 0$ transition (black) of both ^{12}CO and ^{13}CO were measured with the ARO 12m telescope and the $J=2 \rightarrow 1$ transition (gray) for each species were observed with the SMT. The 12m data intensities have been converted from T_R^* to T_A^* in the Figures. Table 3 lists the observed parameters for these data including T_A^* (K), V_{LSR} (km s^{-1}) and the FWHM linewidth, $\Delta V_{1/2}$ (km s^{-1}). Some spectra exhibit galactic contamination

represented by a sharp spike; for example see VY CMa (Fig. 1*l*), AFGL 190 (Fig. 1*a*) and NML Cyg (Fig. 1*t*). Opacity effects are also apparent in these data by the spectral line profiles. Thin resolved emission will have a ‘U’-shape, while thick resolved emission will be parabolic (e.g. IRC +10216, Fig. 1*f*). Unresolved emission will be reflected by either a ‘box’-shape for optically thin or a gaussian for large opacities (e.g. AFGL 865, Fig. 1*c*). Some objects have peculiar line profiles defined by the source geometry, such as V Hya (Fig. 1*g*), VY CMa (Fig. 1*l*), and OH231.8+4.2 (Fig. 1*q*). All objects display a broad linewidth indicative of their large mass loss rates and expansion velocities, except 89 Her. This object has notoriously narrow features attributed to a non-standard circumstellar expansion; perhaps gravitationally bound (Aloclea & Bujarrabal 1995).

The CN measurements included two rotational transitions, $N=1 \rightarrow 0$ and $N=2 \rightarrow 1$. This species has a $X^2\Sigma$ ground state, thus a complex rotation spectrum, Figure 2 (see Savage et al. 2002; Milam et al. 2005). An example of the hyperfine structure in both isotopologs for the $N=1 \rightarrow 0$ transition is shown in Figure 3, which presents spectra observed towards the carbon-rich envelope Y CVn. The strongest features of the $N=1 \rightarrow 0$ rotational transition of both ^{12}CN (top panel: $J=3/2 \rightarrow 1/2$ spin component) and ^{13}CN (bottom panel: $F_1=1 \rightarrow 0$, $F_2=2 \rightarrow 1$ spin component) are displayed. Each transition is split into multiple features resulting from the nuclear spins of nitrogen ($I=1$) and 13-carbon (^{13}CN only; $I=1/2$), whose relative intensities are plotted beneath the observed spectra in Figure 3. This $J=3/2 \rightarrow 1/2$ spin component of ^{12}CN consists of five individual hyperfine (hf) components, indicated by the quantum number F . The $N=2 \rightarrow 1$ spectra of ^{12}CN is far more complex with over 15 observable transitions, Figures 2 and 4, in the large bandwidth of the SMT. Figure 4 shows an example of the full spectrum of the $N=2 \rightarrow 1$ features observed towards Y CVn. The $N=1 \rightarrow 0$ transition in ^{13}CN also consists of five hyperfine

components, but these lie closer in frequency and hence some are blended together. They also have considerably weaker brightness temperatures, thus the strongest component was primarily observed. Furthermore, the ^{13}CN spectrum is more complicated because the ^{13}C nucleus has a spin of $I=1/2$. Hence, two spins are coupled to the rotational motion to generate quantum numbers F_1 , F_2 , and F . The lines shown in Figure 3 correspond to $N=1\rightarrow 0$, $F_1=1\rightarrow 0$, and $F_2=2\rightarrow 1$ of the ^{13}C -isotopolog. The $N=2\rightarrow 1$ transition of ^{13}CN is as highly complex as that of ^{12}CN , however, the strongest feature is a blend of the $F=3\rightarrow 2$, $F=4\rightarrow 3$ and $F=2\rightarrow 1$ components of the $F_1=2\rightarrow 1$, $F_2=3\rightarrow 2$ lines.

Figure 5 (*a-r*) can be found online, which display all the observed CN data with ^{12}CN ($N=1\rightarrow 0$ and $N=2\rightarrow 1$) and ^{13}CN ($N=1\rightarrow 0$ and $N=2\rightarrow 1$). Sample spectra are shown for CIT 6 ($C/O > 1$), χ Cyg ($C/O = 1$), and VY CMa ($C/O < 1$). Only the strongest J for the $N=2\rightarrow 1$ is plotted for ^{12}CN . A stick spectrum of the relative intensities for each isotopolog is shown below the data. Again, the 12m data intensity scale has been converted from T_{R}^* to T_{A}^* via η_{iss} . The observed line parameters are given in Table 4 (full table online) for all components detected including T_{A}^* or T_{R}^* (K), V_{LSR} (km s^{-1}) and $\Delta V_{1/2}$ (km s^{-1}). Upper limits for ^{13}CN are listed as well and displayed in Figure 5.

4. ANALYSIS

4.1. CO

In order to obtain a self consistent, directly comparable dataset, the CO observations were modeled by a radiative transfer code to derive the fractional abundance of each isotopolog and therefore an isotope ratio. The model was employed for those objects that had at least two transitions of ^{12}CO . From the main isotope parameters, the ^{13}CO data was then fit to the observations. For objects with only one measured transition, a $^{12}\text{C}/^{13}\text{C}$ ratio was derived from

the line intensity ratios corrected for beam efficiencies. This methodology is an approximation to the true ratio since opacity effects are not taken into consideration. Thus, a lower limit on the ratio is obtained in these few cases.

The radiative transfer code employed is from Biegging and Tafalla (1993), where a set of statistical equilibrium equations are solved for populating rotational levels of a given molecule assuming a spherically expanding circumstellar shell. The line profiles are modeled for a given molecule, telescope beam size and transition. Input parameters necessary for the modeling are distance to the object, outflow velocity, mass-loss rate, and temperature and density profiles. If a source radius was unknown, this value in cm was determined from:

$$R_*(cm) = 6.96 \times 10^{10} \sqrt{\frac{L_*}{(T_*/5780)^4}} \quad (1),$$

where L_* is in units of L_\odot , and T_* is in K. The gas temperature profile was defined as:

$$T_{Kin} = T_{Kin0} \left(\frac{r}{r_{Kin0}} \right)^{-0.7} \quad (2),$$

The initial temperature, T_{kin0} , was assumed to be the effective temperature of the star and r_{kin0} was defined as the stellar radius. The exponent value of -0.7 was chosen on the basis of other profiles from evolved stars (see Kemper et al. 2003; Keady et al. 1988). This is an averaged temperature distribution over the entire shell and yields comparable abundances for most objects to those studied in detail. A density distribution dependence of r^{-2} was assumed for all calculations, and the outflow velocity was established individually from the line profiles for a given species. The density profile is defined by the given mass loss rate of a particular object. Fits to the observed line profiles were obtained by varying two parameters: the molecular abundance and the source radius. The source radius was defined as the position from the star where the abundance decreased by $1/e$, assuming a spherical distribution. For optically thick

species, this does not necessarily define the total distribution of the molecule in a particular object, due to the fact that a $1/e$ decrease in abundance is likely still observable. Two rotational transitions per molecule were simultaneously fit, in most cases, to constrain these variables. When available, data from other telescopes were incorporated into the model for additional constraints. Surveys from Groenewegen et al. (1996), Greaves and Holland (1997), Bujarrabal et al. (1994), and Teyssier et al. (2006) were primarily employed. These assumptions are highly generalized, though minor effects should cancel out in the ratio obtained. However, by standardizing the model, the analysis is directly comparable from one source to the next. Modeled CO abundances should be taken lightly and emphasis will be placed only on the $^{12}\text{CO}/^{13}\text{CO}$ ratios.

Parameters employed for each source are found in Table 2. The derived fractional abundances of ^{12}CO and ^{13}CO are found in Table 5 with the source radius and $^{12}\text{CO}/^{13}\text{CO}$ isotope ratio. For those objects not modeled, the integrated intensities of each isotopolog are given instead.

4.2. CN

The radiative transfer model was not employed for the CN analysis due to the lack of measured collisional cross sections for the various hyperfine (hf) transitions. However, the $^{12}\text{CN}/^{13}\text{CN}$ isotope ratios can be evaluated based on the relative intensities of the ^{12}CN hyperfine components to derive τ , the optical depth, and T_{ex} , the excitation temperature. The opacity can be directly determined for an individual source based on the measured relative intensities of the hf components via Equation (2):

$$\frac{T_R^*(hf)}{T_R^*(hf_{main})} = \frac{1 - e^{-R_{hf}\tau_{main}}}{1 - e^{-\tau_{main}}}, \quad (3)$$

where R_{hf} is the relative intensity of a given feature and τ_{main} is the opacity for the main hf line. If τ is determined to be thin, then the intensity ratio of the $^{12}\text{CN}/^{13}\text{CN}$ lines, corrected for their relative intensity and beam efficiency, will give an accurate assessment of the $^{12}\text{C}/^{13}\text{C}$ ratio. Though in the optically thick regime, the ratio is derived from:

$$\frac{^{12}\text{C}}{^{13}\text{C}} = \frac{\tau T_{ex}}{T_R(^{13}\text{CN})R_{hf}}. \quad (4)$$

This analytical technique is described in detail by Savage et al. (2002) and Milam et al. (2005). For objects with narrow linewidths, this is a fairly direct technique. However, most sources included in this study have a FWHM $\gg 2$ MHz, therefore blended features need to be accurately accounted for. For such circumstances, the line profiles were modeled, in the optically thin limit, as either gaussian, parabolic, ‘‘U’’-shaped or ‘‘box’’-shaped profiles for each hf component. The synthetic spectra yielded a correction factor for blended features. This factor was applied to the actual observed intensities to account for the true intensity of a given hf line. The corrected intensities were utilized in Equation (3) to derive the optical depth and excitation temperature. The ^{13}CN analysis assumed optically thin emission for both the $N=1 \rightarrow 0$ and $N=2 \rightarrow 1$ transitions and the strongest hf component was used for both transitions as well. Table 7 lists sources with their calculated opacities and T_{ex} for optically thick CN emission (online only). The values derived were between 1.8 and 5.5 for τ and 2.9 and 5.7 for T_{ex} .

5. DISCUSSION

5.1. Peculiar Objects

Not all objects in this survey obey the simplistic ‘‘spherical’’ circumstellar envelope and conform to the proposed modeling employed in this study. These objects were taken into consideration and evaluated on a case-by-case basis.

The carbon-rich AGB star AFGL 809 has had limited studies regarding its molecular composition, evolutionary status, and isotope ratios. Data presented here for CO were not modeled with the radiative transfer code, due to the detection of only the $J=1\rightarrow 0$ transition. Also, the ^{13}CO is merely an upper limit. The feature present in the $^{13}\text{CO } J=1\rightarrow 0$ spectra is galactic contamination, not the actual source. This is verified by the narrow linewidth and LSR velocity observed in the ^{12}CO galactic contamination features.

The proto-planetary nebula CRL 618, carbon-rich, was not observed in CO for this particular study. This object has been well studied by others (e.g. Kahane et al. 1992; Wannier & Sahai 1987) in CO emission at multiple frequencies. The complex structure and kinematics of this object are not easily modeled with the radiative transfer program incorporated in this study. However, both the $N=1\rightarrow 0$ and $N=2\rightarrow 1$ CN transitions of both isotopologs were observed and included in this survey. The opacity was not modeled well by the approach mentioned earlier (§4.2). To evaluate the $^{12}\text{CN}/^{13}\text{CN}$ ratio in this object a simplistic approach was taken assuming the weakest observed component will express the ‘thinnest’ regime of opacity and therefore the lower limit to the true isotope ratio. For the $N=1\rightarrow 0$, this was the $F=1/2\rightarrow 3/2$ transition which yielded a ratio ≥ 32 , assuming the ^{13}CN opacity is optically thin. The $N=2\rightarrow 1$, $J=3/2\rightarrow 1/2$, $F=3/2\rightarrow 1/2$ line gave a ratio of $^{12}\text{CN}/^{13}\text{CN} \geq 17$. These values are in good agreement with previous $^{12}\text{C}/^{13}\text{C}$ measurements, see Table 8.

The proto-typical C-rich AGB envelope, IRC +10216, had interesting results from the CN data. CO was observed in both $J=2\rightarrow 1$ and $J=1\rightarrow 0$ and therefore incorporated into the radiative transfer model. The $^{12}\text{CO}/^{13}\text{CO}$ ratio obtained from this calculation was 25, good agreement with previous results. Modeled results yielded a fractional abundance of ^{12}CO with respect to H_2 of $f(^{12}\text{CO}) \sim 1 \times 10^{-3}$ (see Table 6); recent models by Woods et al. (2003) derived 1

$\times 10^{-3}$ and that of Teysier et al. (2006) had $f \sim 1 \times 10^{-3}$. The agreement found between our analysis and that of others verifies the accuracy of our assumptions and model. The ratio obtained for CN isotopologs were not as straight forward to determine. The methodology described earlier yielded opacities > 1 , or optically thick. However, the line profiles of these data resemble the ‘U’-shape, or optically thin, resolved emission. Thus, the $^{12}\text{CN}/^{13}\text{CN}$ ratio was determined in the same manner as that of CRL 618, where the weakest component was employed to derive the ‘thin-limit’ ratio. While we believe this data is optically thin emission, we still quote only a lower limit to this ratio. The $N=1 \rightarrow 0$ data yield $^{12}\text{C}/^{13}\text{C} \geq 36$, while the $N=2 \rightarrow 1$ profiles suggest $^{12}\text{C}/^{13}\text{C} \geq 37$.

V Hya is a carbon-rich envelope that displays multiple velocity components in both CO and CN profiles (Figs. 1g and 5i). This double-horned structure is likely attributed to a complex bipolar outflow as found in multiple studies (e.g. Stanek et al. 1995; Kahane et al. 1988; Sahai et al. 2003). Thus, the $^{12}\text{CO}/^{13}\text{CO}$ ratios were derived for each flow, the red- and blue-shifted peak intensities, to be 23-35. These values were derived in the optically thin limit, therefore the ratios are lower limits to the true $^{12}\text{C}/^{13}\text{C}$. The analysis for CN is far more complex, thus only the strongest intensity (blue-shifted peak) was employed for the $^{12}\text{CN}/^{13}\text{CN}$ calculations. A ratio of > 16 was found for the CN ratio and constrained by the limits of ^{13}CN detections. Sahai et al. (2003) proposed that this object is in transition of the AGB to a proto-planetary nebula, which is a short lived period rarely observed.

Recent studies have verified the complex structure and associated chemistry found toward the O-rich supergiant, VY CMa (see Ziurys et al. 2007). Three distinct components were labeled as the spherical wind, blue-shifted outflow and the red-shifted flow. The CO spectra clearly display the presence of the three components at their relative LSR velocities near 19, -7,

and 42 km s^{-1} (see Table 3 and Fig. 1*l*). Each component was modeled with the radiative transfer code that includes the outflows with geometric constraints defined in Ziurys et al. (2007). The fractional abundances obtained were 46 for the spherical wind and 25 for the outflows. Only an upper limit was obtained for ^{13}CN , thus the ratio for these data is a lower limit.

There is seemingly some controversy over the evolutionary status of 89 Her in the literature. Some authors suggest that this object has evolved off the Red Giant branch and is now a post-AGB star (Bujarrabal et al. 2007; Fong et al. 2006), while others report this is a high latitude F-supergiant, possibly a binary (Luck et al. 1990). This paper will not debate this issue and accept that the object is a low mass star masquerading as a supergiant with a high light-to-mass ratio. The spectra reveal two components also found in high resolution interferometer maps (Bujarrabal et al. 2007); one being a narrow ‘hot’ component and the other a more extended, possible bipolar, nebula. Due to the large uncertainty in the distance, luminosity, and effective temperature, 89 Her was not modeled via radiative transfer. The $^{12}\text{C}/^{13}\text{C}$ ratio was obtained from the peak intensity ratio of each isotopolog and corrected for efficiency resulting in a value of 3-4.

The bipolar proto-planetary nebula OH231.8+4.2 is a well-studied object. This evolved star has a rich chemistry and known for its large abundance of carbon-rich species, though it still exhibits SiO and H₂O masers indicative of an O-rich chemistry. The spectra denote a complex morphology later revealed by infrared images as well as molecular maps that this is a bipolar flow with an intense nebular center (Sanchez Contreras et al. 1997; Matsuura et al. 2006). Due to the uncertain nature of the kinematic structure of this source, we believe the assumed parameters in §4.1 were unrealistic and therefore did not employ the radiative transfer model to determine a ^{12}CO or ^{13}CO abundance for this object. The $^{12}\text{CO}/^{13}\text{CO}$ ratio was obtained from the

nebular center, or peak intensity. The ratio from the $J=1 \rightarrow 0$ isotopologs agrees well with that obtained for the $J=2 \rightarrow 1$ ratio of ~ 3 . This value is in good agreement with Sanchez Contreras et al. (2000) where $^{12}\text{C}/^{13}\text{C} \sim 5-10$ from various molecular species.

5.2. $^{12}\text{C}/^{13}\text{C}$ Isotope Ratios

The derived $^{12}\text{C}/^{13}\text{C}$ ratios from CO and CN are listed in Table 8. For objects observed in both species, the ratios are in good agreement, even with the lower limit ratios derived for CN. The measure of error becomes obvious in those objects from which both CN and CO ratios were obtained. For these few sources, there is excellent agreement except in the case of IRC +40540. In this particular object the maximum error on the $^{12}\text{C}/^{13}\text{C}$ ratio is obtained as a factor of 2. Table 8 also lists $^{12}\text{C}/^{13}\text{C}$ ratios from the literature with their corresponding references. Again, there is in general good agreement with values obtained from a wide variety of molecules and wavelengths. Some of the objects included in this survey have had little if any measurements of the ratio such as AFGL 809, 89 Her, W Hya, S Cep, among others.

This survey incorporated a variety of objects at different stages of their evolution. A few general categories include: C-rich Asymptotic Giant Branch (AGB) stars (C-type), O-rich AGB (M-type), S-type ($\text{C}/\text{O} \sim 1$), Supergiant, C-rich PPN and O-rich PPN. The ratios found for each category are $^{12}\text{C}/^{13}\text{C} \approx 25-90$ (excluding Y CVn), 10-35, 33, 3-13 (excluding VY CMa), 30-66, and 3-10, respectively. These ranges help constrain the abundances expected for a given chemistry and age. The lowest ratios are found in oxygen-rich envelopes, while the largest values are derived from C-rich AGB envelopes. Only 2 object's $^{12}\text{C}/^{13}\text{C}$ ratios compare to the solar system value of 89 (V Hya and UU Aur), and some are in the range of the local ISM ($^{12}\text{C}/^{13}\text{C} \sim 68$; Milam et al. 2005).

To date, very few studies of the $^{12}\text{C}/^{13}\text{C}$ ratio have included oxygen-rich circumstellar envelopes. Rational behind this was that C-rich AGB envelopes are the main contributors of carbon isotopes to the ISM (e.g. Greaves & Holland 1997). However, objects queried in this study suggest comparable mass-loss rates among both types of AGB stars, as well as good agreement between their CO/H₂ fractional abundances of the order $\sim 10^{-4}$ (see Tables 2 and 5). Ratios obtained from both O-rich and C-rich AGB envelopes have similar $^{12}\text{C}/^{13}\text{C}$ values, implying the carbon enrichment from both chemistries is significant. The oxygen-rich vs. carbon-rich definitions are proving to be insignificant for isotopic and molecular precursors to the ISM (see Ziurys et al. 2007; Ziurys et al., in preparation). The dominating effect is that they are both molecule-rich, high mass-loss objects, and prevalent throughout the Galaxy. The other major molecular and isotope enriching objects are supergiants, with their very high mass-loss rates ($\sim 10^{-4} M_{\odot} \text{ yr}^{-1}$) and extreme $^{12}\text{C}/^{13}\text{C}$ ratios ≤ 13 (excluding VY CMa). Granted, these objects are not as common as their AGB counterparts, though they are short-lived and may play a key role in their direct ISM enrichment.

Observed $^{12}\text{C}/^{13}\text{C}$ ratios in this study may also be under the influence of chemical fractionation effects. Here the ^{13}C isotopolog is favored or enhanced from the chemical reaction of $^{13}\text{C}^+ + ^{12}\text{CO} \rightarrow ^{13}\text{CO} + ^{12}\text{C}^+$, where ΔE is 35 K (see Milam et al. 2005; Watson et al. 1976; Langer 1992); a similar mechanism exists for CN. This reaction should be dominant at low temperatures found in the outer envelopes of Red Giants and AGB stars. However, chemical fractionation competes with selective photodissociation effects that will enhance the ^{12}CO abundances due to the large opacities usually found in CSEs. These two mechanisms are typically found to compensate for each other (Kahane et al. 1992; Jura, Kahane, & Omont 1988). Additionally, the ratios found in this study are in good agreement to photospheric measurements

of Lambert et al. (1986) and Jura et al. (1988), suggesting that the stellar $^{12}\text{C}/^{13}\text{C}$ ratio is reflected by the molecular ratios.

Should any of the above mentioned effects take place in the envelopes of the objects included in the survey, the $^{12}\text{C}/^{13}\text{C}$ values obtained from molecular observations are likely tracing the ISM-contributing isotope ratio. Studies of diffuse clouds and planetary nebulae have suggested that molecules formed in CSEs may survive into the ISM, thereby enriching the local medium with molecular material (Ziurys 2006; E.D. Tenenbaum et al., in preparation). The isotope ratios of at least two gas-phase species, CO and CN, are in agreement suggesting that the $^{12}\text{C}/^{13}\text{C}$ ratios measured in molecular clouds are directly influenced by their stellar neighbors.

5.3. Carbon Nucleosynthesis

Low to intermediate mass stars evolve off the main sequence when there is a He-core and H-burning shell. This is known as the Red Giant Branch (RGB), where the envelope of the star expands with an increase in the stellar luminosity (Herwig 2005). The RGB is terminated with a C/O core and both a He- and H-burning shells, or the Asymptotic Giant Branch (AGB). During these two phases of stellar evolution, the envelopes are highly convective resulting in enrichment of interior nucleosynthesized material at the surface, otherwise known as dredge-up. First dredge-up (FDU) occurs as the star becomes a Red Giant and results in a depletion of ^{12}C . The second dredge-up comes at the end of the He-burning core cycle and most of the carbon and oxygen have been converted into nitrogen from the CNO-cycle. Third dredge-up (TDU) converts the star from being oxygen-rich to carbon-rich (Herwig 2005; Iben & Renzini 1983). At this point, triple- α products from the He/H-burning shells enrich the outer envelope raising the effective $^{12}\text{C}/^{13}\text{C}$ ratio. However, not all objects attain the C-rich phenomena; massive stars

may undergo hot-bottom burning (HBB) that effectively converts dredged-up carbon into nitrogen preventing the C-star formation (Herwig 2005).

For many years, observational measurements of CNO isotopes remained non-reproducible by theoretical models of nucleosynthesis. These unexplained values lead to a focused dedication to Red Giant and AGB yields in the theoretical community. The suggestion of an ‘extra mixing’ phenomena was invoked to reconcile the counterintuitive CNO ratios to theory (Boothroyd & Sackmann 1999). Other mechanisms proposed to account for the low $^{12}\text{C}/^{13}\text{C}$ ratios included rotation (e.g. Charbonnel 1995), magnetic fields (e.g. Hubbard & Dearborn 1980), and most recently molecular weight inversion (Eggleton 2006; Eggleton, Dearborn & Lattanzio 2007).

The three-dimensional nucleosynthetic model of Eggleton et al. (2007) has incorporated deep-mixing influenced by a molecular weight inversion. This theory not only accounts for the low $^{12}\text{C}/^{13}\text{C}$ ratios observed in low mass giants but also the lack of ^3He enrichment of the ISM. These authors found a decrease in the $^{12}\text{C}/^{13}\text{C}$ ratios for $1 M_{\odot}$ stars to range from ~ 30 to 13 , solar metallicity, and $^{12}\text{C}/^{13}\text{C} \sim 27$ to 4 for $Z \sim 1/50 Z_{\odot}$ (Eggleton et al. 2007). These low ratios obtained just after the FDU are in close agreement to those observed by Tsuji (2007).

The low ratios obtained for supergiants in this study seemingly agree with the recent results of Meynet et al. (2006). These authors invoke rotation to account for low $^{12}\text{C}/^{13}\text{C}$ ratios and $\text{C}/\text{O} < 1$ for high mass stars. The envelopes of these objects have CNO by-product enrichment. Observed ratios may also be attributed to hot-bottom burning (HBB), where dredged-up carbon is converted to nitrogen, thus enabling the star to remain in an O-rich state (Herwig 2005) while maintaining a low $^{12}\text{C}/^{13}\text{C}$ ratio ~ 3.5 .

Each model has its own limitations and may not account for the full manifold of observational evidence. However, this is a vastly evolving field and theoretical results are infringing upon results obtained through observational studies.

5.4. Galactic Chemical Evolution

The evolution of the chemical composition of the Galaxy is a function of the star formation rate, the initial mass function, and stellar properties and yields (Prantzos 2007). Enrichment of the ISM of various elements leads to the amount of processed material provided as well as the degree of processing that has occurred (primary vs. secondary). By comparing the observed ISM abundances to those provided by their stellar precursors, at various stages in their evolution as well as individual properties, one can obtain insight into the components of Galactic chemical evolution (GCE).

The low $^{12}\text{C}/^{13}\text{C}$ ratios obtained in this study are embodied in a group of objects found within 2 kpc from the solar system (Table 2). This would suggest that ^{13}C enrichment is occurring in the local ISM effectively lowering the $^{12}\text{C}/^{13}\text{C}$ ratio. Models of Galactic chemical evolution are in worse agreement to current observational findings than older ones, according to a recent review by Tosi (2003). Availability of new stellar yields at various metallicities has yet to improve the observed $^{12}\text{C}/^{13}\text{C}$ ratios found in molecular clouds across the Galaxy (e.g. Milam et al. 2005). However, this may be expected in that these new models also are incapable of reproducing observed ratios towards the envelopes of Red Giant and AGB envelopes (see previous section). Stellar yields reflect nucleosynthesis and other effects such as mixing and/or rotation, which are somewhat model dependent and can significantly alter GCE models (Gavilan et al. 2005). For example, the recent GCE model for CNO isotopes by Romano and Matteucci

(2003) found that the stellar yields employed for AGB envelopes reflected the significance of HBB and agreement with observations only came when this effect was minor.

Improvements to stellar yields require broad datasets of observed ratios including carbon, oxygen, nitrogen, and helium. The poor understanding of AGB and Red Giant nucleosynthesis is likely attributable to the variations found in GCE models (Gavilan et al. 2005). Observational datasets incorporated into these studies are based on typically lower resolution data that have been vastly improved upon – as well as the fact that the surveys are typically biased towards C-rich envelopes, planetary nebulae, and/or low to intermediate mass objects. Results found in this study will help improve these models to be incorporated into GCE models and gain further understanding into carbon-enrichment of the ISM.

5.5. *The Evolving Circumstellar $^{12}\text{C}/^{13}\text{C}$ Circumstellar Ratio*

From these data an evolutionary dependence of the $^{12}\text{C}/^{13}\text{C}$ ratio can be derived. As an object transits from the main sequence, the hydrogen burning shell dredges up core material altering the $^{12}\text{C}/^{13}\text{C}$ ratio. The amount of mixing that actually occurs during this stage is unclear, though observational evidence would suggest a substantial amount. Figure 6 shows the $^{12}\text{C}/^{13}\text{C}$ ratio as a function of the approximate C/O value for the objects included in this study. Within the plot the derived values are incorporated assuming a 1:1, 2:1, 10:1, and full mixing of the hydrogen-burning shell with the original material (gray triangles A, B, C, and D) at $\sim 4 \times 10^7$ K. Here, the initial abundance was assumed to be that of the local interstellar medium with $^{12}\text{C}/^{13}\text{C} \sim 60$ and C/O ~ 0.5 . The hydrogen-burning ashes were taken from Arnett (1996) and mixed at the various percentages. The values obtained for the oxygen-rich envelopes in this study are in good agreement and follow the trend closely. One must note that the C/O ratios for these objects are not well known and are approximated with an error of likely 20%. The full mixing of the

hydrogen-burning shell has terminal values of $^{12}\text{C}/^{13}\text{C} \sim 3$ and $\text{C}/\text{O} \sim 0.7$. Thus, the lower the $^{12}\text{C}/^{13}\text{C}$ ratio, the smaller amount of original material that has survived. This is verified by the large amounts of hydrogen observed suggesting this is primarily attributed to nucleosynthetic processing, not mass-loss.

The next level of complexity comes when the envelope is transformed to carbon-rich and the $^{12}\text{C}/^{13}\text{C}$ ratio is effectively increased, otherwise associated as the helium-flash. To account for this in a simplistic manner, the helium-burning shell ashes were mixed with the “fully mixed” products of the hydrogen shell burning. Again, the values were taken from Arnett (1996) for this procedure. During this stage, all the ^{13}C is destroyed to form carbon and oxygen, which primarily depend on the temperature assumed. The ratios were calculated for a significantly smaller amount of material with only 1%, 2%, 5%, and 10% of the shell material being mixed (see Figure 6) at $\sim 2 \times 10^8$ K. In the completely mixed limit, the $^{12}\text{C}/^{13}\text{C}$ ratio is infinite and the C/O ratio reaches 1.15. This is clearly an extreme value, though it explains the higher ratios found on the diagram. The C/O ratio becomes > 1 at the 2% mixing value and has a $^{12}\text{C}/^{13}\text{C}$ ratio of ~ 27 . These results are in good agreement with both the S-star and most of the C-star results in this study (see Figure 6). The large gray arrow in Figure 6 shows this evolutionary trend and incorporates nearly all objects studied. While this is only a first-order calculation, it describes the observations presented here nicely. The major exceptions found in Figure 6 are IRC +10216 and Y CVn. For the case of IRC +10216, the C/O value can be accounted for by a lower temperature He-flash mixing. Y CVn has been studied by multiple groups and is part of a small group of carbon-rich stars with CNO-equilibrium value $^{12}\text{C}/^{13}\text{C}$ ratios. These objects are not easily explained by a simple model and need other effects such as mass-loss, hot-bottom burning, mass inversion, etc. to properly define the mechanisms by which they are governed.

6. CONCLUSIONS

An independent assessment of the $^{12}\text{C}/^{13}\text{C}$ isotope ratio was obtained from measurements of both CO and CN isotopologs in multiple stars of various chemistries, mass, and evolutionary status. The ratios determined from both species are in good agreement and are also comparable to previous measurements. All values are lower than the solar $^{12}\text{C}/^{13}\text{C}$ ratio of ~ 89 , suggesting a large presence of carbon-13 enrichment in the local interstellar medium in agreement with Galactic ratios previously measured (e.g. Milam et al. 2005). Ratios obtained towards oxygen-rich envelopes are comparable to those of their carbon-rich counterparts; therefore, these objects play a key role in contributing carbon to the ISM. Simplistic treatment of basic nucleosynthesis is in good agreement with the results obtained in this study and suggests two processes to model the observed values. Initial shell hydrogen-burning processes during the Red Giant branch describes the low $^{12}\text{C}/^{13}\text{C}$ ratios found in oxygen-rich envelopes. This is followed by shell helium-burning dredge-up events to explain the evolution to a carbon-rich envelope with a higher isotope ratio. However, not all cases abide by these two processes and should be further investigated. Results presented will help define stellar yields of carbon and its isotopes from various types of objects to the interstellar medium and constrain models of Galactic chemical evolution.

Acknowledgements: This material is based upon work supported by the National Aeronautics and Space Administration through the NASA Astrobiology Institute under Cooperative Agreement No. CAN-02-OSS-02 issued through the Office of Space Science. S.N.M. would like to thank the Phoenix Chapter of ARCS, specifically the Mrs. Scott L. Libby, Jr. endowment, for partial funding.

References:

- Alcolea, J. & Bujarrabal, V. 1995, *A&A*, 303, L21
- Arnett, D. 1996, *Supernovae and Nucleosynthesis*, (Princeton: Princeton University Press)
- Bieging, J.H. & Tafalla, M. 1993, *AJ*, 105, 576
- Boothroyd, A.I. and Sackmann I-J 1999, *ApJ*, 510, 232
- Bujarrabal, V., Fuente, A., & Omont, A. 1994, *A&A*, 285, 247
- Bujarrabal, V., van Winckel, H., Neri, R., Alcolea, J., Castro-Carrizo, A., & Deroo, P. 2007, *A&A*, 468, 45
- Charbonnel, C. 1995, *ApJ*, 453, L41
- Eggleton, Peter P., Dearborn, David S. P., & Lattanzio, John C. 2006, *Science*, 314, 1580
- Eggleton, Peter P., Dearborn, David S. P., & Lattanzio, John C. 2007, preprint (astro-ph/0611609)
- Fong, D., Meixner, M., Sutton, E.C., Zalucha, A., & Welch, W.J. 2006, *ApJ*, 652, 1626
- Fuente et al. 1998, *A&A*, 330, 232
- Gavilán, M., Buell, J. F., & Mollá M. 2005, *A&A*, 432, 861
- Geballe, T.R., Wollman, E.R., & Rank, D.M. 1972, *ApJ*, 177, L27
- Greaves, J.S. & Holland, W.S. 1997, *A&A*, 327, 342
- Groenewegen, M.A.T., Baas, F., de Jong, T., & Loup, C. 1996, *A&A*, 306, 241
- Herwig, F. 2005, *ARA&A*, 43, 435
- Hinkle, K.H., Lambert, D.L., & Snell, R.L. 1976, *ApJ*, 210, 684
- Huggins, P.J. 1987, *ApJ*, 313, 400
- Iben, I., Jr. and Renzini, A. 1983, *ARA&A*, 21, 271
- Jura, M., Kahane, C., & Omont, A. 1988, *A&A* 201, 80

- Kahane, C. et al. 1992, *A&A*, 256, 235
- Kahane, C., Maizels, C., & Jura, M. 1988, *ApJ*, 328, L25
- Keady, J.J., Hall, D.N.B., & Ridgway, S.T. 1988, *ApJ*, 326, 832
- Kemper, F., Stark, R., Justtanont, K., de Koter, A., Tielens, A.G.G.M., Waters, L.B.F.M., Cami, J., & Dijkstra, C. 2003, *A&A*, 407, 609
- Lambert, David L., Gustafsson, Bengt, Eriksson, Kjell, Hinkle, & Kenneth H. 1986, *ApJS*, 62, 373
- Lauria, E. F., Kerr, A. R., Reiland, G., Freund, R. F., Lichtenberger, A. W., Ziurys, L. M., Metcalf, M., & Forbes, D. 2006 First Astronomical Observations with an ALMA Band 6 (211-275 GHz) Sideband-Separating SIS Mixer-preamp (ALMA Memo No. 553); <www.alma.nrao.edu/memos/>
- Luck, R. Earle, Bond, Howard E., & Lambert, David L. 1990, *ApJ*, 357, 188
- Matsuura, M., et al. 2006, *ApJ*, 646, L123
- Matteucci, F. 2003, *Ap&SS*, 284, 539
- Meynet, G., Ekström, S., & Maeder, A. 2006, *A&A*, 447, 623
- Milam, S. N., Savage, C., Brewster, M. A., Ziurys, L. M., & Wyckoff, S. 2005, *ApJ*, 634, 1126
- Nercessian, E., Guilloreau, S., Omont, A., & Benayoun, J. J. 1989, *A&A*, 210, 225
- Ohnaka, K. & Tsuji, T. 1996, *A&A*, 310, 933
- Olofsson, H. et al. 1991, *A&A*, 245, 611
- Penzias, A.A. 1980, *Science*, 208, 663
- Prantzos, N. 2007, preprint (astro-ph/0709.0833)
- Sahai, R., Morris, M., Knapp, G. R., Young, K., & Barnbaum, C. 2003, *Nature*, 426, 261
- Sanchez Contreras, C., Bujarrabal, V., & Alcolea, J. 1997, *A&A*, 327, 689

- Sanchez Contreras, C., Bujarrabal, V., Neri, R., & Alcolea, J. 2000, *A&A*, 357, 651.
- Savage, C., Apponi, A.J., Ziurys, L.M., and Wyckoff, S. 2002, *ApJ*, 578, 211
- Schoier, F.L. & Olofsson, H. 2000, *A&A*, 359, 586
- Stanek, K.Z., Knapp, G.R., Young, K., & Phillips, T.G. 1995, *ApJS*, 100, 169
- Teyssier, D., Hernandez, R., Bujarrabal, V., Yoshida, H., & Phillips, T. G. 2006, *A&A*, 450, 167
- Tosi, M. 2003, in *ASP Conference Series 304, CNO in the universe*, ed. Corinne Charbonnel, Daniel Schaerer, and Georges Meynet (San Francisco, CA), p.390
- Tsuji, T. 2007, preprint (astro-ph/0610180v1)
- Wannier, P.G. & Sahai, R. 1987, *ApJ*, 319, 367
- Watson, W.D., Anicich, V.G., and Huntress, W.T., Jr. 1976, *ApJ*, 205, L165
- Wilson, T.L., and Rood, R.T. 1994, *ARA&A*, 32, 19
- Woods, P. M., Schöier, F.L., Nyman, L.-Å., & Olofsson, H. 2003, *A&A*, 402, 617
- Ziurys, L.M., Milam, S.N., Apponi, A.J., & Woolf, N.J. 2007, *Nature*, 447, 1094

Table 1: Observed Molecular Transitions, Relative Intensities and Related Telescope Efficiencies

Line	Transition	Component	Frequency (MHz)	Relative Intensity	η_c (12m)	η_b (10m)			
¹² CO	J=1→0		115271.202		0.84				
	J=2→1		230537.990			0.78			
¹³ CO	J=1→0		110201.353		0.85				
	J=2→1		220398.676			0.78			
¹² CN	N=1→0	J=3/2→1/2	F=3/2→1/2	113488.142	0.1235	0.82			
			F=5/2→3/2	113490.985	0.3333				
			F=1/2→1/2	113499.643	0.0988				
			F=3/2→3/2	113508.934	0.0988				
			F=1/2→3/2	113520.414	0.0123				
	N=2→1	J=3/2→3/2	F=1/2→1/2	226287.393	0.0062	0.53	0.78		
				F=1/2→3/2	226298.896			0.0049	
				F=3/2→1/2	226303.049			0.0049	
				F=3/2→3/2	226314.552			0.0120	
				F=3/2→5/2	226332.519			0.0053	
		J=3/2→1/2		F=5/2→3/2	226341.919			0.0053	
				F=5/2→5/2	226359.887			0.0280	
				F=1/2→3/2	226616.520			0.0062	
				F=3/2→3/2	226632.176			0.0494	
				F=5/2→3/2	226659.543			0.1667	
J=5/2→3/2		F=1/2→1/2	226663.685	0.0494					
		F=3/2→1/2	226679.341	0.0617					
		F=5/2→3/2	226874.183	0.1680					
		F=7/2→5/2	226874.764	0.2667					
		F=3/2→1/2	226875.896	0.1000					
		F=3/2→3/2	226887.399	0.0320					
		F=5/2→5/2	226892.151	0.0320					
¹³ CN	N=1→0		F=3/2→5/2	226905.366	0.0013				
		F ₁ =1→0					0.84		
			F ₂ =2→1	F=3→2	108780.200	0.2000			
					F=2→1	108782.374		0.1070	
					F=1→0	108786.982		0.0480	
					F=1→1	108793.753		0.0360	
		F=2→2	108796.400	0.0360					
	N=2→1	F ₁ =2→1				0.55	0.78		
		F ₂ =3→2	F=4→3	217467.150	0.1550				
				F=3→2	217467.150			0.1068	
				F=2→1	217469.155			0.0724	
				F=2→2	217480.559			0.0138	
			F=3→3	217483.606	0.0138				

Table 2: Source Parameters

Source	Type	α (B1950.0)	δ (B1950.0)	Distance (pc)	L (L_{\odot})	T_{eff} (K)	R_* (cm)	\dot{M} ($M_{\odot} \text{ yr}^{-1}$)	Reference
AFGL 190	Carbon	$01^{\text{h}}14^{\text{m}}26.3^{\text{s}}$	$66^{\circ}58'08''$	2300	10000	2500^{a}	3.7×10^{13}	6.8×10^{-5}	1
AFGL 809	Carbon	$05^{\text{h}}40^{\text{m}}33.3^{\text{s}}$	$32^{\circ}40'49''$	1450	9400	2500^{a}	3.6×10^{13}	1.7×10^{-5}	1
AFGL 865	Carbon	$06^{\text{h}}01^{\text{m}}17.4^{\text{s}}$	$07^{\circ}26'06''$	1760	9200	2500^{a}	3.6×10^{13}	2.3×10^{-5}	1
IRC +40540	Carbon	$23^{\text{h}}32^{\text{m}}01.3^{\text{s}}$	$43^{\circ}16'37''$	630	9000	2000	3.5×10^{13}	1.5×10^{-5}	2,3
CRL 2688	Proto-PN (C)	$21^{\text{h}}00^{\text{m}}20.0^{\text{s}}$	$36^{\circ}29'44''$	1000	20000	6500	9.0×10^{12}	1.7×10^{-4}	4,5,6
CRL 618	Proto-PN (C)	$04^{\text{h}}39^{\text{m}}34.0^{\text{s}}$	$36^{\circ}01'16''$	1700	30000	30000	4.5×10^{11}	2.0×10^{-4}	2
CIT 6	Carbon	$10^{\text{h}}13^{\text{m}}10.9^{\text{s}}$	$30^{\circ}49'17''$	410	10000	2445	4.0×10^{13}	6.5×10^{-6}	1,7
IRC +10216	Carbon	$09^{\text{h}}45^{\text{m}}14.8^{\text{s}}$	$13^{\circ}30'40''$	150	18000	2320	6.5×10^{13}	1.0×10^{-5}	2,8
V Hya	Carbon	$10^{\text{h}}49^{\text{m}}11.3^{\text{s}}$	$-20^{\circ}59'04''$	330	14000	2650	4.0×10^{13}	2.5×10^{-6}	1,2
Y CVn	Carbon	$12^{\text{h}}42^{\text{m}}47.1^{\text{s}}$	$45^{\circ}42'48''$	220	4400	2700	2.0×10^{13}	2.0×10^{-7}	2
S Cep	Carbon	$21^{\text{h}}35^{\text{m}}52.7^{\text{s}}$	$78^{\circ}23'58''$	400	7300	1500	1.1×10^{14}	2.5×10^{-6}	2,9
IRC +10420	F-Supergiant	$19^{\text{h}}24^{\text{m}}26.7^{\text{s}}$	$11^{\circ}15'11''$	5000	700000	6200	7.5×10^{13}	3.0×10^{-4}	2,3
α Ori	Supergiant	$05^{\text{h}}52^{\text{m}}27.8^{\text{s}}$	$07^{\circ}23'58''$	190	100000	3650	4.0×10^{13}	1.0×10^{-6}	10,11,12
VY CMa	Supergiant	$07^{\text{h}}20^{\text{m}}54.7^{\text{s}}$	$-25^{\circ}40'12''$	1500	500000	3368	1.4×10^{14}	2.0×10^{-4}	13
IRC +00365	Carbon	$18^{\text{h}}39^{\text{m}}48.3^{\text{s}}$	$-02^{\circ}20'24''$	960	10400 ??	2500^{a}	4.0×10^{13}	2.2×10^{-5}	14
UU Aur	Carbon	$06^{\text{h}}33^{\text{m}}06.6^{\text{s}}$	$38^{\circ}29'16''$	260	6900	3000	3.0×10^{13}	3.5×10^{-7}	2
89 Her	F-Supergiant	$17^{\text{h}}53^{\text{m}}24.1^{\text{s}}$	$26^{\circ}03'24''$	1000	9000	7000	3.0×10^{12}	4.0×10^{-6}	2
χ Cyg	S-type	$19^{\text{h}}48^{\text{m}}38.5^{\text{s}}$	$32^{\circ}47'10''$	150	9300	2000	3.0×10^{13}	5.0×10^{-7}	1,9
OH231.8+4.2	Proto-PN (O)	$07^{\text{h}}39^{\text{m}}58.9^{\text{s}}$	$-14^{\circ}35'44''$	1500	10000	2900	4.6×10^{13}	2.3×10^{-4}	2
TX Cam	Oxygen	$04^{\text{h}}56^{\text{m}}40.6^{\text{s}}$	$56^{\circ}06'28''$	317	8400	2600	2.0×10^{13}	4.0×10^{-6}	15,16
W Hya	Supergiant	$13^{\text{h}}46^{\text{m}}12.2^{\text{s}}$	$-28^{\circ}07'07''$	115	11050	2500	4.0×10^{13}	2.3×10^{-6}	17
NML Cyg	Supergiant	$20^{\text{h}}44^{\text{m}}33.8^{\text{s}}$	$39^{\circ}55'57''$	2000	500000	2500	2.6×10^{14}	1.6×10^{-4}	18
IK Tau	Oxygen	$03^{\text{h}}50^{\text{m}}43.6^{\text{s}}$	$11^{\circ}15'32''$	270	2000	2100	2.1×10^{13}	4.5×10^{-6}	3,19

^{a)} Assumed value.

References: (1) Ivezić & Elitzur 1995; (2) Fong et al. 2006; (3) Teyssier et al. 2006; (4) Skinner et al. 1997; (5) Truong-Bach et al. 1990; (6) Jaminet et al. 1992; (7) Bergat & Chevallier 2005; (8) Agundez & Cernicharo 2006; (9) Bujarrabal et al. 1989; (10) van Loon et al. 2005; (11) Bujarrabal et al. 1994; (12)

Levesque et al. 2005; (13) Humphreys et al. 2007; (14) Greaves & Holland 1997; (15) Olofsson et al. 1991; (16) Cherchneff 2006; (17) Zubko & Eilizar 2000; (18) Zubko et al. 2004; (19) Duari et al. 1999

Table 3: CO Observed Parameters

Source	Transition	Isotopolog	T_R^* or T_A^* (K) ^{a)}	$\Delta V_{1/2}$ (km s ⁻¹)	V_{LSR} (km s ⁻¹)
AFGL 190	J=1→0	¹² CO	0.17 ± 0.02	31.2 ± 5.2	-39.8 ± 5.2
		¹³ CO	0.009 ± 0.002	32.6 ± 5.4	-39.3 ± 5.4
AFGL 809	J=1→0	¹² CO	0.17 ± 0.02	36.4 ± 5.2	-36.2 ± 5.2
		¹³ CO	≤ 0.006	~ 36	~ -31 ^{b)}
AFGL 865	J=1→0	¹² CO	0.32 ± 0.02	26.0 ± 5.2	43.0 ± 5.2
		¹³ CO	0.025 ± 0.007	29.9 ± 5.4	41.6 ± 5.4
IRC +40540	J=1→0	¹² CO	1.05 ± 0.03	26.0 ± 5.2	-17.0 ± 5.2
		¹³ CO	0.074 ± 0.010	27.2 ± 5.4	-17.0 ± 5.2
	J=2→1	¹² CO	1.51 ± 0.02	24.7 ± 2.6	-17.0 ± 2.6
		¹³ CO	0.11 ± 0.01	27.2 ± 2.7	-16.6 ± 2.7
CIT 6	J=1→0	¹² CO	1.7 ± 0.1	31.2 ± 5.2	-1.0 ± 5.2
		¹³ CO	0.092 ± 0.013	35.4 ± 5.4	-2.4 ± 5.2
	J=2→1	¹² CO	2.49 ± 0.05	31.2 ± 2.6	-2.3 ± 2.6
		¹³ CO	0.22 ± 0.01	34.0 ± 2.7	-1.7 ± 2.7
IRC +10216	J=1→0	¹² CO	6.00 ± 0.07	26.0 ± 5.2	-26.0 ± 5.2
		¹³ CO	0.89 ± 0.04	27.2 ± 5.4	-26.0 ± 5.4
	J=2→1	¹² CO	15.0 ± 0.5	24.7 ± 2.6	-26.7 ± 2.6
		¹³ CO	1.60 ± 0.02	28.6 ± 2.7	-26.0 ± 2.7
V Hya ^{c)}	J=1→0	¹² CO	0.58 ± 0.03	~ 13	-23.8 ± 5.2
		¹³ CO	0.022 ± 0.006	~ 11	-21.4 ± 5.4
	J=2→1	¹² CO	1.14 ± 0.02	~ 10	-25.1 ± 2.6
		¹³ CO	0.044 ± 0.008	~ 10	-24.2 ± 2.7
V Hya ^{d)}	J=1→0	¹² CO	0.75 ± 0.03	~ 13	-8.2 ± 5.2
		¹³ CO	0.022 ± 0.006	~ 11	-10.6 ± 5.4
	J=2→1	¹² CO	1.50 ± 0.02	~ 10	-9.5 ± 2.6
		¹³ CO	0.064 ± 0.008	~ 11	-9.2 ± 2.7
Y CVn	J=1→0	¹² CO	0.16 ± 0.02	13.0 ± 5.2	22.1 ± 5.2
		¹³ CO	0.074 ± 0.015	13.6 ± 5.4	21.2 ± 5.4
	J=2→1	¹² CO	0.36 ± 0.01	13.0 ± 2.6	20.8 ± 2.6
		¹³ CO	0.17 ± 0.01	15.0 ± 2.7	21.2 ± 2.7
S Cep	J=1→0	¹² CO	0.27 ± 0.02	41.6 ± 5.2	-15.3 ± 5.2
		¹³ CO	0.008 ± 0.003	43.5 ± 5.4	-15.3 ± 5.4
IRC +10420	J=1→0	¹² CO	0.17 ± 0.01	67.6 ± 5.2	76.8 ± 5.2
		¹³ CO	0.020 ± 0.006	70.7 ± 5.4	73.2 ± 5.4
	J=2→1	¹² CO	0.39 ± 0.01	66.3 ± 2.6	78.1 ± 2.6
		¹³ CO	0.045 ± 0.008	66.6 ± 2.7	77.3 ± 2.7
α Ori	J=1→0	¹² CO	0.048 ± 0.010	26.0 ± 5.2	5.4 ± 5.2
		¹³ CO	0.008 ± 0.002	21.8 ± 5.4	4.7 ± 5.4
	J=2→1	¹² CO	0.32 ± 0.01	26.0 ± 2.6	2.8 ± 2.6
		¹³ CO	0.048 ± 0.009	25.8 ± 2.7	3.3 ± 2.7
VY CMa ^{e)}	J=1→0	¹² CO	0.041 ± 0.008	~ 23	~ 20
	J=2→1	¹² CO	0.38 ± 0.01	~ 20	~ 19
VY CMa ^{f)}	J=1→0	¹³ CO	0.011 ± 0.004	~ 18	~ 19
		¹² CO	0.075 ± 0.008	~ 16	~ -3
	J=2→1	¹² CO	0.40 ± 0.01	~ 17	~ -3
		¹³ CO	0.019 ± 0.004	~ 14	~ -3
VY CMa ^{g)}	J=1→0	¹² CO	0.046 ± 0.008	~ 18	~ 42
		¹² CO	0.35 ± 0.01	~ 22	~ 42
	J=2→1	¹³ CO	0.014 ± 0.004	~ 20	~ 43
		¹² CO	0.20 ± 0.02	65.0 ± 5.2	1.7 ± 5.2
IRC +00365	J=1→0	¹³ CO	0.006 ± 0.003	70.7 ± 5.4	3.0 ± 5.4

	J=2→1	¹² CO	0.32 ± 0.01	62.4 ± 2.6	3.0 ± 2.6
		¹³ CO	0.009 ± 0.004	65.3 ± 2.7	3.7 ± 2.7
UU Aur	J=1→0	¹² CO	0.14 ± 0.02	20.8 ± 5.2	7.3 ± 5.2
		¹³ CO	0.005 ± 0.002	24.5 ± 5.4	4.6 ± 5.4
	J=2→1	¹² CO	0.39 ± 0.01	18.2 ± 2.6	7.3 ± 2.6
		¹³ CO	0.012 ± 0.004	23.1 ± 2.7	6.6 ± 2.7
89 Her	J=1→0	¹² CO	0.06 ± 0.01	7.8 ± 2.6	-7.7 ± 2.6
		¹³ CO	0.02 ± 0.01	8.2 ± 2.7	-9.5 ± 2.7
	J=2→1	¹² CO	0.20 ± 0.05	8.8 ± 1.3	-8.0 ± 1.3
		¹³ CO	0.054 ± 0.005	6.8 ± 1.4	-8.1 ± 1.4
χ Cyg	J=1→0	¹² CO	0.90 ± 0.06	15.6 ± 5.2	9.5 ± 5.2
		¹³ CO	0.025 ± 0.009	16.3 ± 5.4	9.5 ± 5.4
	J=2→1	¹² CO	1.60 ± 0.01	14.3 ± 2.6	10.2 ± 2.6
		¹³ CO	0.083 ± 0.006	16.3 ± 2.7	9.5 ± 2.7
OH231.8+4.2	J=1→0	¹² CO	0.22 ± 0.02	41.6 ± 5.2	32.3 ± 5.2
		¹³ CO	0.054 ± 0.011	35.4 ± 5.4	35.1 ± 5.4
	J=2→1	¹² CO	0.58 ± 0.02	41.6 ± 2.6	36.2 ± 2.6
		¹³ CO	0.22 ± 0.01	38.1 ± 2.7	35.1 ± 2.7
TX Cam	J=1→0	¹² CO	0.32 ± 0.03	28.6 ± 5.2	10.5 ± 5.2
	J=2→1	¹² CO	0.75 ± 0.01	28.6 ± 2.6	10.5 ± 2.6
		¹³ CO	0.03 ± 0.01	28.6 ± 2.7	10.6 ± 2.7
W Hya	J=1→0	¹² CO	0.044 ± 0.010	10.4 ± 5.2	41.0 ± 5.2
	J=2→1	¹² CO	0.34 ± 0.01	14.3 ± 2.6	39.7 ± 2.6
		¹³ CO	0.011 ± 0.004	13.6 ± 2.7	41.0 ± 2.7
NML Cyg	J=1→0	¹² CO	0.13 ± 0.03	57.2 ± 5.2	-2.4 ± 5.2
	J=2→1	¹² CO	0.69 ± 0.05	50.7 ± 2.6	-1.1 ± 2.6
		¹³ CO	0.06 ± 0.01	50.3 ± 2.7	-0.9 ± 2.7
IK Tau	J=1→0	¹² CO	0.44 ± 0.01	31.2 ± 5.2	34.5 ± 5.2
	J=2→1	¹² CO	1.23 ± 0.01	31.2 ± 2.6	34.5 ± 2.6
		¹³ CO	0.13 ± 0.01	34.0 ± 2.7	35.2 ± 2.7

All measurements were taken with 1 MHz resolution.

a) T_R^* for 12m data (J=1→0) and T_A^* for SMT (J=2→1) unless otherwise noted. For "U"-shape profiles this value was measured at the peak intensity.

b) Assumed value.

c) Blue-shifted component.

d) Red-shifted component.

e) For spherical flow (see text).

f) Blue-shifted flow (see text).

g) Red-shifted flow (see text).

Table 4 (Sample): CN Observed Parameters

Source	Isotopolog	Transition	T_R^* or T_A^* (K) ^{a)}	$\Delta V_{1/2}$ (km s ⁻¹)	V_{LSR} (km s ⁻¹)
Y CVn	¹² CN	N=1→0			
		J=3/2→1/2			
		F=5/2→3/2 ^{b)}	0.15 ± 0.01	10.6 ± 5.3	24.9 ± 5.3
		F=1/2→1/2	0.028 ± 0.009	7.9 ± 5.3	24.9 ± 5.3
		F=3/2→3/2	0.028 ± 0.009	7.9 ± 5.3	24.9 ± 5.3
		N=2→1			
		J=3/2→3/2			
		F=5/2→5/2	0.023 ± 0.005	14.5 ± 2.6	22.3 ± 2.6
		J=3/2→1/2			
		F=3/2→3/2	0.034 ± 0.005	13.2 ± 2.6	20.9 ± 2.6
		F=5/2→3/2 ^{d)}	0.096 ± 0.005	11.9 ± 2.6	19.6 ± 2.6
		F=3/2→1/2	0.043 ± 0.005	11.9 ± 2.6	20.9 ± 2.6
		J=5/2→3/2			
		F=7/2→5/2 ^{e)}	0.15 ± 0.01	10.6 ± 2.6	19.6 ± 2.6
		F=5/2→5/2 ^{c)}	0.028 ± 0.005	9.2 ± 2.6	19.6 ± 2.6
¹³ CN	N=1→0				
	F ₁ =1→0				
	F ₂ =2→1				
	F=3→2	0.011 ± 0.002	13.8 ± 5.5	22.7 ± 5.5	
	N=2→1				
	F ₁ =2→1				
F ₂ =3→2					
F=4→3 ^{h)}	0.058 ± 0.012	8.3 ± 2.8	21.4 ± 2.8		
VY CMa	¹² CN	N=2→1			
		J=3/2→1/2			
		F=5/2→3/2 ^{d)}	0.008 ± 0.004	60.7 ± 2.6	17.7 ± 2.6
		J=5/2→3/2			
		F=7/2→5/2 ^{e)}	0.016 ± 0.004	64.0 ± 2.6	19.0 ± 2.6
		F=3/2→3/2 ^{c)}	0.006 ± 0.004	~ 60	~ 19
		N=2→1			
		F ₁ =2→1			
		F ₂ =3→2			
F=4→3 ^{h)}	≤ 0.003	~ 60	~ 19		

All values measured from 1 MHz resolution unless otherwise noted.

^{a)} T_R^* for 12m data (N=1→0) and T_A^* for SMT (N=2→1) unless otherwise noted.

^{b)} Blended with the F=3/2→1/2 line (¹²CN: N=1→0).

^{c)} Partially blended feature.

^{d)} Assumed value.

^{e)} 2 MHz resolution.

^{f)} Blended with the F=1/2→1/2 line (¹²CN: N=2→1).

^{g)} Blended with the F=5/2→3/2 and F=3/2→1/2 lines (¹²CN: N=2→1).

^{h)} Blended with the F=3→2 and F=2→1 lines (¹³CN: N=2→1).

Table 4: CN Observed Parameters

Source	Isotopolog	Transition	T_R^* or T_A^* (K) ^{b)}	$\Delta V_{1/2}$ (km s ⁻¹)	V_{LSR} (km s ⁻¹)	
AFGL 190	¹² CN	N=1→0				
		J=3/2→1/2				
		F=5/2→3/2 ^{b)}	0.013 ± 0.003	23.8 ± 5.3	-39.3 ± 5.3	
			F=1/2→1/2 ^{c)}	~ 0.004	-	-39 ^{d)}
			F=3/2→3/2 ^{c)}	~ 0.004	-	-39 ^{d)}
		¹³ CN	N=1→0			
AFGL 809 ^{e)}	¹² CN	F ₁ =1→0				
		F ₂ =2→1				
		F=3→2	≤ 0.0014	-	-39 ^{d)}	
			N=1→0			
			J=3/2→1/2			
			F=5/2→3/2 ^{b)}	0.024 ± 0.004	18.5 ± 5.3	-33.6 ± 5.3
		F=1/2→1/2 ^{c)}	~ 0.008	-	-34 ^{d)}	
		F=3/2→3/2 ^{c)}	~ 0.008	-	-34 ^{d)}	
	¹³ CN	N=1→0				
		F ₁ =1→0				
		F ₂ =2→1				
		F=3→2	≤ 0.002	-	~ -31 ^{d)}	
AFGL 865 ^{e)}	¹² CN	N=1→0				
		J=3/2→1/2				
		F=5/2→3/2 ^{b)}	0.035 ± 0.006	29.0 ± 5.3	47.0 ± 5.3	
			F=1/2→1/2 ^{c)}	~ 0.015	-	43 ^{d)}
			F=3/2→3/2 ^{c)}	~ 0.015	-	43 ^{d)}
		¹³ CN	N=1→0			
		F ₁ =1→0				
		F ₂ =2→1				
		F=3→2	≤ 0.002	-	43 ^{d)}	
IRC +40540	¹² CN	N=1→0				
		J=3/2→1/2				
		F=5/2→3/2 ^{b)}	0.16 ± 0.01	26.4 ± 5.3	-17.0 ± 5.3	
		F=1/2→1/2 ^{c)}	0.036 ± 0.010	~ 24	~ -20	
		F=3/2→3/2 ^{c)}	0.036 ± 0.010	~ 24	~ -20	
		F=1/2→3/2	≤ 0.010	-	-17 ^{d)}	
		N=2→1				
	J=3/2→1/2					
	F=3/2→3/2	0.014 ± 0.007	11.9 ± 2.6	-13.0 ± 2.6		
	F=5/2→3/2 ^{d)}	0.042 ± 0.007	23.8 ± 2.6	-18.3 ± 2.6		
	F=3/2→1/2	0.019 ± 0.007	18.5 ± 2.6	-15.7 ± 2.6		
	J=5/2→3/2					
	F=7/2→5/2 ^{g)}	0.096 ± 0.007	22.4 ± 2.6	-15.7 ± 2.6		
	F=3/2→3/2	0.031 ± 0.007	~ 22	~ -17		
F=5/2→5/2	0.031 ± 0.007	~ 22	~ -17			

CRL 2688 ⁱ⁾	¹³ CN	N=1→0				
		F ₁ =1→0				
		F ₂ =2→1				
		F=3→2	0.005 ± 0.002	30.4 ± 5.5	-19.8 ± 5.5	
		N=2→1				
	F ₁ =2→1					
	F ₂ =3→2					
	F=4→3 ^{h)}	≤ 0.004	-	-17 ^{d)}		
	¹² CN	N=1→0				
		J=3/2→1/2				
F=5/2→3/2 ^{b)}		0.50 ± 0.01	25.4 ± 5.3	-32.5 ± 5.3		
F=1/2→1/2 ^{c)}		0.22 ± 0.01	15.8 ± 5.3	-36.3 ± 5.3		
F=3/2→3/2 ^{c)}		0.20 ± 0.01	18.1 ± 5.3	-37.5 ± 5.3		
F=1/2→3/2		0.07 ± 0.01	22.7 ± 5.3	-38.4 ± 5.3		
N=2→1						
J=3/2→1/2						
F=3/2→3/2		0.10 ± 0.02	15.5 ± 2.1	-38.9 ± 2.1		
F=5/2→3/2 ^{d)}		0.23 ± 0.02	19.6 ± 2.1	-37.9 ± 2.1		
F=3/2→1/2 ^{c)}	0.07 ± 0.02	13.4 ± 2.1	-38.5 ± 2.1			
J=5/2→3/2						
F=7/2→5/2 ^{g)}	0.45 ± 0.02	22.7 ± 2.1	-35.4 ± 2.1			
F=5/2→5/2 ^{c)}	0.18 ± 0.02	11.3 ± 2.1	-37.4 ± 2.1			
CRL 618 ⁱ⁾	¹³ CN	N=1→0				
		F ₁ =1→0				
		F ₂ =2→1				
		F=3→2	0.033 ± 0.005	25.8 ± 5.5	-38.6 ± 5.5	
		N=2→1				
	F ₁ =2→1					
	F ₂ =3→2					
	F=4→3 ^{h)}	0.020 ± 0.007	21.6 ± 2.4	-37.1 ± 2.4		
	¹² CN	N=1→0				
		J=3/2→1/2				
F=5/2→3/2 ^{b)}		0.19 ± 0.01	24.6 ± 5.3	-19.7 ± 5.3		
F=1/2→1/2 ^{c)}		0.074 ± 0.010	16.9 ± 5.3	-26.9 ± 5.3		
F=3/2→3/2 ^{c)}		0.070 ± 0.010	16.9 ± 5.3	-24.4 ± 5.3		
F=1/2→3/2		0.025 ± 0.010	21.4 ± 5.3	-23.0 ± 5.3		
N=2→1						
J=3/2→1/2						
F=5/2→3/2 ^{d)}		0.15 ± 0.04	19.2 ± 2.1	-22.0 ± 2.1		
F=3/2→1/2 ^{c)}		0.09 ± 0.04	17.7 ± 2.1	-27.2 ± 2.1		
J=5/2→3/2						
F=7/2→5/2 ^{g)}	0.23 ± 0.04	23.9 ± 2.1	-22.0 ± 2.1			
F=5/2→5/2 ^{c)}	0.09 ± 0.04	19.8 ± 2.1	-24.6 ± 2.1			
CIT 6 ⁱ⁾	¹³ CN	N=1→0				
		F ₁ =1→0				
		F ₂ =2→1				
		F=3→2	0.013 ± 0.006	27.6 ± 5.5	-22.0 ± 5.5	
		N=2→1				
	F ₁ =2→1					
	F ₂ =3→2					
	F=4→3 ^{h)}	~ 0.02	-	-22 ^{d)}		
	¹² CN	N=1→0				
		J=3/2→1/2				
F=5/2→3/2 ^{b)}		0.42 ± 0.01	29.0 ± 5.3	-1.0 ± 5.3		
F=1/2→1/2 ^{c)}		0.11 ± 0.01	~ 29	~ -1.0		
F=3/2→3/2 ^{c)}		0.10 ± 0.01	~ 29	~ -1.0		

		N=2→1			
		J=3/2→1/2			
		F=5/2→3/2 ^{f)}	0.10 ± 0.02	26.8 ± 2.1	-3.0 ± 2.1
		J=5/2→3/2			
		F=7/2→5/2 ^{g)}	0.22 ± 0.02	26.8 ± 2.1	-1.0 ± 2.1
		F=3/2→3/2 ^{c)}	0.07 ± 0.02	~ 27	~ -1.0
	¹³ CN	N=1→0			
		F ₁ =1→0			
		F ₂ =2→1			
		F=3→2	0.007 ± 0.002	27.6 ± 5.5	-3.8 ± 5.5
		N=2→1			
		F ₁ =2→1			
		F ₂ =3→2			
		F=4→3 ^{b)}	0.012 ± 0.005	29.0 ± 2.8	-2.4 ± 2.8
IRC +10216	¹² CN	N=1→0			
		J=3/2→1/2			
		F=5/2→3/2 ^{b)}	2.03 ± 0.02	29.0 ± 5.3	-24.7 ± 5.3
		F=1/2→1/2 ^{c)}	0.70 ± 0.02	~ 24	~ -26
		F=3/2→3/2 ^{c)}	0.61 ± 0.02	~ 24	~ -26
		F=1/2→3/2	0.16 ± 0.02	26.4 ± 5.3	-24.7 ± 5.3
		N=2→1			
		J=3/2→3/2			
		F=5/2→3/2 ^{c)}	0.070 ± 0.03	~ 26	~ -26
		F=5/2→5/2	0.20 ± 0.03	29.0 ± 2.6	-26.0 ± 2.6
		J=3/2→1/2			
		F=3/2→3/2	0.20 ± 0.03	29.0 ± 2.6	-27.3 ± 2.6
		F=5/2→3/2 ^{f)}	0.58 ± 0.03	29.0 ± 2.6	-28.6 ± 2.6
		F=3/2→1/2 ^{c)}	0.20 ± 0.03	~ 30	~ -26
		J=5/2→3/2			
		F=7/2→5/2 ^{g)}	1.50 ± 0.03	25.1 ± 2.6	-26.7 ± 2.6
		F=5/2→5/2 ^{c)}	0.50 ± 0.03	~ 29	~ -26
	¹³ CN	N=1→0			
		F ₁ =1→0			
		F ₂ =2→1			
		F=3→2	0.074 ± 0.007	30.4 ± 5.5	-27.4 ± 5.5
		N=2→1			
		F ₁ =2→1			
		F ₂ =3→2			
		F=4→3 ^{b)}	0.05 ± 0.02	29.0 ± 2.8	-27.7 ± 2.8
V Hya	¹² CN	N=1→0			
		J=3/2→1/2			
		F=5/2→3/2 ^{b)}	0.082 ± 0.010	23.8 ± 5.3	-16 ± 5.3
		F=1/2→1/2 ^{c)}	~ 0.018	-	-16 ^{d)}
		F=3/2→3/2 ^{c)}	~ 0.018	-	-16 ^{d)}
		N=2→1			
		J=3/2→3/2			
		F=3/2→3/2	~ 0.011	-	-16 ^{d)}
		J=3/2→1/2			
		F=3/2→3/2	0.019 ± 0.005	11.9 ± 2.6	-16.0 ± 2.6
		F=5/2→3/2 ^{f)}	0.047 ± 0.005	18.5 ± 2.6	-16.0 ± 2.6
		F=3/2→1/2 ^{c)}	0.022 ± 0.005	17.2 ± 2.6	-13.4 ± 2.6
		J=5/2→3/2			
		F=7/2→5/2 ^{g)}	0.11 ± 0.01	21.1 ± 2.6	-18.6 ± 2.6
		F=5/2→5/2 ^{c)}	0.039 ± 0.005	~ 19	~ -16
	¹³ CN	N=1→0			
		F ₁ =1→0			

			$F_2=2 \rightarrow 1$				
			$F_3=3 \rightarrow 2$	≤ 0.003	-		$-16^d)$
			$N=2 \rightarrow 1$				
			$F_1=2 \rightarrow 1$				
			$F_2=3 \rightarrow 2$				
			$F_4=4 \rightarrow 3^b)$	≤ 0.02	-		$-16^d)$
Y CVn	^{12}CN	$N=1 \rightarrow 0$					
			$J=3/2 \rightarrow 1/2$				
			$F=5/2 \rightarrow 3/2^b)$	0.15 ± 0.01	10.6 ± 5.3		24.9 ± 5.3
			$F=1/2 \rightarrow 1/2$	0.028 ± 0.009	7.9 ± 5.3		24.9 ± 5.3
			$F=3/2 \rightarrow 3/2$	0.028 ± 0.009	7.9 ± 5.3		24.9 ± 5.3
		$N=2 \rightarrow 1$					
			$J=3/2 \rightarrow 3/2$				
			$F=5/2 \rightarrow 5/2$	0.023 ± 0.005	14.5 ± 2.6		22.3 ± 2.6
			$J=3/2 \rightarrow 1/2$				
			$F=3/2 \rightarrow 3/2$	0.034 ± 0.005	13.2 ± 2.6		20.9 ± 2.6
			$F=5/2 \rightarrow 3/2^d)$	0.096 ± 0.005	11.9 ± 2.6		19.6 ± 2.6
			$F=3/2 \rightarrow 1/2$	0.043 ± 0.005	11.9 ± 2.6		20.9 ± 2.6
			$J=5/2 \rightarrow 3/2$				
			$F=7/2 \rightarrow 5/2^g)$	0.15 ± 0.01	10.6 ± 2.6		19.6 ± 2.6
			$F=5/2 \rightarrow 5/2^c)$	0.028 ± 0.005	9.2 ± 2.6		19.6 ± 2.6
		^{13}CN	$N=1 \rightarrow 0$				
			$F_1=1 \rightarrow 0$				
			$F_2=2 \rightarrow 1$				
			$F_3=3 \rightarrow 2$	0.011 ± 0.002	13.8 ± 5.5		22.7 ± 5.5
		$N=2 \rightarrow 1$					
			$F_1=2 \rightarrow 1$				
			$F_2=3 \rightarrow 2$				
			$F_4=4 \rightarrow 3^b)$	0.058 ± 0.012	8.3 ± 2.8		21.4 ± 2.8
S Cep	^{12}CN	$N=1 \rightarrow 0$					
			$J=3/2 \rightarrow 1/2$				
			$F=3/2 \rightarrow 1/2^c)$	0.09 ± 0.01	~ 40		~ -15
			$F=5/2 \rightarrow 3/2^c)$	0.13 ± 0.01	~ 40		~ -15
			$F=1/2 \rightarrow 1/2^c)$	0.04 ± 0.01	~ 40		~ -15
			$F=3/2 \rightarrow 3/2^c)$	0.03 ± 0.01	~ 40		~ -15
		^{13}CN	$N=1 \rightarrow 0$				
			$F_1=1 \rightarrow 0$				
			$F_2=2 \rightarrow 1$				
			$F_3=3 \rightarrow 2$	~ 0.003	-		$-15^d)$
VY CMa	^{12}CN	$N=2 \rightarrow 1$					
			$J=3/2 \rightarrow 1/2$				
			$F=5/2 \rightarrow 3/2^d)$	0.008 ± 0.004	60.7 ± 2.6		17.7 ± 2.6
			$J=5/2 \rightarrow 3/2$				
			$F=7/2 \rightarrow 5/2^g)$	0.016 ± 0.004	64.0 ± 2.6		19.0 ± 2.6
			$F=3/2 \rightarrow 3/2^c)$	0.006 ± 0.004	~ 60		~ 19
		$N=2 \rightarrow 1$					
			$F_1=2 \rightarrow 1$				
			$F_2=3 \rightarrow 2$				
			$F_4=4 \rightarrow 3^b)$	≤ 0.003	~ 60		~ 19
IRC +00365	^{12}CN	$N=1 \rightarrow 0$					
			$J=3/2 \rightarrow 1/2$				
			$F=5/2 \rightarrow 3/2^b)$	0.036 ± 0.005	55.4 ± 5.3		3.0 ± 5.3
			$F=1/2 \rightarrow 1/2^c)$	~ 0.015	-		$3^d)$
			$F=3/2 \rightarrow 3/2^c)$	~ 0.015	-		$3^d)$
		^{13}CN	$N=1 \rightarrow 0$				
			$F_1=1 \rightarrow 0$				

UU Aur	¹² CN	F ₂ =2→1				
		N=1→0	F=3→2	≤ 0.003	-	3 ^d
		J=3/2→1/2				
		F=5/2→3/2 ^{b)}		0.008 ± 0.003	23.8 ± 5.3	8.6 ± 5.3
		F=1/2→1/2 ^{c)}		≤ 0.003	-	7 ^{d)}
¹³ CN	N=1→0	F=3/2→3/2 ^{c)}		≤ 0.003	-	7 ^{d)}
		F ₁ =1→0				
		F ₂ =2→1				
		F=3→2		≤ 0.004	-	7 ^{d)}
χ Cyg	¹² CN	N=1→0				
		J=3/2→1/2				
		F=5/2→3/2 ^{b)}		0.014 ± 0.005	18.5 ± 5.3	9.5 ± 5.3
		F=1/2→1/2		≤ 0.005	-	9 ^{d)}
		F=3/2→3/2		≤ 0.005	-	9 ^{d)}
		N=2→1				
	J=3/2→1/2					
	F=3/2→3/2		0.012 ± 0.004	10.6 ± 2.6	9.5 ± 2.6	
	F=5/2→3/2 ^{d)}		0.034 ± 0.004	15.8 ± 2.6	8.2 ± 2.6	
	F=3/2→1/2		0.015 ± 0.004	14.5 ± 2.6	8.2 ± 2.6	
	J=5/2→3/2					
	F=7/2→5/2 ^{g)}		0.070 ± 0.004	17.2 ± 2.6	8.2 ± 2.6	
	F=5/2→5/2 ^{c)}		0.011 ± 0.004	~ 18	~ 9	
¹³ CN	N=1→0	F ₁ =1→0				
		F ₂ =2→1				
		F=3→2		≤ 0.002	-	9 ^{d)}
		N=2→1				
		F ₁ =2→1				
		F ₂ =3→2				
TX Cam	¹² CN	N=2→1				
		J=3/2→1/2				
		F=3/2→3/2		0.003 ± 0.002	23.8 ± 2.6	6.6 ± 2.6
	F=5/2→3/2 ^{d)}		0.008 ± 0.002	31.7 ± 2.6	9.2 ± 2.6	
	J=5/2→3/2					
	F=7/2→5/2 ^{g)}		0.013 ± 0.002	37.0 ± 2.6	9.2 ± 2.6	
¹³ CN	N=2→1	F ₁ =2→1				
		F ₂ =3→2				
		F=4→3 ^{h)}		≤ 0.003	-	9 ^{d)}
NML Cyg	¹² CN	N=2→1				
		J=3/2→1/2				
		F=5/2→3/2 ^{e)}		0.004 ± 0.002	54.1 ± 2.6	~ -2
	J=5/2→3/2					
	F=7/2→5/2 ^{g)}		0.005 ± 0.002	50.2 ± 2.6	-2.4 ± 2.6	
¹³ CN	N=2→1	F ₁ =2→1				
		F ₂ =3→2				
		F=4→3 ^{h)}		≤ 0.003	-	9 ^{d)}
IK Tau	¹² CN	N=2→1				
		J=3/2→1/2				
		F=3/2→3/2		0.004 ± 0.002	25.1 ± 2.6	34.5 ± 2.6
		F=5/2→3/2 ^{d)}		0.007 ± 0.002	38.3 ± 2.6	35.2 ± 2.6
J=5/2→3/2						

37

¹³ CN	N=2→1	F=7/2→5/2 ^{g)}	0.006 ± 0.002	31.7 ± 2.6	33.2 ± 2.6
		F ₁ =2→1			
		F ₂ =3→2			
		F=4→3 ^{h)}	≤ 0.005	-	34 ^{d)}

All values measured from 1 MHz resolution unless otherwise noted.

ⁱ⁾ T_R^{*} for 12m data (N=1→0) and T_A^{*} for SMT (N=2→1) unless otherwise noted.

^{j)} Blended with the F=3/2→1/2 line (¹²CN: N=1→0).

^{k)} Partially blended feature.

^{l)} Assumed value.

^{m)} 2 MHz resolution.

ⁿ⁾ Blended with the F=1/2→1/2 line (¹²CN: N=2→1).

^{o)} Blended with the F=5/2→3/2 and F=3/2→1/2 lines (¹²CN: N=2→1).

^{p)} Blended with the F=3→2 and F=2→1 lines (¹³CN: N=2→1).

^{q)} N=2→1 data from 12m, with resolution of 0.782 MHz.

Table 5: Modeled CO Fractional Abundances Relative to H₂

Source	$f(^{12}\text{CO})$	$f(^{13}\text{CO})$
AFGL 190		
AFGL 809		
AFGL 865		
IRC +40540	8.0×10^{-4}	2.0×10^{-5}
CRL 2688		
CRL 618		
CIT 6	1.5×10^{-3}	5.0×10^{-5}
IRC +10216	1.5×10^{-3}	6.0×10^{-5}
V Hya		
Y CVn	5.0×10^{-4}	2.0×10^{-4}
S Cep		
IRC +10420	5.0×10^{-4}	3.5×10^{-5}
α Ori	8.0×10^{-4}	1.0×10^{-4}
VY CMa	4.6×10^{-5} ^{a)}	1.0×10^{-6} ^{a)}
	2.5×10^{-4} ^{b)}	1.0×10^{-5} ^{b)}
IRC +00365	7.0×10^{-4}	1.0×10^{-5}
UU Aur	9.0×10^{-4}	1.0×10^{-5}
89 Her		
χ Cyg	5.0×10^{-4}	1.5×10^{-5}
OH231.8+4.2		
TX Cam	4.0×10^{-4}	1.3×10^{-5}
W Hya	7.0×10^{-5}	2.0×10^{-6}
NML Cyg	4.0×10^{-4}	3.0×10^{-5}
IK Tau	8.0×10^{-5}	8.0×10^{-6}

^{a)} Spherical Wind (see text).

^{b)} Outflows (see text).

Table 7: Derived CN Opacities and Excitation Temperatures

Source	CN: N=1→0		CN: N=2→1	
	τ (CN)	T_{ex} (CN)	τ (CN)	T_{ex} (CN)
IRC +40540			3.0 ± 0.5	2.9 ± 0.2
CRL 2688	3.3 ± 0.3	3.4 ± 0.6	3.2 ± 0.3	3.3 ± 0.2
CRL 618	2.5 ± 0.6	3.0 ± 0.1	5.5 ± 0.8	3.0 ± 0.5
IRC +10216	1.8 ± 0.1	5.7 ± 0.1	1.2 ± 0.1	5.5 ± 0.2

Table 8: Carbon Isotope Ratios in Circumstellar Envelopes From CN and CO

Source	$^{12}\text{CO}/^{13}\text{CO}$	$^{12}\text{CN}/^{13}\text{CN}$	Other
AFGL 190	≥ 20	> 5	$> 22^a$
AFGL 809	≥ 28	> 5	-
AFGL 865	≥ 13	> 14	$> 15^a$
IRC +40540	40	15-20	55^f
CRL 2688	-	57-66	$32^d, 20^h$
CRL 618	-	> 32	$30^d, 12^h$
CIT 6	30	11-37	$12-35^e, 17-31^{a,d}$
IRC +10216	25	> 36	$32^b, 25-45^c, 44^d, 50^f$
V Hya	23-35	> 16	$33^e, 69^j$
Y CVn	3	2-8	$2.5^f, 3.4^e$
S Cep	37	> 16	$> 15^e$
IRC +10420	14	-	7^i
α Ori	8	-	$7^g, 4^k$
VY CMa	46, 25*	> 3	36^j
IRC +00365	70	> 7	$\sim 57^b$
UU Aur	90	-	$\sim 45^f$
89 Her	3-4	-	-
χ Cyg	33	> 11	$25^g, 35-63^h$
OH231.8+4.2	~ 3	-	$5-10^l$
TX Cam	31	> 3	-
W Hya	35	-	-
NML Cyg	13	> 1	10^l
IK Tau	10	> 1	10^l

References: Italicized values are measurements derived from the photosphere. (a) Groenewegen, et al. 1996 – CO; (b) Greaves & Holland 1997 – CO; (c) Woods et al. 2003 – CO and CN; (d) Kahane et al. 1992 – CO (e) Jura, Kahane, & Omont 1988 – CO (f) Schoier & Olofsson 2000 – CO; (g) Hinkle, Lambert, & Snell 1976 – photosphere CO and CN; (h) Wannier and Sahai 1987 – CO; (i) Lambert et al. 1986 – photosphere CN; (j) Sanchez Contreras et al. 2000 – HCN; (k) Huggins 1987 – CO; (l) Nercissian et al. 1989 – HCN

* From outflows vs. spherical wind (see text).

Figure Captions:

Figure 1: ^{12}CO (upper panel) and ^{13}CO (lower panel) spectra obtained from the ARO 12m and SMT. Data are plotted as a function of LSR velocity and T_A^* (K), where the 12m data has been converted from T_R^* to T_A^* by $\eta_{\text{fss}} = 0.68$.

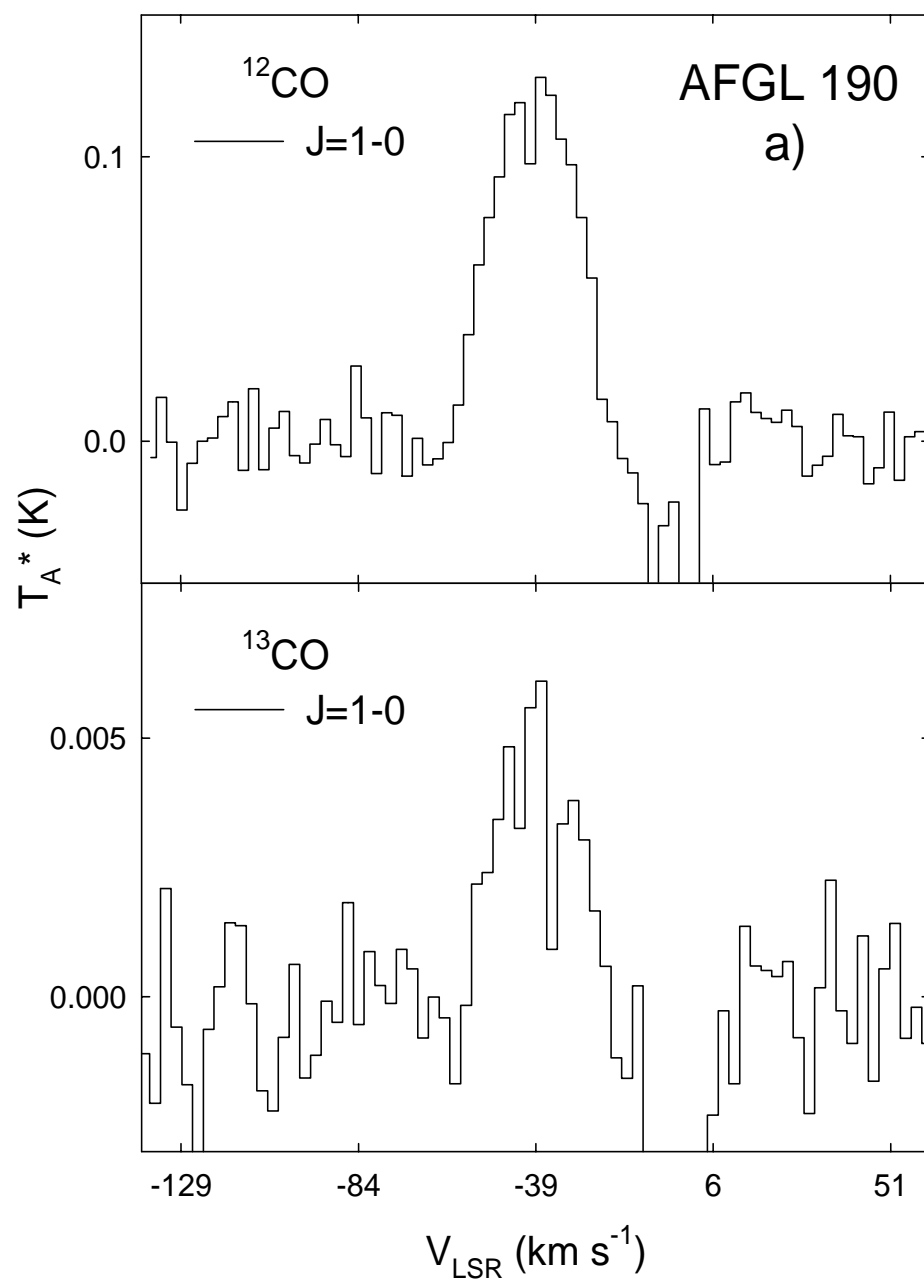
Figure 2: Energy level diagram of ^{12}CN for $N=0, 1, \text{ and } 2$. Energy scale is arbitrary. Observed transitions are indicated by the arrows.

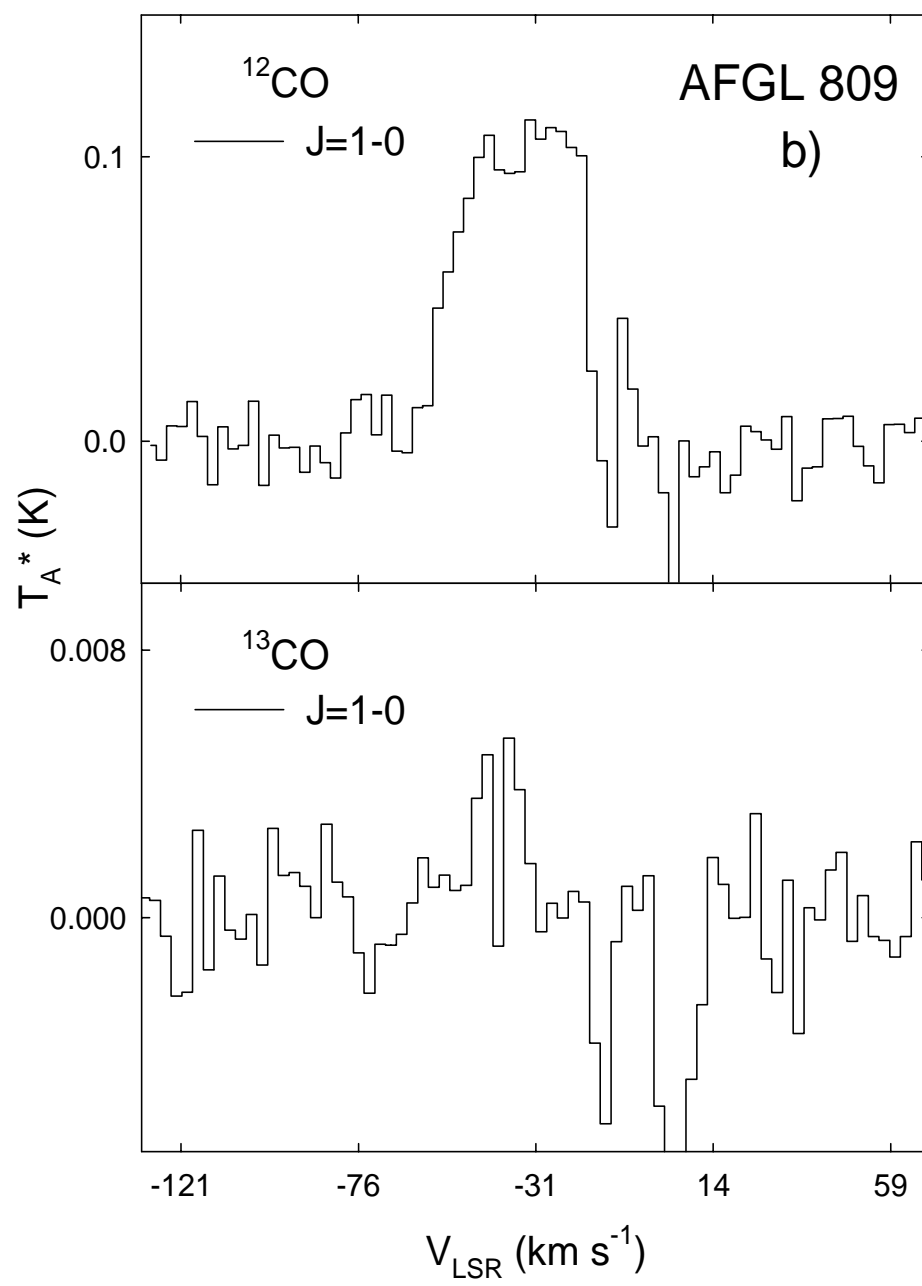
Figure 3: The $N=1 \rightarrow 0$ hyperfine splitting of ^{12}CN (upper panel) and ^{13}CN (lower panel). Relative intensities are plotted below each spectrum and are labeled by F, the hyperfine transition.

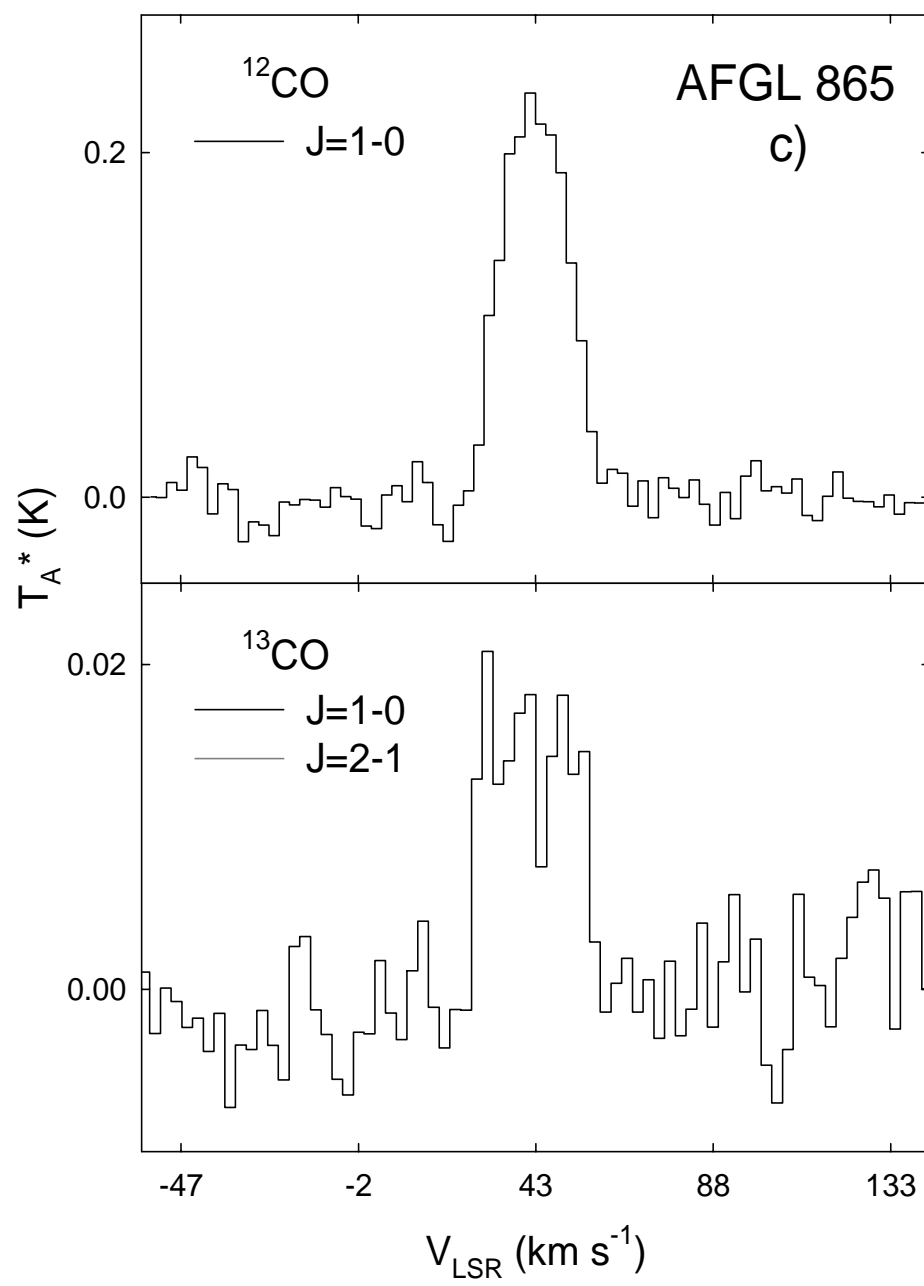
Figure 4: The $N=2 \rightarrow 1$ fine and hyperfine splitting of ^{12}CN . The relative intensities are plotted below each spectrum and are labeled by their respective hyperfine transition found in Table 1.

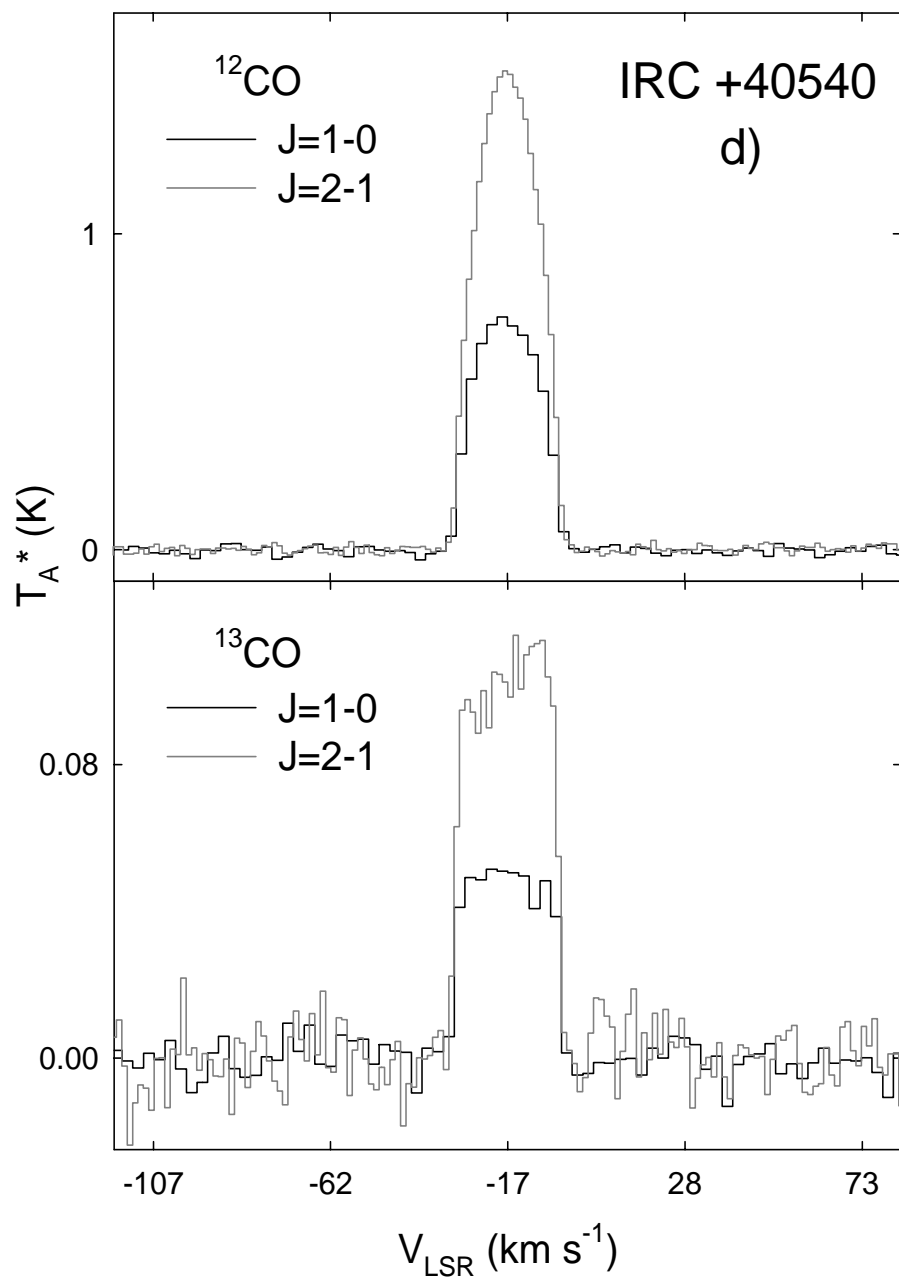
Figure 5: Observed CN spectra isotopologs for $N=1 \rightarrow 0$ and $N=2 \rightarrow 1$. The ^{12}CN , $N=2 \rightarrow 1$ data are represented by $J=5/2 \rightarrow 3/2$. All data are in 1 MHz resolution, excluding SgrB2(OH), W33, G34.3, Orion A, Orion KL, NGC 2024, NGC 7538, and W3(OH) where the resolution is 782 kHz. Hyperfine structure and respective relative intensities are plotted below each spectrum.

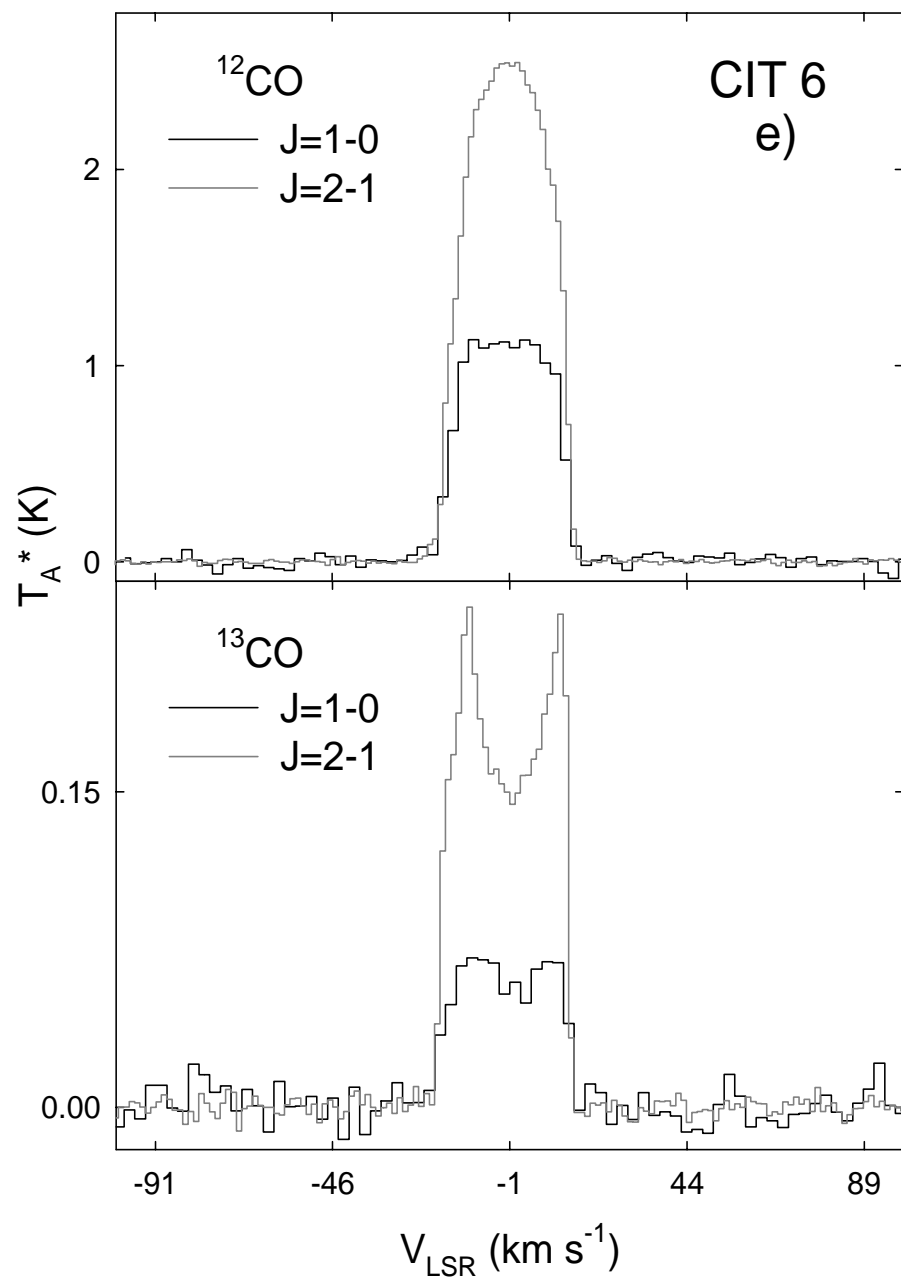
Figure 6: C/O vs. $^{12}\text{C}/^{13}\text{C}$ ratios for sample stars (black dots). The local ISM value is plotted with a black dashed line to denote the $^{12}\text{C}/^{13}\text{C}$ ratio ~ 60 . Gray dotted line marks the Solar C/O ratio and the Gray dash-dot line displays a C/O value of 1. The gray triangles are modeled values where the hydrogen-burning shell mixing levels are 1:1 (A), 2:1 (B), 10:1 (C), and all (D). These are followed by the helium-burning shell mixing levels of 1% (E), 2% (F), and 5% (G). The large gray arrow shows an evolutionary path of the C/O ratio with $^{12}\text{C}/^{13}\text{C}$ (see text).

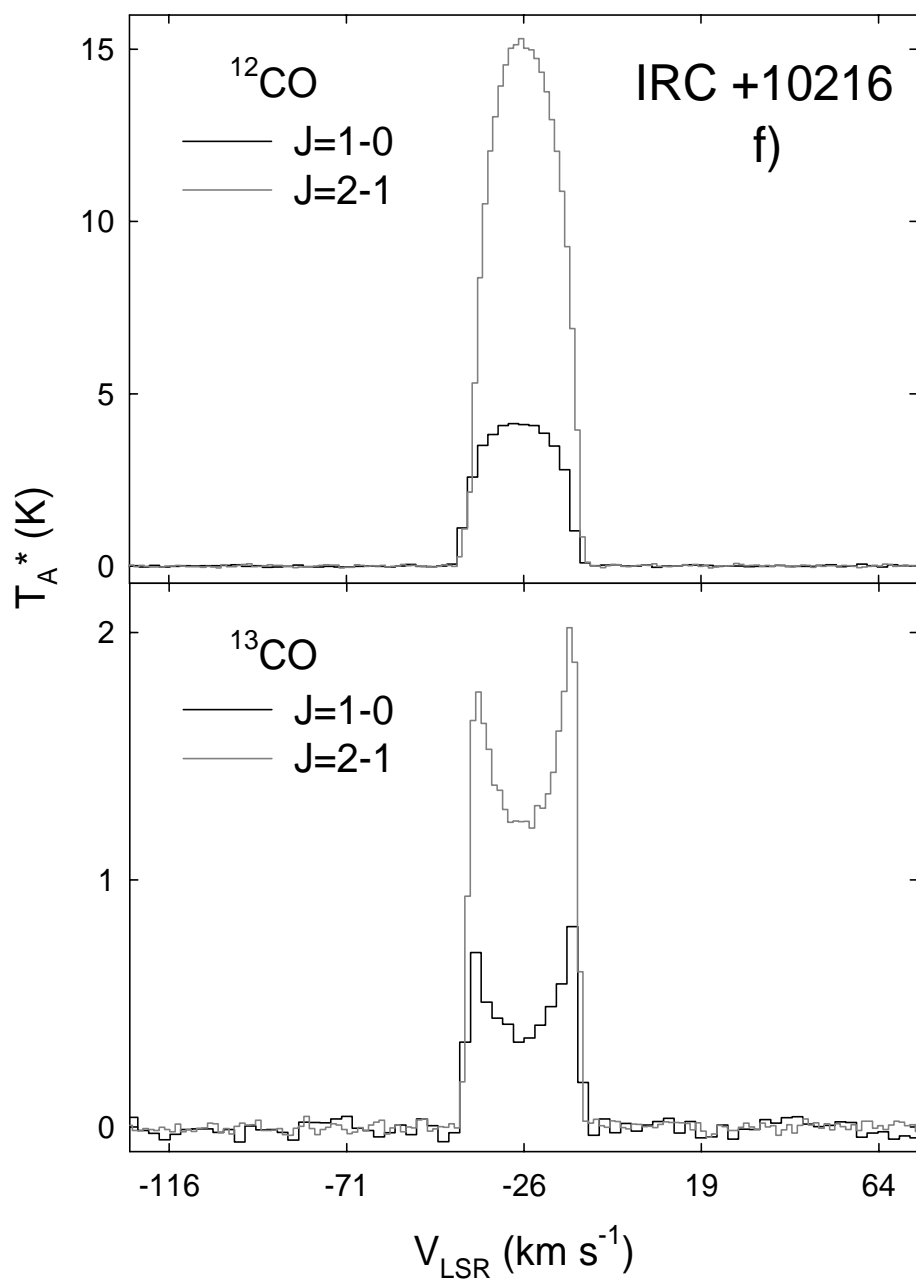


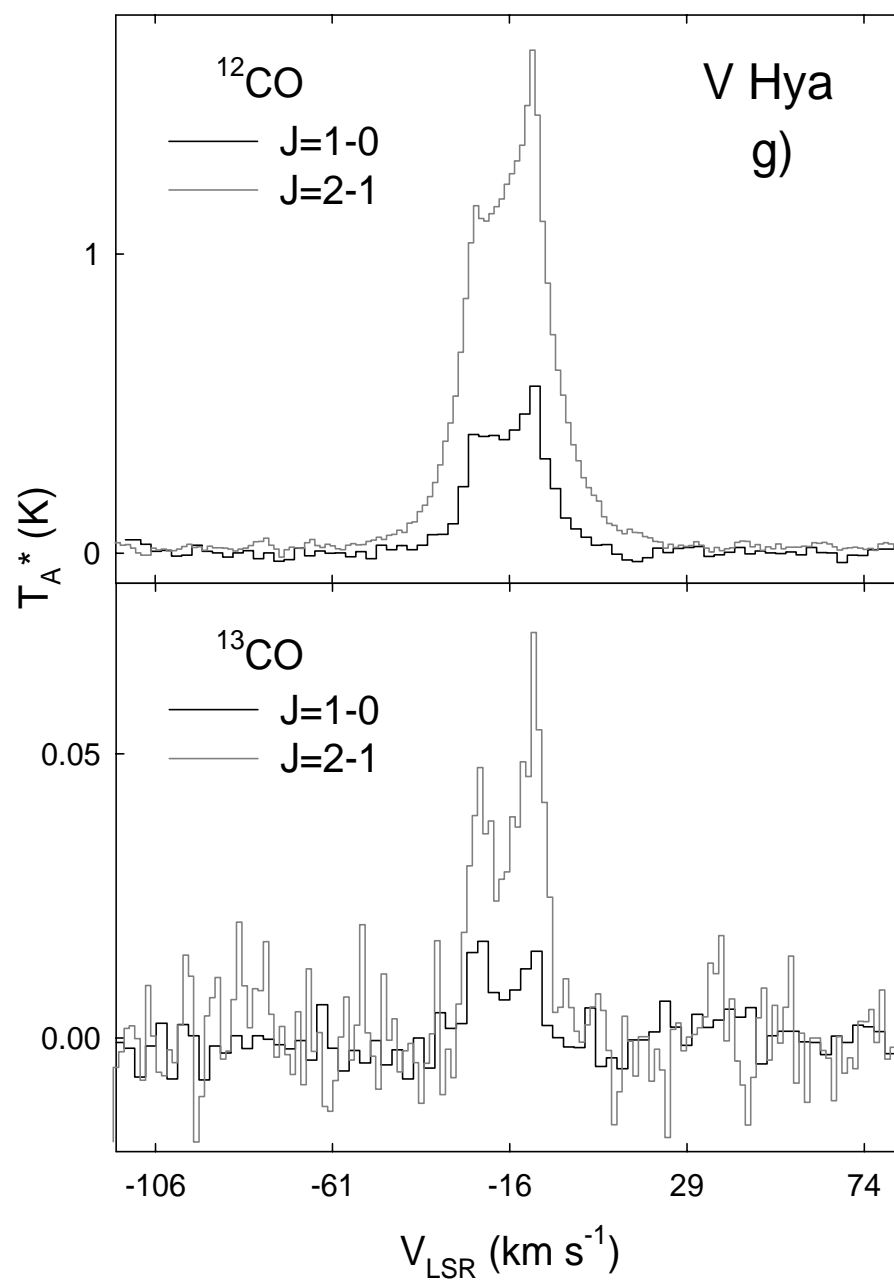


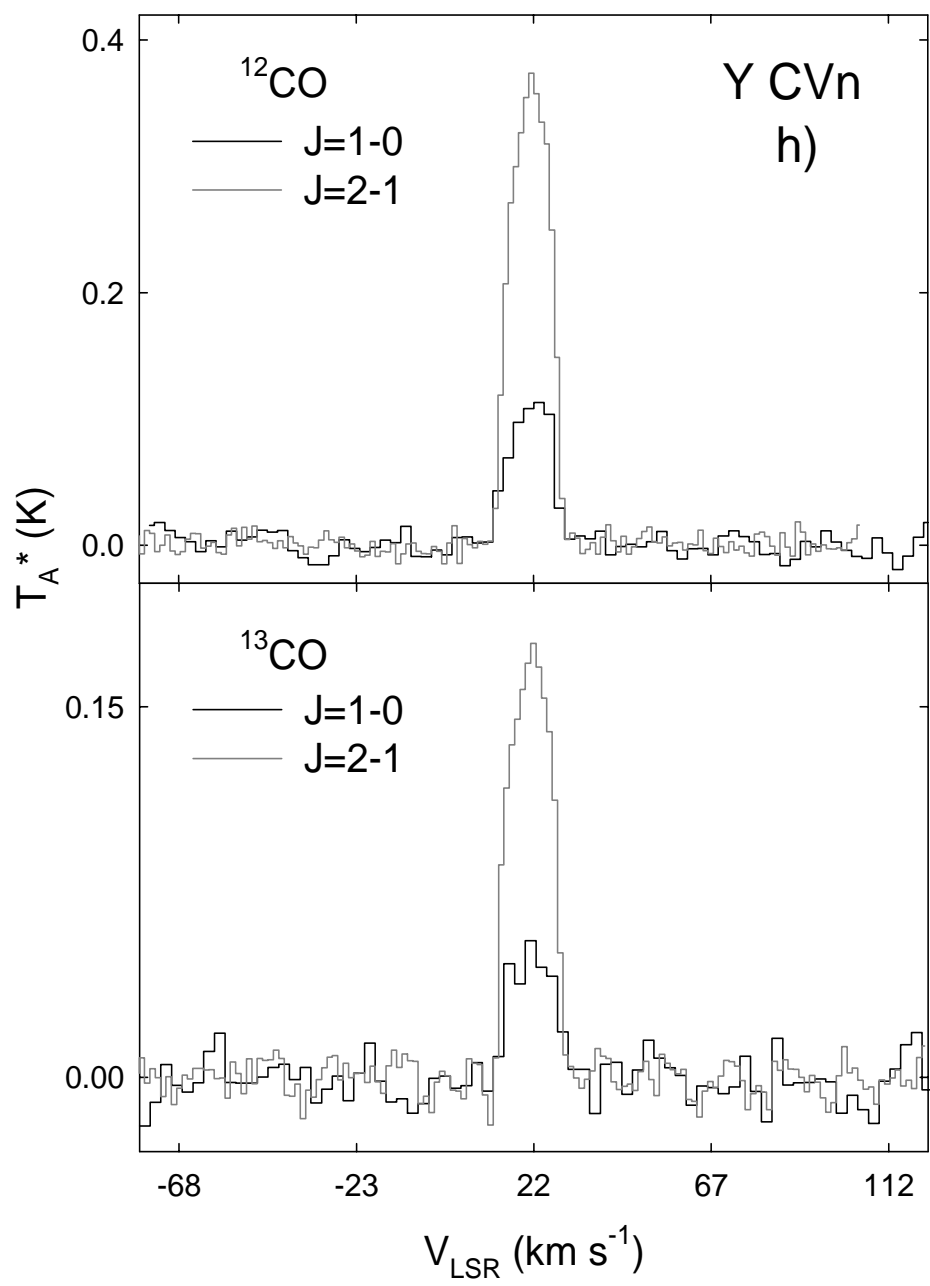


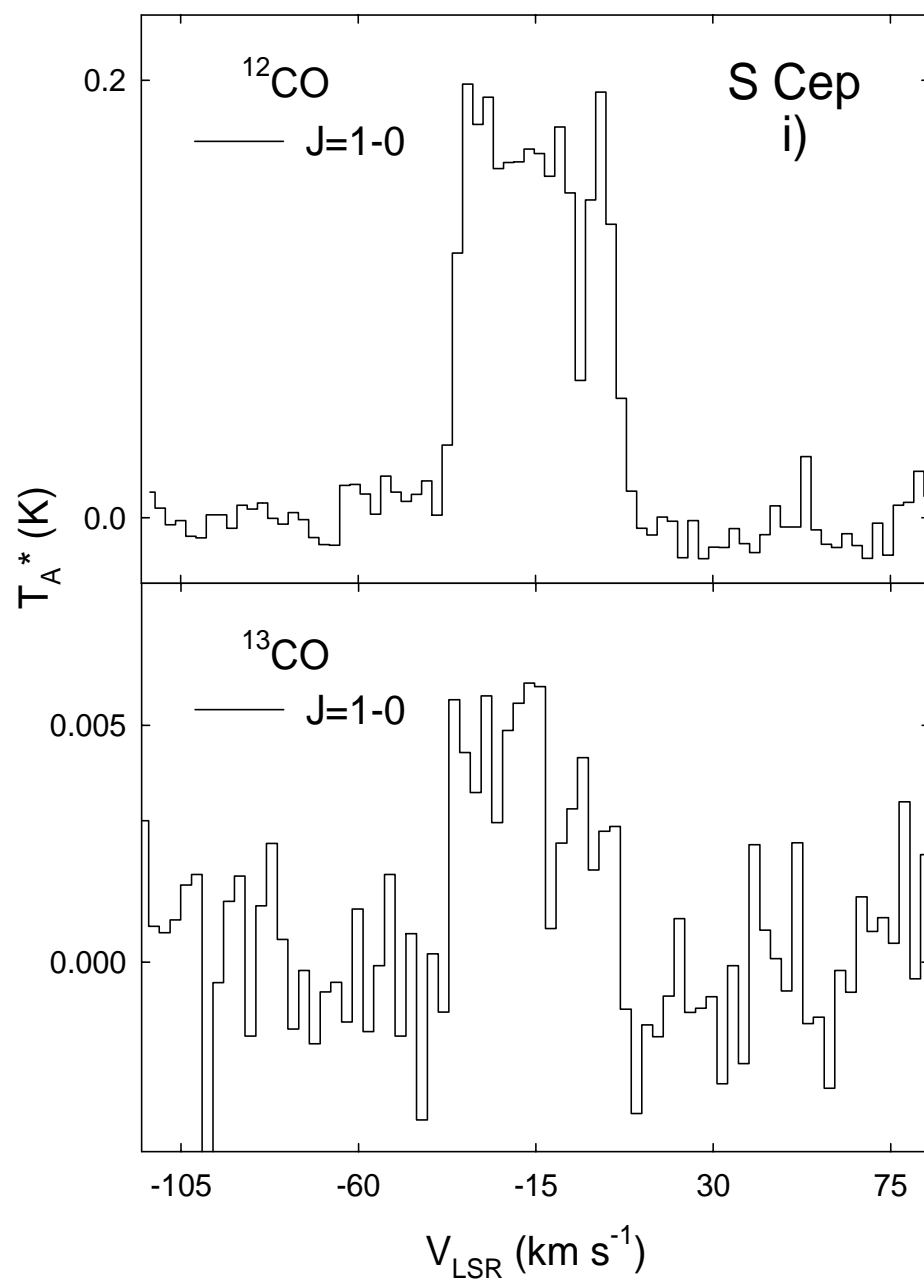


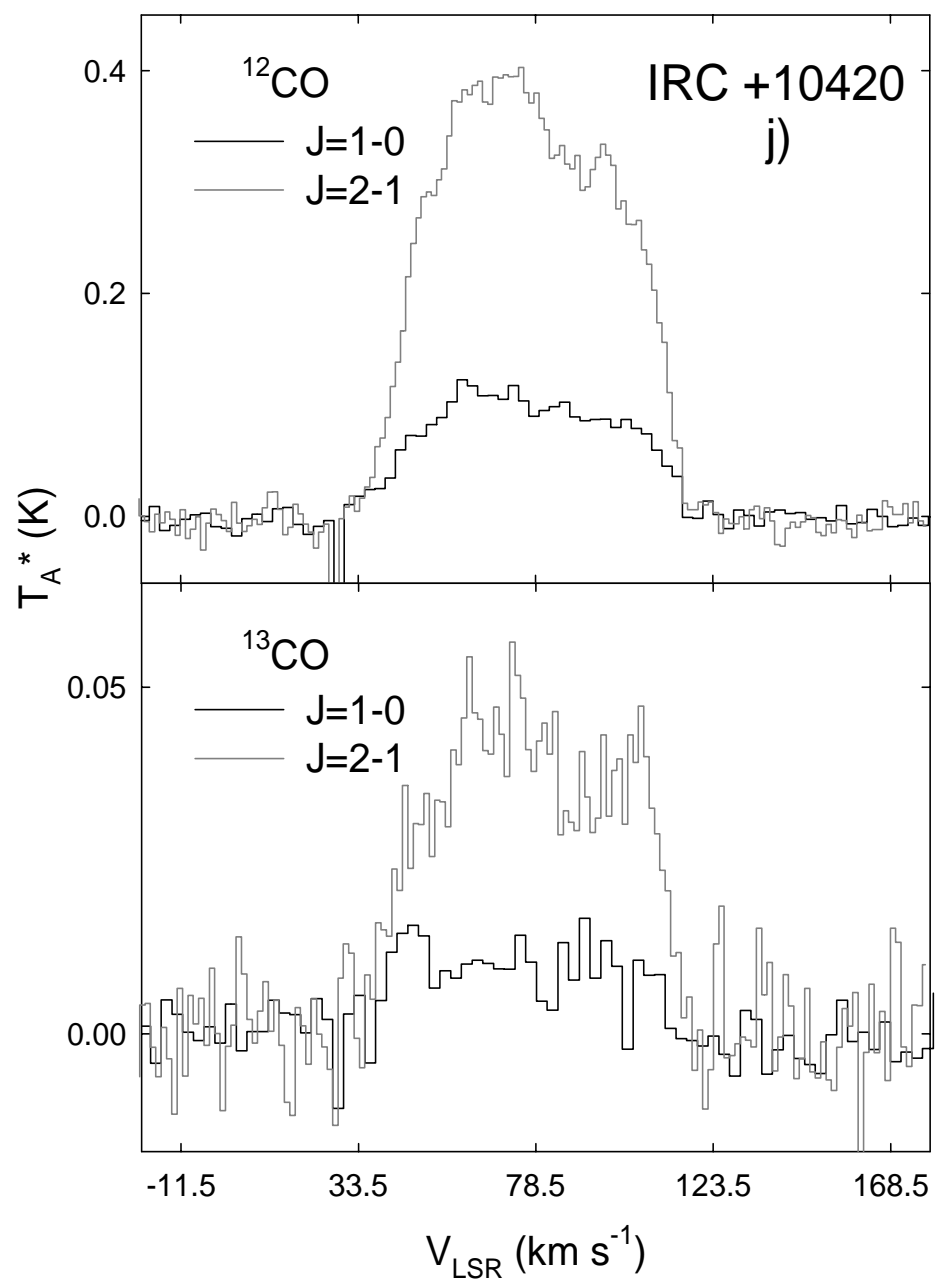


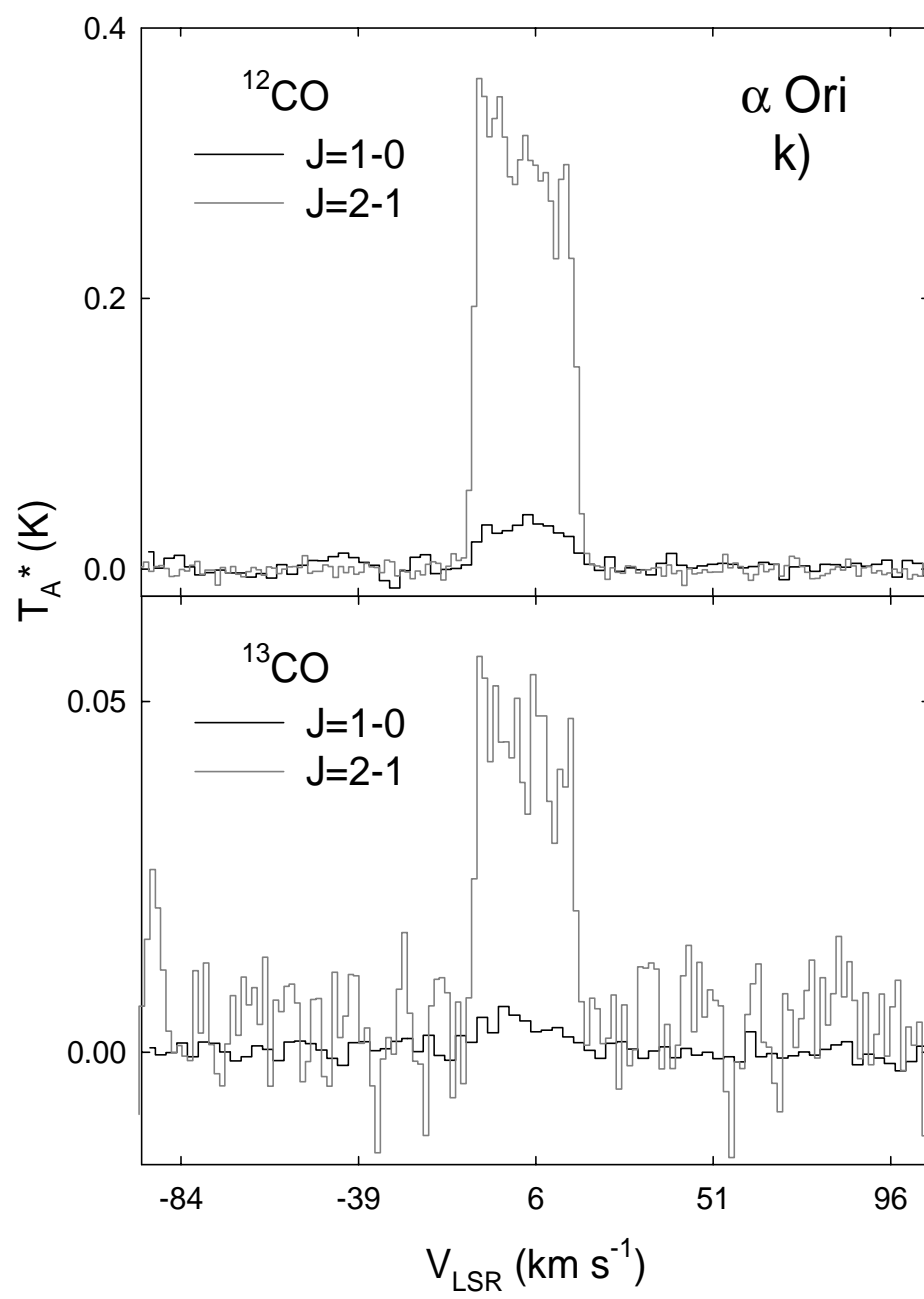


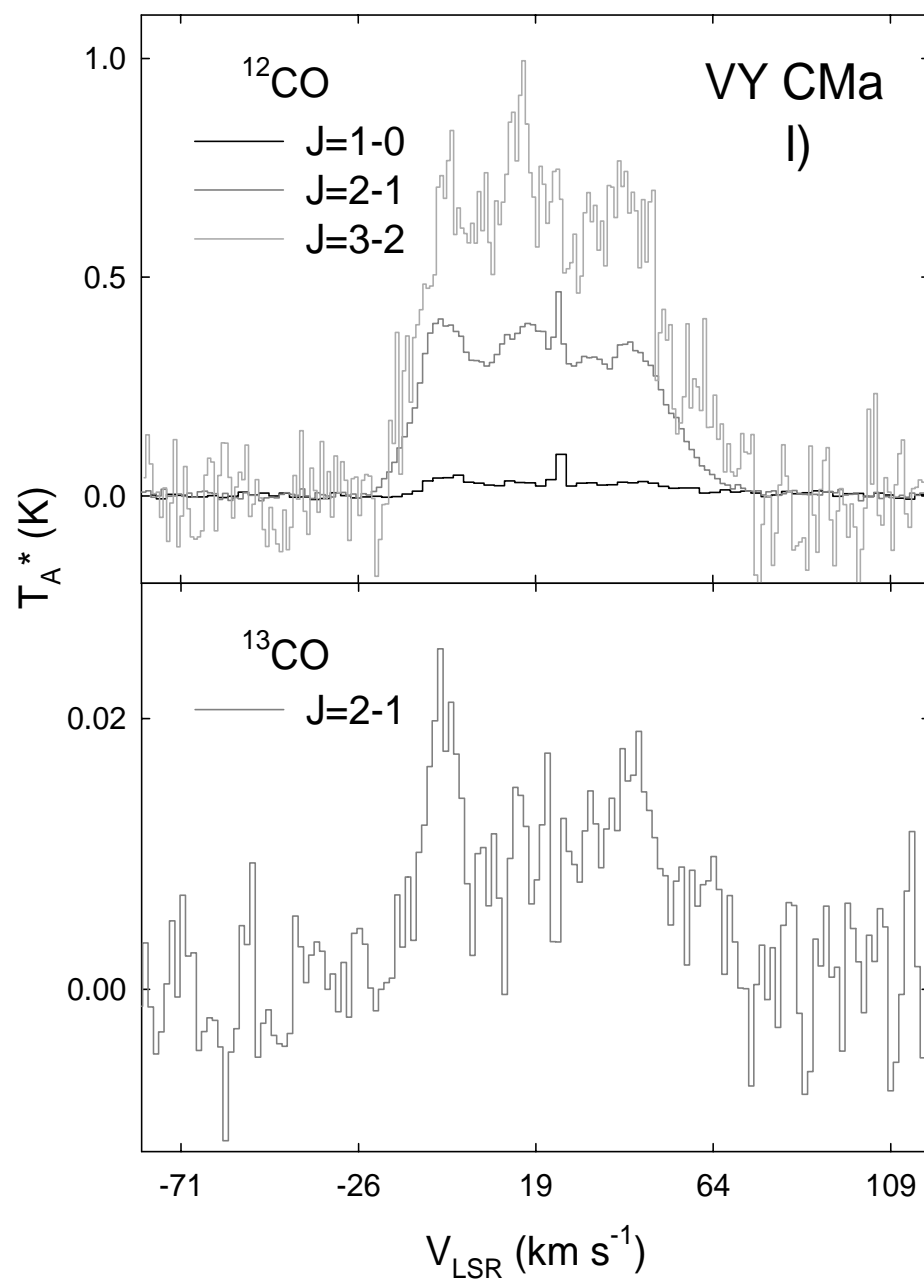


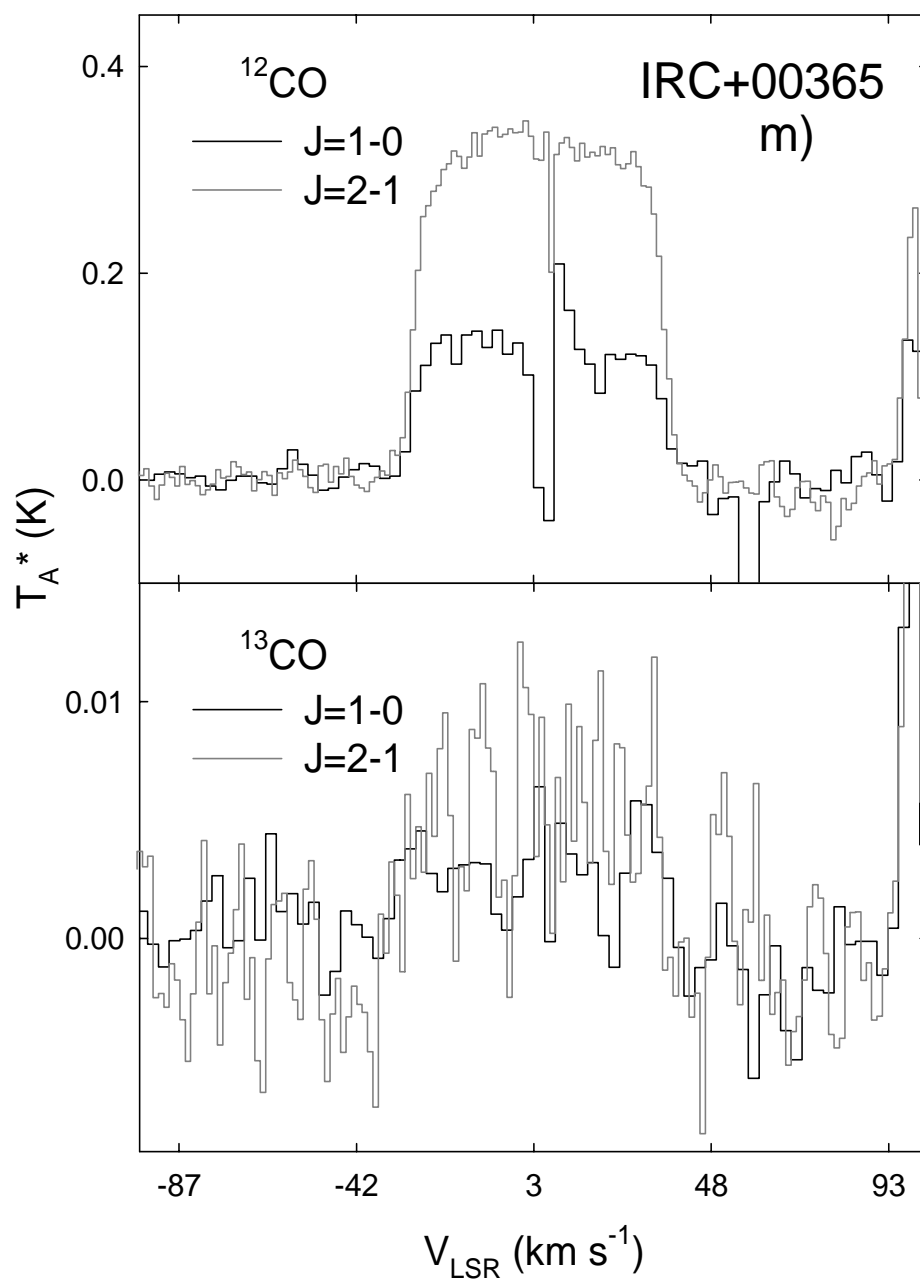


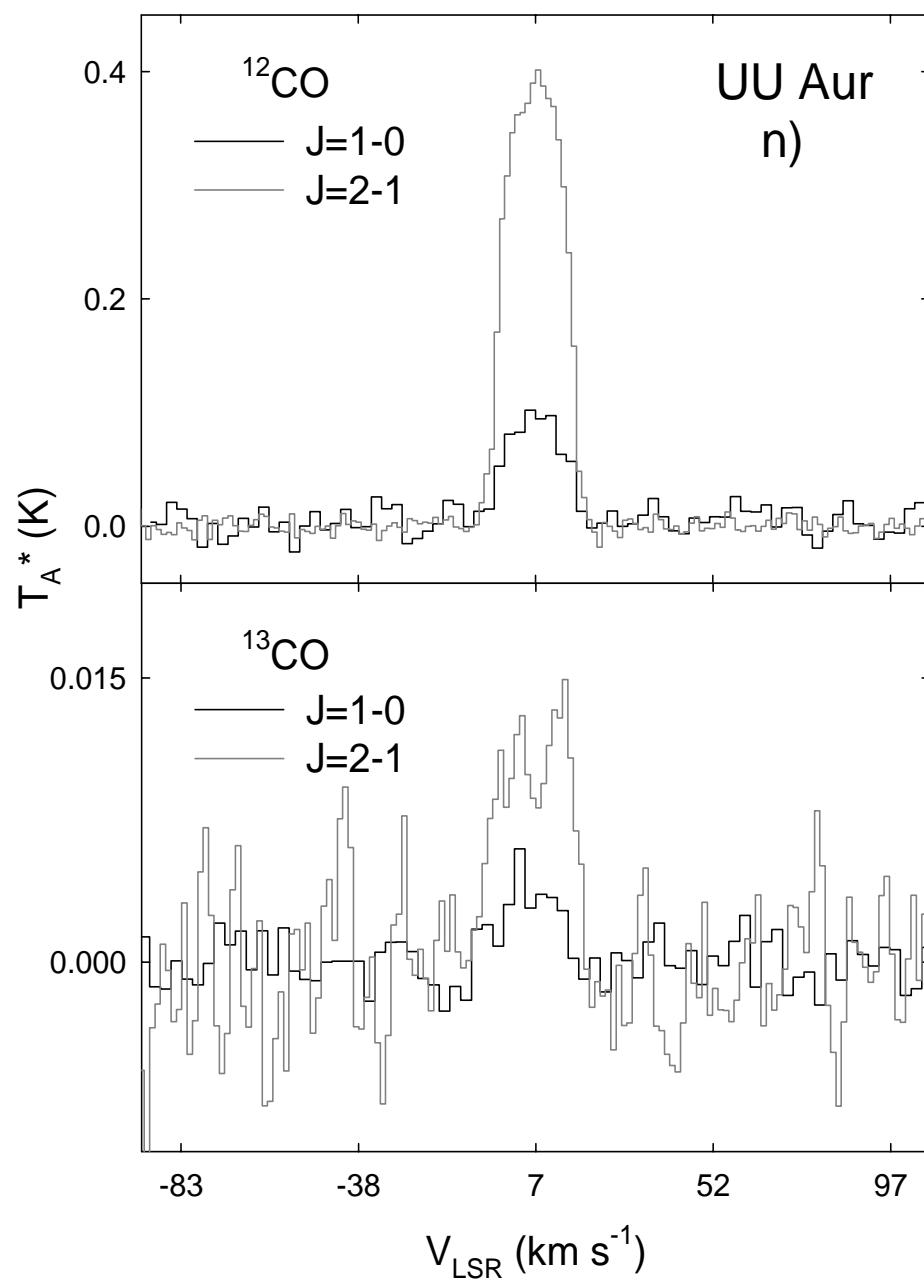


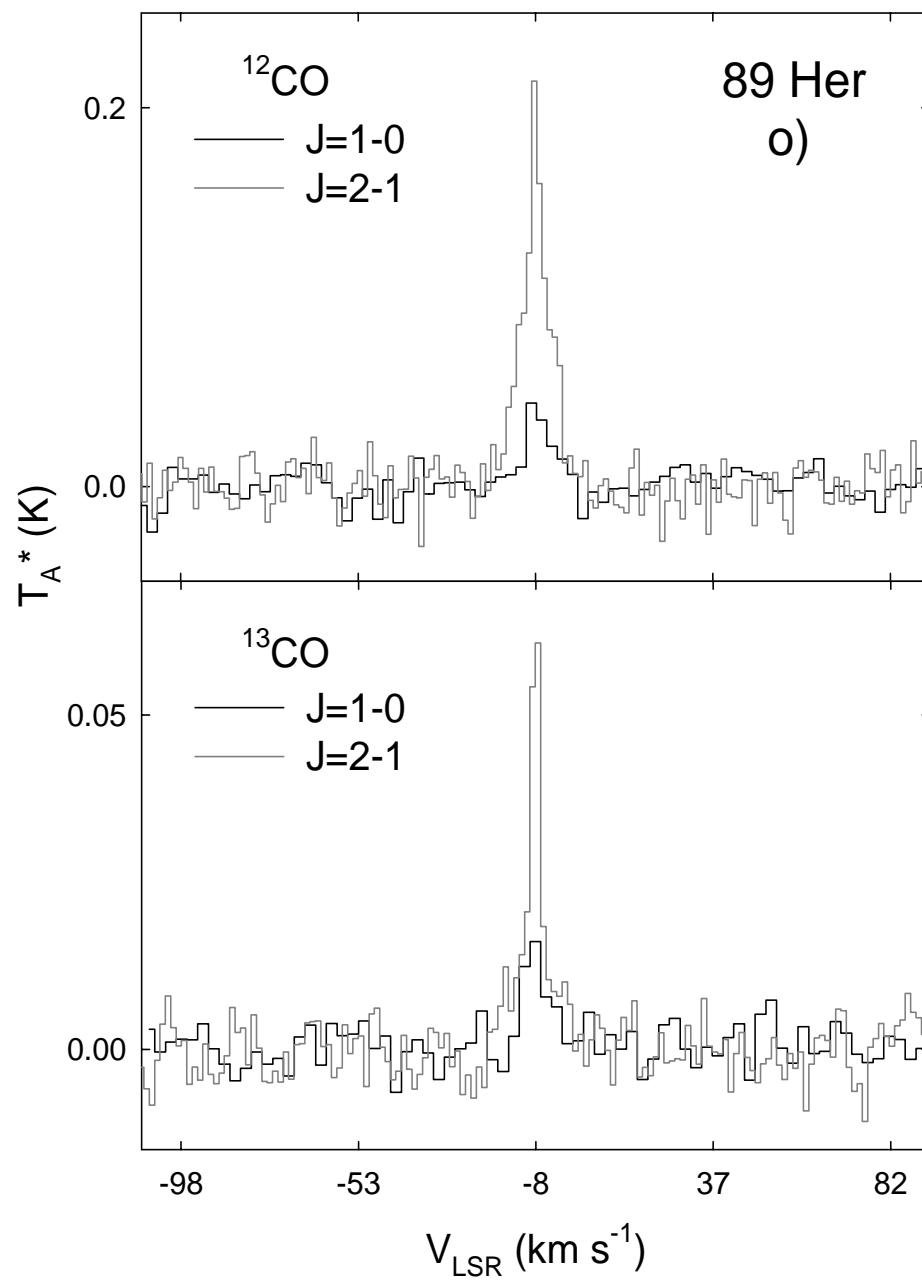


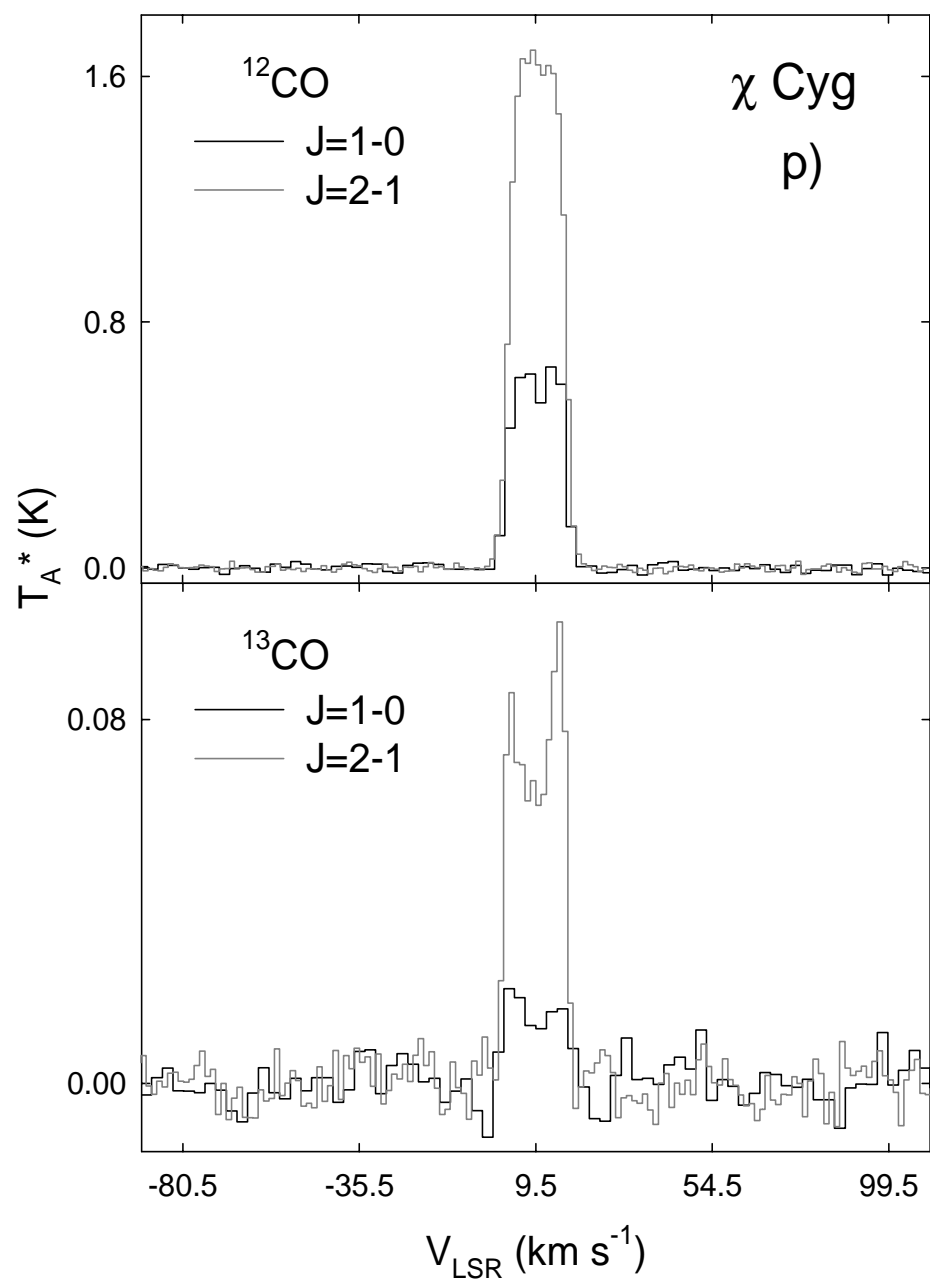


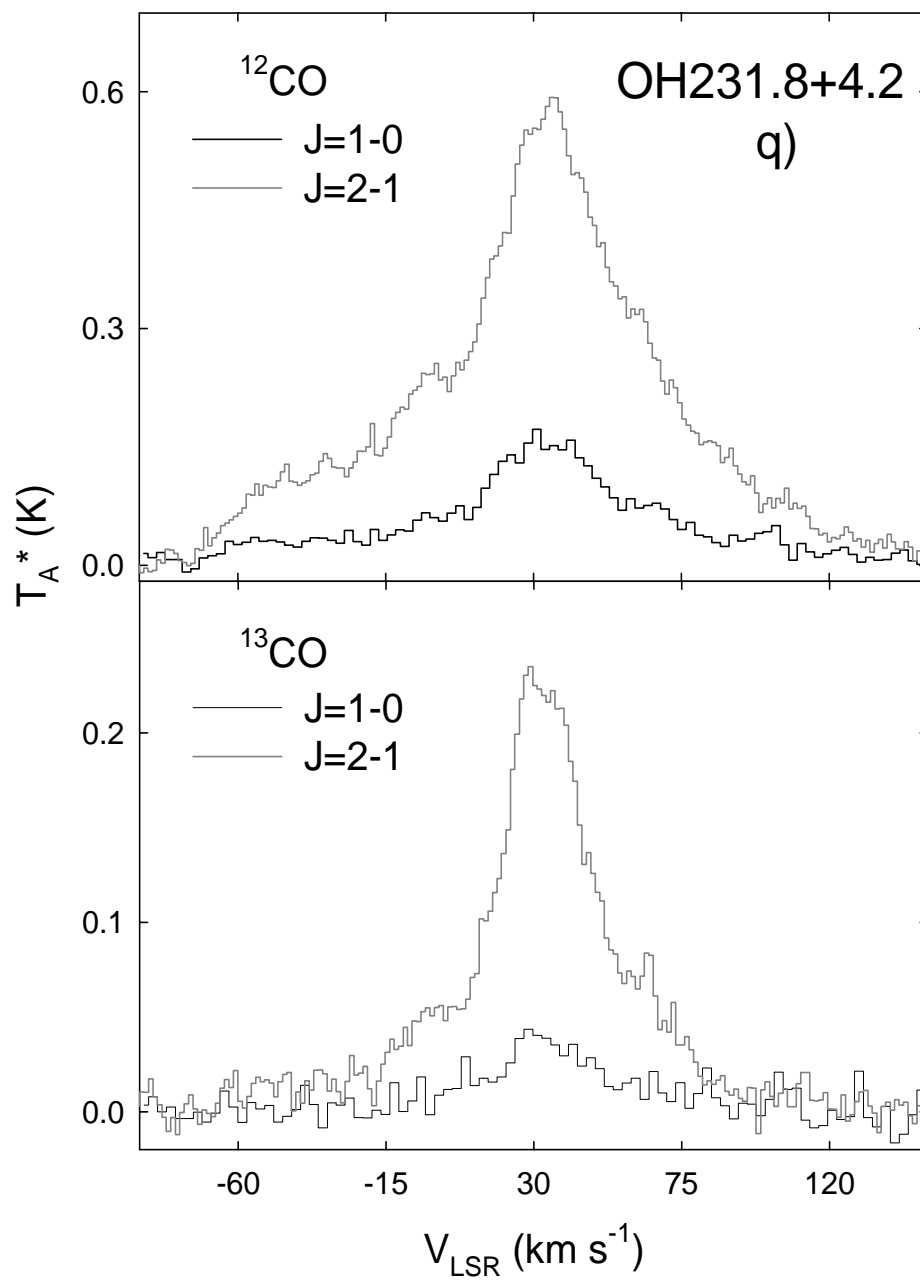


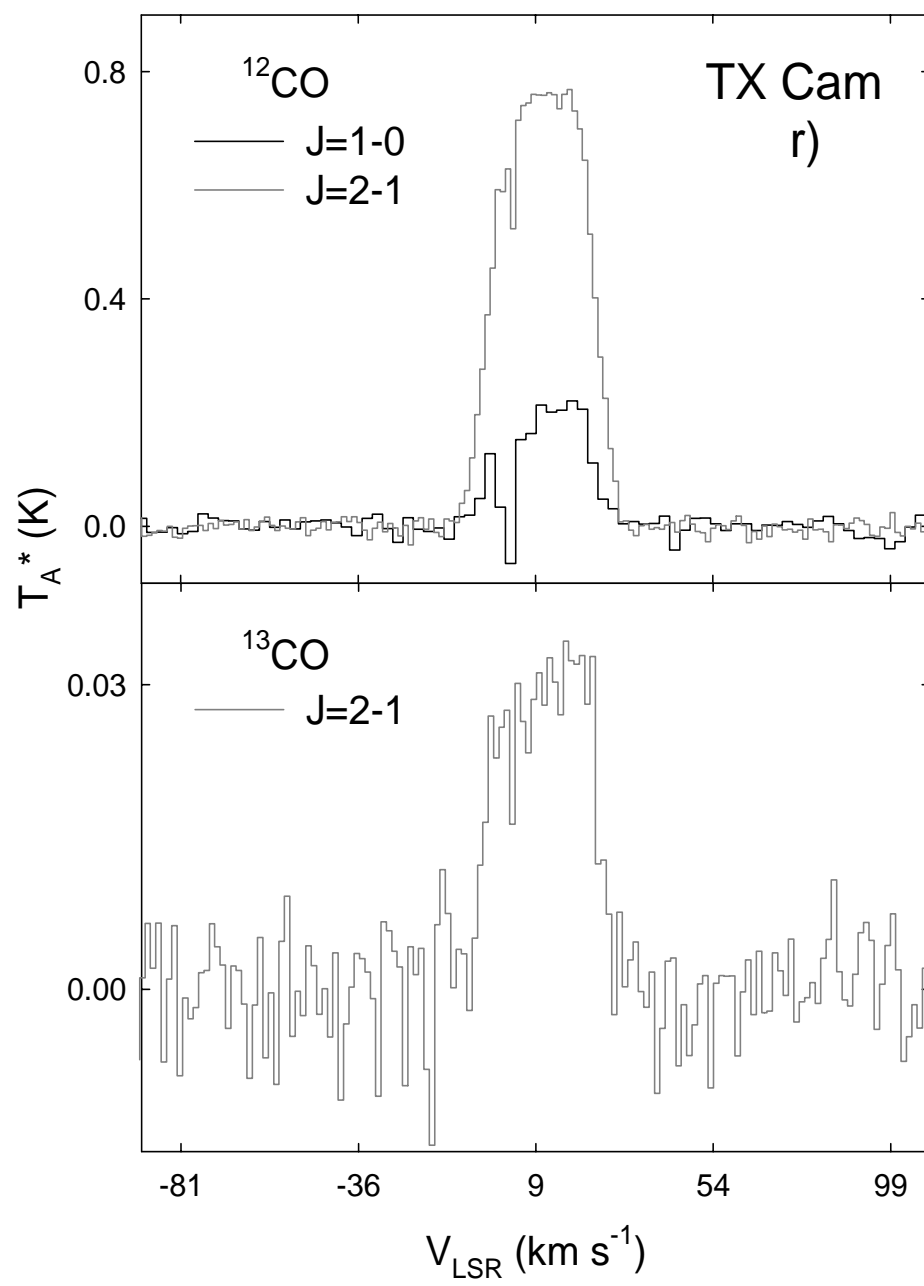


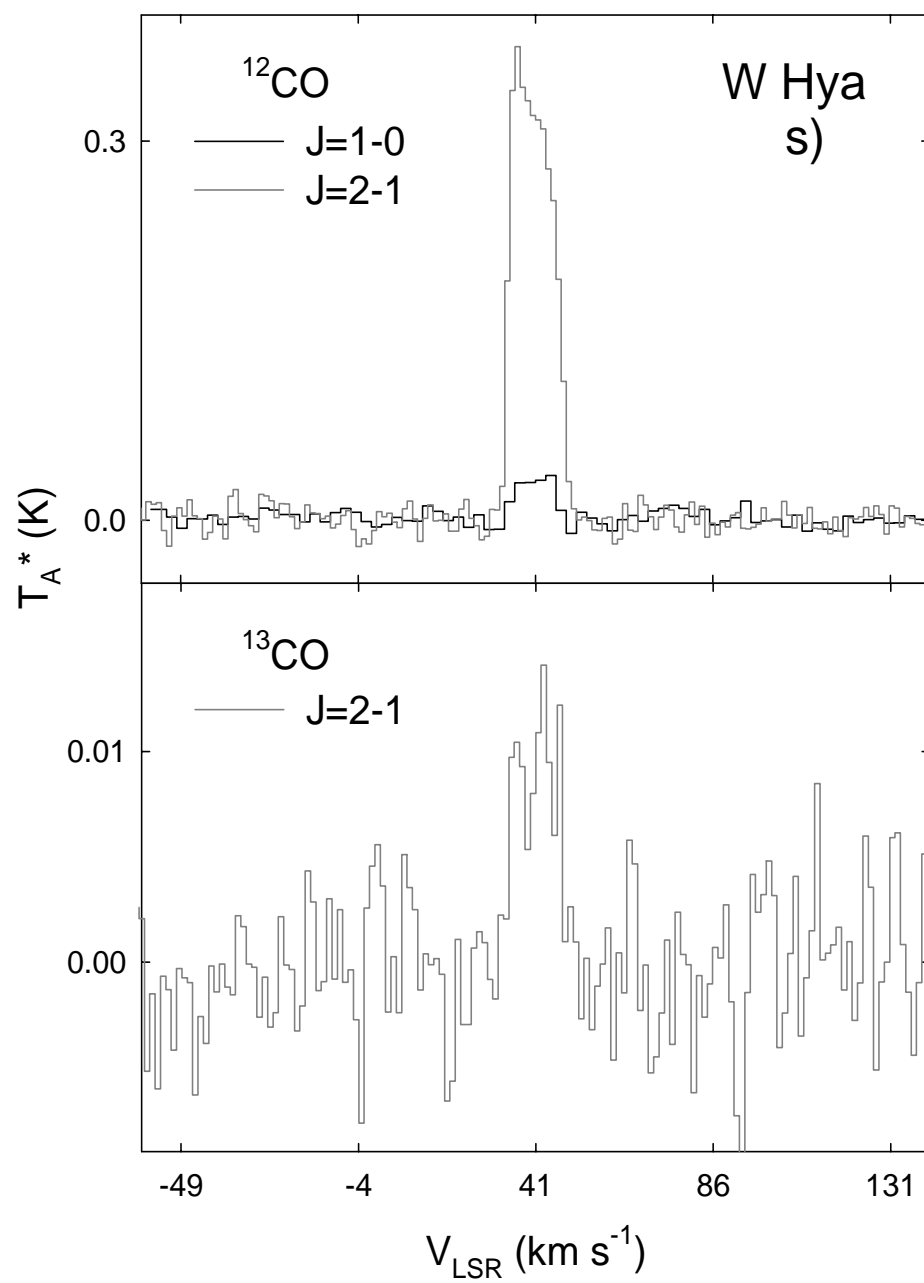


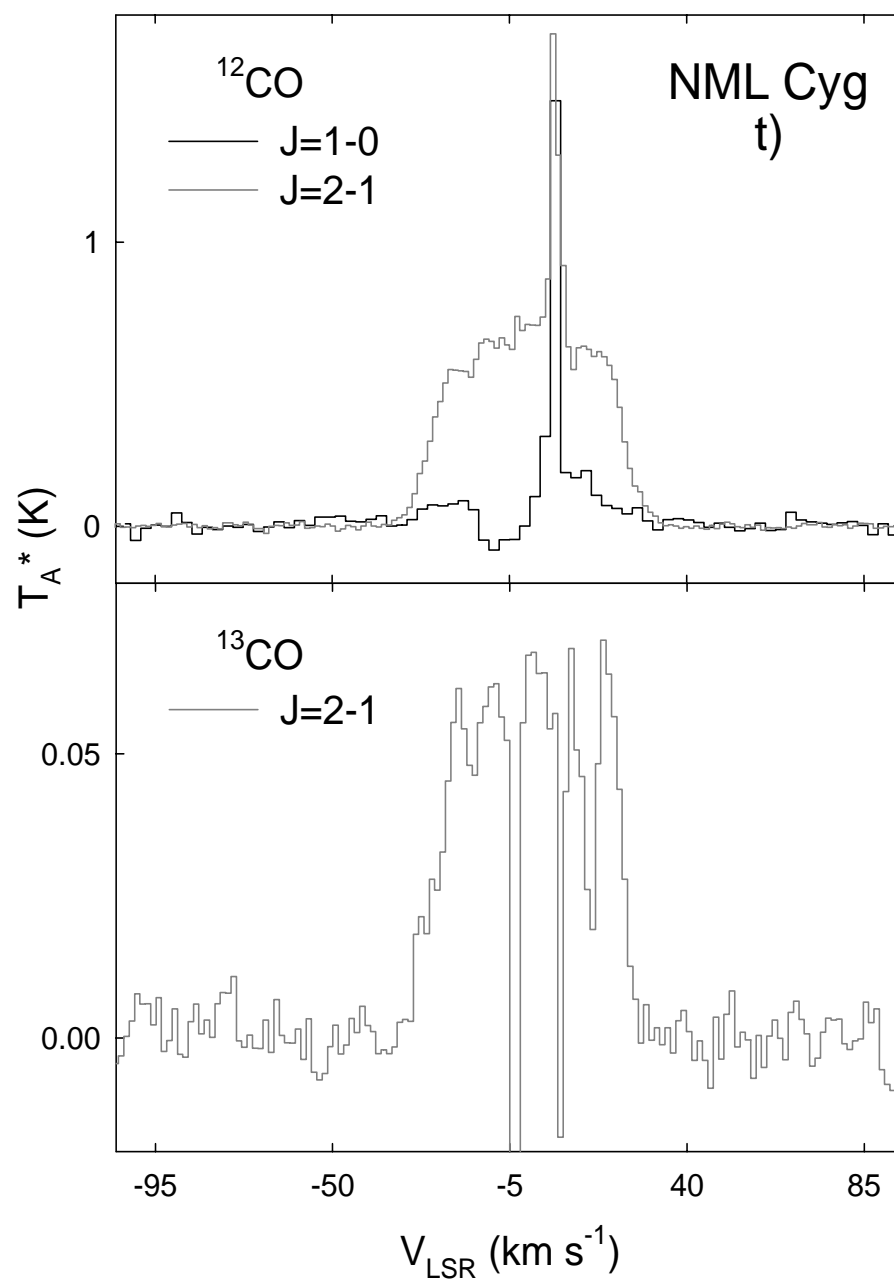


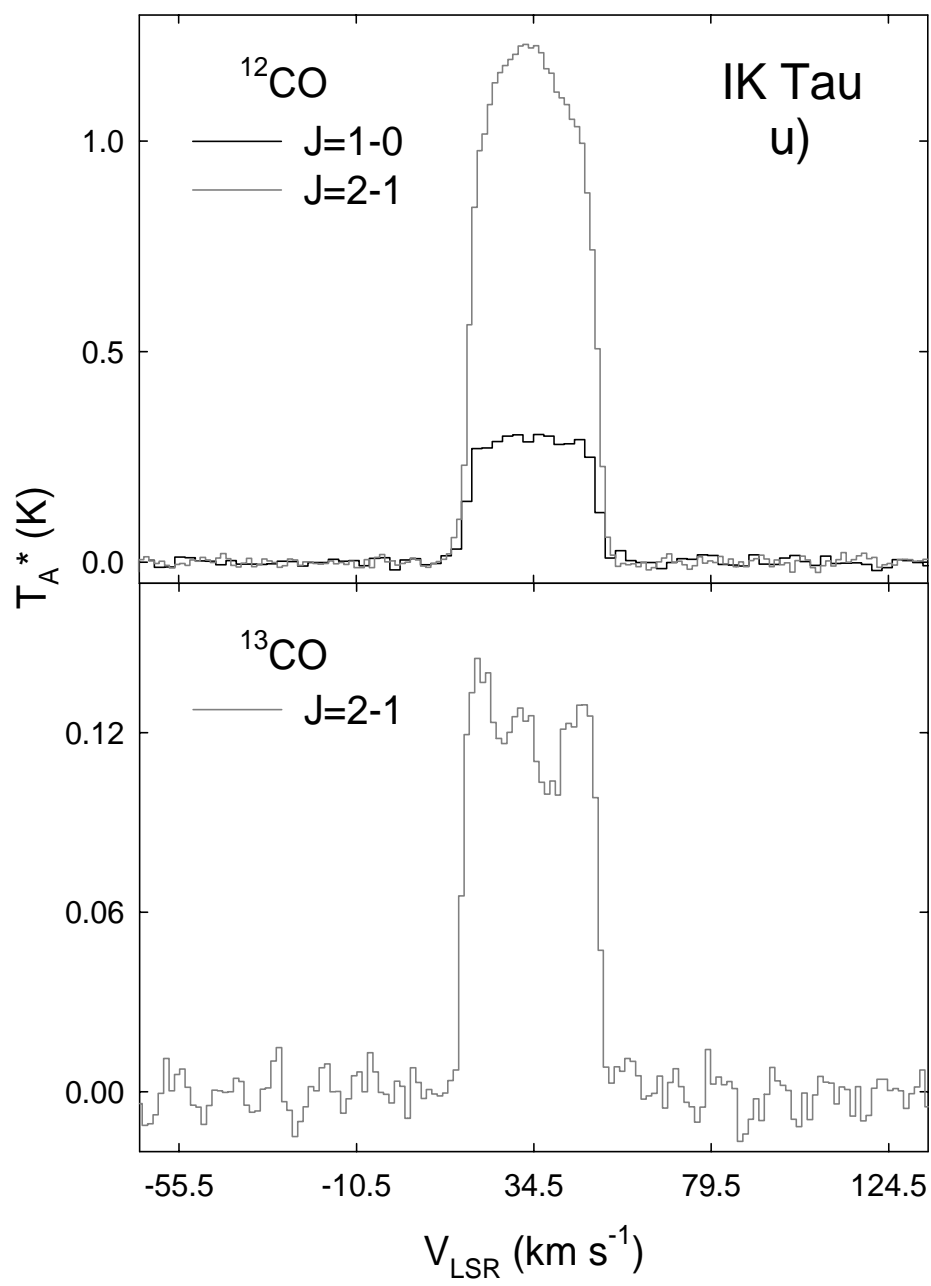


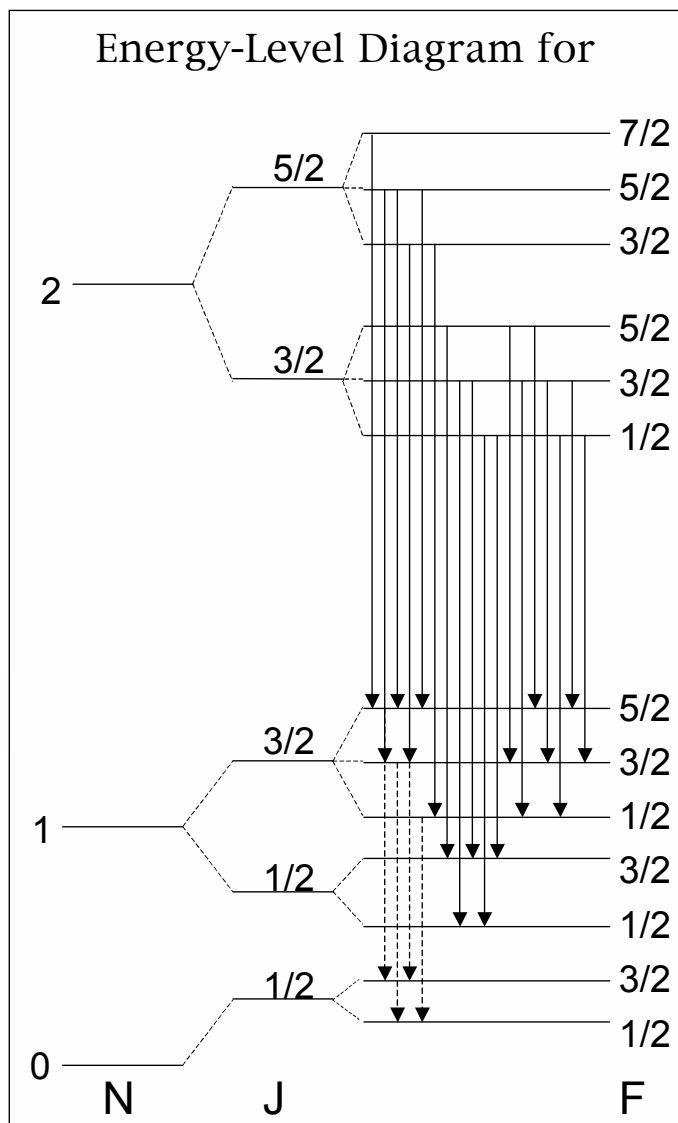


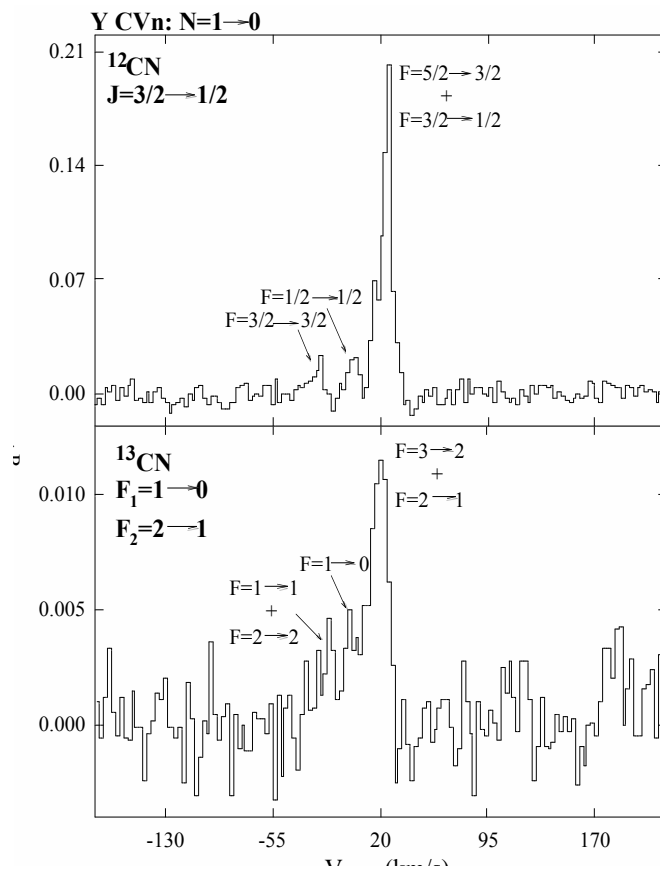


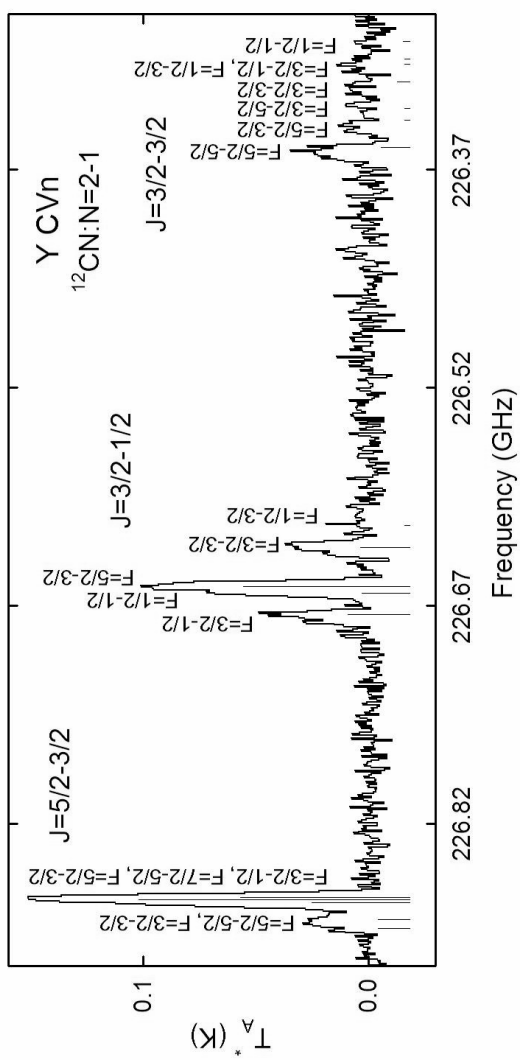


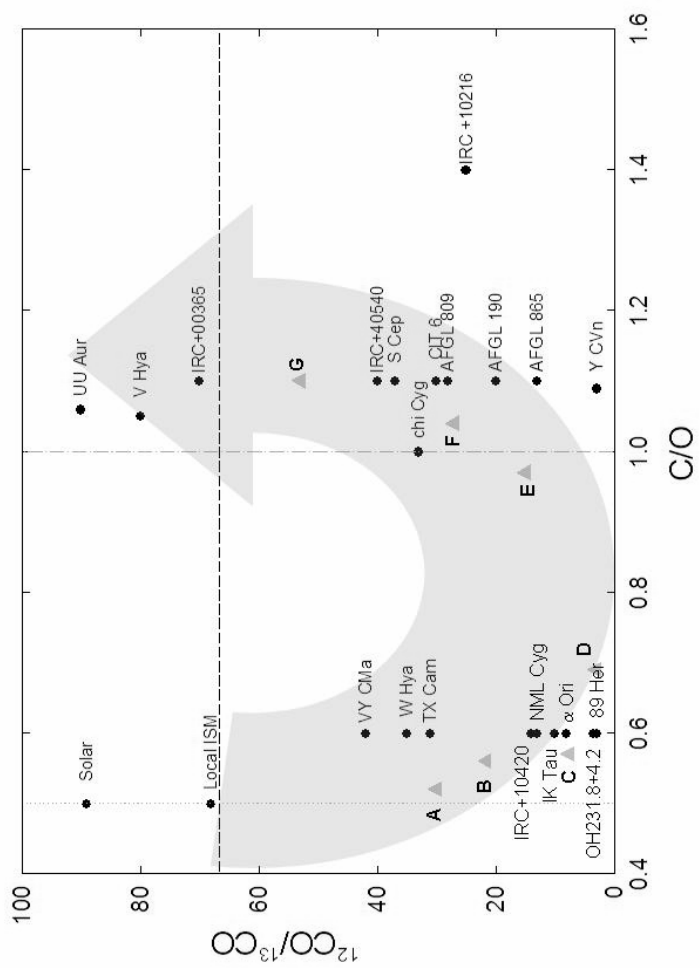


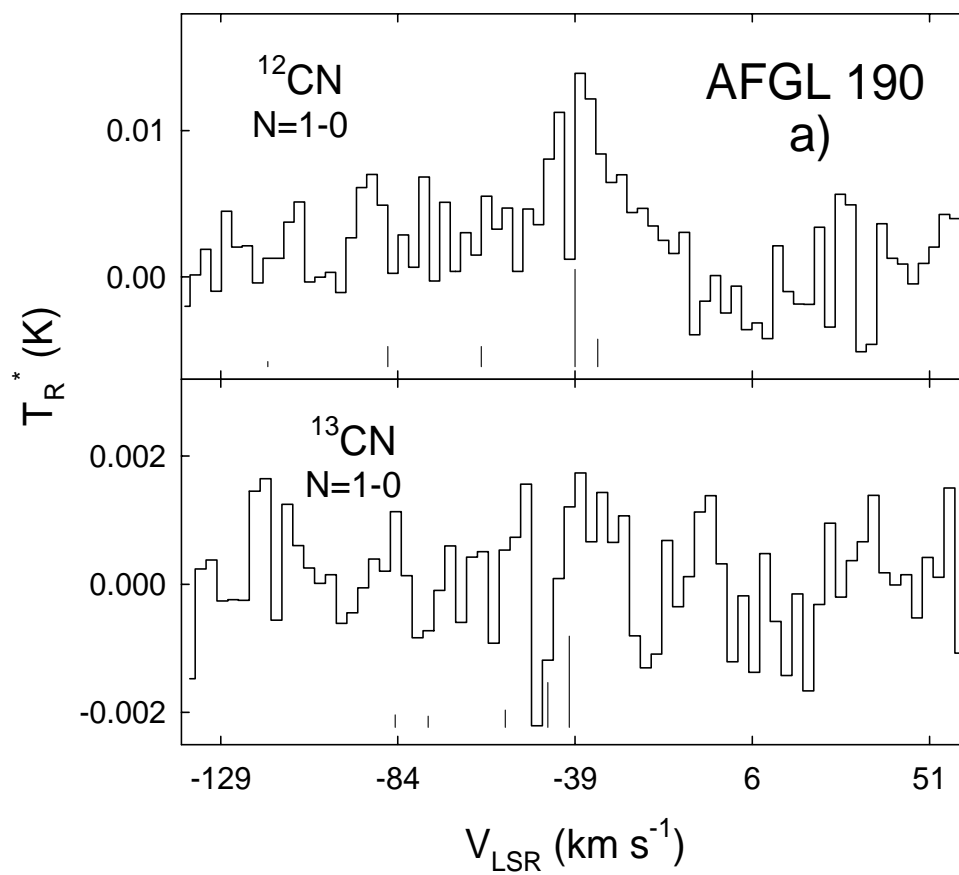


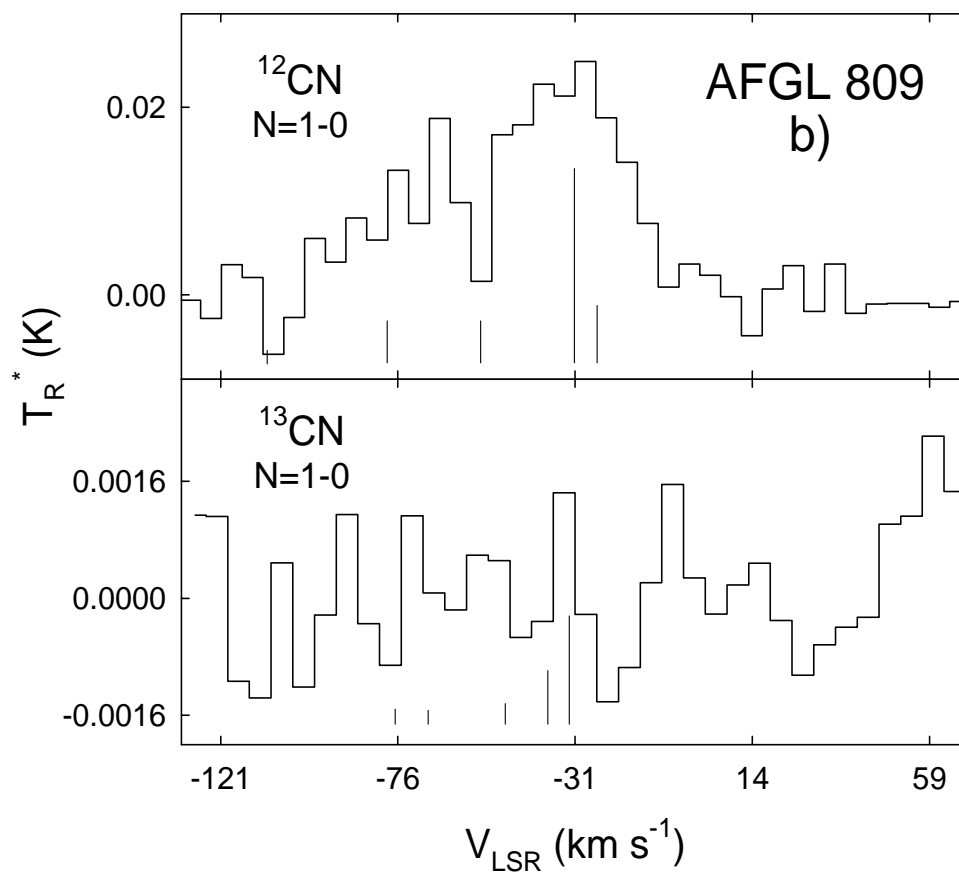


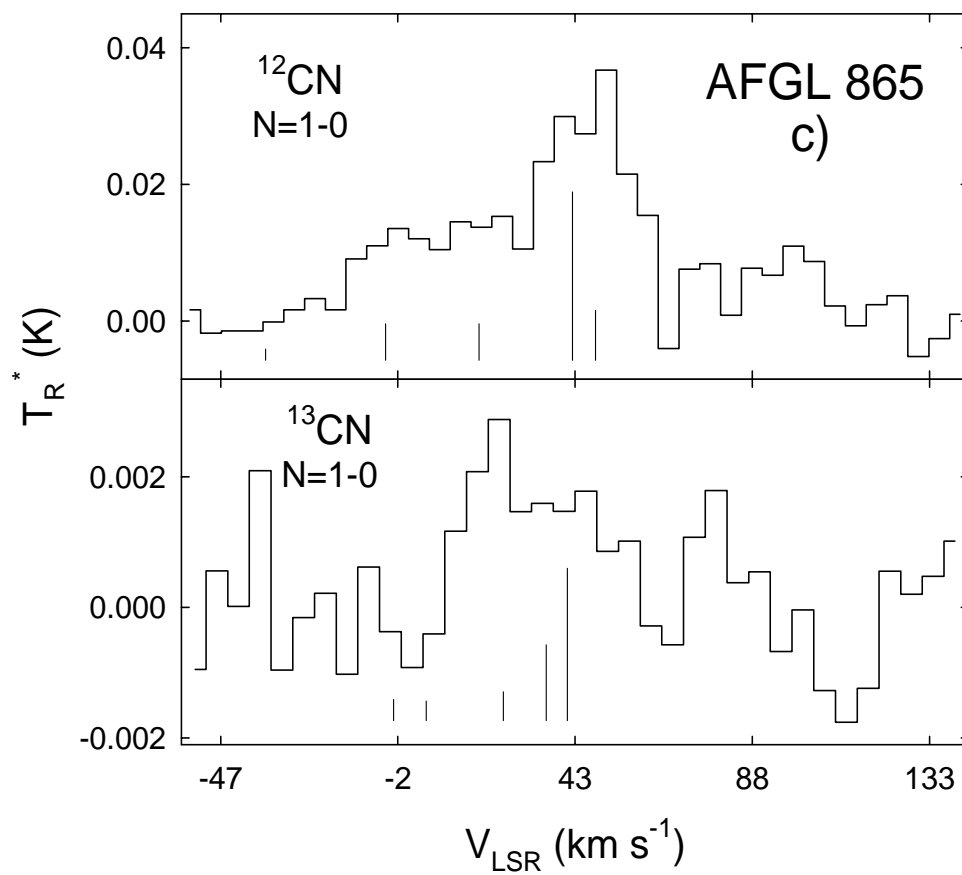


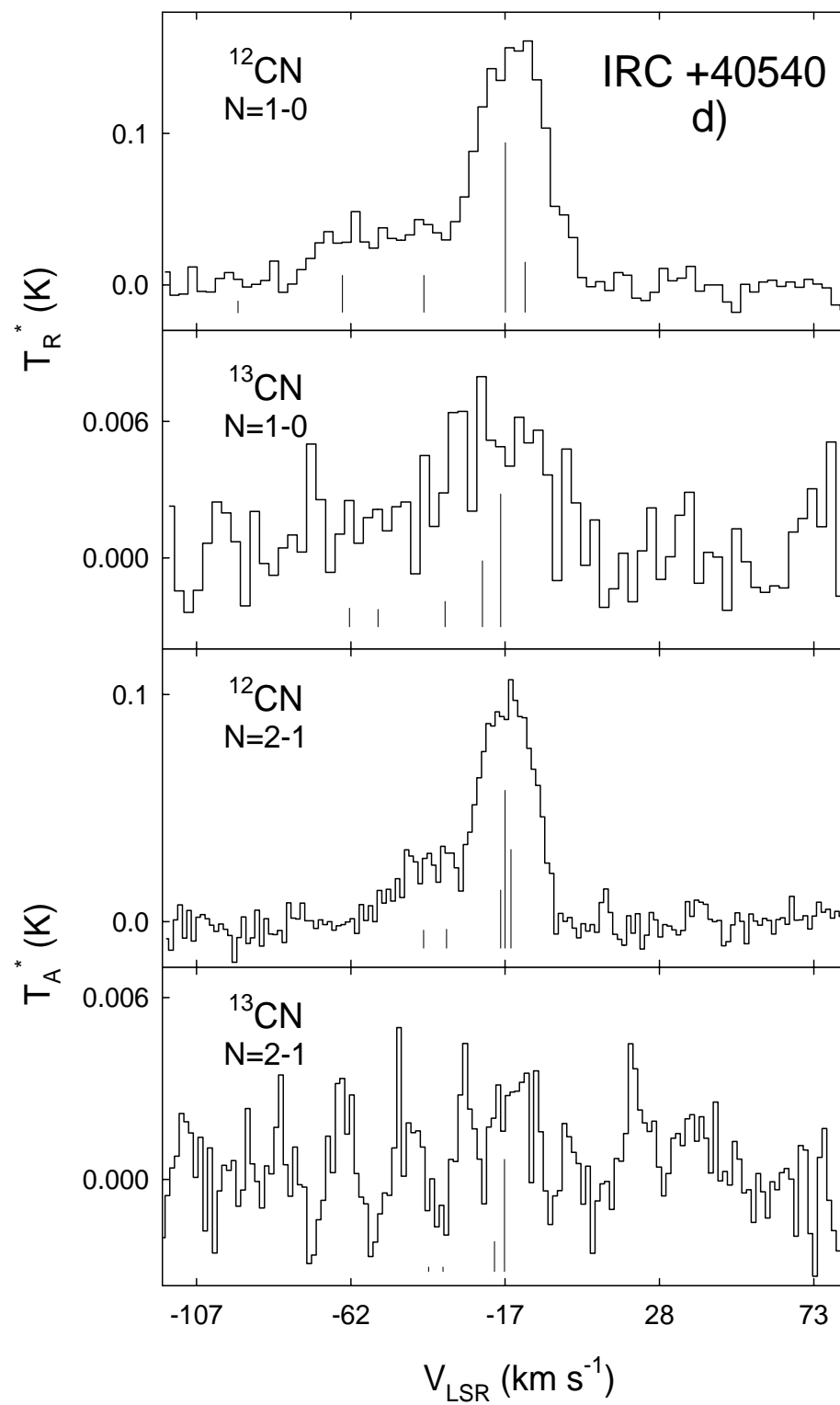


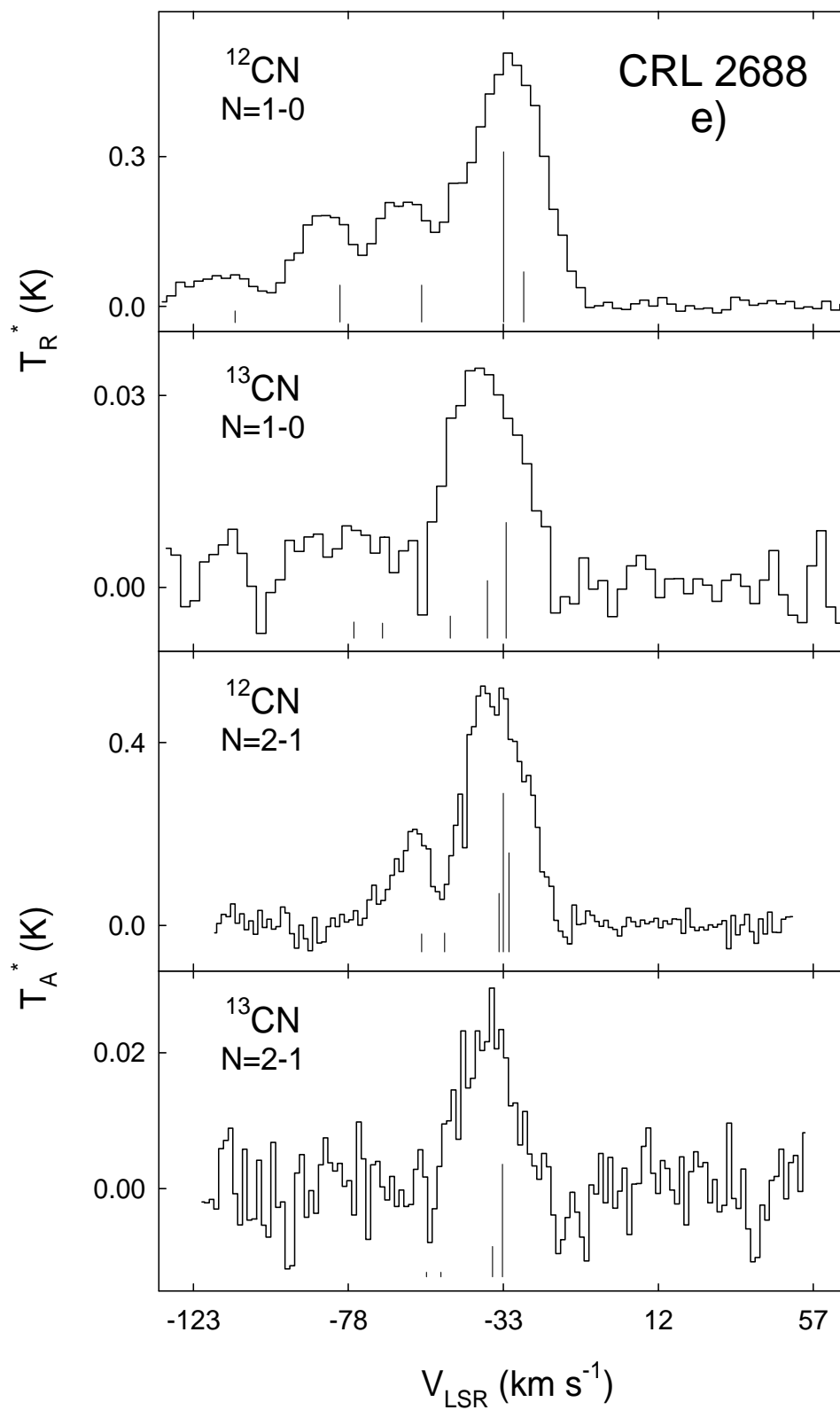


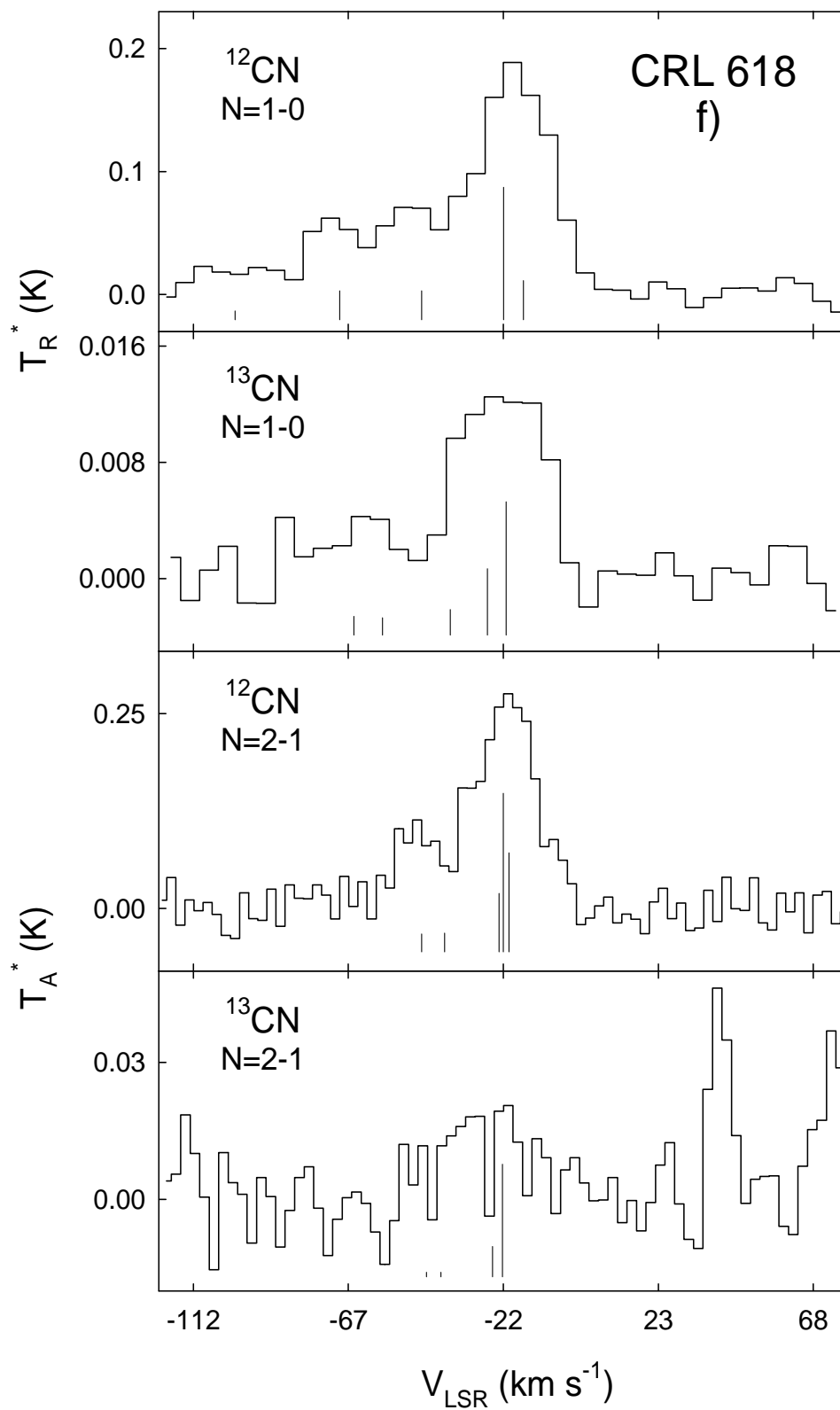


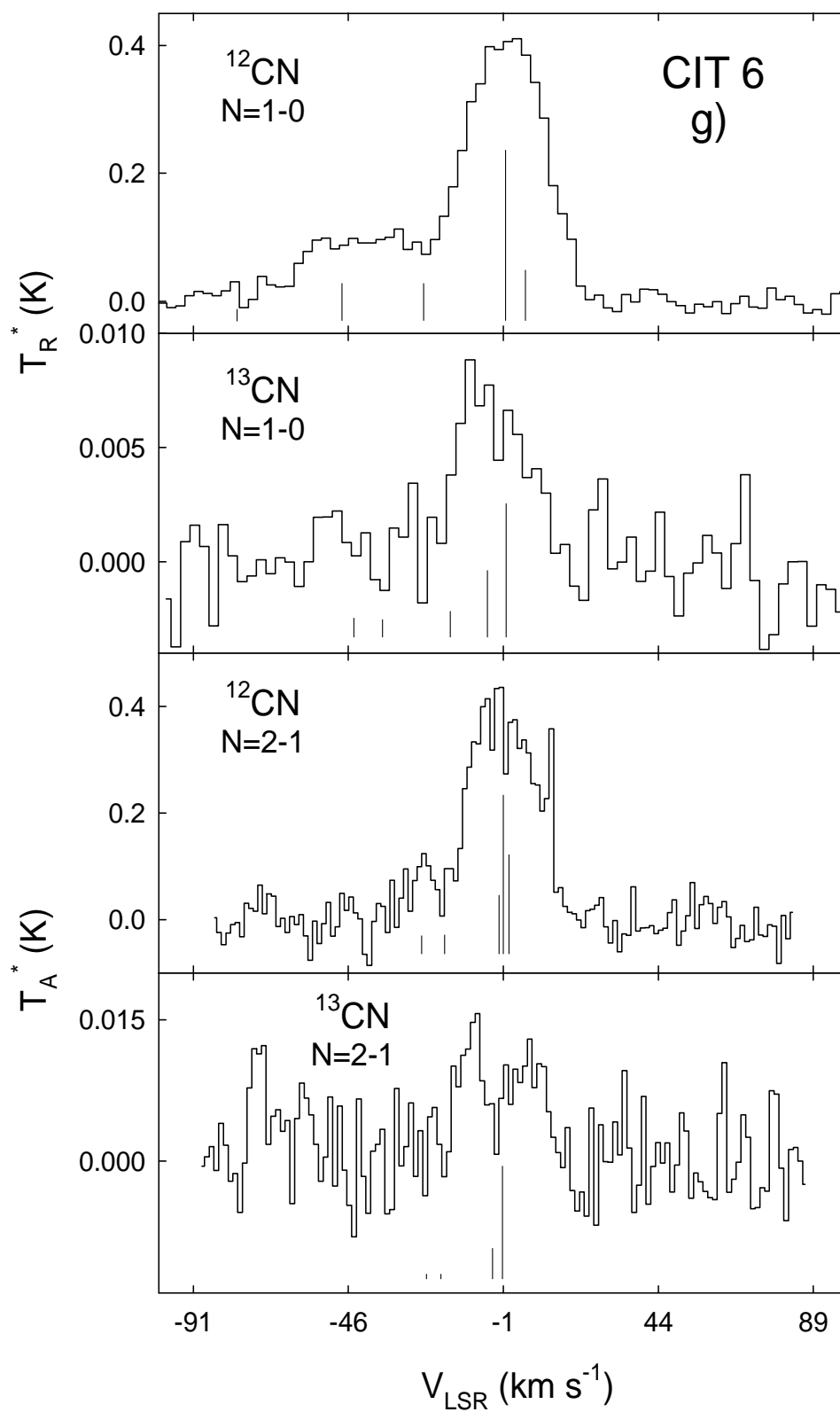


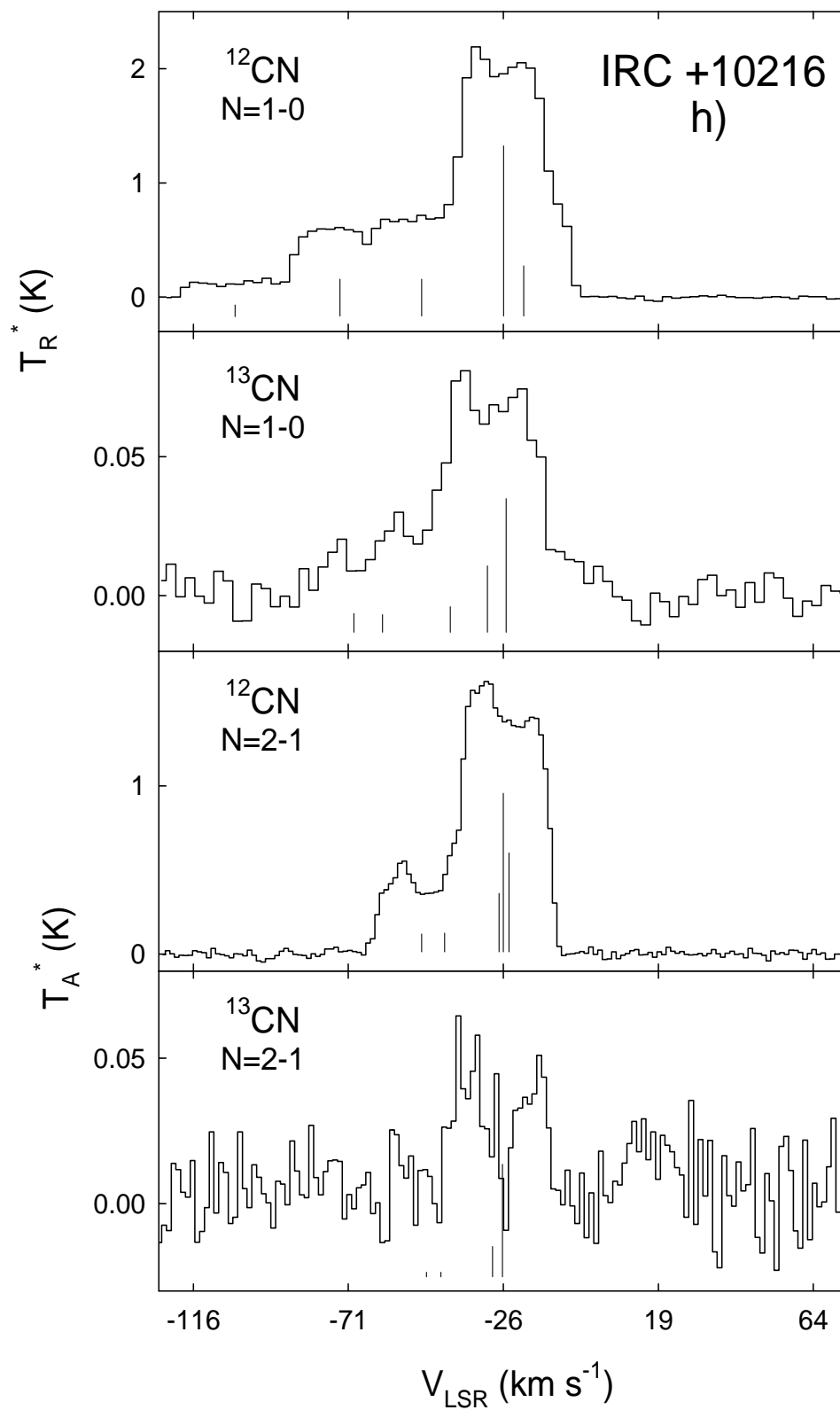


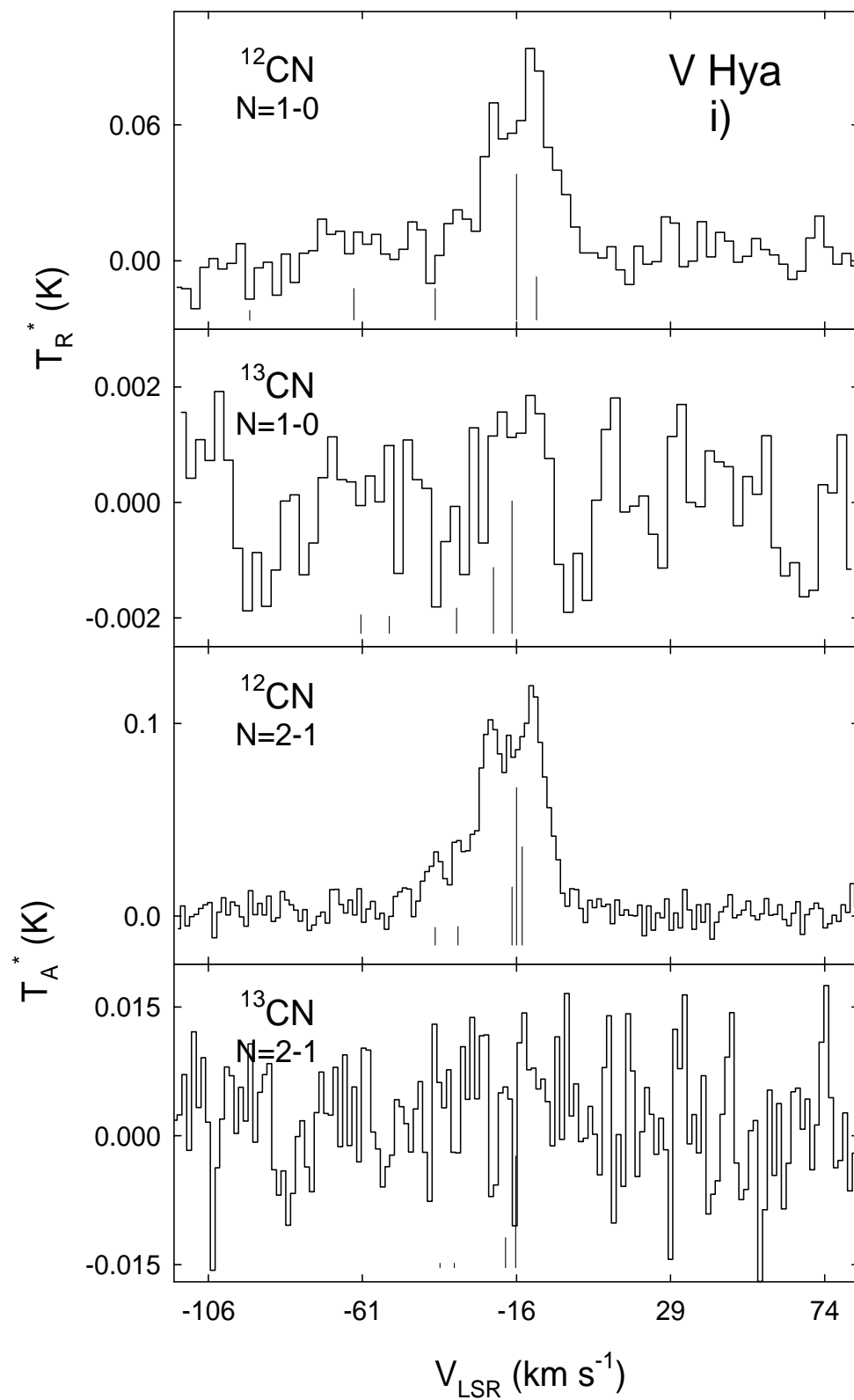


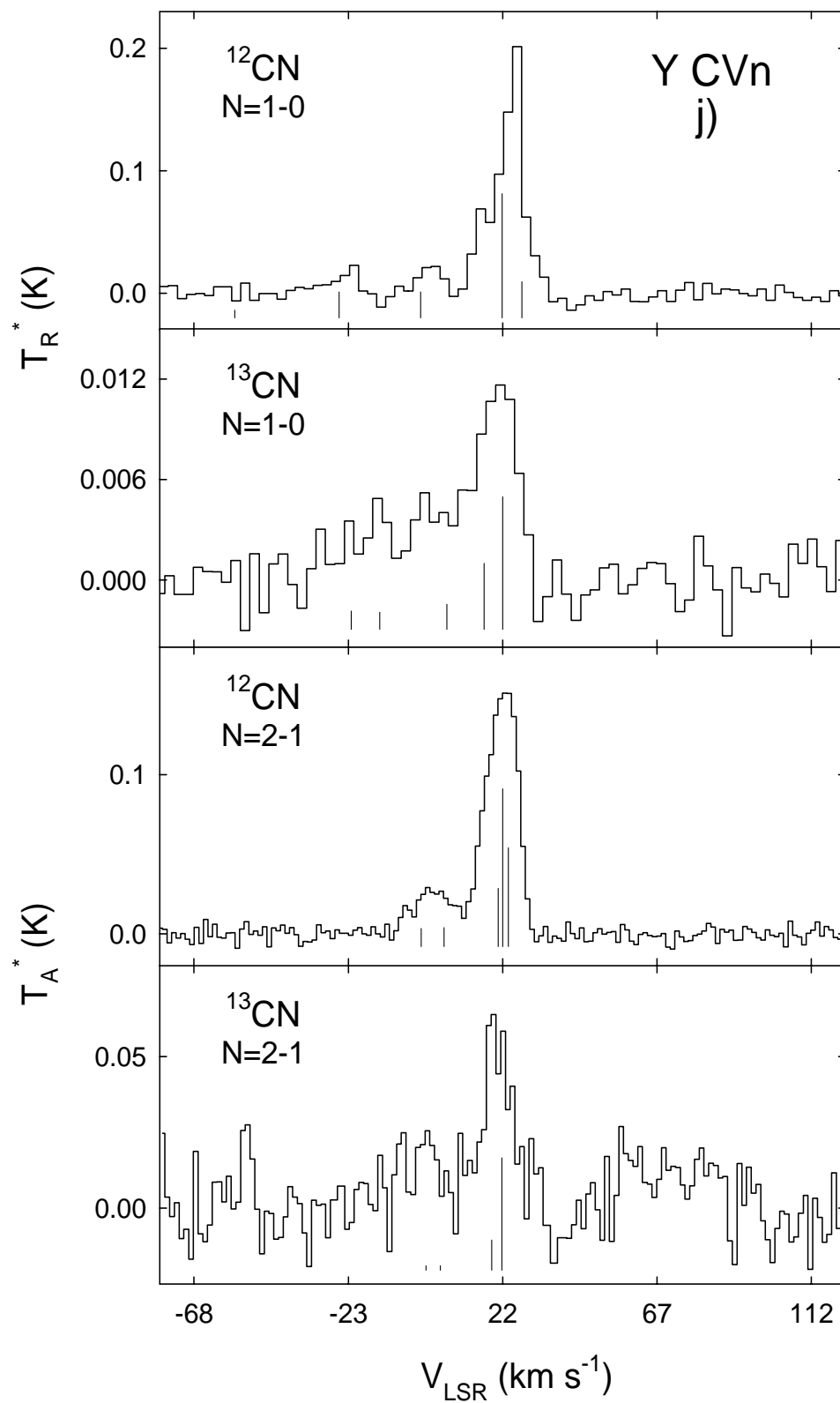


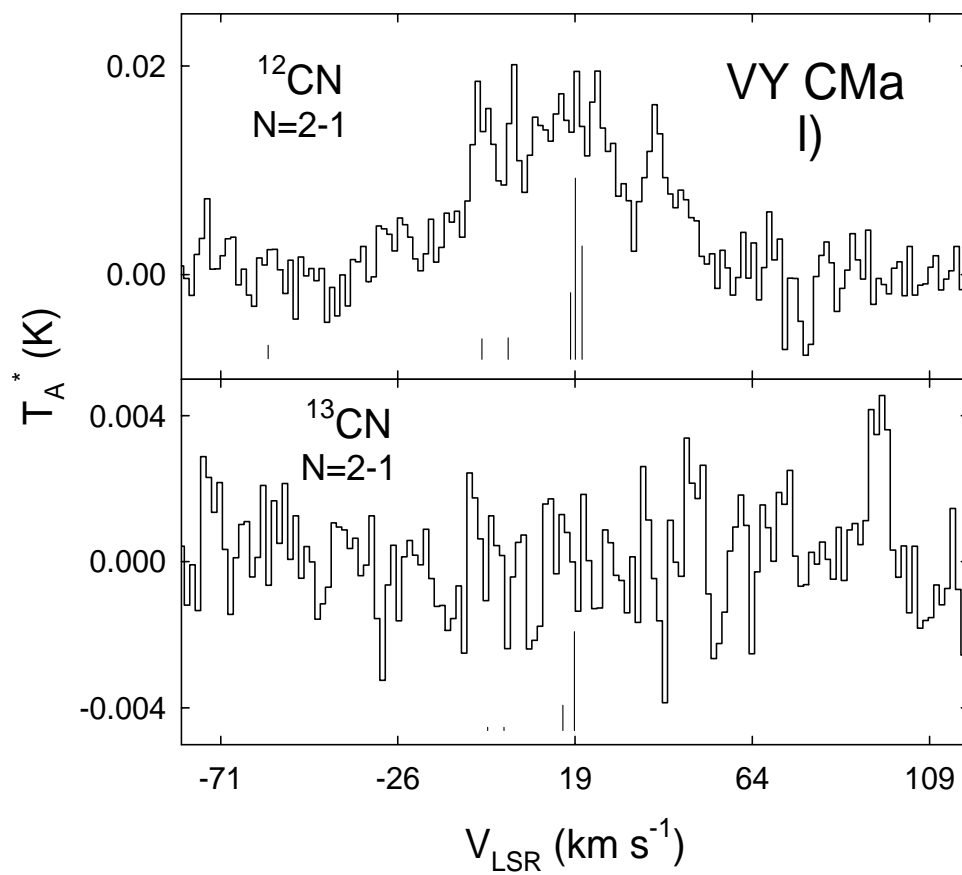


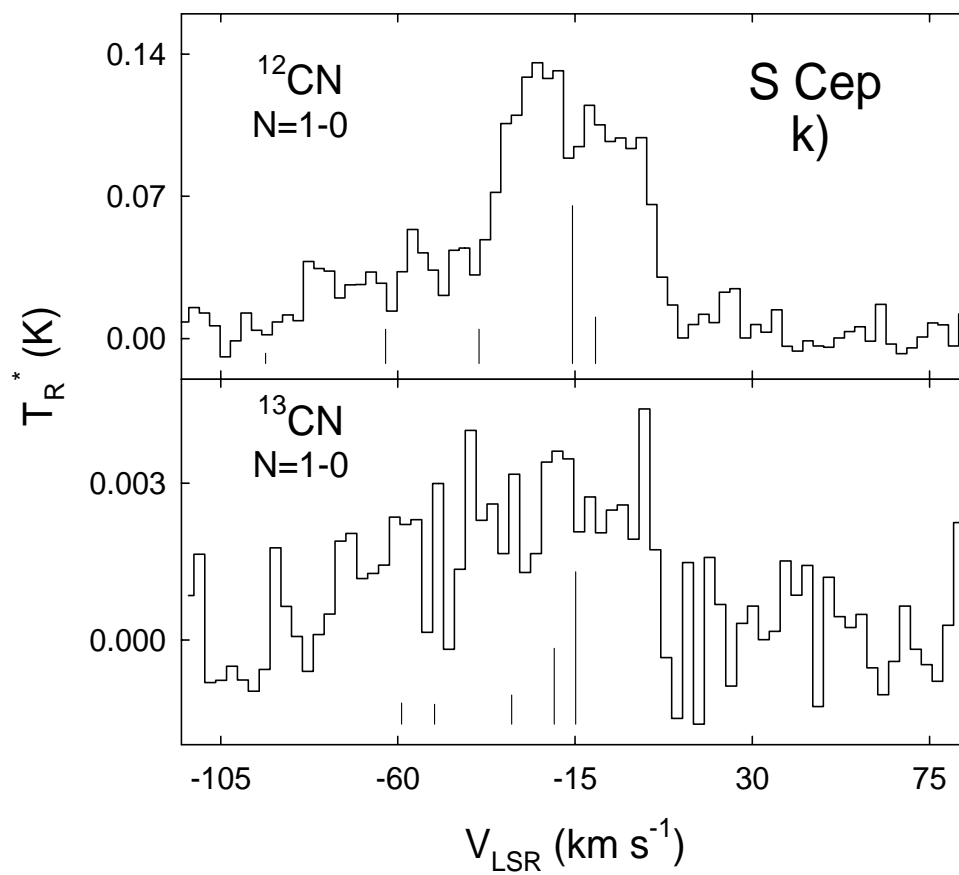


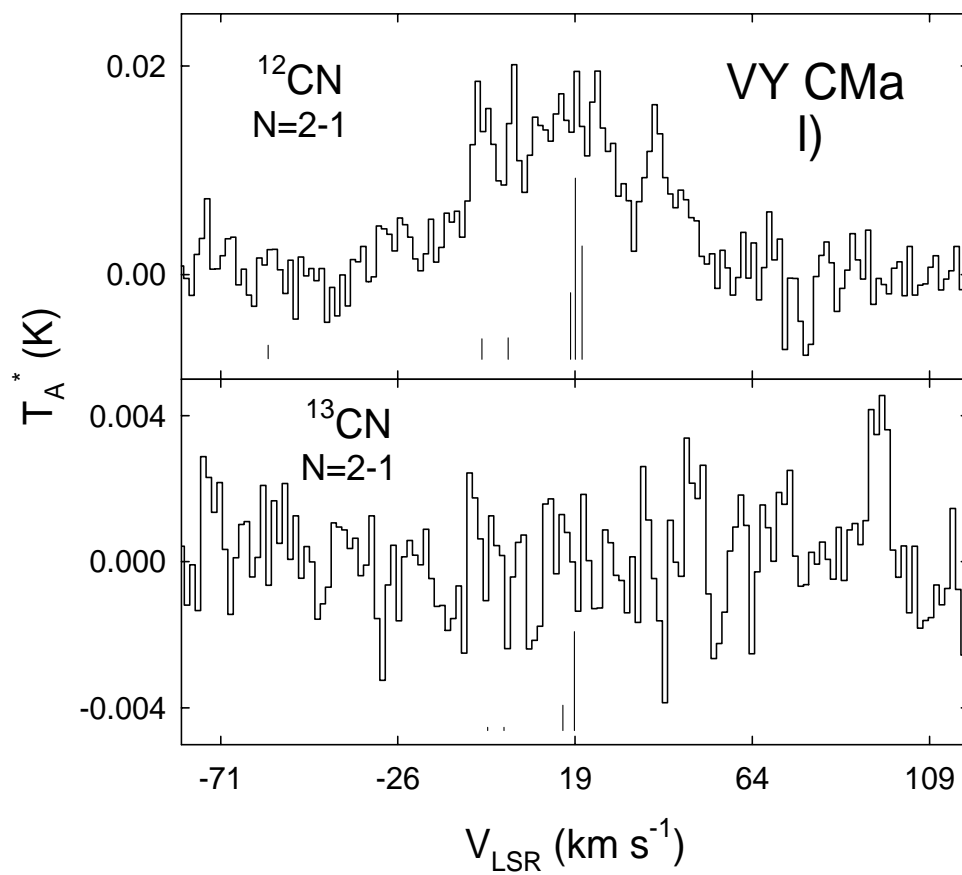


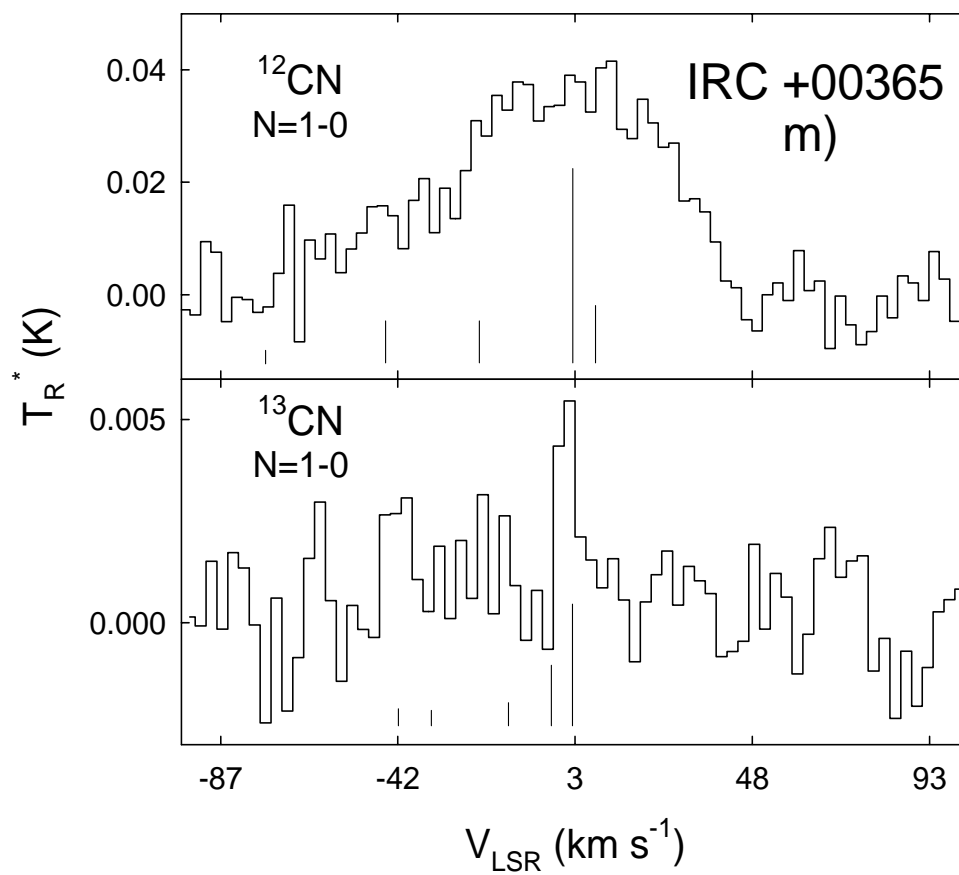


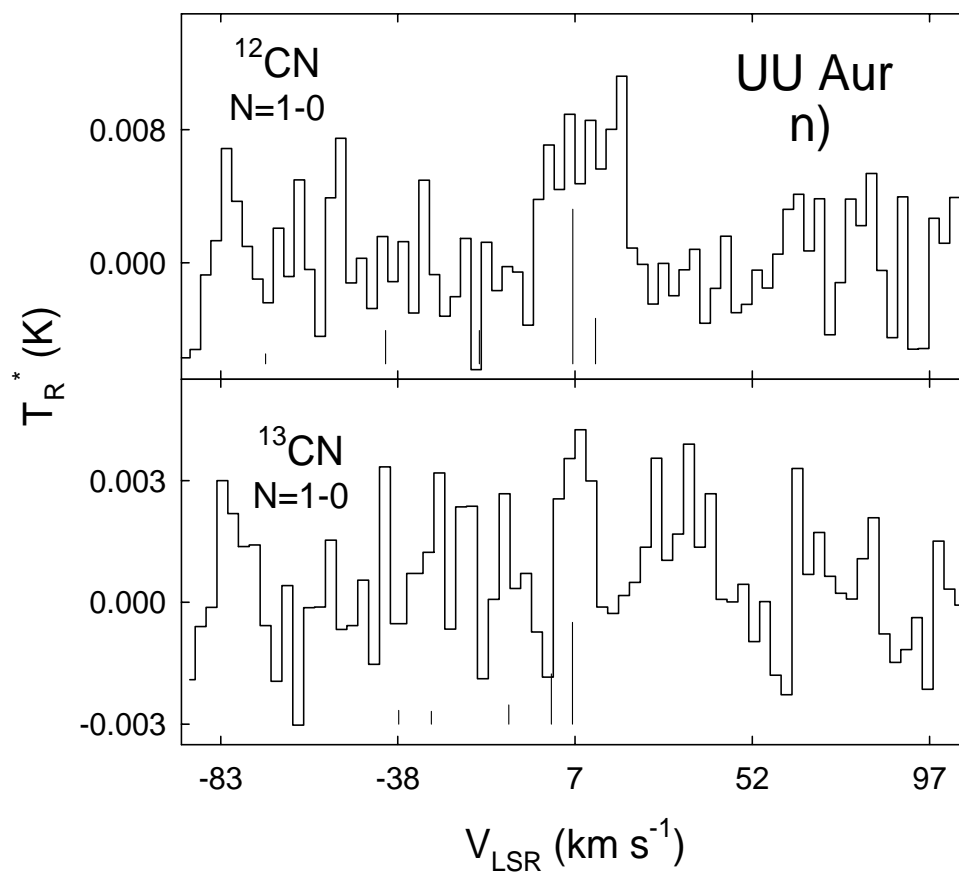


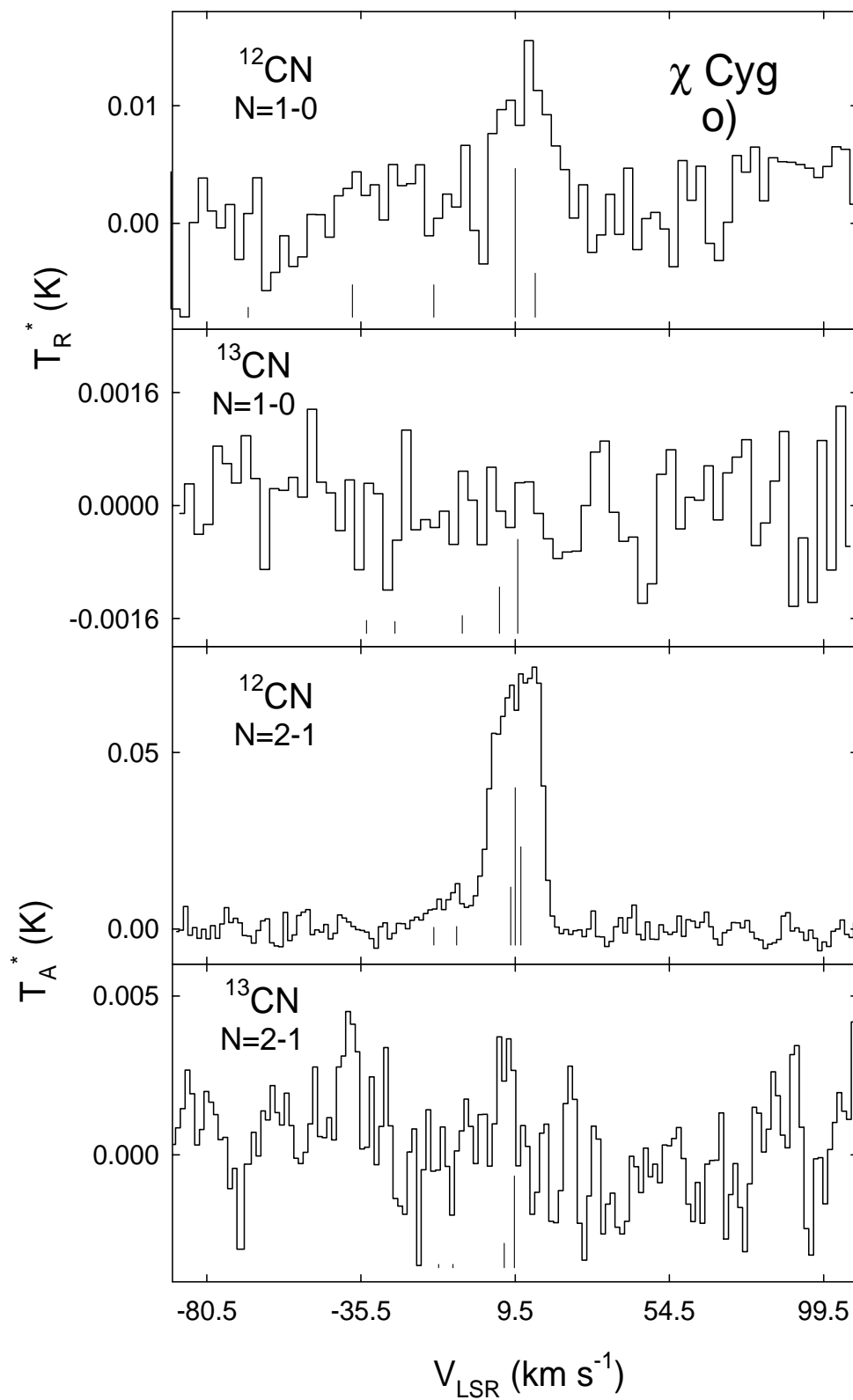


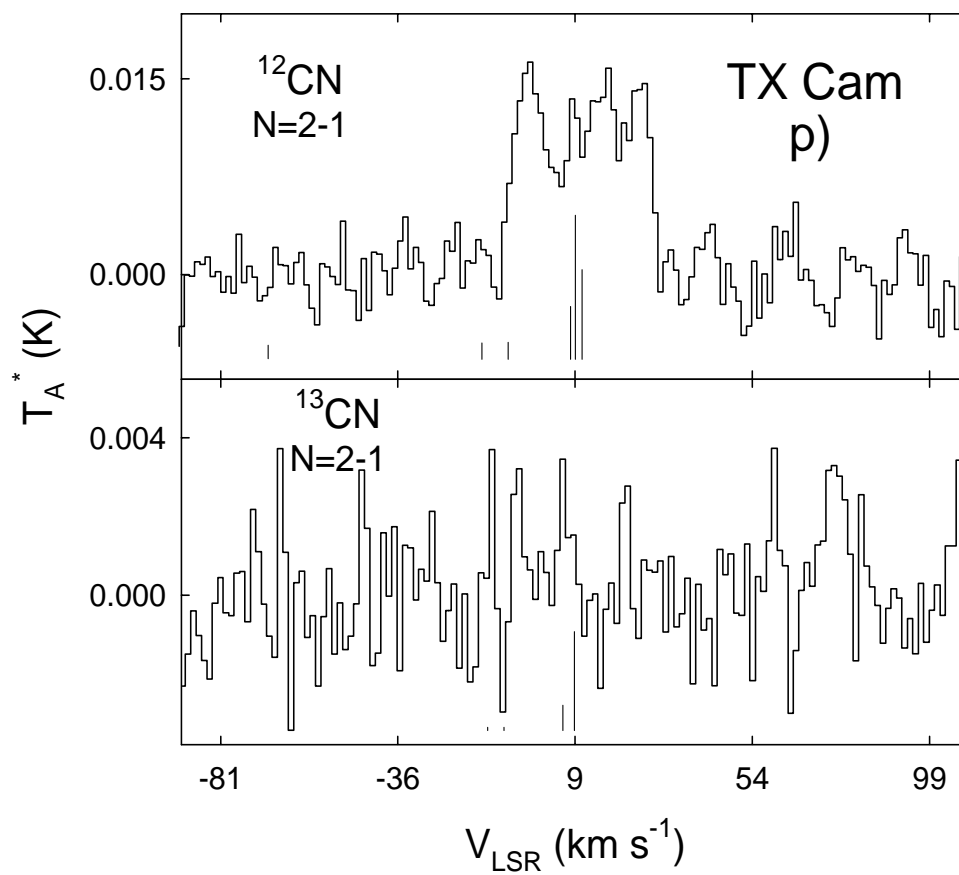


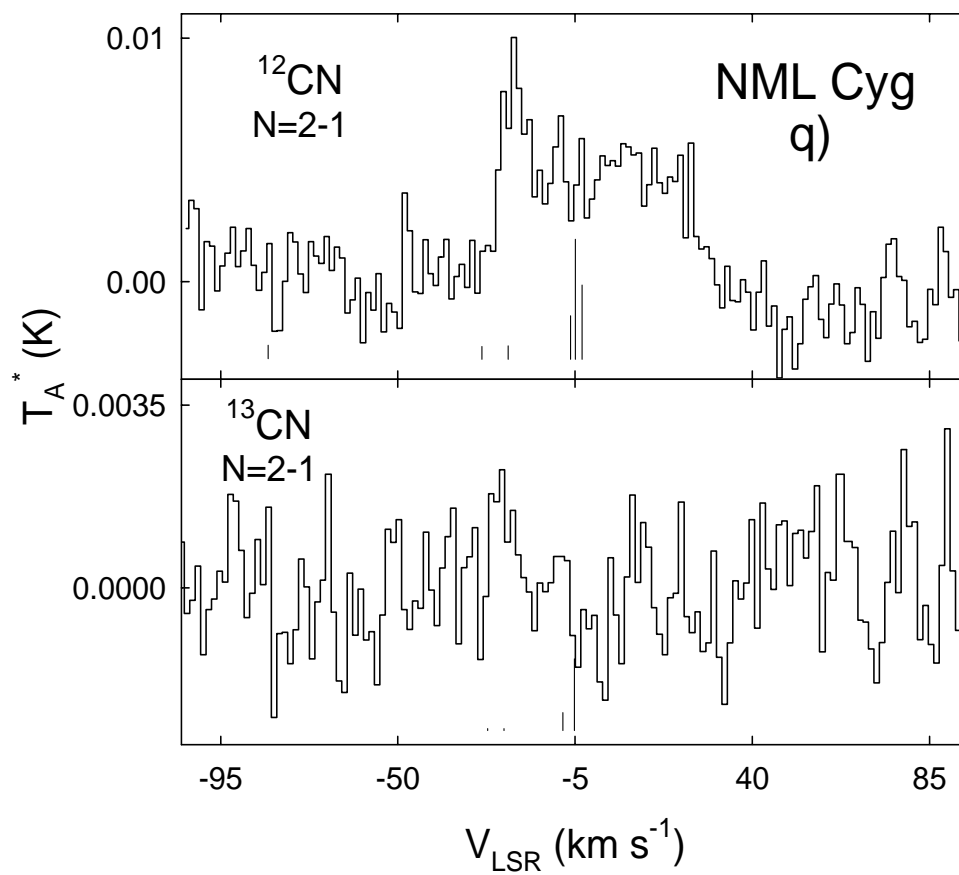


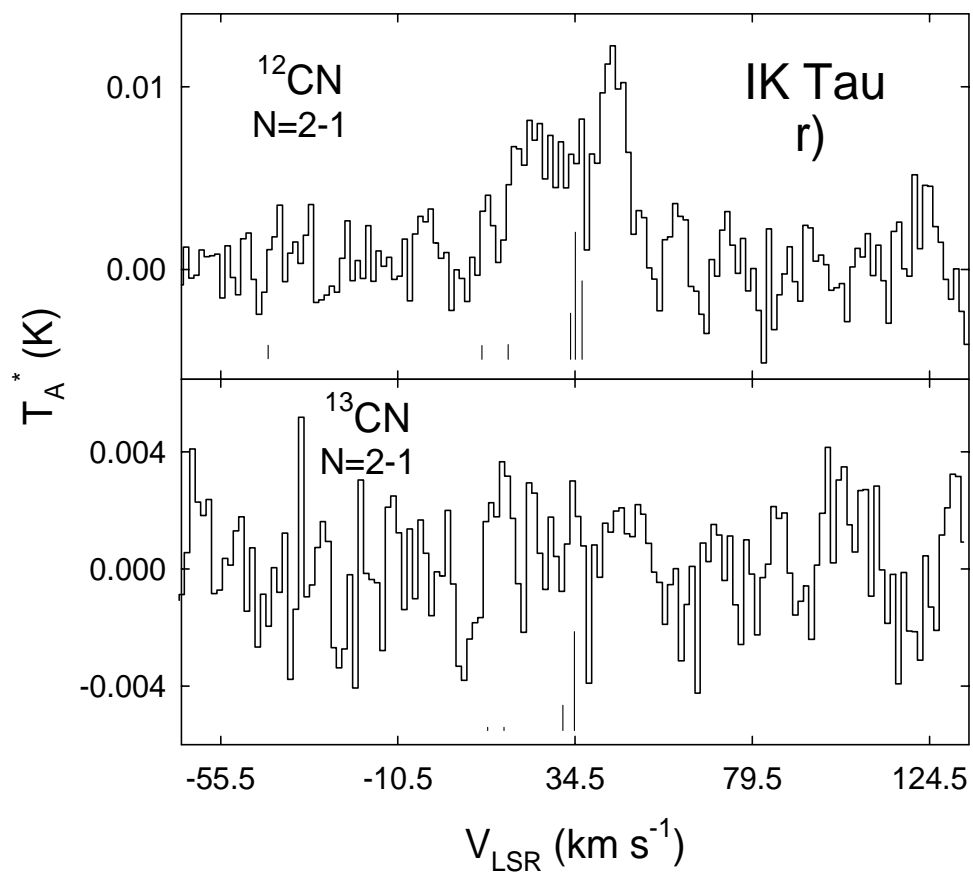








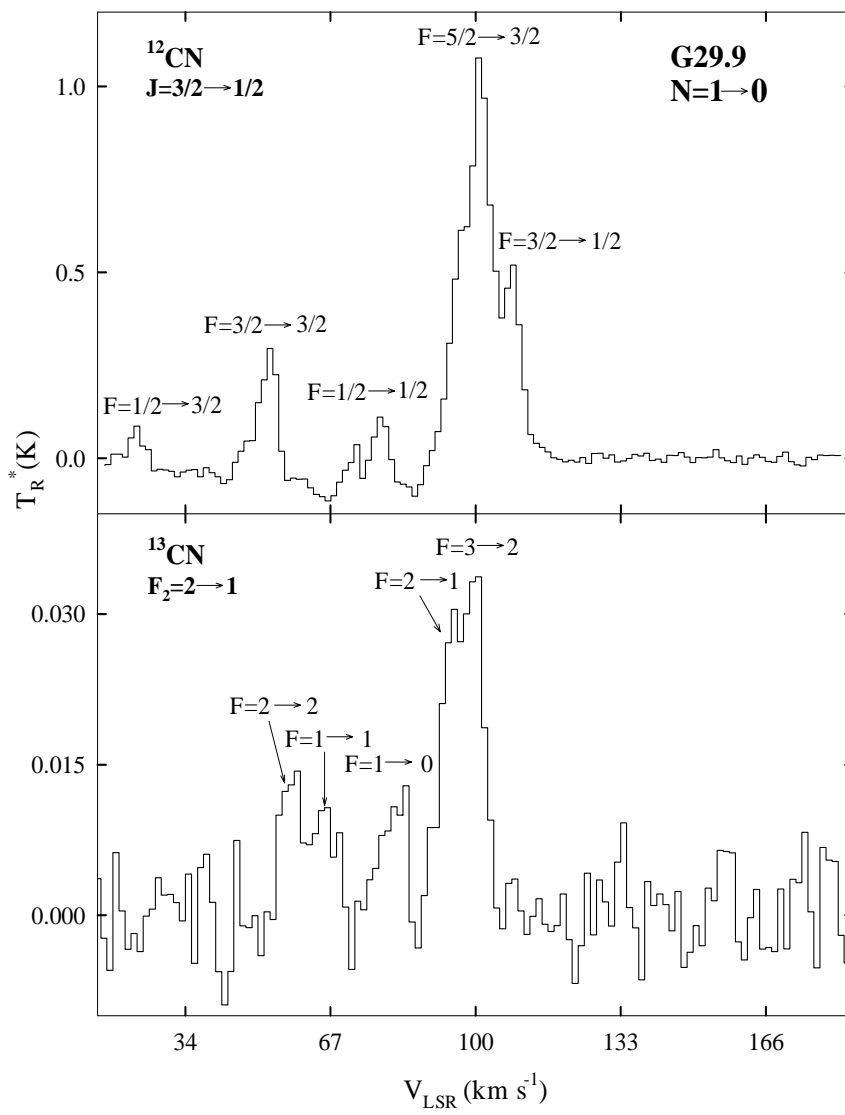


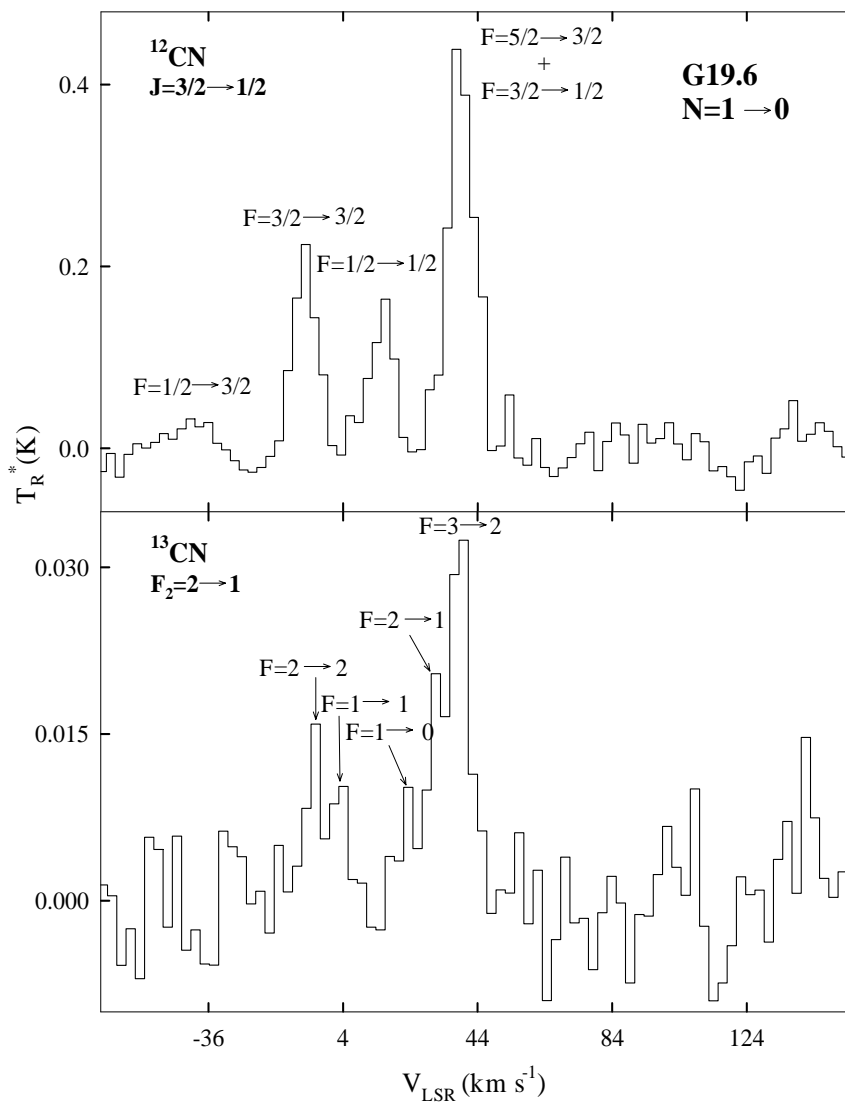


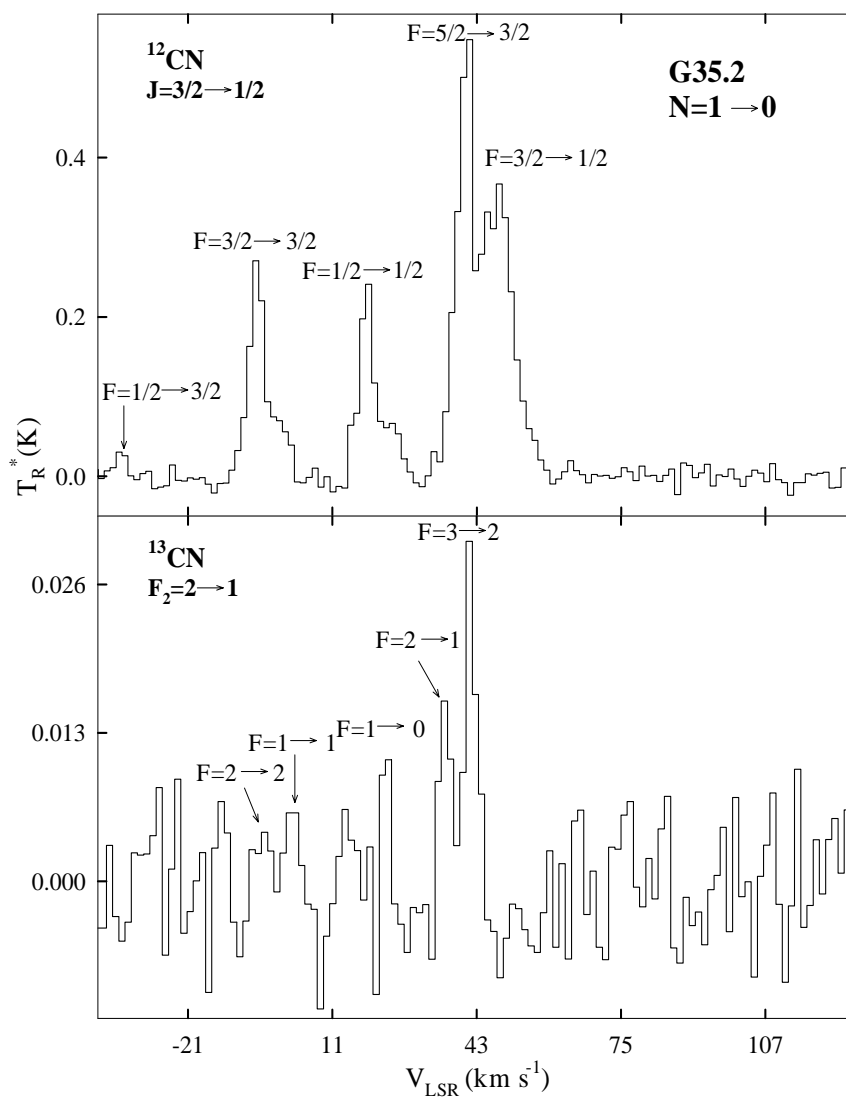
APPENDIX I

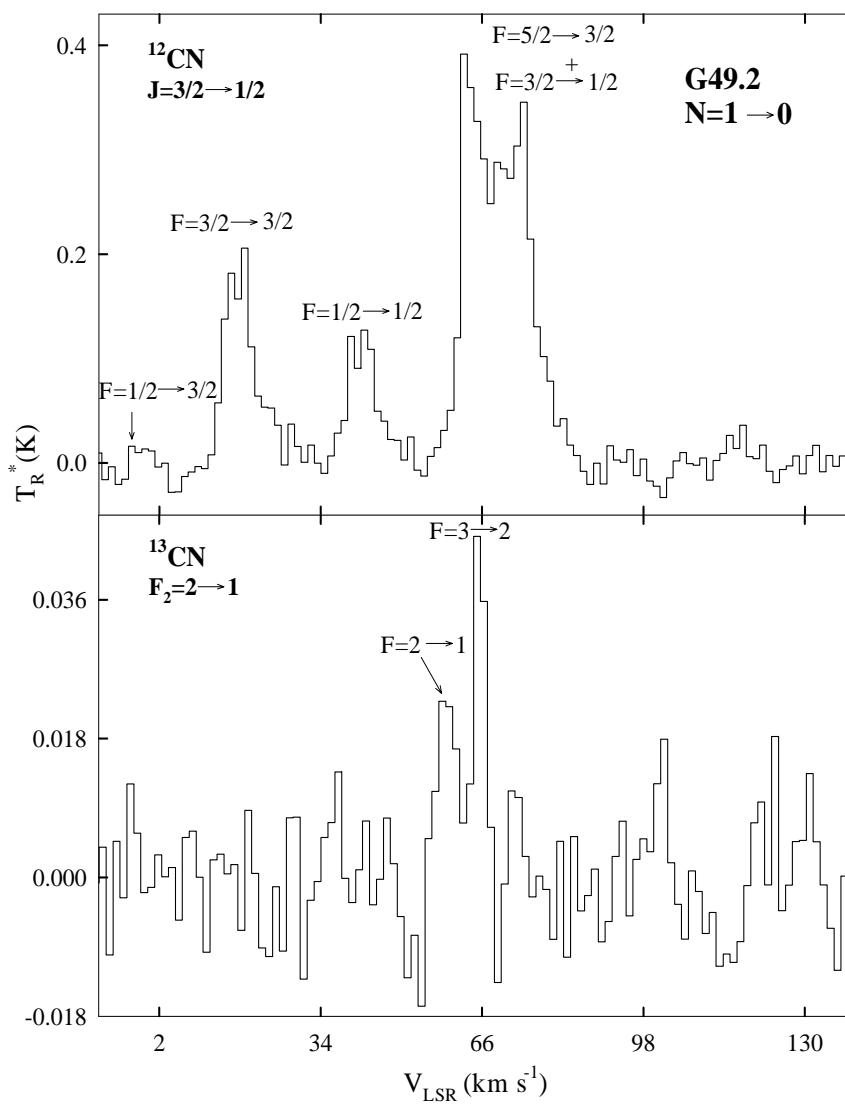
THE CN N=2→1 ISOTOPE GRADIENT: FURTHER STUDIES OF GALACTIC
CHEMICAL EVOLUTION

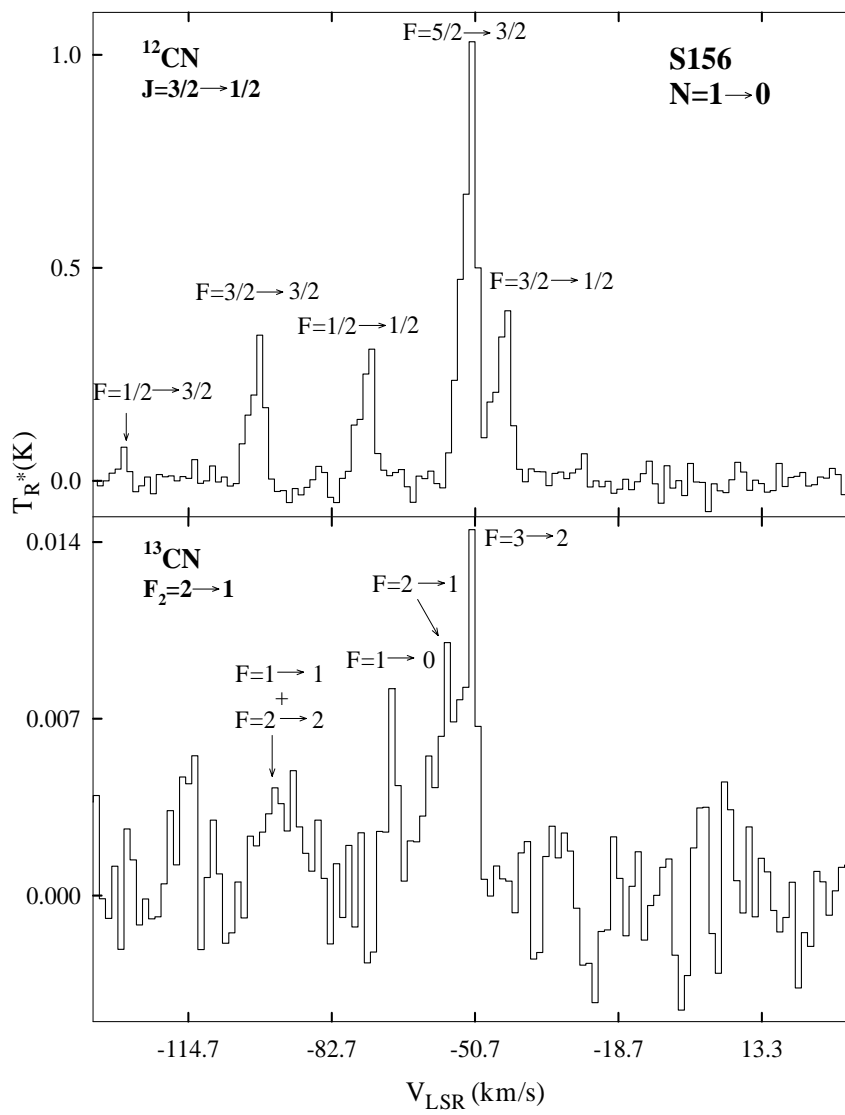
S.N. Milam, D.K. Qasim, S. Wyckoff, & L.M. Ziurys, in preparation.

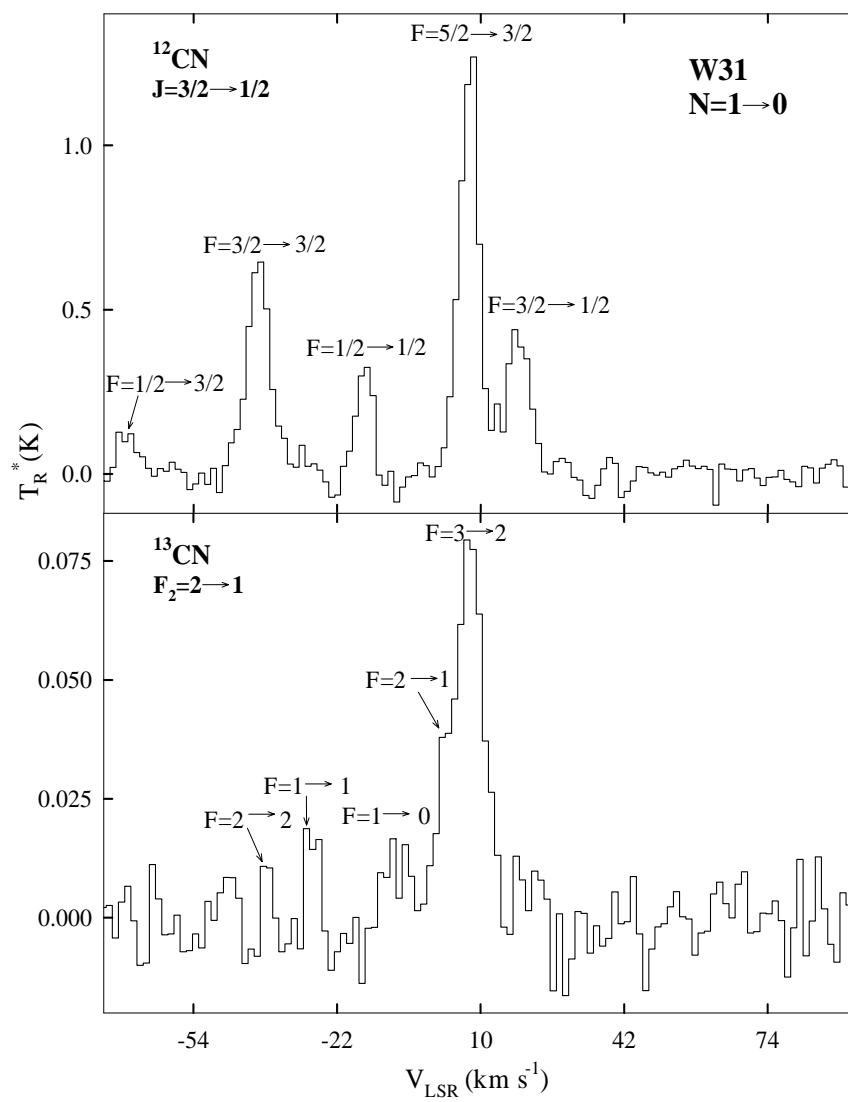


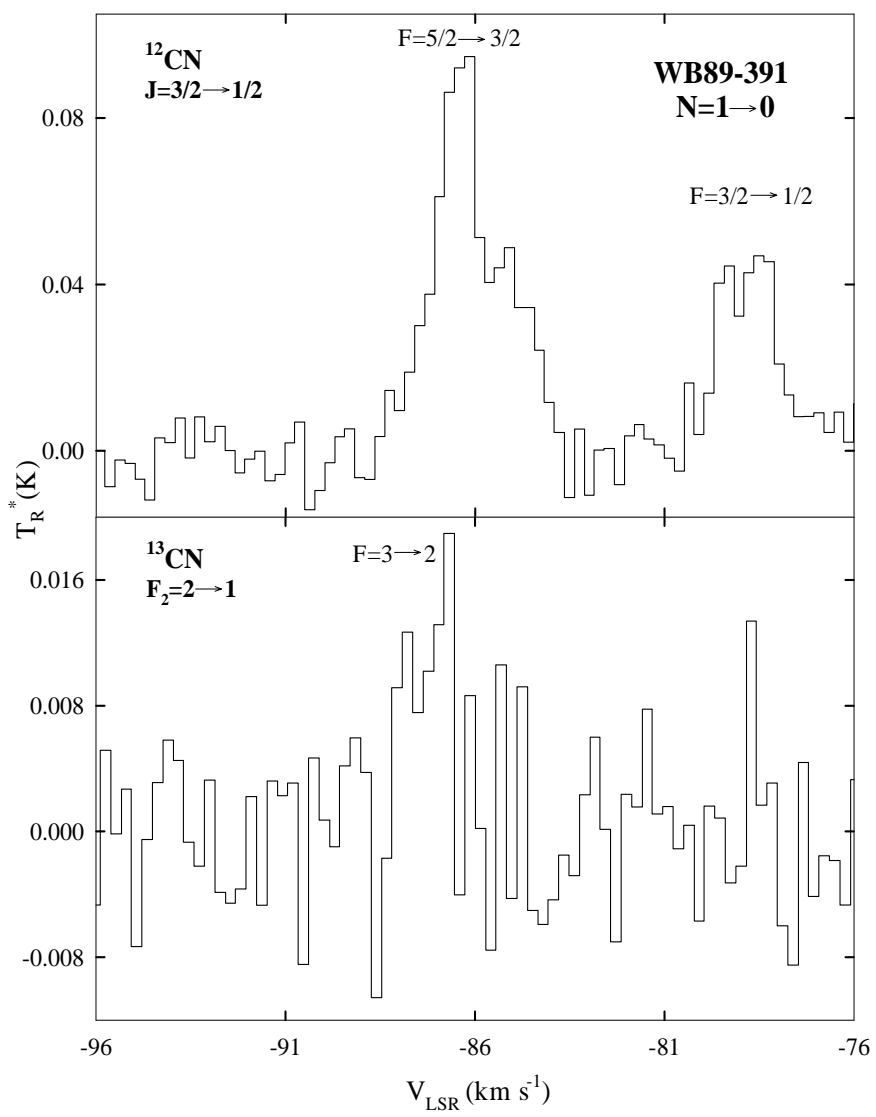


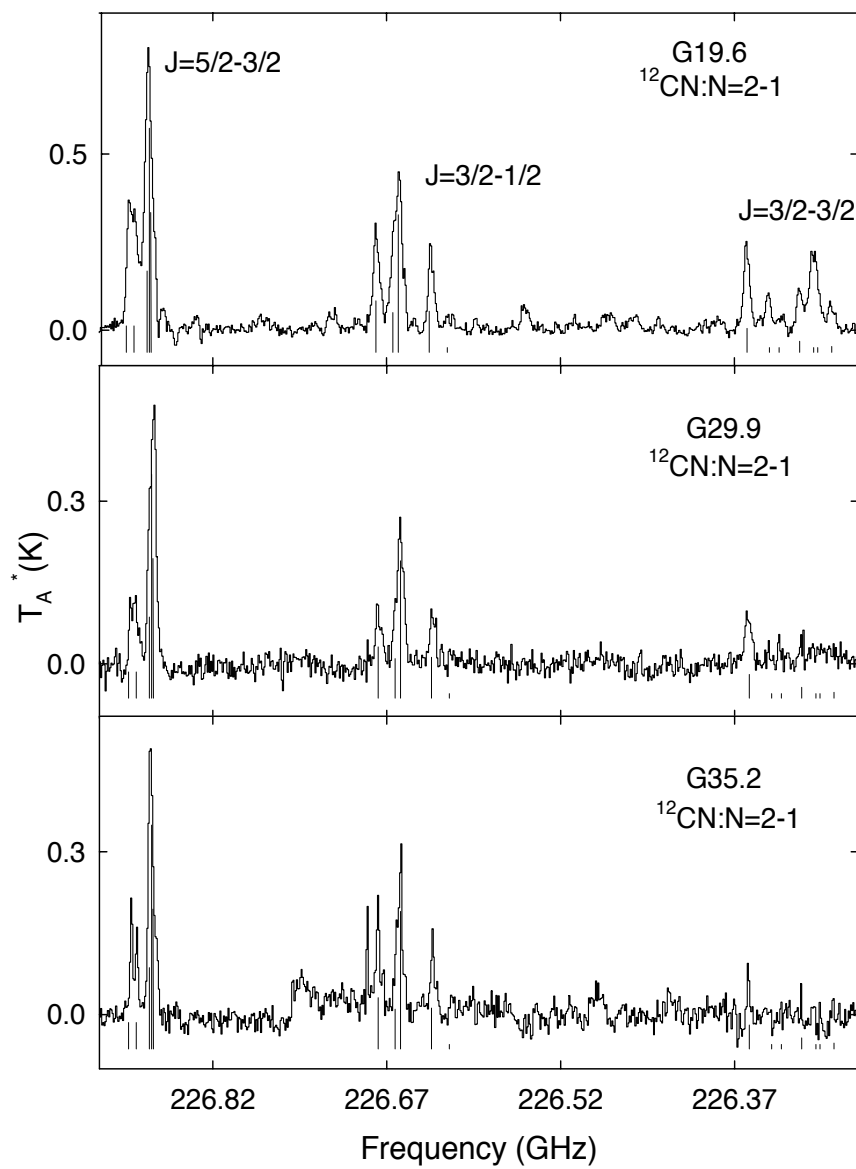


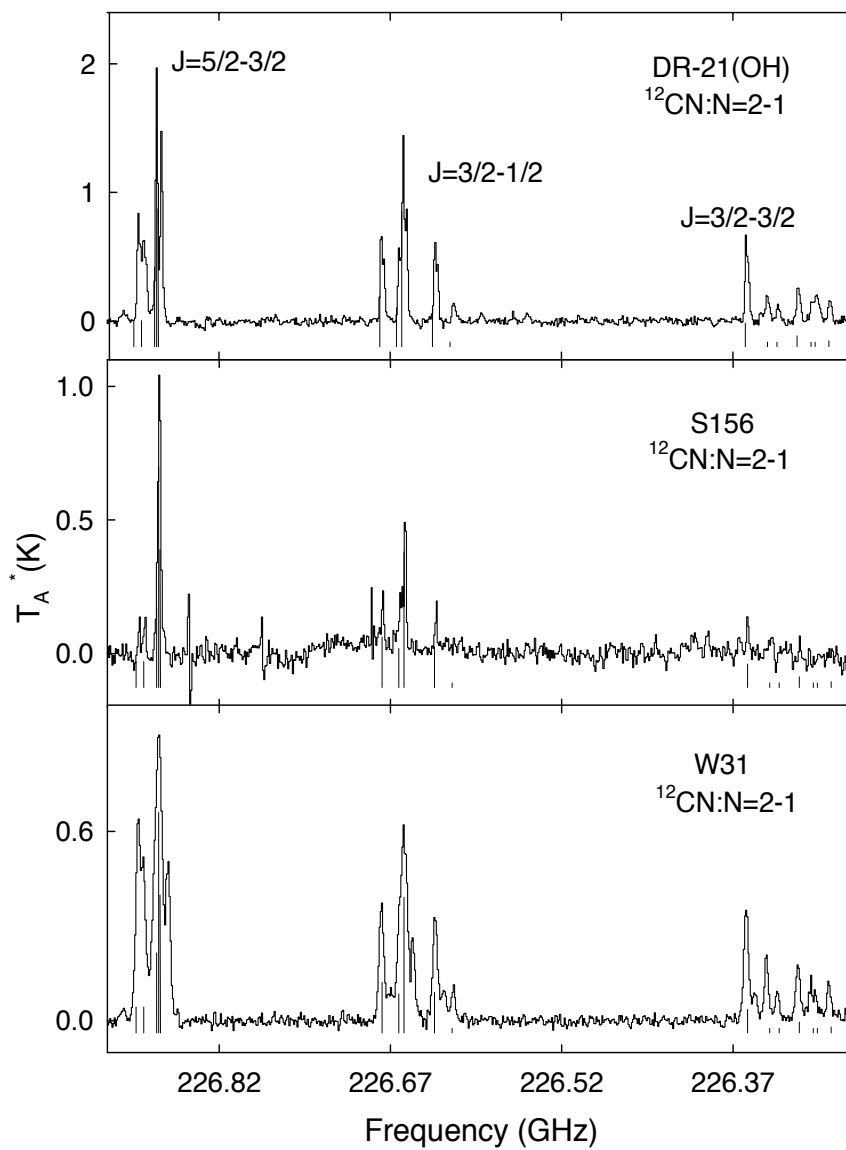


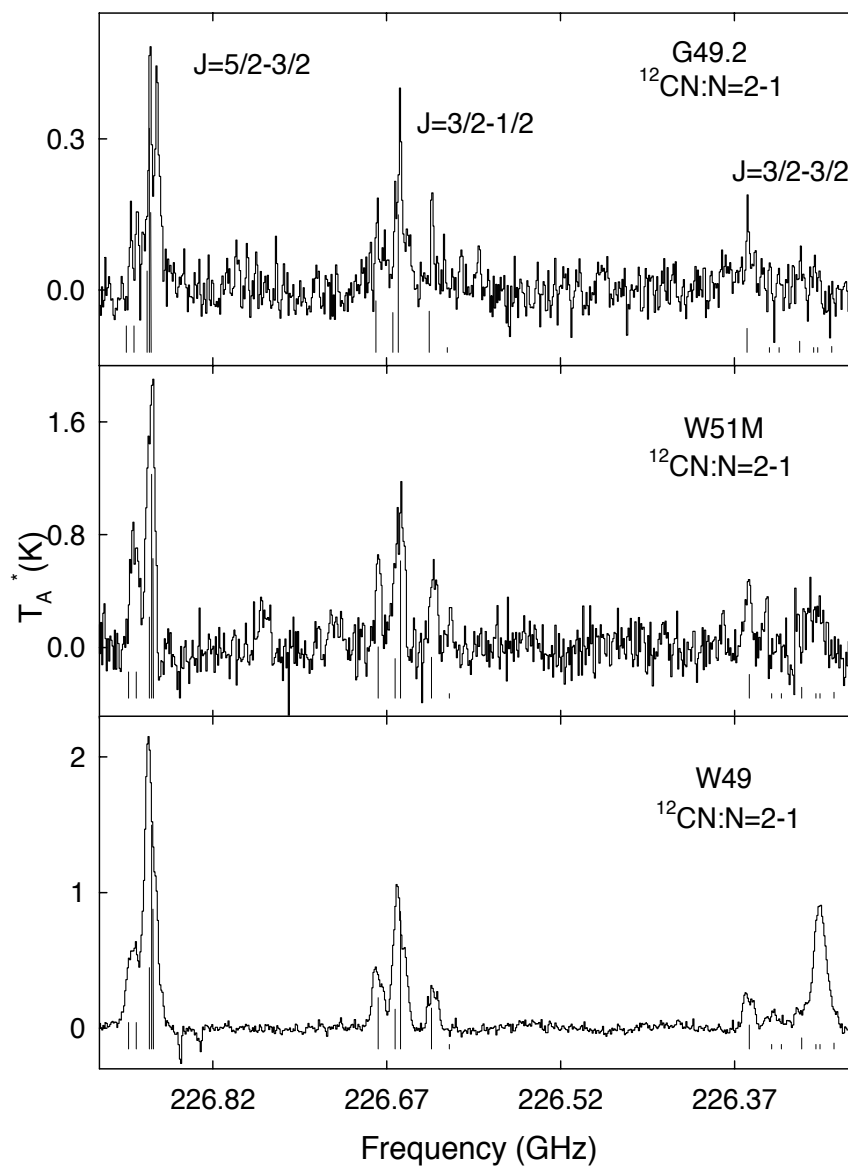


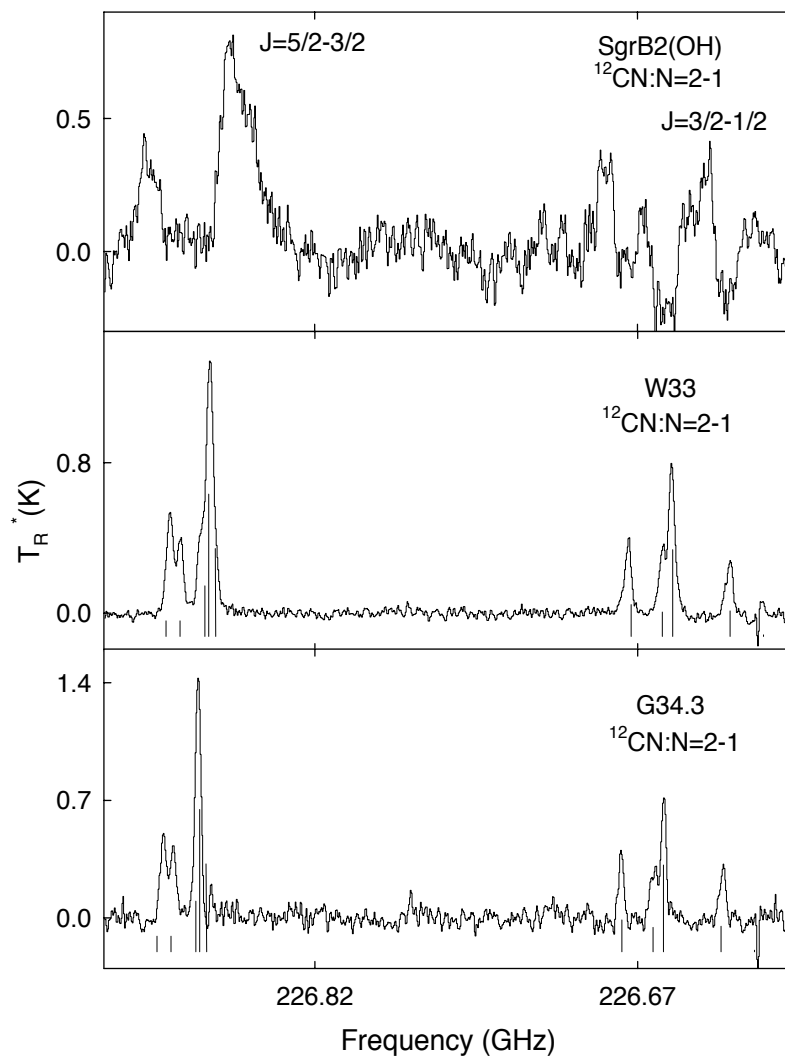


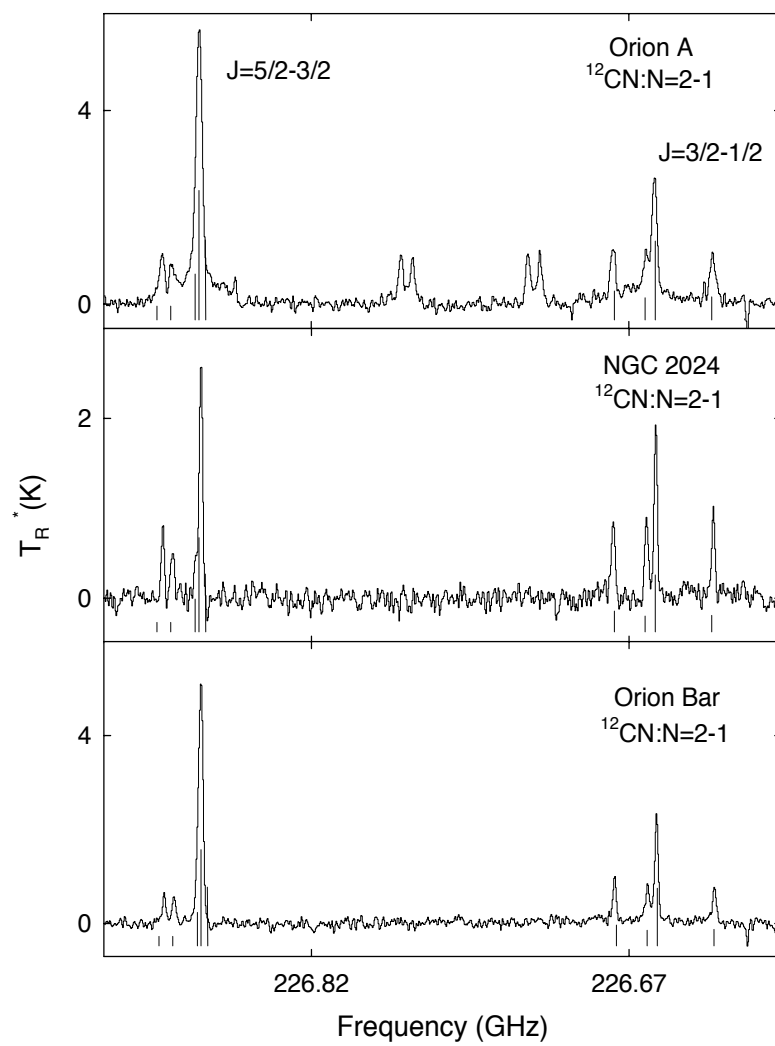


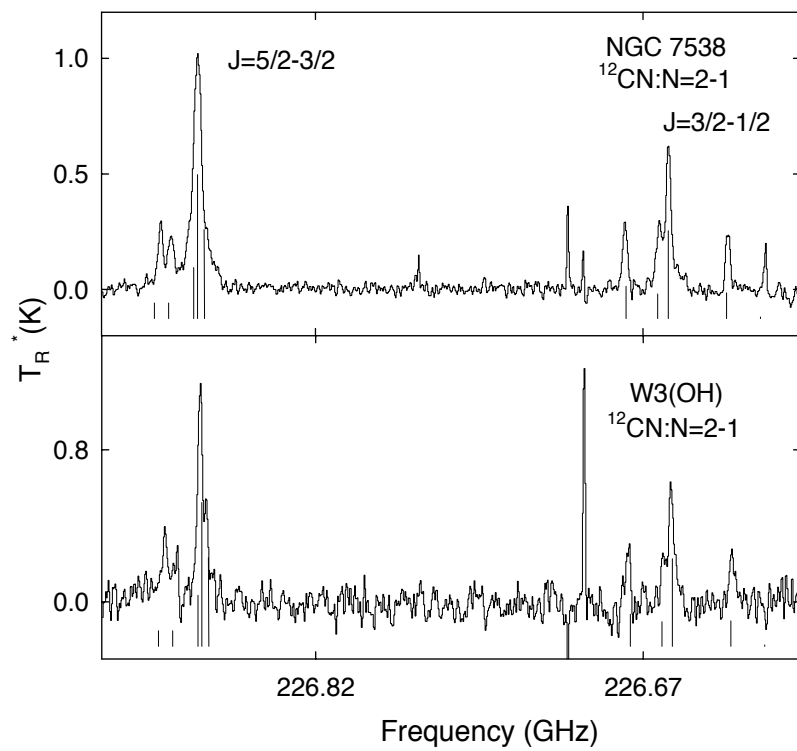


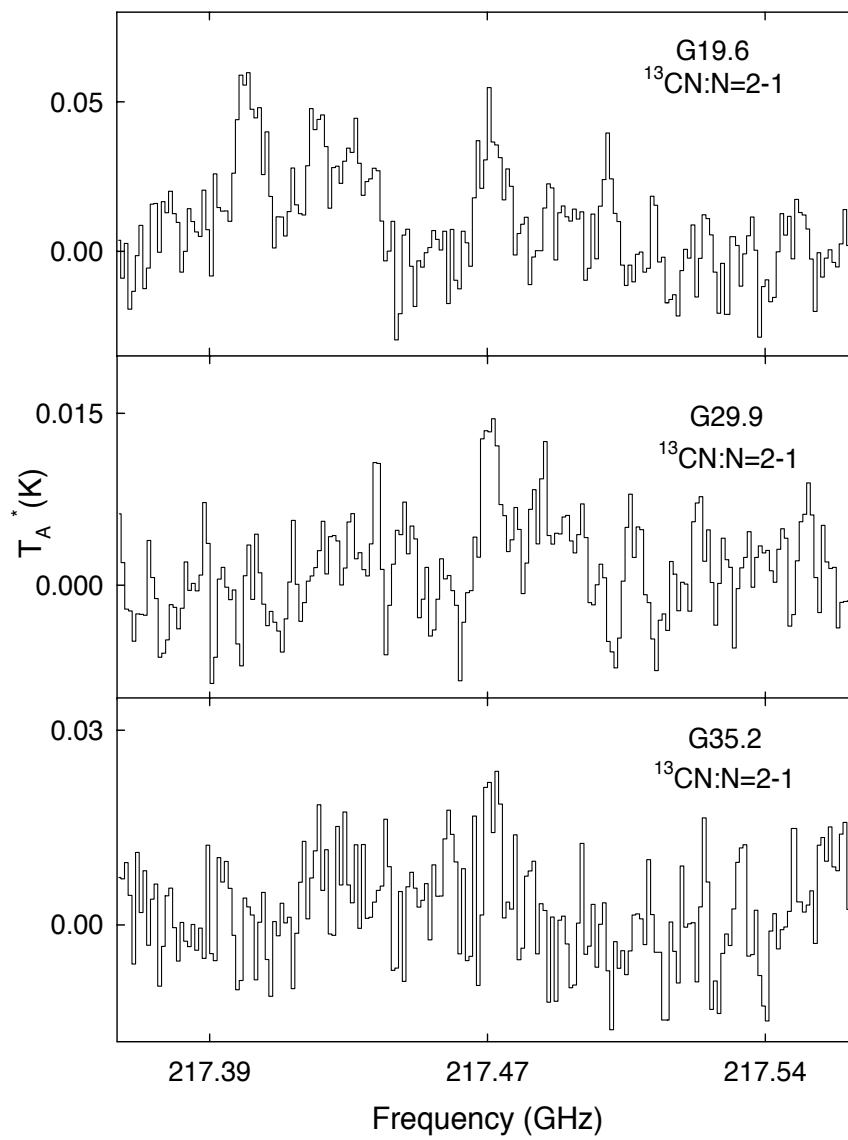


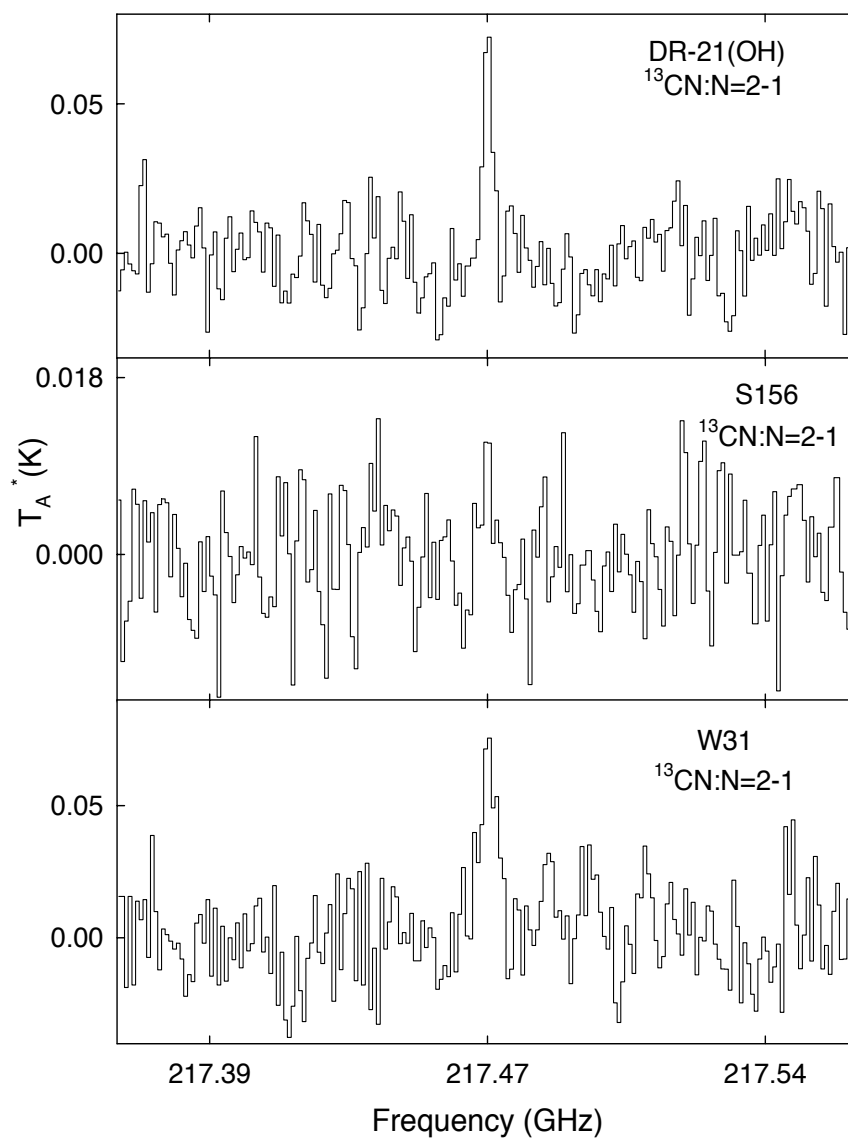


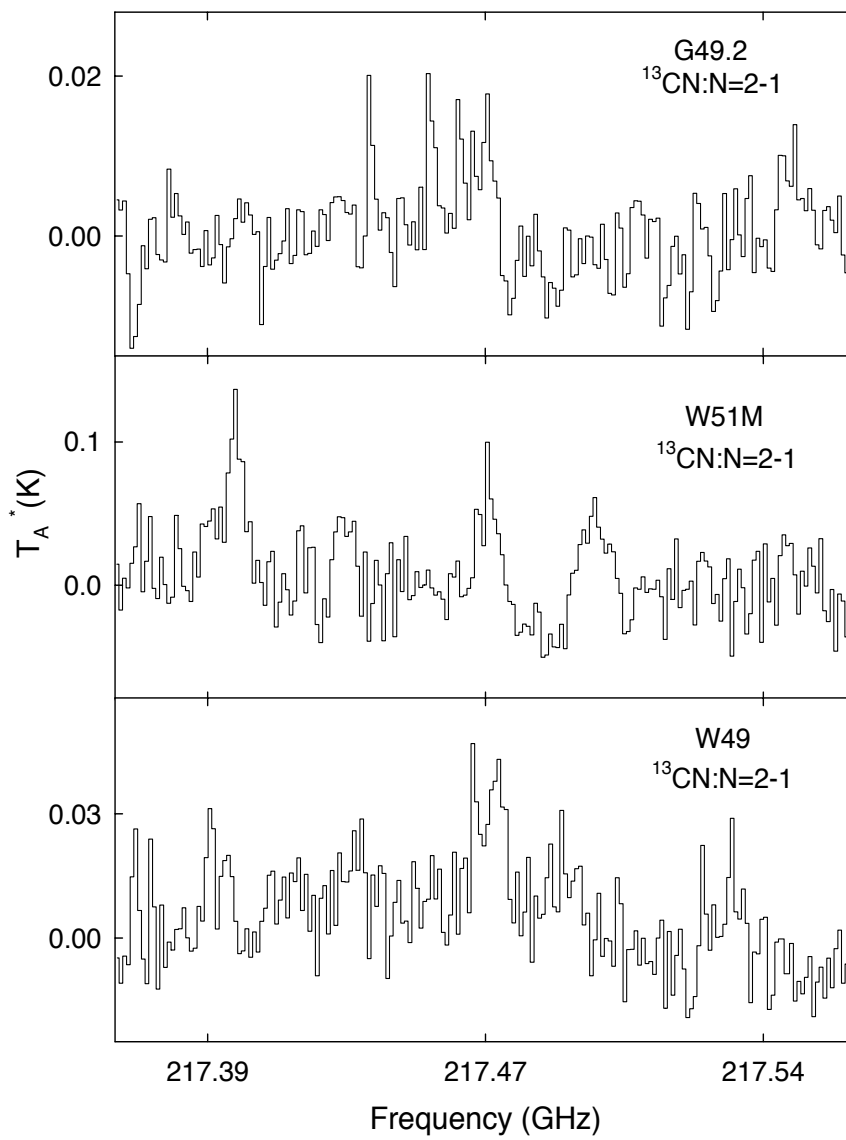


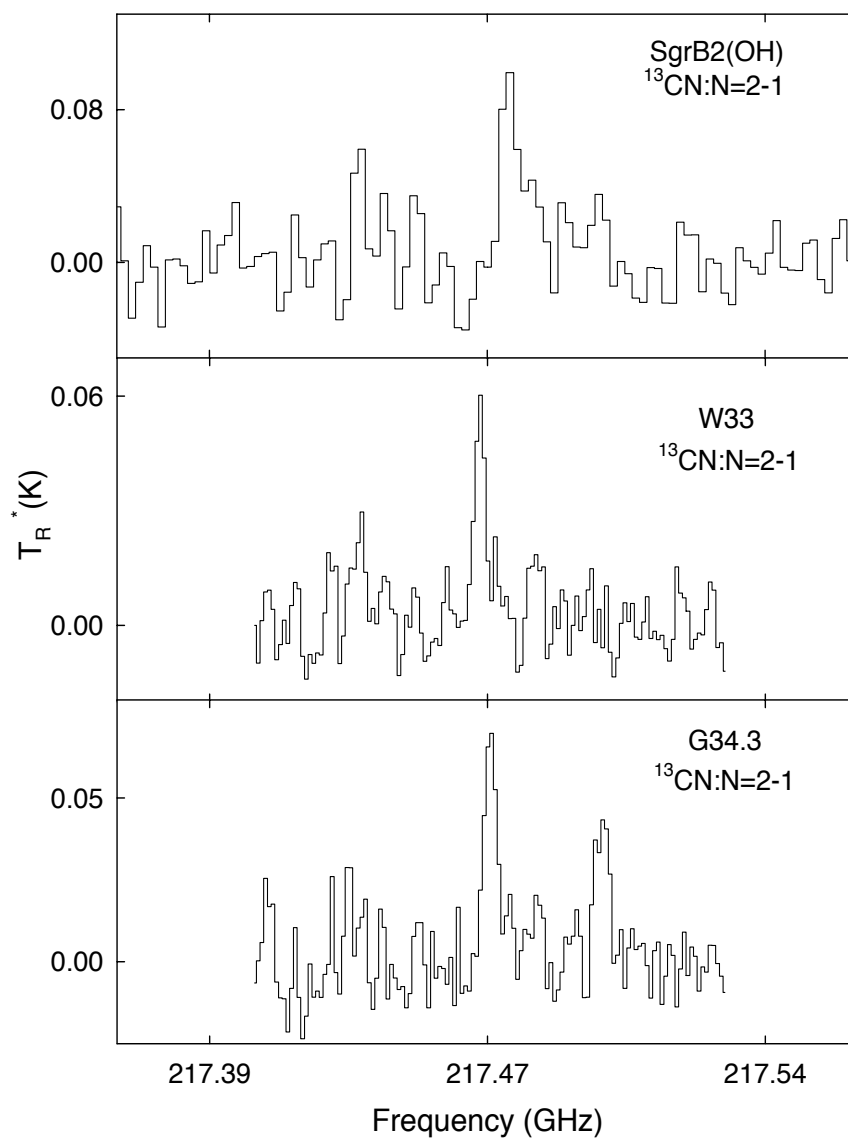


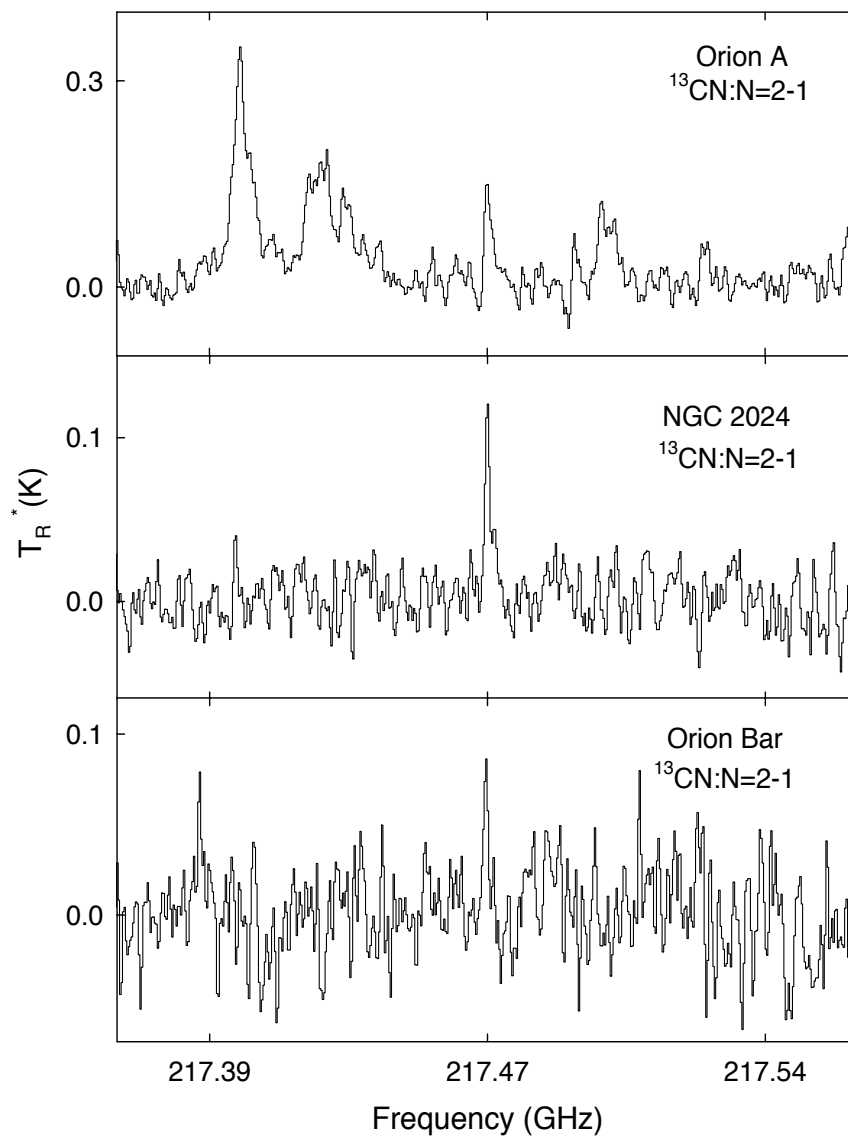


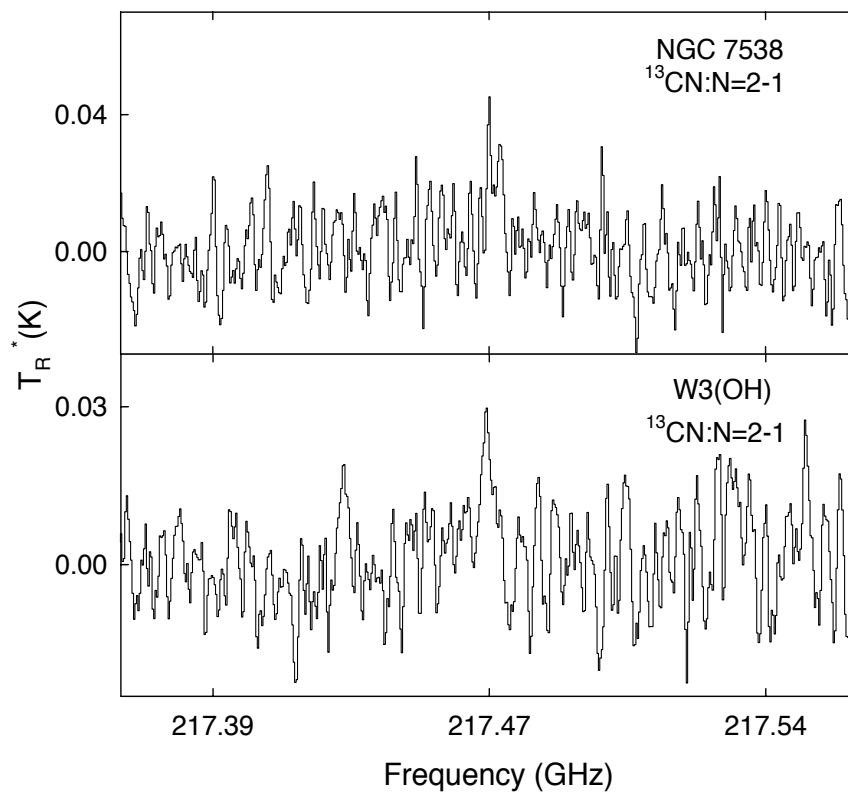


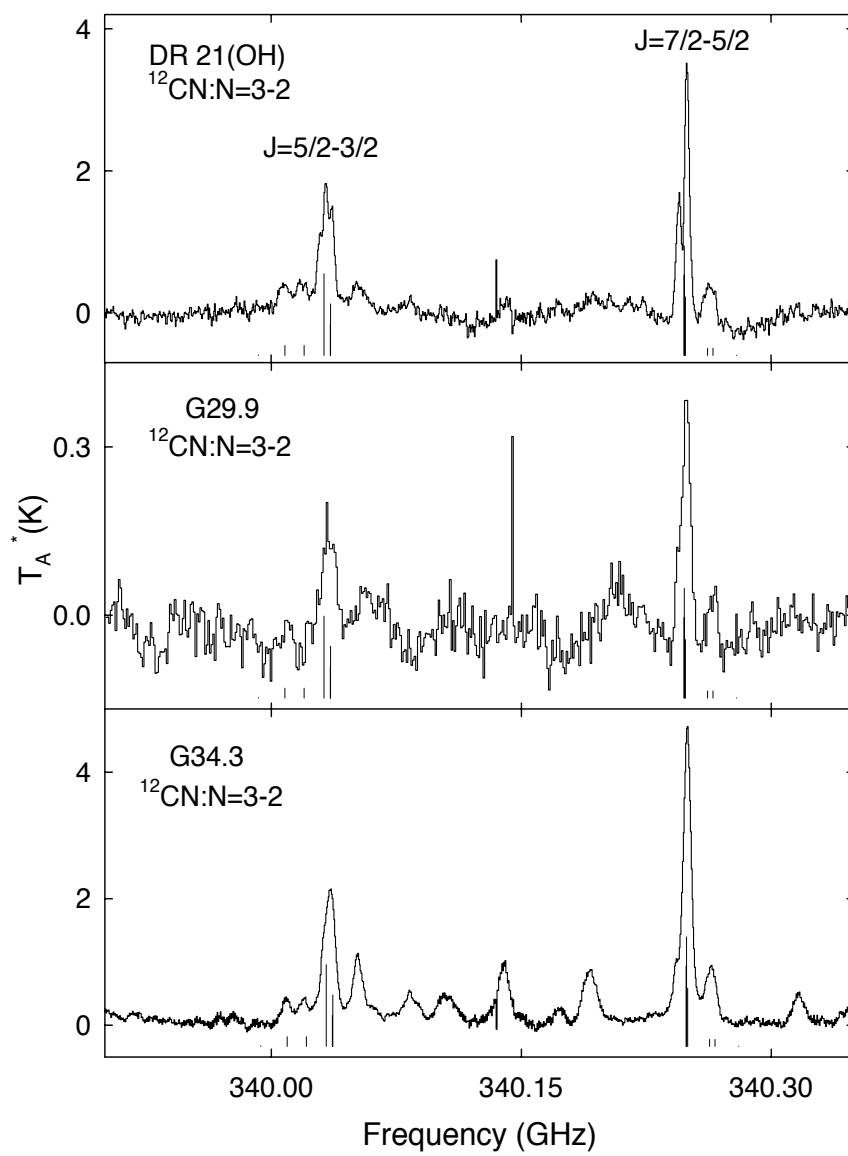


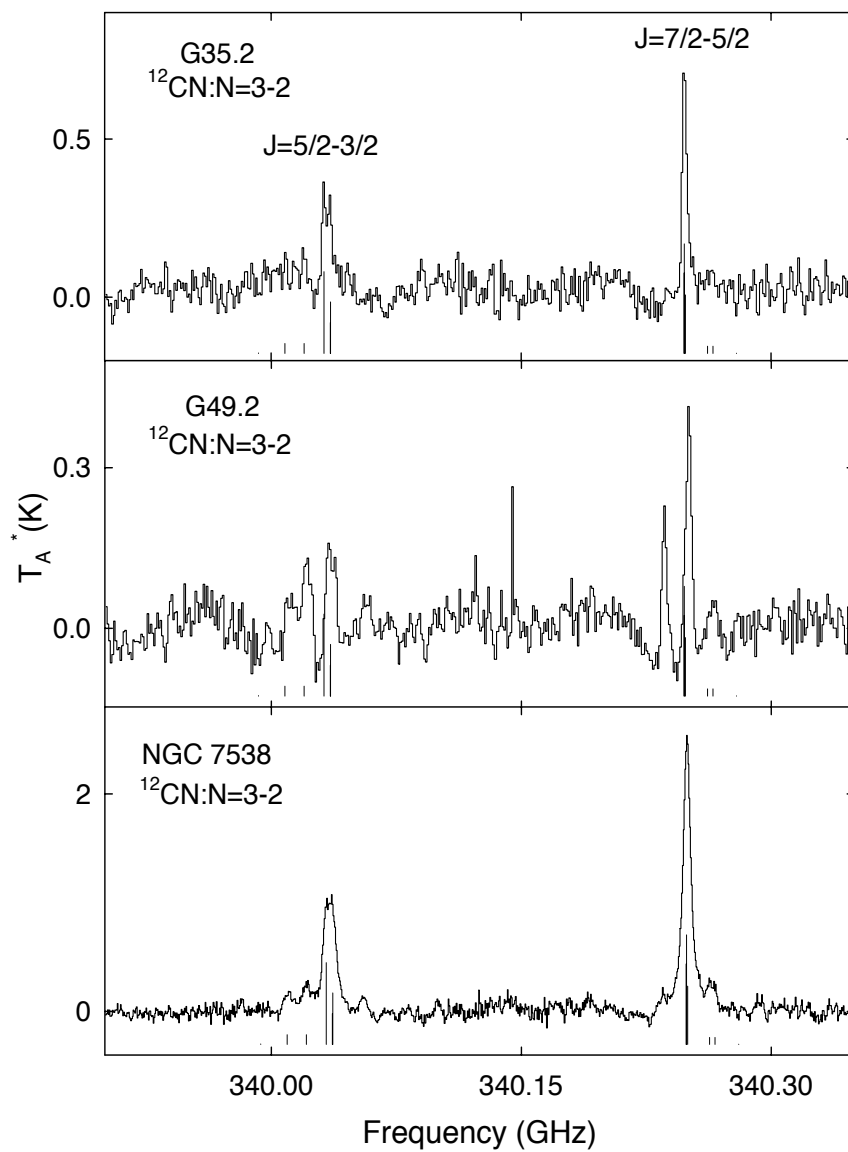


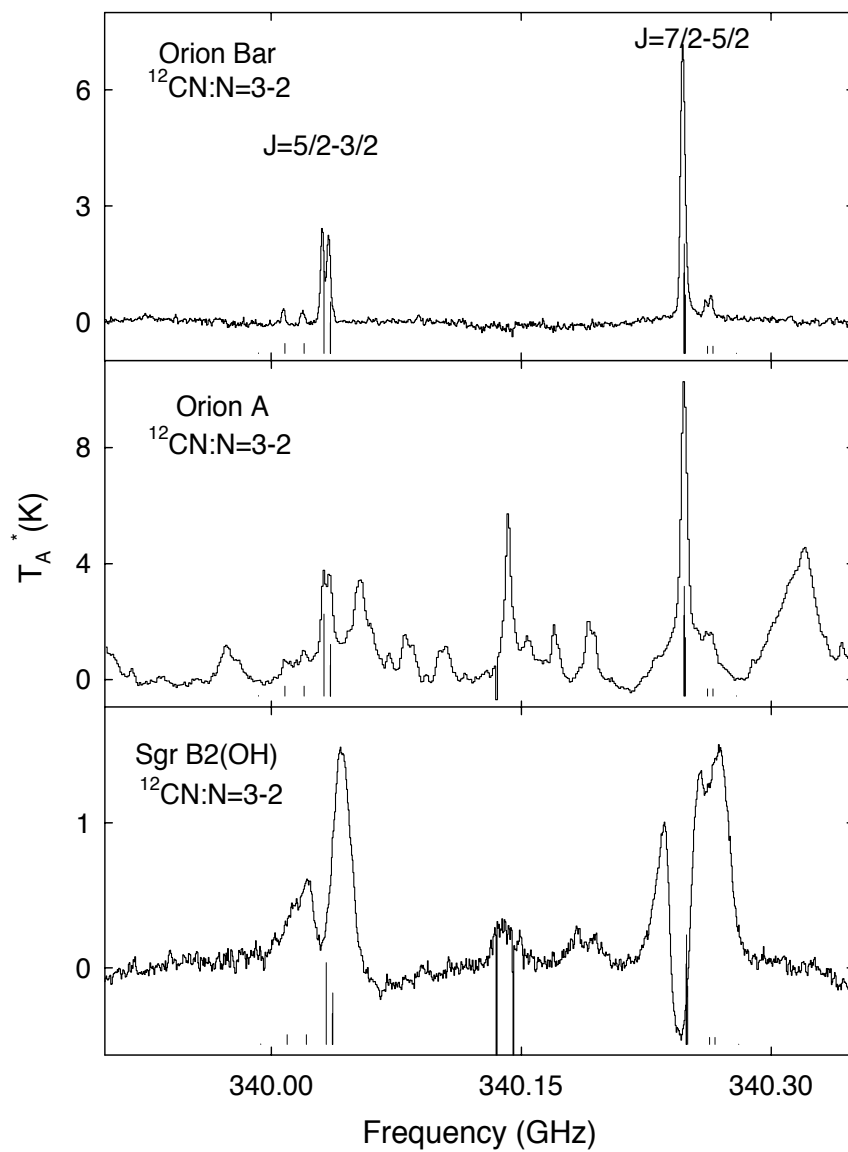


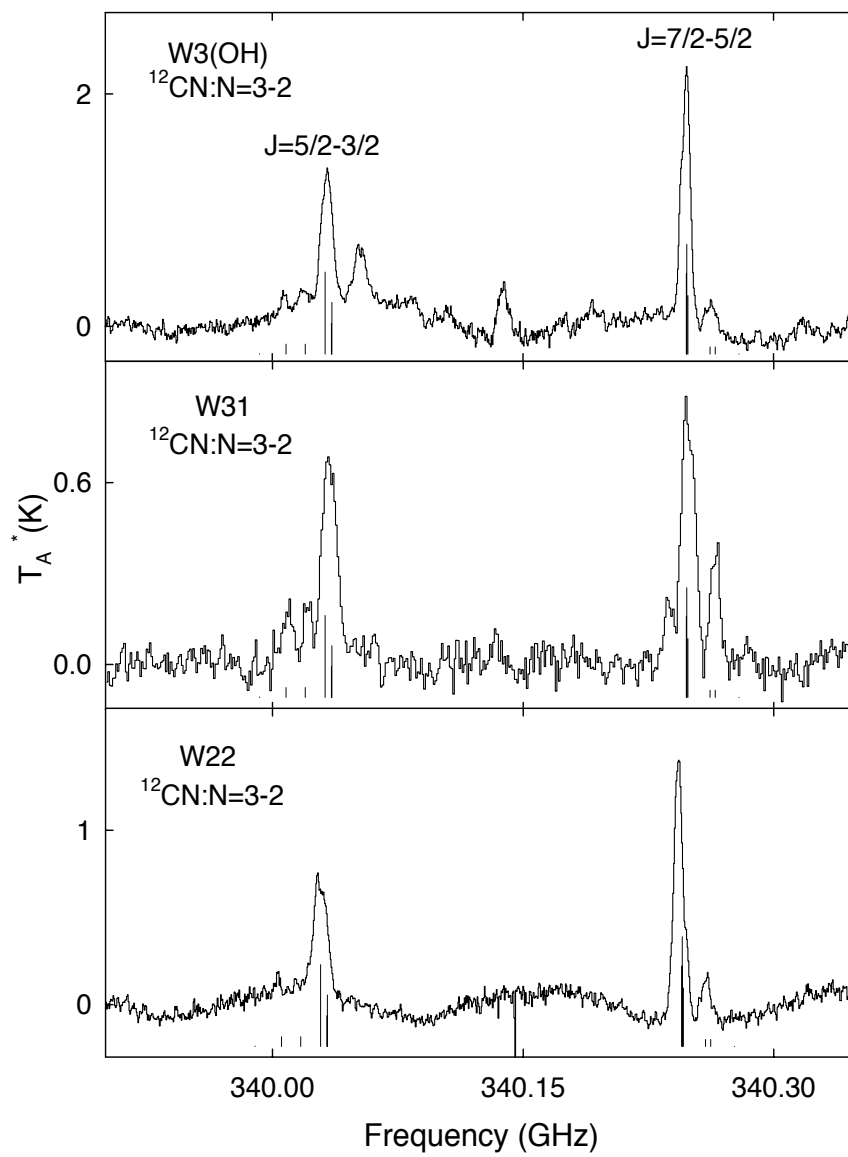


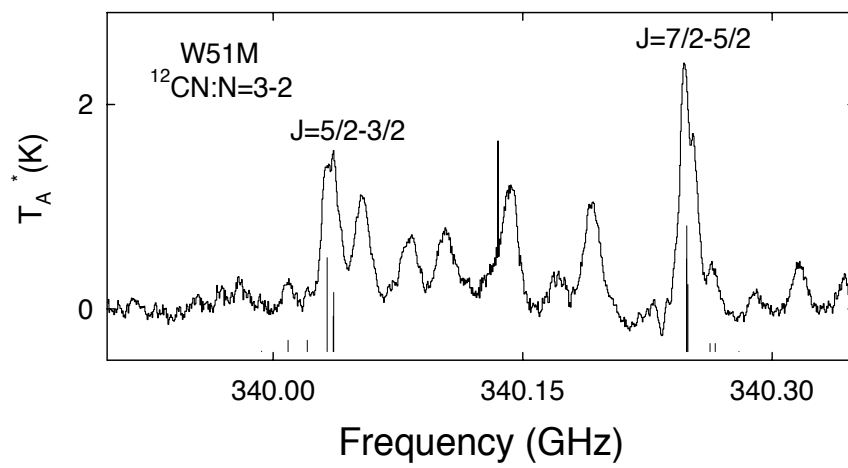


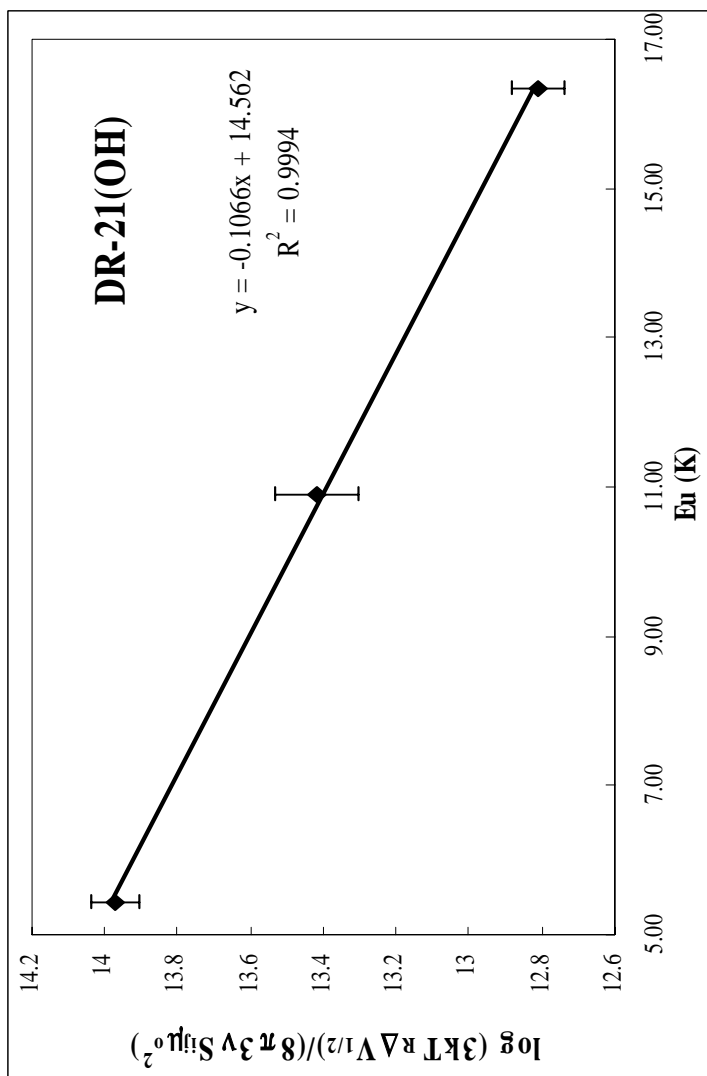


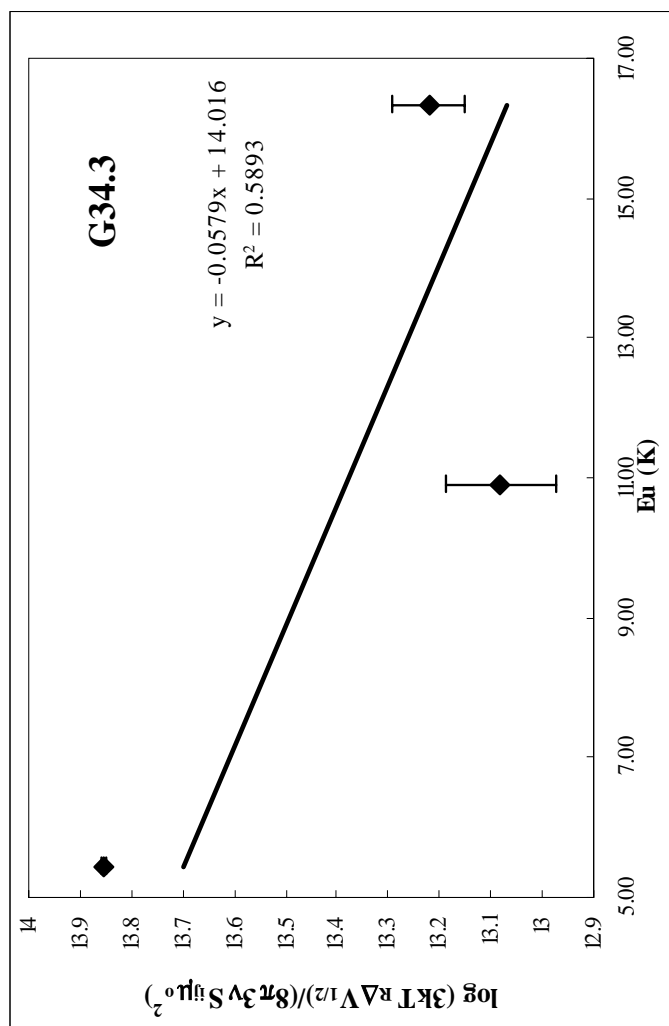


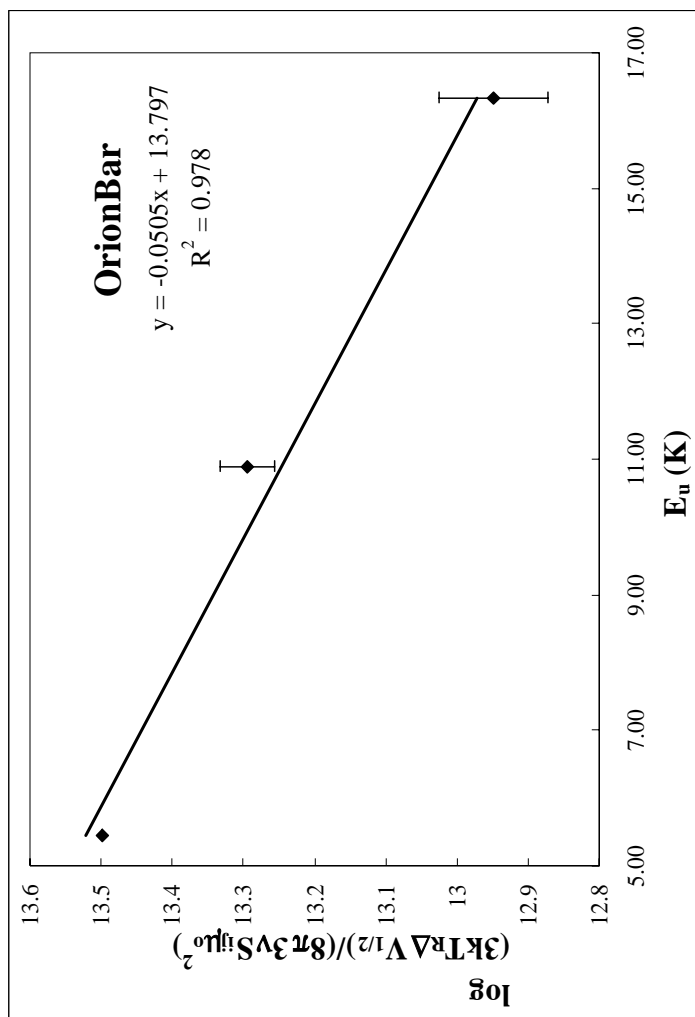


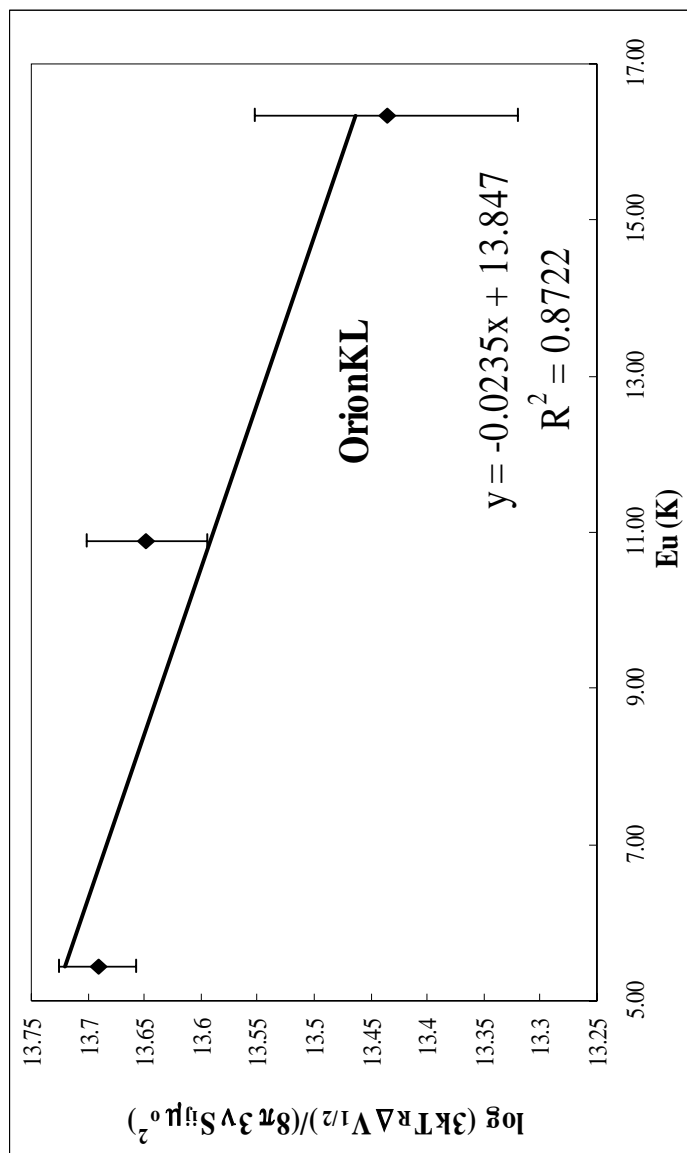


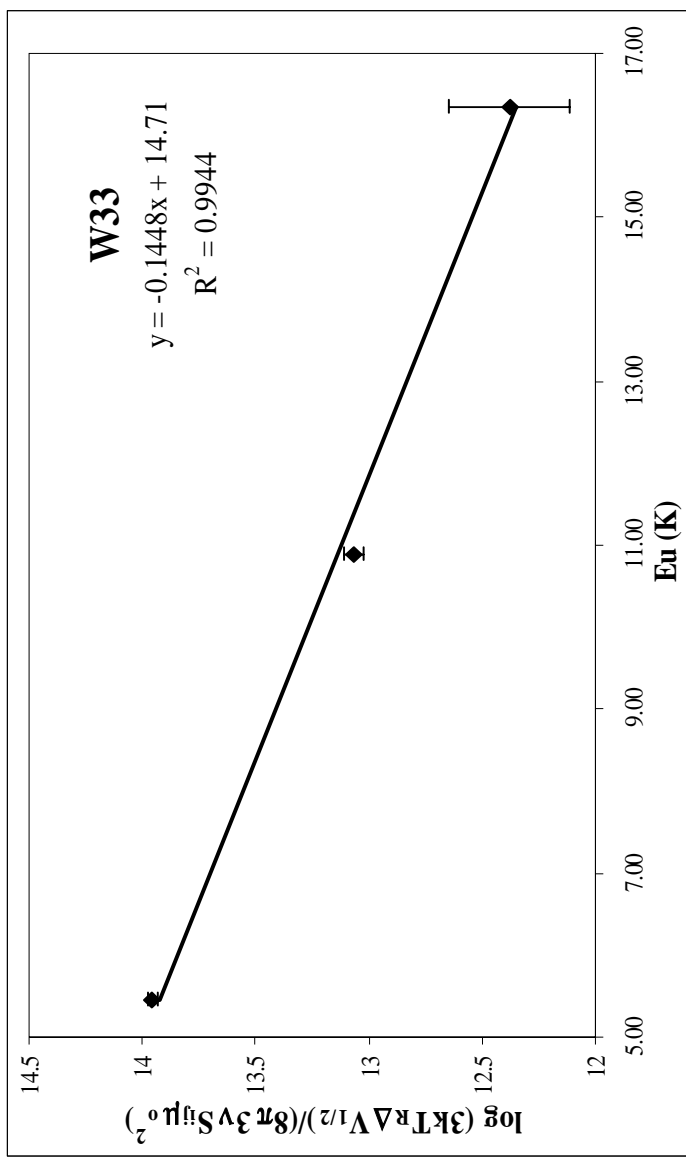


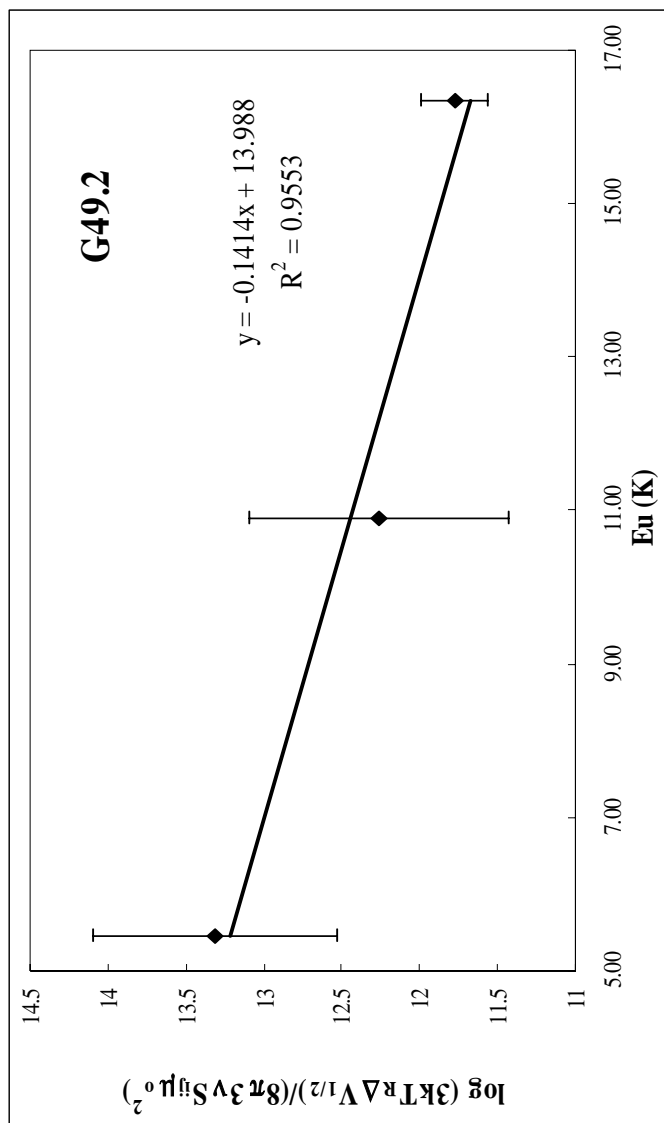


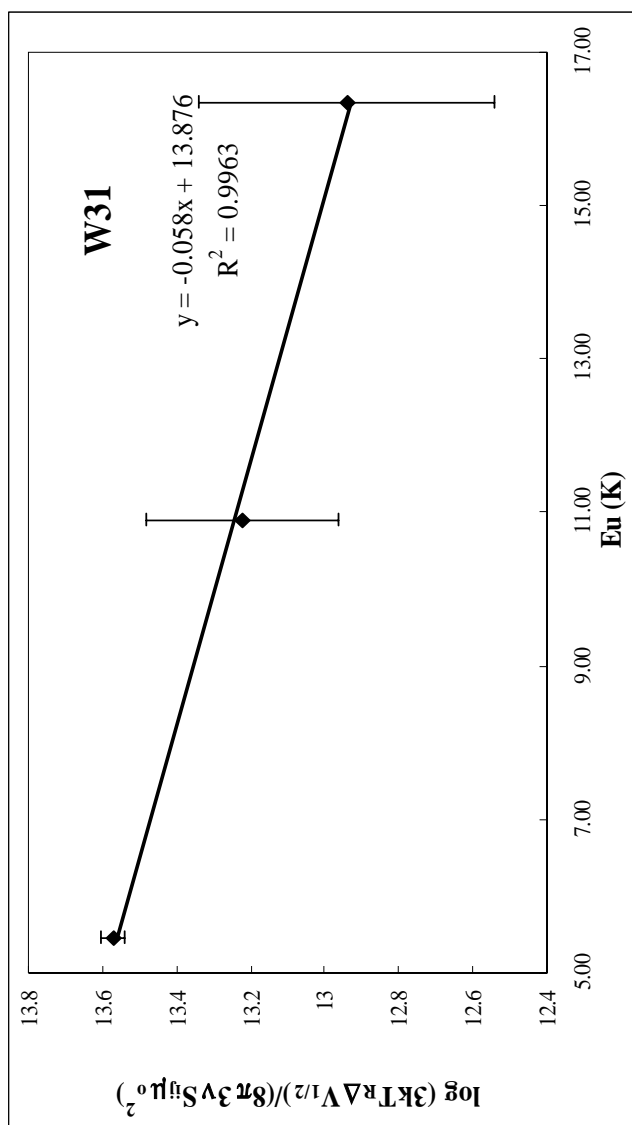


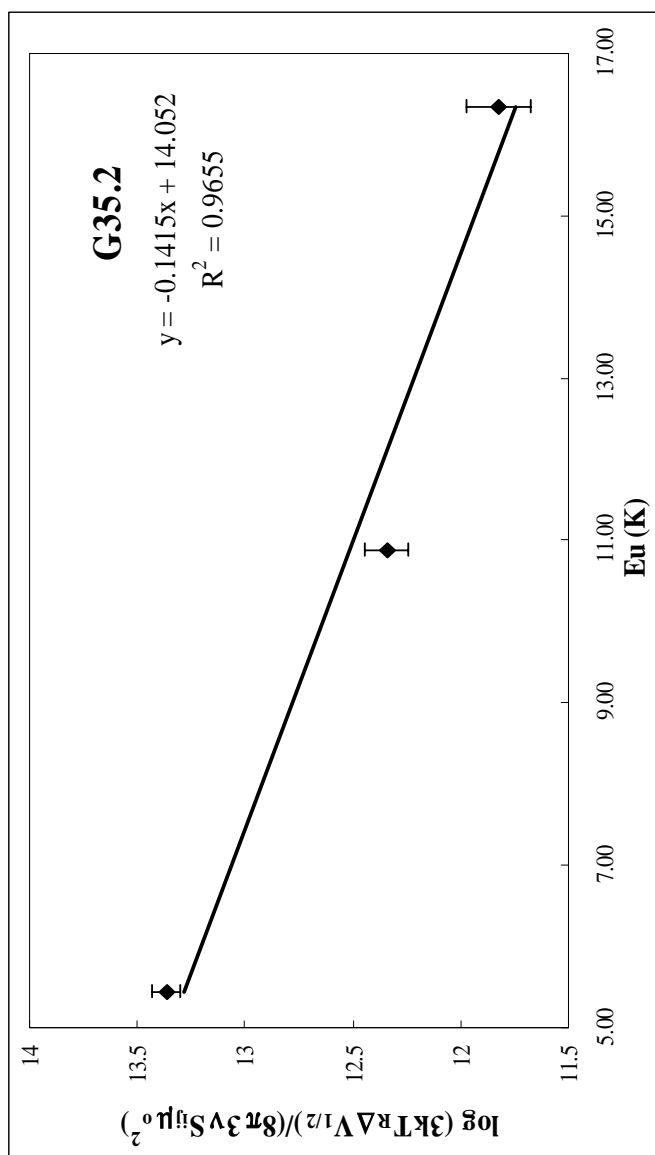


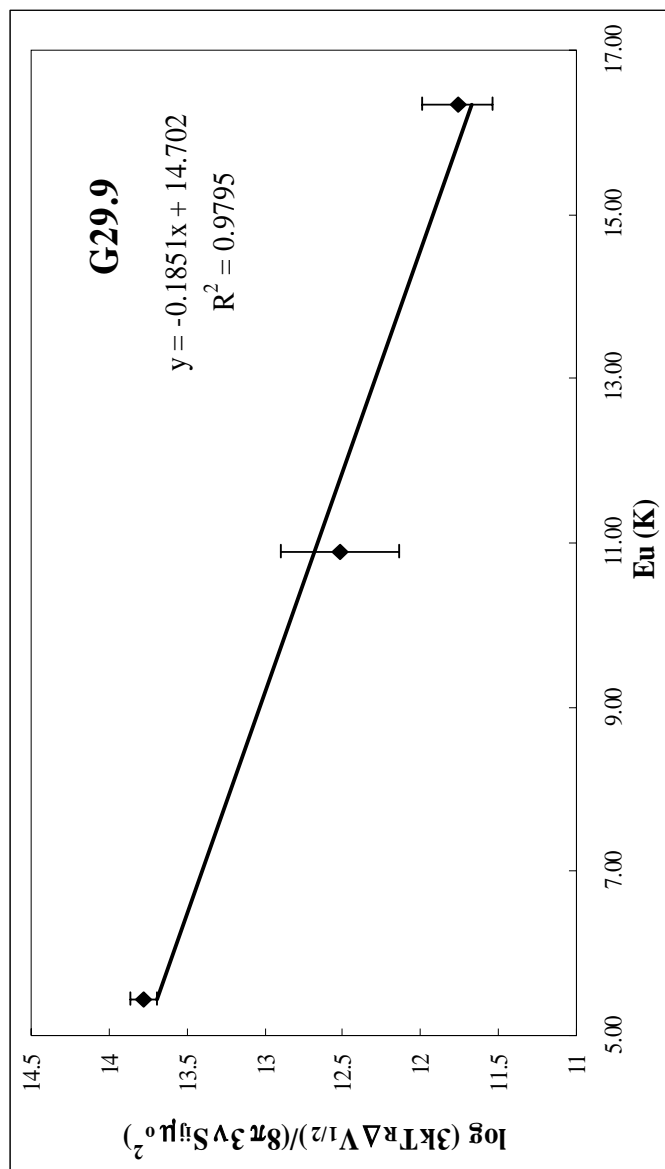


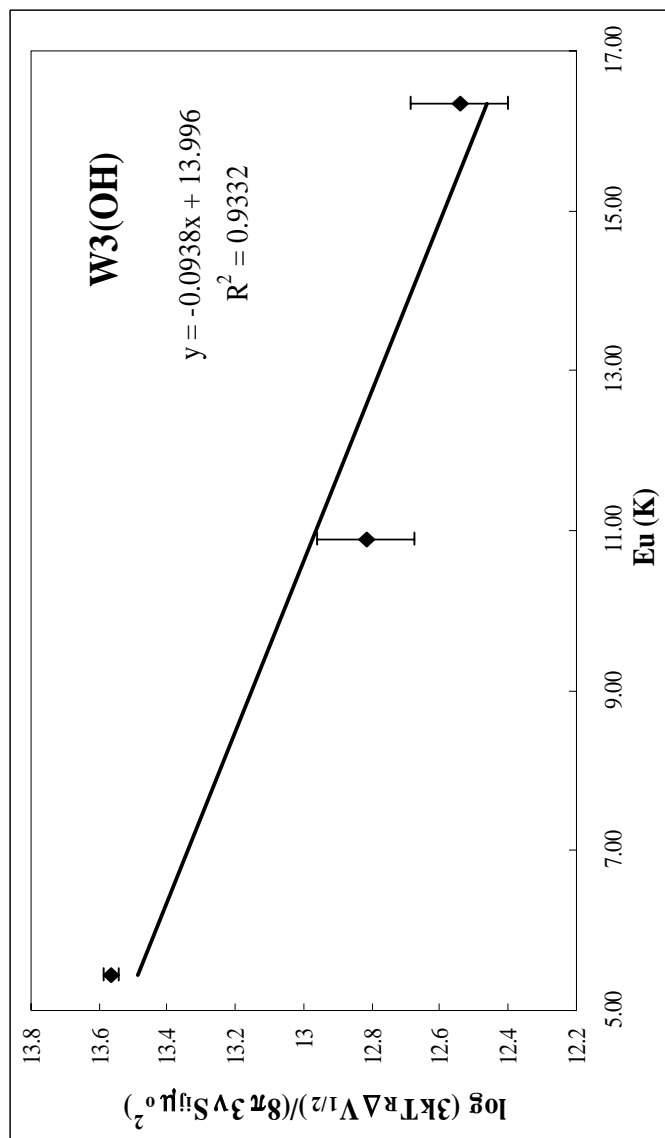


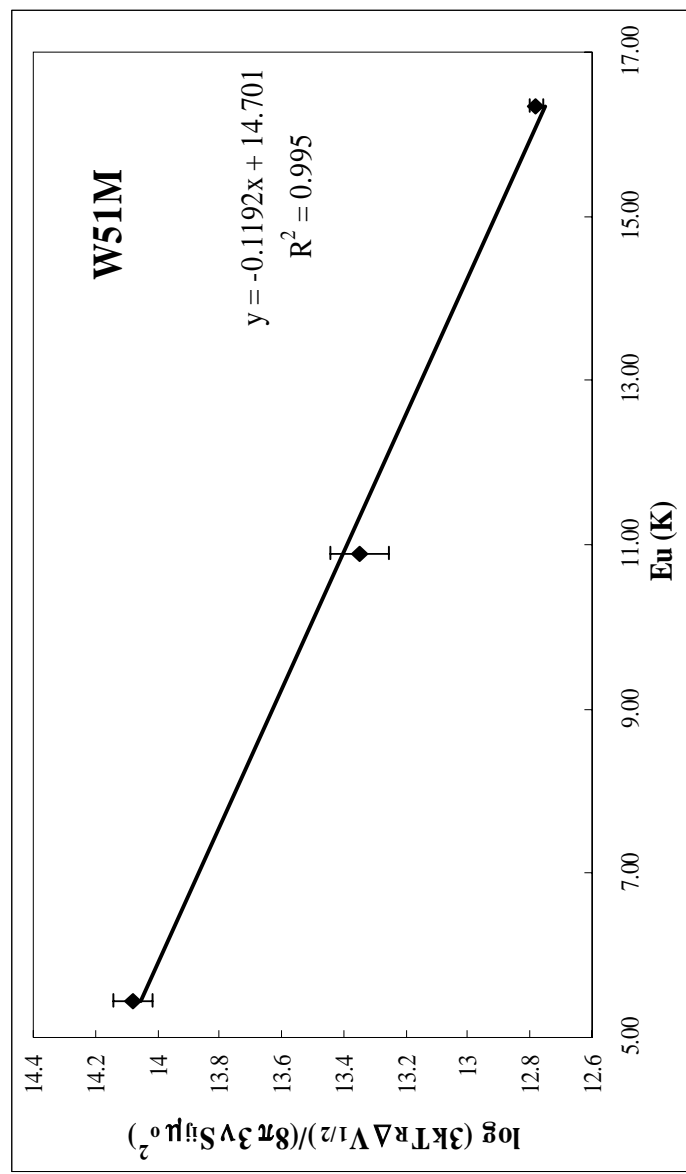


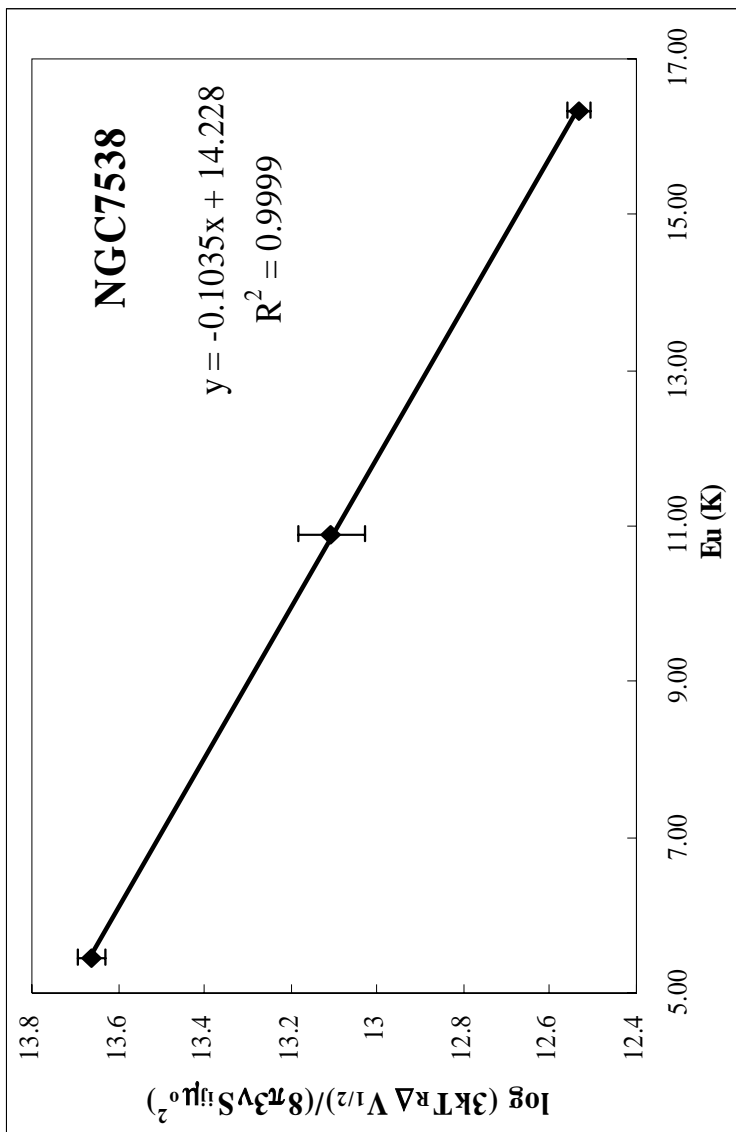












REFERENCES

- Ali, A., Shalabiea, O.M., El-Nawawy, M.S., & Millar, T.J. 2001, MNRAS, 325, 881
- Bachiller, R., Forveille, T., Huggins, P.J., & Cox, P. 1997a, A&A, 324, 1123
- Biegging, J. H. & Tafalla, M. 1993, AJ, 105, 576
- Black, J.H., & van Dishoeck, E.F. 1988, ApJ, 331, 986
- Bockelee-Morvan, D., Crovisier, J., Mumma, M. J. & Weaver, H. A. The composition of cometary volatiles. In Festou, M. C., Keller, H. U. & Weaver, H. A. (eds.) Comets II, 391–423 (Univ. Arizona Press, Tucson, 2005)
- Bockelee-Morvan, D., Despois, D., Paubert, G., Colom, P., & Crovisier, J. 1990, IAU Circ., 5020
- Boothroyd, A.I. and Sackmann I-J 1999, ApJ, **510**, 232
- Bujarrabal, V., Fuente, A., & Omont, A. 1994, A&A, 285, 247
- Charbonnel, C. 1995, ApJ, 453, L41
- Churchwell, E. 1980, ApJ, 240, 811
- Crovisier, J. & Bockelee-Morvan, D. 1999, SSRv, 90, 19
- Crovisier, J. et al. 2004, A&A, 418, 1141
- Dame, T.M. et al. 1987, ApJ, 322, 706
- Daniel, F., Cernicharo, J., & Dubernet, M.-L. 2006, ApJ, 648, 461
- Eggleton, Peter P., Dearborn, David S. P., & Lattanzio, John C. 2006, Science, 314, 1580
- Eggleton, Peter P., Dearborn, David S. P., & Lattanzio, John C. 2007, preprint (astro-ph/0611609)
- Greaves, J.S. & Holland, W.S. 1997, A&A, 327, 342
- Groenewegen, M.A.T., Baas, F., de Jong, T., & Loup, C. 1996, A&A, 306, 241
- Halfen, D.T. et al. 2006, ApJ, 639, 237

- Henkel, C., Güsten, R., and Gardner, F.F. 1985, *A&A*, **143**, 148
- Henkel, C., Walmsley, C.M., and Wilson, T.L. 1980, *A&A*, **82**, 41
- Henkel, C., Wilson, T.L., and Bieging, J. 1982, *A&A*, **109**, 344
- Henkel, C., Wilson, T.L., Walmsley, C.M., and Pauls, T. 1983, *A&A*, **127**, 388
- Herwig, F. and Austin, S.M. 2004, *ApJ*, **613**, L73
- Hinkle, K.H., Lambert, D.L., & Snell, R.L. 1976, *ApJ*, 210, 684
- Howe, D.A., Hartquist, T.W., & Williams, D.A. 1994, *MNRAS*, 271, 811
- Hubbard, E.N. & Dearborn, D.S.P. 1980, *ApJ*, 239, 248
- Huggins, P.J. 1987, *ApJ*, 313, 400
- Humphreys, R.M., Helton, L.A., & Jones, T.J. 2007, *AJ*, 133, 2716
- Iben, I., Jr. and Renzini, A. 1983, *ARA&A*, **21**, 271
- Josselin, E., & Bachiller, R. 2003, *A&A*, 397, 659
- Jura, M., Kahane, C., & Omont, A. 1988, *A&A* 201, 80
- Kahane, C. et al. 1992, *A&A*, 256, 235
- Kawakita, H. et al. 2004, *ApJ*, 601, L191
- Keady, J. J., Hall, D. N. B., & Ridgway, S. T. 1988, *ApJ*, 326, 832
- Kemper, F., Stark, R., Justtanont, K., de Koter, A., Tielens, A. G. G. M., Waters, L. B. F. M., Cami, J., & Dijkstra, C. 2003, *A&A*, 407, 609
- Korth, A. et al. 1986, *Nature*, 321, 335
- Kwok, S. 2004, *Nature*, 430, 985
- Lambert, David L., Gustafsson, Bengt, Eriksson, Kjell, Hinkle, & Kenneth H. 1986, *ApJS*, 62, 373
- Langer, W.D. and Penzias, A.A. 1990, *ApJ*, **357**, 477

- Lauria, E. F., Kerr, A. R., Reiland, G., Freund, R. F., Lichtenberger, A. W., Ziurys, L. M., Metcalf, M., & Forbes, D. 2006 First Astronomical Observations with an ALMA Band 6 (211-275 GHz) Sideband-Separating SIS Mixer-preamp (ALMA Memo No. 553); <www.alma.nrao.edu/memos/>
- Liszt, H. S., & Lucas, R. 1995, *A&A*, 299, 847
- Liszt, H. S., & Lucas, R. 1996, *A&A*, 314, 917
- Liszt, H. S., & Lucas, R. 1998, *A&A*, 339, 561
- Liszt, H., & Lucas, R. 2001, *A&A*, 370, 576
- Liszt, H., & Lucas, R. 2002, *A&A*, 999, 888
- Liszt, H.S., Lucas, R., & Pety, J. 2006, *A&A*, 448, 253
- Lucas, R., & Liszt, H. 1998, *A&A*, 337, 246
- Lucas, R., & Liszt, H. S. 1996, *A&A*, 307, 237
- Lucas, R., & Liszt, H. S. 2000, *A&A*, 358, 1069
- Lucas, R., & Liszt, H. S. 2002, *A&A*, 384, 1054
- Meier, R., Eberhardt, P., Krankowsky, D., & Hodges, R.R. 1993, *A&A*, 277, 677
- Milam, S.N., Apponi, A.J., Woolf, N.J., & Ziurys, L.M. 2007, *ApJ*, 668, L131
- Milam, S.N., Savage, C., Ziurys, L.M., & Wyckoff, S. 2004, *ApJ*, 615, 1054
- Milam, S. N., Savage, C., Brewster, M. A., Ziurys, L. M., & Wyckoff, S. 2005, *ApJ*, 634, 1126
- Mitchell, D., Lin, R., Carlson, C., Korth, A., Reme, H., & Mendis, D. 1992, *Icarus*, **98**, 125
- Nercessian, E., Guilloteau, S., Omont, A., & Benayoun, J. J. 1989, *A&A*, 210, 225
- Penzias, A.A. 1980, *Science*, **208**, 663
- Pratap, P., Dickens, J.E., Snell, R.L., Miralles, M.P., Bergin, E.A., Irvine, W.M., & Schloerb, F.P. 1997, *ApJ*, 486, 862

- Sanchez Contreras, C., Bujarrabal, V., Neri, R., & Alcolea, J. 2000, *A&A*, 357, 651.
- Savage, C., Apponi, A.J., Ziurys, L.M., and Wyckoff, S. 2002, *ApJ*, **578**, 211
- Schoier, F.L. & Olofsson, H. 2000, *A&A*, 359, 586
- Schutte, W.A., Allamandola, L.J., & Sandford, S.A. 1993, *Icarus*, 104, 118
- Snyder, L. E., Palmer, P., & de Pater, I. 1989, *AJ*, 97, 246
- Sorrell, W.H. 2001, *ApJ*, 555, L129
- Teyssier, D., Hernandez, R., Bujarrabal, V., Yoshida, H., & Phillips, T. G. 2006, *A&A*, 450, 167
- Timmes, F.X., Woosley, S.E. and Weaver, T.A. 1995, *ApJSS*, **98**, 617
- Tsuji, T. 1973, *A&A*, 23, 411
- Wannier, P.G. & Sahai, R. 1987, *ApJ*, 319, 367
- Wickramasinghe, N.C. 1975, *MNRAS*, 170, 11
- Woods, P. M., Schöier, F.L., Nyman, L.-Å., & Olofsson, H. 2003, *A&A*, 402, 617
- Ziurys, L. M., Milam, S. N., Apponi, A. J. & Woolf, N. J. 2007, *Nature*, 447, 1094
- Ziurys, L.M. 2006, *PNAS*, 103, 12274
- Zolensky, M.E. et al. 2006, *Science*, 314, 1735